STRESS WAVE PROPAGATION IN A "SIMPLIFIED SURROGATE TIBIA" SUBJECTED TO BLAST LOADING

By

Davison Takawira Seenzayi

A thesis presented in fulfillment of the requirements for the degree of Master of Science in Mechanical Engineering.

October 2023

ACKNOWLEDGEMENTS

The Blast Impact and Survivability Research Unit (BISRU) has a fundamental mission of safeguarding the lives of those exposed to landmines through its research endeavours. Being part of this exceptional academic community, surrounded by dedicated researchers committed to preserving life, has been an extraordinary and privileged experience during my pursuit of a postgraduate degree.

I am deeply indebted to Professor Steeve Chung Kim Yuen, who served as my supervisor, providing invaluable guidance and insights that allowed me to maintain focus and analyse the outcomes of this dissertation. Additionally, I extend my gratitude to Professor Gerald Nurick and Dr Trevor Cloete, whose expertise in the field of high strain rate impact and assistance with instrumentation and data collection during the blast tests were instrumental to the success of this study.

Special recognition goes to the skilled team of technical officers within the Department of Mechanical Engineering at UCT. Pierre Smith and Laureen Bailey deserve heartfelt acknowledgment for their invaluable practical advice and their exceptional contributions to the manufacturing of simplified tibia components, strain gauge mounting, and the horizontal ballistic pendulum.

I am sincerely grateful to all the individuals who crossed my path and provided support throughout the completion of this study. Lastly, I wish to express my profound appreciation to UCT and the Beit Trust Foundation for their financial support, without which this study would not have been possible

PLAGIARISM DECLARATION

I, Davison Takawira Seenzayi, affirm that this dissertation represents my original work. It is being submitted as a partial fulfilment of the requirements for the Master of Science in Engineering degree at the University of Cape Town and has not been presented in this or any other form for a degree at any other university.

Signed by candidate

Davison Takawira Seenzayi

October 2023

ABSTRACT

Landmines are a continuous and serious threat to mankind, resulting in thousands of casualties globally each year. Casualties have risen due to the proliferation of improvised explosive devices (IEDs), cluster munition remnants, and other explosive remnants of war. In these terrible occurrences, both the civilians and military and security personnel suffer great losses. Despite anti-mine awareness programs and the development of new mitigating measures, the number of landmine victims continues to rise. While anti-vehicle and anti-personnel landmines offer major hazards, anti-vehicle landmines create much larger energy transfers than anti-personnel landmines, resulting in more severe and complicated lower limb injuries frequently presenting distinct rehabilitation issues.

Understanding the mechanics leading to tibia injuries in anti-vehicle landmine occurrences helps develop and enhance safety and well-being of vehicle occupants exposed to anti-vehicle landmine blast scenario. The study of stress wave propagations in the tibia during an anti-vehicle landmine blast aids in scientific understanding of blast injuries produced by anti-vehicle landmines by refining current ideas, discovering novel phenomena, and filling information gaps. This study aimed to understand the stress wave propagation through the tibia caused by an anti-vehicle landmine explosion. Simplified tibia models were developed and used in an experimental approach for capturing blast-induced stress wave propagations through the tibia. The floor of a vehicle was represented by deformable and non-deformable witness plates. Aluminium tubular structures were used to develop simplified surrogate tibia models with different cross-sections which used to calibrate a Finite Element Model (FEM). Strain gauges were installed on the centre of tubular structure to record the direct stress induced by the blast load.

A numerical model, developed using LS-Dyna software, was validated using the experimental blast test stress results on the tubular structures. Once validated, the numerical model was updated by replacing the tubular structures with a 3D CAD tibia. The replacement of tubular structures with tibia model was undertaken to enable the investigation of stress distribution within the tibia with greater precision and accuracy. A parametric study was, thereafter, carried out investigating the effect of geometry on stress propagations and its correlation with associated injuries. The parametric study successfully explored the blast induced stress waves propagations and its distribution within the tibia model during a blast event. The tibia model experienced a compressive load cycle followed by a tensile load cycle as the stress waves got reflected upon encountering boundaries. Analysis of stress-time response graphs revealed the highest strain levels at the interface between the tibia model and the witness plate, indicating greater susceptibility to blast injuries in the lower extremities, particularly at the point of contact.

In the numerical simulations aluminium was implemented as the “bone” material for simplification. It should be noted that bone is a complex composite material which is hard to characterise and not considered in the scope of this study. The focus of this study was to gain an understanding how the stress wave resulting from the blast load would propagate in a structure with varying geometries such as a tibia and analysis of the peak stresses. The information gained from these simulations provided valuable insights into injuries caused by blast and their potential effects on the tibia when subjected to anti-vehicle landmine explosions. The severity of the injury depends on the material properties and geometry of the tibia. Additionally, the study explored the effect of deformable and non-deformable witness plate on the load transmitted to the tibia, resulting in different injury mechanisms and patterns.

TABLE OF CONTENTS

LIST OF FIGURES

LIST OF TABLES

NOMENCLATURE

The Ottawa Treaty

Formally known as the "Convention on the Prohibition of the Use, Stockpiling, Production and Transfer of Anti-Personnel Mines and on their Destruction," this international treaty was established as binding law on March 1, 1999 [1]. Its primary objective is to prohibit the manufacturing, trading, and utilization of anti-personnel mines while mandating countries to eliminate their existing stockpiles and clear their territories of these mines. Furthermore, the treaty calls upon governments to aid poor nations in their efforts to clear affected land and support the rehabilitation of survivors. However, it is important to note that the scope of the treaty is limited to anti-personnel mines and does not encompass other types of explosive devices targeting individuals.

Countries that have become parties to the treaty are referred to as States Parties and are obligated to destroy their stockpiles within a period of four years and clear mine-affected areas within ten years [1]. Financial aid for both mine victims and mine clearance are also required. The treaty defines an "anti-personnel mine" as a mine designed to be detonated through the presence, proximity, or contact of a person, resulting in incapacitation, injury, or death to one or more persons. Additionally, the treaty defines an "anti-vehicular/anti-tank mine" as a mine intended to be detonated through the presence, proximity, or contact of a vehicle and equipped with an anti-handling device [1].

The Mine Ban Treaty, with participation from over 80% of countries worldwide, stands as one of the most widely accepted international agreements. Currently, among the 164 States Parties, 132 countries have both signed and ratified the treaty, while 32 countries have acceded to it. It is noteworthy that most of these non-party states do not engage in the production or use of anti-personnel mines [2].

NATO Task Group

The establishment of the NATO Task Group HFM-089/TG-024 aimed to investigate and evaluation of the existing test methods utilized for analysing protective footwear. Their objectives were to identify the advantages and constraints associated with these different test methods and to establish comprehensive testing guidelines. The goal was to ensure that test results obtained by different nations would be both meaningful and comparable [3].

The Canadian Centre for Mine Action Technologies

The Canadian Centre for Mine Action Technologies (CCMAT) was established in 1998 to develop low-cost, sustainable technologies for mine action and to work towards their successful deployment in the field through research and development, testing and evaluation, and active communication with the user community [4].

LIST OF ABBREVIATIONS

AP	Anti-personnel
ATD	Anthropomorphic Test Devices
AV	Anti-vehicle
BISRU	Blast Impact and Survivability Research Unit
CCMAT	Canadian Centre for Mine Action Technologies
CLL	Complex Lower Leg
CSIR	Council for Scientific and Industrial Research
DRDC	Defense Research and Development Canada
DSTL	Defense Science and Technology Laboratory
FEM	Finite Element Model
FSL	Frangible Surrogate Leg
HUMOS	Human Model for Safety
IABG	Industrieanlagen-Betriebsgesellschaft (German)
IED	Improvised explosive device
LEAP	Lower Extremity Assessment Procedure
LLI	Lower Limb Impactor
MIL-Lx	Military Lower Extremity
MTS	Mine Trauma Score
NATO	North Atlantic Treaty Organization
PMHS	Postmortem Human Surrogates
PPE	Personal protective equipment
SHPB	Split-Hopkinson Pressure Bar
SSL	Simplified Surrogate Leg
TROSS	Test Rig for Occupant Safety System

LIST OF SYMBOLS

A	Gain Amplification
B	Bridge Factor
BW	Body weight
d	Diameter
E	Modulus of Elasticity
F	Strain gauge factor for Aluminium
H_{exp}^{d}	Heat of detonation of the actual explosive
H_{TNT}^{d}	Heat of detonation of the TNT
J	Polar moment of inertia
L	Length
R	Distance away from the epicentre of the volume of the explosive
P	Pressure
P_{so}	Over-peak Pressure
P_o	Ambient pressure
V	Voltage
V_{in}	Input voltage
V_{out}	Output voltage
W	Charge mass
W_{eq}	TNT equivalent weight
W_{exp}	Weight of the actual explosive
Z	Scaled distance
ρ	Density
ν	Poisson ratio
σ	Stress-induced
ε_m	Strain induced

CHAPTER 1 – INTRODUCTION

1.1 Background Information

Landmines have posed a significant threat to humanity for decades, resulting in numerous casualties reported globally each year. Prior to the proliferation of improvised explosive devices (IEDs), landmines were the primary cause of explosive injuries in conflict zones. For example, during the Vietnam War, over 40,000 people were killed and 60,000 maimed by landmines [5]. The widespread presence of landmines in Afghanistan during Operation Enduring Freedom and Iraq during Operation Iraqi Freedom also led to thousands of casualties[6]. Recently, in the 2022 Russia-Ukraine conflict, landmines and other explosive remnants of war were responsible for over 300 casualties in early 2023, accounting for about 77 % of the total casualties that year [7].

The increase in landmine injuries has been further exacerbated in the last few decades by the widespread use of IEDs, cluster munition remnants, and other explosive remnants of war. These injuries disproportionately affect civilians, who accounted for over 75 % of landmine casualties in recent years [8]. Understanding the biomechanical response of the lower limbs to blast loading from landmines and IEDs provides valuable insights into the injury mechanisms. The lower limbs are particularly susceptible given their proximity to the explosive detonation, and over half of recorded blast injuries from recent conflicts involved the lower extremities [9].

By concentrating analysis on the tibia, the unique challenges and consequences of lower limb blast injuries can be addressed. The tibia is frequently injured in both antipersonnel and anti-vehicle landmine blasts [10]. The NATO Task Group HFM-089/TG-024 was established to study tibia injuries from blast loading to aid the development of preventive measures and treatment strategies. Additional task groups, including HFM-198 and HFM-271, have expanded on this work in recent years[11]. Through biomechanical analysis of tibia response to blast, targeted interventions can be developed to mitigate the devastating impact of landmine injuries.

1.2 Problem Identification

Despite ongoing efforts to ban landmines, landmines continue pose a significant danger, as recent conflicts have shown the devastating and indiscriminate impact [5] [6] [7]. Landmine explosions frequently affect lower limbs due to their proximity to the explosive detonation. The challenge lies in the complex loading circumstances associated with a mine explosion, which requires significant blast mitigation technologies and therapeutic interventions for landmines victims. The tibia is susceptible to damage in both antipersonnel and anti-vehicle explosions due to its proximity to the blast and has relatively little protective muscular cushioning compared to the thigh [12]. It also plays a weight-bearing role hence studying how blast waves propagate through the tibia provides unique insights into lower limb injury mechanisms and allows validation against cadaveric data to inform the development of protective solutions.

Surrogate legs had been designed and developed to investigate the injuries due to landmines. However, existing surrogate leg models using precision synthetic materials have been prohibitively expensive, posing two key challenges for blast injury research [13]. Firstly, the high costs created financial barriers, restricting accessibility for investigating injury biomechanics. Secondly, prior models had lacked intricate anatomy, limiting understanding of actual injury mechanisms and hazards from blasts. The study at that time focused on the development of an affordable, simplified tubular structure to represent the tibia in carrying out blast experiments, thereby eliminating the financial obstacles to the blast injury research. A Finite Element Model for the blast experiment was developed, validated, and subsequently enhanced by incorporating a more complex tibia model. The intricate anatomy of the tibial model used helped to overcome the limitations of comprehending the true injury mechanisms.

1.3 Aim and Objectives

The aim of this study was to gain an understanding of how the blast induced stress waves propagate through a simplified tibia structure subjected to blast loading through deformable and non-deformable witness plate.

The main objectives of this research were to:

- Design and develop an experiment to perform blast tests on tubular structures with various cross sections representing a tibia.
- Modify an existing horizontal ballistic pendulum to accommodate tubular structures with various cross sections.
- Design and develop a numerical model in LS-Dyna to simulate the experimental blast tests performed.
- Validate the numerical model with experimental blast test results and update the model to include a human tibia model.
- Assess how stress wave propagate in a 3D Tibia model and perform a parametric study to assess “geometry” effect.
- Draw conclusions and recommendations based on the results and discussions.

1.4 Scope and limitations

The study was focused on understanding the propagation of blast-induced stress waves through a simplified surrogate tibia when subjected to blast loading. Tibia has a complex shape that presents challenges in modelling and manufacturing, hence the most effective approach to investigate its response was using Finite Element Method (FEM). Consequently, experiments were conducted using aluminium tubular structures with various cross-sections to validate the accuracy and reliability of the FEM model. Once the FE model was successfully validated, it was updated by incorporating a three-dimensional (3D) CAD model of the tibia.

The research was limited to the blast response of the tibia and did not include the femur or foot bones, as well as soft tissue since it is a major weight-bearing bone and tibia injuries are often more severe and have greater clinical implications compared to injuries in other parts of the lower limb. This may have limited the ability of the study to accurately represent the overall response of the tibia to blast loading.

Furthermore, the study encountered limitations in the bone modelling process, particularly in obtaining accurate material data of the tibia bone, given the variations in bone properties along its thickness and length. Therefore, Aluminium was adopted as a homogeneous material in the models in achieving the primary aim on investigating stress wave magnitude and propagation, serving as an initial step towards comprehending the complexities associated with the geometry of the bone.

1.5 Plan of Development

A literature review was presented in Chapter 2 aimed to define the nature and characteristics of landmines, including their blast wave properties. Clinical data related to landmine victims and the anatomy of the human lower leg were also discussed. Additionally, the review provided a brief overview of surrogate lower leg models and the experimental methods used to study landmine-related injuries.

In Chapter 3, the report described the geometry and material characterization process carried out to determine the shape and materials used in the development of surrogate tibia models. Details about the experimental procedures and the collection of test results were also included. Chapter 4 then presented the obtained outcomes and a comprehensive discussion of the results from the conducted blast experiments.

Chapter 5 explained the numerical method employed to simulate the blast experiments, along with the design of the finite element model utilized in the simulations. The results obtained from the numerical modelling were presented in Chapter 6, along with a detailed discussion and comparison between the experimental data and the numerical results.

Chapter 7 focused on a parametric study that utilized numerical modelling to analyse blast loading on a pre-designed 3D CAD Model of a tibia. The discussions in this chapter examined the anticipated injury characteristics and the impact of cross-sectional shape and witness plate thickness.

Lastly, Chapter 8 drew conclusions regarding the injury mechanism based on the findings and provided recommendations to improve the precision of both experimental and numerical methodologies employed. The plan of development of the research report established a clear structure and logical flow of information, as depicted in Figure 1, which highlights the key sections and their emphasis in the report.

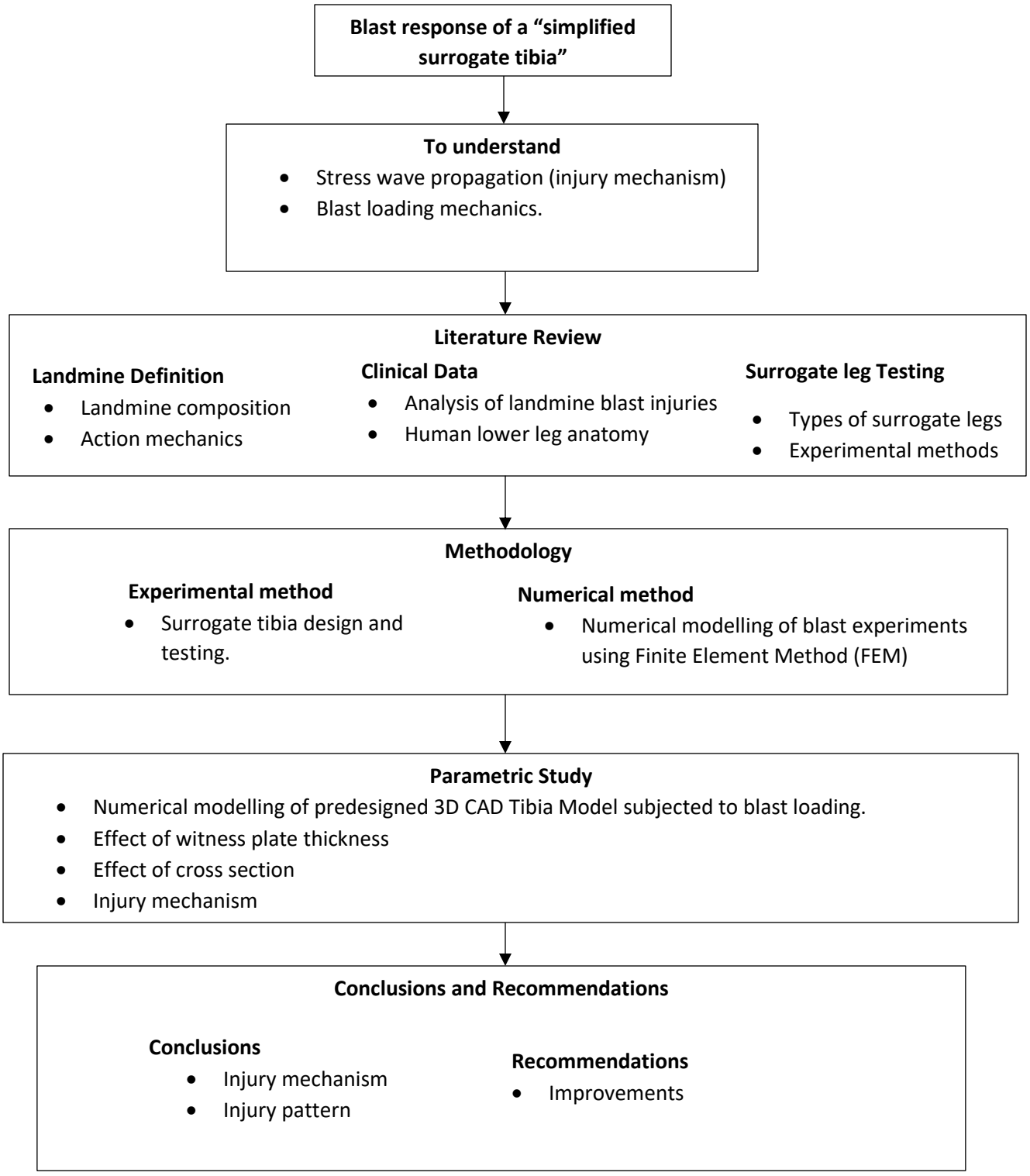

Figure 1 : The flowchart showing the primary sections of the report and highlights the key aspects examined.

CHAPTER 2 - LITERATURE REVIEW

2.1 Introduction

The conflicts in the world have led to an increase in the number of casualties and loss of vehicles due to anti-personnel (AP) and anti-vehicle (AV) landmine detonations recorded globally[12]. In a traditional military setting, landmines are used to double the defence forces and limit the movement of enemy forces. Landmines have proven to be effective weapons in inflicting significant injuries to enemy forces and causing severe damage to vehicles since they are relatively cheap to acquire and easy to use. As a result, landmines have become one of the main causes of death and injury to security forces, civilians, and landmine-clearing agents [12]. Detonation of landmines results in the transfer of immense blast overpressure waves through the incident surface to the intended target (people or vehicle). Previous studies have shown that there is a 45 % chance that the victims of landmine detonations will suffer severe lower limb injuries compared to the other body regions [14]. However, survivability of landmine victims has improved from about 70% to 90% recently in Iraq[14].The improvements in design and development of personal and vehicle protection technologies, therapeutic technologies, and rapid evacuation logistics to institutions with optimized expertise in landmine injuries. Furthermore, different strategies have been employed to better understand the blast physics caused by different types of landmine blast scenarios and their pathophysiological effects on the mechanism of injury on the lower extremities.

A collaborative approach that implements clinical, experimental, and numerical methods have been employed to investigate and comprehend the blast physics and injury mechanisms that result in physiological dysfunction in human beings. To better understand the lower limb injury pattern, researchers mainly rely on extrapolating injury profiles from studies based on impact/blast loading of human surrogate models in a controlled environment.

Blast injury investigations have been conducted through various methods, including the development of injury models, blast injury experiments, biomimetic leg representations, computational models, and analysis of the physical properties of cellular, molecular, and skeletal tissue [8]. Conclusions from these investigations have led to the development of several mitigation strategies such as personal protective equipment and modifications in vehicle design to minimize the effects of landmine blasts.

This literature review provides a comprehensive overview of landmine compositions and action mechanisms, the anatomy of the human lower leg, different lower leg representation models, and injury mechanisms and classification.

2.2 Landmines

Landmines and explosive hazards, such as unexploded ordnance, abandoned military vehicles and equipment, as well as Improvised explosive devices (IEDs), may provide a concern to anyone who operates in places that have seen armed conflict. Even decades after a conflict ended, the remains of unexploded explosive devices obstruct access to the area either to pass through or use as project sites[15]. Organizations and individuals operating in these regions should exercise caution regarding the physical hazards associated with the diverse array of weapons that remain from past and ongoing armed conflicts. It is crucial to maintain awareness and refrain from tampering with unfamiliar objects to prevent the inadvertent detonation of these devices.

2.2.1 Landmine Composition

The explosive charge is often composed of materials such as TNT (trinitrotoluene) or RDX (cyclotrimethylene trinitramine). The explosive is responsible for the destructive force generated upon detonation. The detonation mechanism, which can vary depending on the type of landmine, initiates the explosion when triggered by pressure, tripwires, or other mechanisms.

Landmines have a casing or housing that serves to protect the internal components and ensure their stability over time. The housing may be manufactured from materials like plastic, metal, or a combination of both [16]. The design and materials used in the casing can impact factors such as the concealability of landmines, resistance to environmental factors, and ease of detection. A typical landmine consists of five main components [17] as depicted by Figure 2.

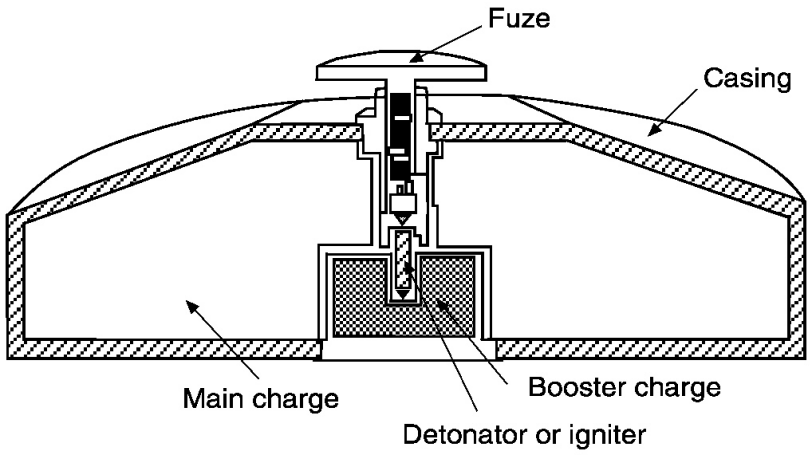

Figure 2 : Schematic diagram showing the main components of a typical landmine [16]

- **Mine casing -** a shell that encloses and protects the mine components from the surrounding environment. To prevent detection by electronic mine detectors, non-metallic casings have been developed.
- **Pressure plate/fuse** - is a component that interacts with the victim, initiating detonation of the booster charge.

- **Booster charge** - a highly explosive chemical that initiates detonation and causes an overpressure shock wave.
- **Main charge** - it consists of stable explosives usually TNT, Composition B or RDX. It is detonated by the booster charge explosion.
- **Detonator** – receives the signal from the fuse to ignite booster charge.

Chemical explosives often used in landmines are categorized as either low or high explosives. Low-explosive chemicals have a low rate of reaction and produce low-pressure waves whereas high explosives exhibit the opposite characteristics. The explosive chemicals are used as the booster charge and main charge. The common chemicals used as explosives in landmines include:

a) TNT (Trinitrotoluene)

Trinitrotoluene is a highly stable, yellow crystalline solid chemical often used as an explosive material in the manufacturing of landmines. It is a stable chemical which makes it easy to handle and fewer results in accidental detonation. When 1 g of TNT explodes, it releases about 4.184 kJ of energy. The low sensitivity property of TNT also allows it to be cast forming the main charge of the landmine. It has a detonation velocity of 6,900 m/s [18].

b) RDX (Cyclotrimethylenetrinitramine)

RDX is a highly sensitive, white crystalline chemical known as Cyclotrimethylenetrinitramine. It is a high explosive chemical, very sensitive compared to TNT and is used as booster charge material in landmine manufacturing. It is often mixed with other explosives and plasticizers to make it stable and easy to handle. When 1 g of RDX explodes, it releases about 6.276 kJ of energy which is 1.5 times that of TNT. It has a detonation velocity of 8,750 m/s [18].

c) Composition B

Composition B is a stable and castable explosive mixture of mainly TNT and RDX chemical explosives. It often consists of 59.5 % RDX and 39.4% TNT, and bout 1 % of paraffin wax as a stabilizing agent. It is used a as primer and booster charge in landmine manufacturing. It has a detonation velocity of 7,620 m/s [19].

d) C-4 (Composition C-4)

Composition C consists of mixture of 91 % RDX explosive, 5.3 % dioctyl sebacate (DOS), 1.6 % of a mineral oil and 2.1 % polyisobutylene (PIB). It is often mixed with other chemicals to increase the plasticity and binders to bond all other chemicals together. C-4 is reliable and safe to use since it is less likely to self-detonate because it requires both heat and pressure to be applied. It has energy content of 6.7 MJ/kg [19].

2.2.2 Landmine Classification

Landmines are classified based on various factors, including their design, functionality, purpose, and method of deployment. Landmines are commonly categorized based on their intended purpose. One classification is anti-personnel landmines, which are purposefully designed to target and incapacitate or potentially cause fatalities to individuals [15]. Anti-personnel landmines are activated by pressure, typically resulting from a person stepping on or near the mine. Their primary aim is to inflict casualties among both military personnel and civilians.

Another classification is anti-vehicle landmines, which are specifically engineered to target and destroy armoured vehicles like tanks or armoured personnel carriers. These landmines are generally larger in size and contain a more substantial explosive charge to effectively penetrate the armoured protection of vehicles. Their purpose is to disable or destroy military vehicles during conflicts or defensive operations. Landmines maybe be sub-categorized based on its action mechanism that is either blast landmines or fragmentation mines [15].

2.2.2.1 Anti-Personnel Landmines

Anti-personnel mines are compact explosives that measure between 5 to 15 cm in diameter [20]. They can be planted manually in the ground slightly below the surface or dispersed through dispensers. These devices can be triggered either by direct contact or by a trip wire. They are intended to be easily portable and can be deployed in large quantities to maim or kill people. Anti-personnel mines, as shown in Figure 3, come in various types, with differences in their structure, the type of explosive used, and their size. On average, AP landmine contains around 40 g of explosives, although the explosive content can range between 20-200 g [20]. Anti-Personnel landmines are not entirely made using highly sensitive booster charge to reduce the cost of manufacturing since booster charge is expensive. Also using less sensitive charge resulted in a stable device minimizing the chances of accidental detonation [21].

Figure 3 : Photographs of typical examples of AP landmines [22]

Anti-Personnel Landmine Action Mechanism

Anti-personnel landmines employ various action mechanisms to cause harm or incapacitate individuals who encounter them. The action mechanism is intended to trigger the explosive charge of the landmine and inflict casualties. AP landmines can be subdivided into two basic categories based on their mechanism of action when it interacts with the target AP landmines can be activated through two primary methods: either by stepping on the trigger mechanism directly or through a command or remote activation [22]. Figure 4 illustrates the two ways in which an anti-personnel landmine can be triggered to target its victim which are either by command or stepping on the trigger. The action mechanism of anti-personnel landmines is used to subdivide them into blast and fragmentation anti-personnel landmines.

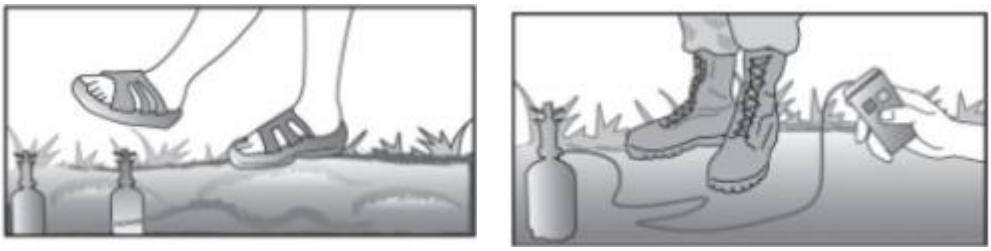

(a) victim activated (b) command activated

Figure 4 : Schematic diagram showing the activation of AP Landmine [22]

a) Blast Anti-Personnel Landmine

The most prevalent type of anti-personnel landmine is the blast landmine, which is activated by applying a minimum pressure of 19.62 Pascal (Pa) to the pressure plate [23]. Blast mines are specifically designed to inflict harm, injury, and fatality upon individuals who encounter them. Upon detonation, the main charge of the mine generates a shockwave accompanied by a high-velocity shock front. The shock front carries the by-products of detonation and hot gases from the explosion.

The resulting shockwave exerts a significant upward force on the target, primarily affecting the footwear, foot, and other parts of the lower limb. This force induces longitudinal stress waves, which contribute to the potential injuries sustained by the individual in contact with the landmine [23].

b) Fragmentation Anti-Personnel Landmine

Fragmentation anti-personnel landmines are designed to project lethal steel fragments across a wide area upon detonation, striking individuals around it. Fragmentation mines are designed to cause fragmentation wounds or death to individuals within its proximity[16]. Fragmentation anti-personnel landmines are generally heavier than blast anti-personnel landmines and contain large amounts of ferrous metal, making them easy to detect [16]. Fragmentation antipersonnel landmines are further classified based on their action mechanisms.

i. Bounding

The landmine is either activated by pressure or tripwire. Upon a detonation, a propelling charge creates a lifting a force that carries the mine to about 1 m above the ground [24]. The main charge then detonates producing a spray of lethal steel fragments to its surroundings.

ii. Directional

Directional fragmentation mine is designed to direct projection of fragments and blast load towards the direction of the victim.

iii. Stake

Stake fragmentation AP Landmines are laid at height above the ground covered vegetation. The mine warhead mounted on a stake and often detonated by tripwire [25].

Anti-Personnel Landmine Injury Mechanism

Injury mechanisms resulting from AP Landmines are commonly classified based on the specific action displayed by the detonation of the anti-personnel mines. Fragmentation mines disperse fragments outward in a radial pattern, leading to ballistic injuries on exposed areas of the enemy target. On the other hand, blast mines release a substantial amount of explosive energy in the form of a shockwave that penetrates the body of the victim, causing injury. The flow of detonation products can induce torsional stresses, potentially resulting in traumatic amputation of limb segments [23]. Figure 5 illustrates the interaction between an AP landmine and the lower limb. In summary, AP Landmine injuries are caused by a combination of thermal effects, propagation of stress waves, and the effects of detonation products.

i. Thermal effect

As a result of the combustion of explosive material, heat is generated and transferred to the parts of the victim causing burns.

ii. Stress wave interaction

The interaction of stress waves is a consequence of the shockwave generated by a blast mine which travels through the lower limb at an incredibly high speed, causing cellular and soft tissue disruption, as well as bone fractures.

iii. Products of detonation

When a mine explodes, it produces sharp fragments that come from various sources such as the mine components, soil, and footwear. These fragments quickly accelerate upwards, impacting the lower parts of the body. Consequently, the victim experiences ballistic injuries due to the intense displacement caused by bending and torsional stresses on their body. Additionally, the sharp fragments can penetrate the body, causing penetrating injuries. Soil, footwear, and mine components are driven into the limb from the bottom or sides, as well as the perineum area [26].

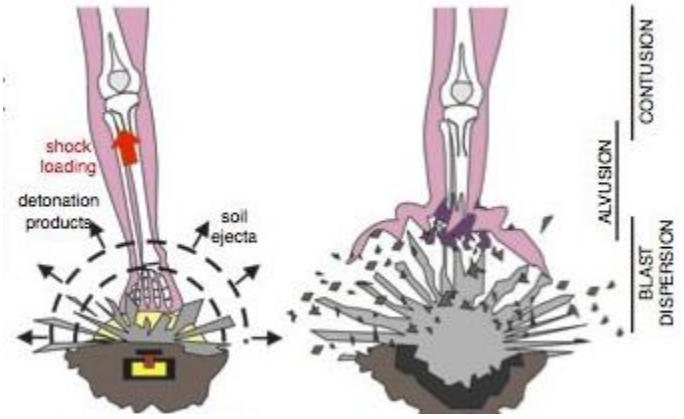

Figure 5 : A schematic diagram showing the injury mechanisms caused by AP Landmine [27]

Anti-Personnel Injury Classification

The injury patterns because of AP landmine explosions are often classified into three categories based on the explosion circumstances.

i. Primary injuries

Severe injuries occurring on lower limb, perineal and genital are common when the victim steps on a blast mine. May result in traumatic amputation of lower limb parts.

ii. Secondary injuries

Injury occurring on lower limb, head, and upper body area common when the victim triggers the trip wire detonating fragmentation mine. The injuries are less severe compared to pattern 1. It is because the victim being away from the epicentre of the explosion.

iii. Tertiary injuries

Usually occurs because of the surrounding objects interacting with the victim. Severe injuries occurring on the face, hands, and upper limb due to accidental detonation when handling the mine [23].

2.2.2.2 Anti-Vehicle (AV) Landmines

Anti-vehicle (AV) landmines also referred to as Anti-Tank (AT) landmines are explosive devices specifically designed to disable or eliminate vehicles or tanks. They are typically deployed on or beneath roadways or other areas where vehicle traffic is anticipated. Anti-vehicle landmines are activated by pressure or magnetic sensors which trigger the landmine [28]. In some cases, anti-vehicle landmines can be remotely detonated, providing the operator with control over the timing of the explosion to maximize its impact [28].

The effects of anti-vehicle mines on targeted vehicles can be severe, leading to destruction or often rendering the vehicle inoperable. The explosion can also result in injuries or fatalities to the occupants of the vehicle, as well as bystanders. Figure 6 provides examples of commonly encountered AV landmines.

Figure 6 : Image showing typical examples of AV landmines [22]

a) Anti-Vehicle Blast Landmines

The primary objective of anti-vehicle blast landmines is to immobilize or destroy vehicles, disrupting military operations, and creating obstacles for enemy forces. These landmines are designed to generate a shockwave, heat, and fragmentation upon detonation, which can cause extensive damage to the targeted vehicle.

b) Self-forging/ Fragmentation Anti-Vehicle Landmines

The self-forging fragmentation AV landmine is commonly known as an explosively formed penetrator (EFP). Self-forging fragmentation Anti-Vehicle landmine combines the destructive effects of a blast mine with the penetrating capabilities of a projectile. They may contain a ductile metal plate or disk, typically made of copper, which transforms into a high-velocity missile upon detonation. The mine incorporates a specific shaped charge, either in the form of a disk or a cone, to concentrate the blast energy and generate an explosive penetrator. and can take the shape of a slug or rod-like missile that is propelled towards the

base of the targeted vehicle [28]. Figure 7 provides schematic diagrams illustrating the action mechanism of fragmentation AV landmines upon detonation.

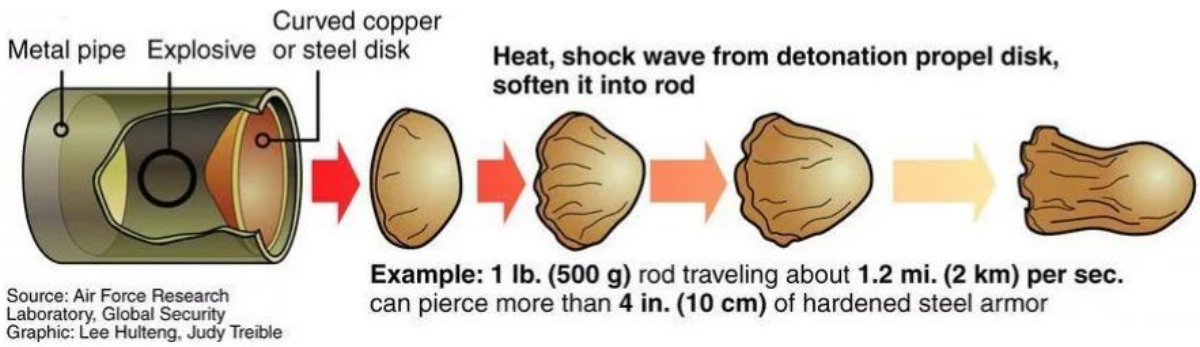

Figure 7 : A schematic diagram showing the detonation process of a self-forging fragmentation AV landmine [28]

Anti-Vehicle Landmine Injury Mechanism

When an AV landmine is triggered, the booster charge detonates, creating an intense overpressure shock wave. The shock wave is partially reflected towards the centre of the explosion when it reaches the soil interface, causing the main charge to detonate and fragment the mine components, releasing toxic gases. The combination of mine and soil fragments and superheated toxic gases vent through the soil interface hole, affecting the base of the vehicle [14].

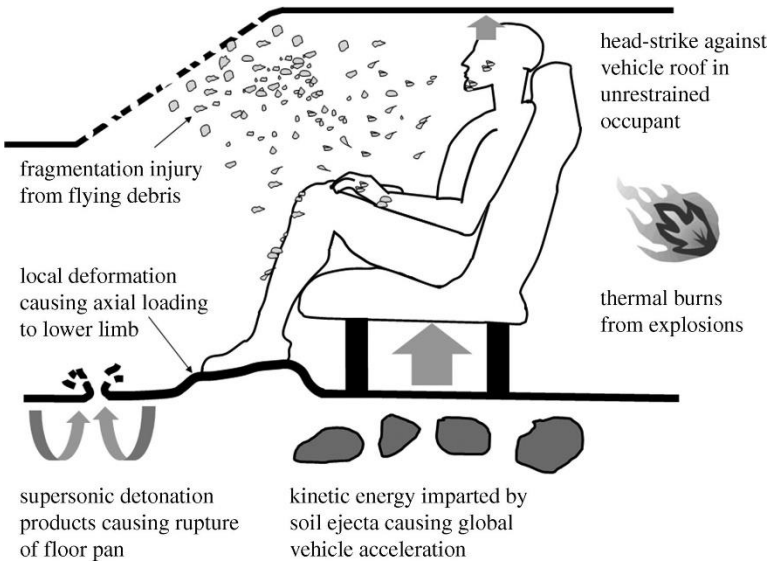

Figure 8 : An illustration showing the interaction of the vehicle and its occupants when an AV Landmine detonates [14]

The released detonation products and superheated gas travel at high velocities, capable of penetrating 100 mm of hardened steel armour, and result in the destruction of the vehicle, injuring or killing the occupants depending on the explosion circumstances [24]. Figure 8 illustrates the AV landmine mechanism of action. The intense overpressure shockwave and missiles transmitted from the landmine explosion onto the vehicle floor result in the rapid acceleration, deflection, tearing and penetration of the vehicle body. The induced stresses propagate through the vehicle body into the body of the occupants which may cause injury or death. The lower limb is most affected by the detonation of anti-vehicle landmines because it is closest to the blast and fragmentation effects.

As a result, the lower limbs of the occupants are exposed to high induced stresses that cause injury to the lower limb mostly. Figure 9 illustrates the ratio of injuries suffered by the vehicle occupants under an Anti-Vehicle landmine blast.

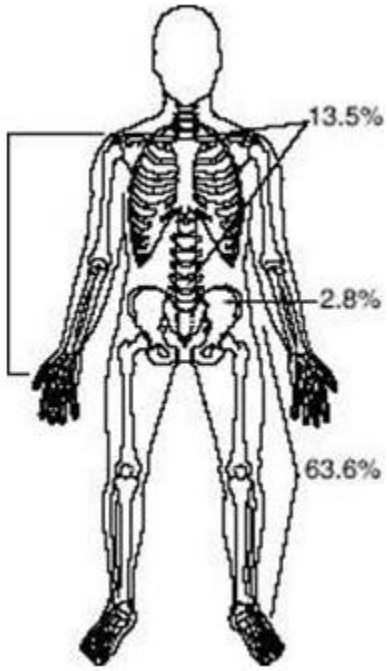

Figure 9 : A schematic diagram showing the distribution of fracture sites caused by AV Landmines [29]

In a study conducted by Grigoriadis [30], it was determined that the positioning of the lower limb, specifically the angles of the knee and ankle joints in the sagittal plane, has a substantial impact on the injury mechanism caused by underbelly blasts. The study involved testing on post-mortem human subjects (PMHSs) and revealed that the posture with a 120-120° angle (where both the knee and ankle joints are fully extended) resulted in more severe fractures that are challenging to treat compared to the posture with a 90-90° angle (where both joints are bent at a 90-degree angle). Therefore, the position of the lower limb in relation to the severity of injuries sustained during underbelly blast events is crucial as it affects the injury mechanism.

i. Thermal Effect

Detonation of the mine is because of the combustion of explosive material. It results in heat being generated and transferred to the parts of the vehicle. The breaching of the vehicle floor exposes the occupants to heat resulting in burn injuries being suffered by occupants. The release of toxic fumes from burning of Teflon material used in armoured vehicles affects the central nervous system[28].

ii. The Blast Shockwave

This is as result of shockwave produced by blast mine. Stress waves induced of the vehicle floor is transferred to the human body causing cellular, soft tissue disruption and fracture of bones. The stress waves are concentrated by reflection and when they reach tibia bone may lead to fracture.

iii. Explosively Formed Penetrator (EFP)

The detonation AV Landmine generates missiles from mine components, fragments from toning of vehicle floor travelling at extremely high speeds. The flow of these fragments causes ballistic injuries resulting in intense displacement, bending stresses and torsion induced on the victim body parts. The sharp fragments may result in penetrating injuries[28].

iv. Movement of Vehicle

Detonation of the anti-vehicle landmine results in rapid acceleration of the vehicle upwards and deformation of its parts. The translational movement induces impact loads on the occupant lower limb, thoracolumbar spine, and cervical spine [31].

Anti-Vehicle landmine Injury Classification

The injury patterns because of AV landmine blast are classified into three categories based on the explosion circumstances.

i. Primary Injuries

The overpressure shockwave affects the pressure-sensitive organs such as the ears, chest, and lungs. The resulting pressure exerted on the chest wall may cause it to move inward, resulting in increased rigidity of the chest and abdomen, which hampers the normal breathing process. Consequently, this may result in damage to the lungs, trachea, and abdominal organs.[14].

i. Secondary Injuries

Projectiles from the fine fragments results in ballistic injuries and penetration wounds to the exposed body organs such as skin and may cause blunt force trauma[14].

i. Tertiary Injuries

The impact/movement of the vehicle during and after explosion of landmine causes impact injuries to the body of the occupants [26].

2.3 Blast Waves

Blast waves from detonation of landmines can be represented by a different wave form as shown in Figure 10. The commonly used wave forms used are the ideal blast wave (Friedlander-type) and real blast wave (complex wave form). The major difference between a Friedlander-type blast wave and a complex wave lies in their waveforms and characteristics. The Friedlander wave is a simplified idealized waveform with a single positive-pressure peak followed by a negative-pressure phase, while a complex wave consists of multiple pressure peaks and oscillations due to real-world complexities. The Friedlander wave is useful for understanding basic blast wave principles, while complex waves are more representative of real-world scenarios. Both wave types are relevant in analysing the effects of blast waves, with the Friedlander wave providing a simplified model and complex waves capturing the dynamics and interactions of blast waves more accurately. Considering both wave types allow for a

comprehensive understanding of blast wave effects and facilitates accurate assessments and the development of protective measures [32].

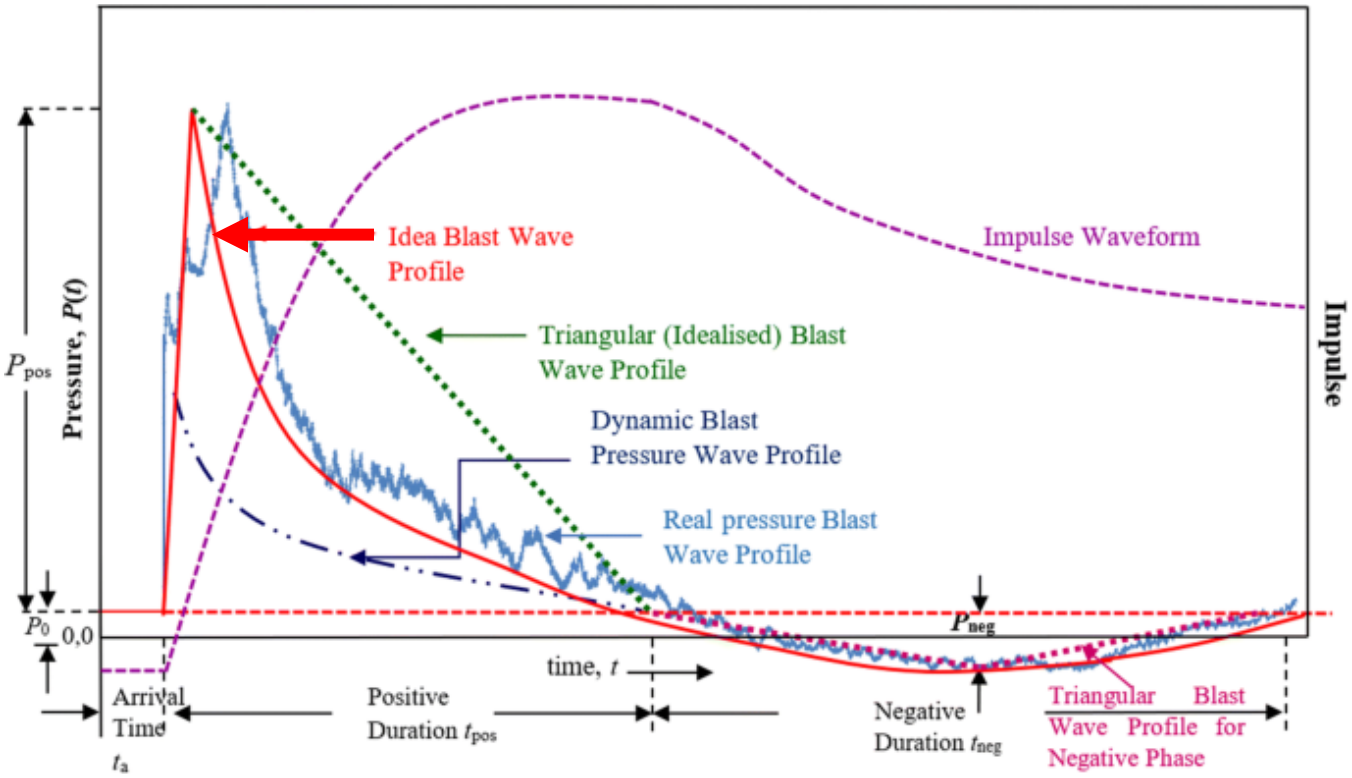

Figure 10 : Schematic diagram showing the blast wave profiles on a pressure-time graph [33]

As depicted by the ideal blast wave profile illustrated in Figure 10, the pressure remains at the atmospheric level until the blast wave reaches a specific location, indicating a time of arrival. Subsequently, there is a notable escalation in the peak overpressure, signifying the maximum pressure exerted by the blast wave upon reaching that location. Following the peak, the pressure gradually diminishes. It is worth noting that the blast wave also generates a suction or negative pressure phase, which is frequently disregarded in analyses despite its potential significance on the surrounding environment and structures [33]. Moreover, the positive phase of the blast wave, characterized by the increasing pressure, is often simplified through the adoption of a triangular pulse model. This simplification facilitates calculations and enhances the ease of analysis regarding the effects of the blast wave.

The Friedlander equation is widely used to the calculate analytical solution to describe the rate of change of pressure after detonation of the charge, as shown in Equation 1 [33].

$$P\,(t) = P_{so}\left(1 - \frac{t}{t_0}\right) e^{-b\frac{t}{t_0}}$$

Equation 1

Where, P_{so} is the ambient pressure,
t_0 is the positive phase duration,
b is a decay coefficient of the waveform,
t is the time elapsed.

A non-linear fitting technique can be employed to analyse the positive phase of an experimental pressure-time curve and determine the decay coefficient (b). Several factors, including peak positive pressure ((P_{so}), positive phase duration (t_{pos}), under pressure (P_{neg}), negative duration (t_{neg}), wave decay parameters (b), and impulse (I), collectively influence the blast loading experienced by structures. These parameters are essential in defining blast wave characteristics and reflected pressures [33].

In terms of design considerations, the blast wave pulse impulse (calculated using Equation 2 [28]) holds even greater significance than peak pressure, as it represents the overall force per unit area that the blast exerts on an object. For most design scenarios, only the positive phase is considered, as it yields the highest impulse and is thus critical in preventing design failure [33] [29].

$$i_s = \int_{t_A}^{t_A+t_0} P_s(t)dt$$

Equation 2

Scaling of blast waves

Scaling of blast waves is a crucial principle that enables the prediction of blast waves properties for explosive charges of different magnitudes. Hopkinson–Cranz or cube-root law is often used to scale blast experiments . A scaled distance parameter, Z, shown in Equation 3 is based on the normalized blast data obtained using the TNT equivalency approach [34] is used to determine blast wave characteristics of different charge properties, mass, and shape [30]

$$Z = \frac{R}{W^{\frac{1}{3}}}$$

Equation 3

where Z, ($m/kg^{\frac{1}{3}}$), R is the range in m and W is the charge mass in kg.

Due to the large range of explosives, Trinitrotoluene (TNT) explosive has been adopted and is utilized for all calculations of blast characteristics because its explosion properties are predominant in most solid explosive types. The ratio of the weight of the selected explosive to the equivalent weight of TNT is equivalent to the ratio of the heat generated by the selected charge to heat generated the TNT upon detonation is shown in Equation 4 [35]. Examples of common explosives and their properties are shown in Table 1

$$W_e = \mathrm{W}_{\mathrm{exp}} \frac{H_{exp}^d}{H_{TNT}^d}$$

Equation 4

where, W_e is the TNT equivalent weight (kg),
$\mathrm{W}_{\mathrm{exp}}$ is the weight of the actual explosive (kg),

H_{exp}^{d} is the heat of detonation of the actual explosive (MJ/kg), and
H_{TNT}^{d} is the heat of detonation of the TNT (MJ/kg)

Table 1 : Types of explosives and their heat of detonation energy per kilogram [35]

Explosive	Heat of Detonation (MJ/Kg)
TNT	4.10-4.55
C4/PE4	5.86
RDX	5.13-6.19
PETN	6.69
PENTOLITE 50/50	5.86
AMON. /NIT. (AN)	1.59

Various methods and correlations are employed to calculate the pressure level at a specific distance from an explosion. The scaled distance calculation relies on factors such as the explosive mass and the distance from the centre of the explosion. Among these methods, the Kingery-Bulmash approach holds broad acceptance and is widely used for determining blast parameters, providing incident, and reflected pressure values for both spherical (free air bursts) and hemispherical pressure waves (surface bursts). In a study conducted by Karlos [30], a comparison was made between the Kinney, Mills, Newmark, and Kingery-Bulmash methods to predict blast parameters of an explosion. It was found that the Kinney method consistently predicted over-peak pressure over a wide range of scaled distances. Unlike some other methods that rely solely on peak pressure measurements, the Kinney method considers the decay of pressure with increasing distance from the blast source. This decay is influenced by factors such as air attenuation and the geometrical spreading of the blast wave. By incorporating these factors, the Kinney method offers a more comprehensive and realistic representation of the blast load [35].

The relationship between the blast wave parameters and the described by Kinney [35] is shown in Equation 5. The scaled distance blast parameter has a significant impact on the method used to predict blast parameters. As the scaled distance increases, the blast wave undergoes changes in its intensity, duration, and shape which affects the peak overpressure, duration of positive pressure, and impulse of the blast wave [35]

$$P_{so} = P_0 \frac{808\left[1+\left(\frac{Z}{4.5}\right)^2\right]}{\left\{\left[1+\left(\frac{Z}{0.048}\right)^2\right]\left[1+\left(\frac{Z}{0.32}\right)^2\right]\left[1+\left(\frac{Z}{1.35}\right)^2\right]\right\}^{0.5}}$$

Equation 5

where Z is scaled distance $(m/kg^{\frac{1}{3}})$,

P_{so} is the over-peak pressure (MPa)

P_o is the ambient pressure (MPa)

2.4 Blast Injury

2.4.1 Human Lower Limb Anatomy

The lower limb is one of the four extremities of the human body, located between the hip and the foot. It consists of several bones, joints, muscles, and soft tissues that work together to support the body weight, facilitate movement, and maintain balance. The lower limb is divided into four major parts: the hip, thigh, leg, and foot. The lower limb also contains various muscles, tendons, ligaments, nerves, and blood vessels that provide strength, stability, and mobility [36]. These structures work together to perform a range of movements, including walking, running, jumping, and standing. The bone structure of the lower limb of a human being is as shown in Figure 11. The tibia bone, also known as the shin bone, is the larger and more weight-bearing bone in the lower leg, and it is located closer to the surface of the skin compared to the fibula bone. The tibia (shown in Figure 12) is the second largest bone in the human body with a triangular shape and is connected to four joints. The upper part of the tibia bone has two condyles that articulate with the femur, forming the knee joint. The lower part articulates with the talus bone, forming the ankle joint [37]. The tibial tuberosity is where the cruciate and patellar ligaments and menisci attach. The tibia is more susceptible to the effects of blast waves from a landmine explosion since it absorbs and transmits significant amounts of energy during an explosion than other parts of the lower leg. It may suffer severe injury or amputation which may be costly and complex to resuscitate [12].

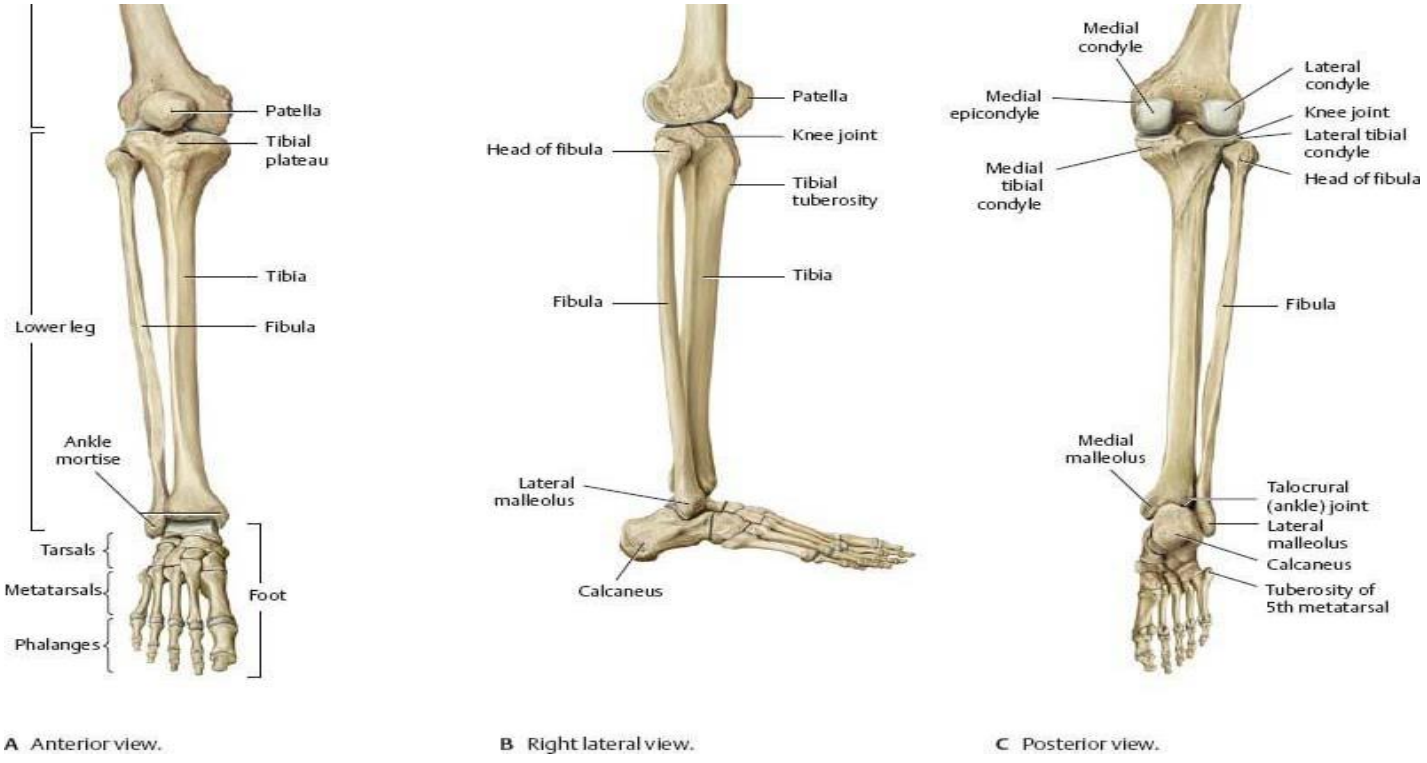

Figure 11 : Schematic diagram showing the Human lower leg bone structure [34]

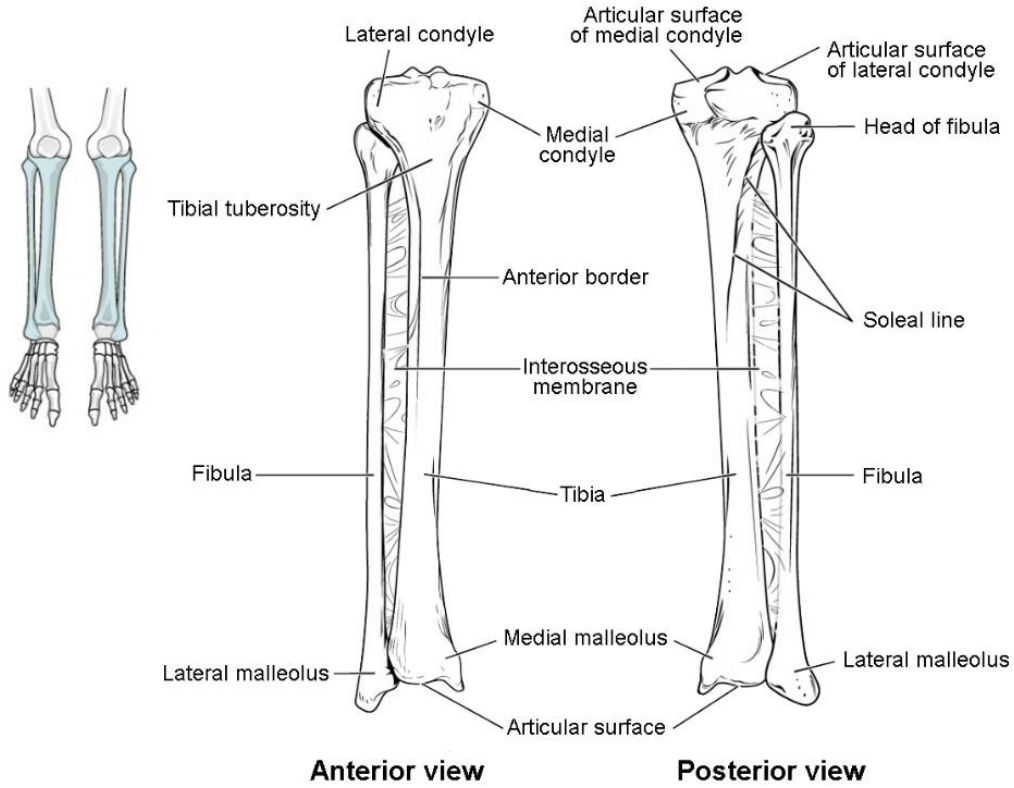

Figure 12 : A schematic diagram showing Tibia anterior position on the left and the posterior on the right-hand side [37]

2.4.2 Biomechanical Properties of Human Bones

Determination of the biomechanical properties of a human bone is an extremely complicated process. The biomechanical properties are influenced by material properties such as brittleness, toughness, fracture energy and mineral density [38]. Various other factors, such as genetics, lifestyle, physical activity, and overall health, also contribute to the biomechanical properties of bones. Also, the macroscopic geometry - shape and dimension of a bone as a whole and microscopic- geometry-orientation of osteons and micro-porosity within the bone tissue also plays also affects the mechanical properties of the tibia bone.

An investigation of biomechanical properties conducted with tibias of 17 adult males aged between 17 and 46 years, concluded that there is a relationship between bone quality and morphology. The tibias were obtained and preserved in a controlled environment with the assistance of the Musculoskeletal Transplant Foundation (Edison, NJ, USA) [38]. From each tibia bone, three cortical bone samples from the diaphysis region were carefully cut at 10% intervals spans between 30% - 70% of the total length, as depicted in Figure 13. Cross-sectional samples with a thickness of 3 mm were taken at 30%, 50%, and 70% positions along the mid-diaphysis to examine the morphology of the tibial cross-sections. Narrower tibias consisted of more brittle tissue are and susceptible to cumulative fatigue damage whereas wider tibia tissue has the lesser characteristics[38].

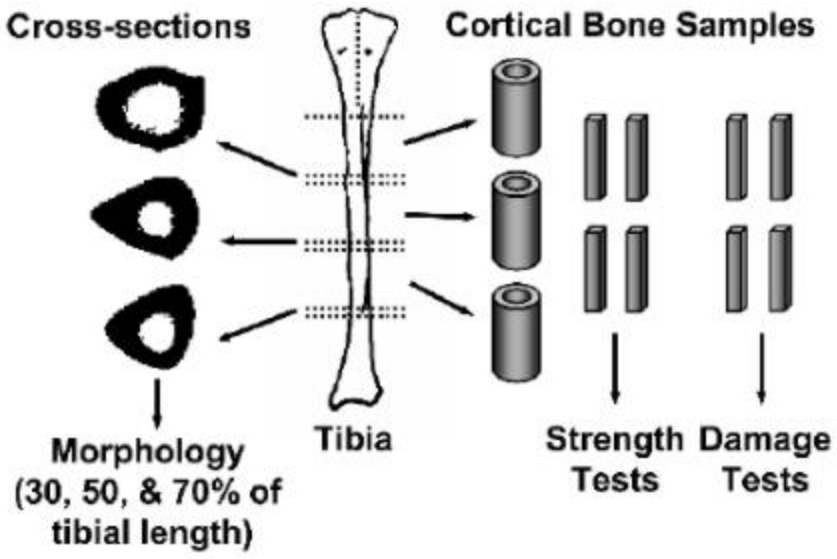

Figure 13 : Schematic tibial cross-sectional morphology and cortical bone samples used biomechanical testing [38]

A slenderness index (S) is defined as the ratio of the anteroposterior and medial-lateral section modulus values, respectively, to tibial length and body mass. The slenderness index can be calculated by Equation 7 [38].

$$S = 1/\left\{\left[\frac{2J}{width}\right] \div [LxBW]\right\}$$

Equation 6

where J is the polar moment of inertia $width$ (m), L is the tibia length (mm) and BW is the body weight (kg).

The study concluded that bone morphology affects the fragility and the risk of stress fractures. The average mechanical properties of the cortical tissue vary depending on the overall size of the bone. The tibia with a large slenderness index value is narrow and bare a less amount of load before it fractures. A small slenderness index value represents a wide tibia and bares a substantial amount of load before it fractures [38]. The study highlighted the importance of considering bone quality parameters related to damageability when assessing the risk of stress fractures in individuals with different bone sizes.

2.4.3 Clinical Data

A forensic investigation was conducted at Field Hospital located in Southern Afghanistan to examine the injury mechanisms resulting from landmine blast incidents. Over a consecutive six-month period, a total of 62 radiographs of landmine casualties from both free-field and in-vehicle explosions were examined to analyse the injury patterns [39]. The findings suggested that the injury pattern was dependent on the environment. The AP Landmine casualties mainly suffered primary and secondary injuries, while tertiary injuries were more predominant in AV Landmine casualties. Moreover, the lower extremities were found to be more susceptible to severe injuries in comparison to the other regions of the body since they would be closer to the centre of detonation. The cause and effect of landmine explosions and their correlation with specific types of landmines have been established through prior inquiries and analyses conducted on individuals injured by landmines, presented in Table 2 [39].

Table 2 : The classification of landmine Injury mechanisms and mitigation techniques developed [37]

Blast injury	**Injury mechanism**	**Clinical effects**	**Landmine Type**
Primary	Overpressure shock wave	Harm to the gastrointestinal tract, primary blast lung, soft tissue deformation, fractures caused by the Brisance effect, and amputation	AV and AP Landmine
Secondary	Projectiles from mine fragmentation	Penetrating wounds, especially to the lower extremity, as well as face injuries from glass fragments; fractures in the extremities from direct contact	AV and AP Landmine
Tertiary	Vehicle acceleration, floor deformation and impact with surrounding objects	Severe axial stress resulting in head injuries from a collision with a car roof, lower limb (particularly the calcaneal), pelvic, and spinal injuries	AV Landmine
Quaternary	Thermal burns	Severe burns	AV and AP Landmine

2.4.4 Landmine Trauma

The Canadian Centre for Mine Action Technologies (CCMAT) conducted an experiment using the FSL surrogate using the LEAP (Lower Extremity Assessment Procedure) to assess the injury to the lower leg subjected to blast loading several tests were conducted using different tubular structures under different types of landmine charges [26]. After each test, photographs of the damaged leg were taken and returned to a cold storage. The tubular structures were examined using medical X-rays and scan methods. The Mine Trauma Score (MTS), shown in Table 3, was developed which records the severity and nature of injury [40]. The severity and distribution of the blast injury were found to depend on:

- Type, weight, and energy content of the explosive
- The detonation location relative to the protective structures for example armoured vehicles and protective clothing.
- The magnitude and reinforcement of the pressure by its interaction with the ground.

Table 3 : The Mine Trauma Score (MTS) and the resulting level of amputation required [40]

Score	Injury	Level of amputation required
0	Minimal	No major surgery required
1	Closed	Salvageable limb
1A	Open contained	
1B	Open contaminated	
2	Closed	Below Knee amputation
2A	open contained	
2B	Open contaminated	
3	Open contaminated	Below or above-knee amputation
4	Open contaminated	Above knee amputation
Closed Injury: any injury that does not Violate the skin and for which there is minimal risk of infection.		
Open contained: any injury that violates (lacerations, tears) the skin, but that is not contaminated by environmental debris		
Open contaminated: any injury that violates the skin and that is contaminated by environmental debris.		

Figure 14 illustrates the major causes and severity of injury experienced by the victim depending on the distance at which the victim is located with respect to the centre of the explosion. The victims at the centre of the explosion suffers most of the injury due to high velocity of travelling fragments and intensity blast wave and thermal from the explosion [29]. The magnitude of the effects from the landmine explosion decreases as the victim moves further away from the epicentre of the explosion. The furthest victims are likely to experience tertiary injuries due to fragments of the landmine components.

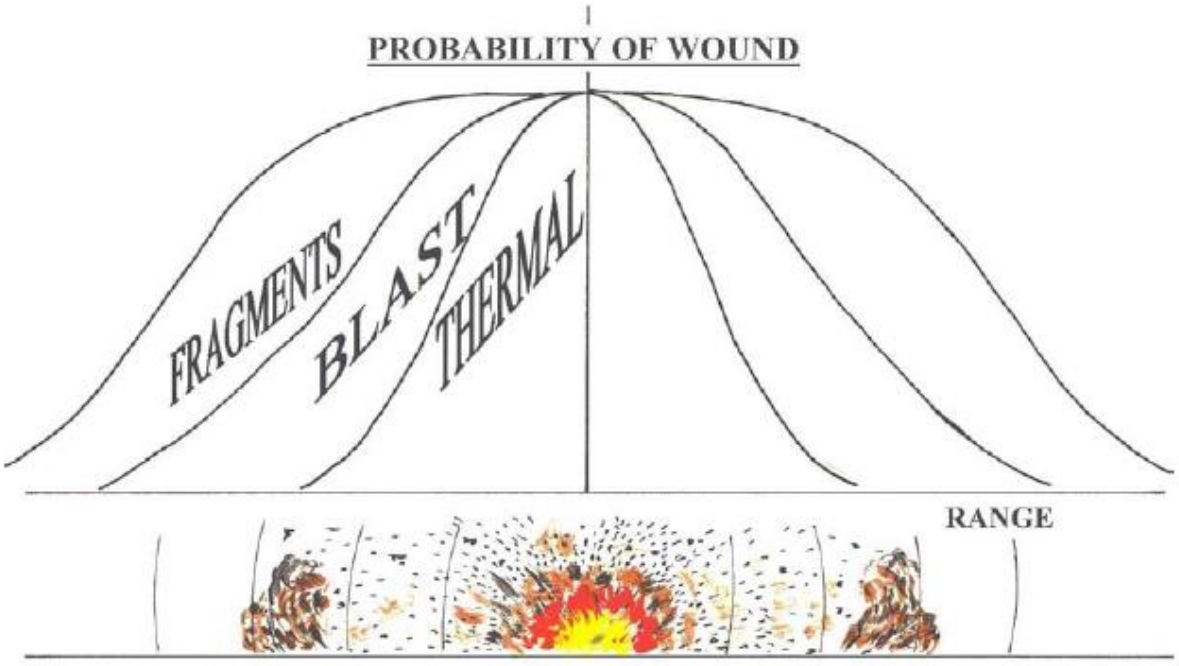

Figure 14 : An illustration of showing the probability cause of wounds from Landmine detonation with respect to distance from the centre of explosion [29]

2.5 Human Lower Leg Representations and Test Methods

The Research and Technology Organisation (RTO) of NATO identified the need to assess the data surrounding the injury criterion associated with the landmine explosions [41]. Human lower leg surrogates were developed to assess injuries suffered by vehicle occupants due to AV landmine blasts. The human surrogates were designed to mimic the Post Mortem Human Subjects (PMHS) response as they are exposed to blast loading. The experimental results enabled the determination of injury mechanisms and patterns which can be used to predict injuries sustained by the landmine victims. The types of human lower leg surrogates designed were classified as biomechanical/mechanical and frangible surrogates.

Surrogate legs have been mostly used in blast testing due to ethical and practical considerations. The use of human cadavers for such testing would raise ethical concerns as it involves the use of deceased human bodies for scientific purposes. Additionally, the availability of human cadavers for testing purposes may be limited due to legal, cultural, or logistical reasons.

The use of surrogate legs allows the repeated use of the same object without ethical concerns. Surrogate legs allow for flexibility since they can be designed to have specific features, such as bone density or muscle mass, to simulate the leg structures of certain populations, such as military personnel or athletes. Moreover, surrogate legs are more practical to use in blast testing since they allow consistent and repeatable test results. Surrogate legs make use of sensors to collect data on the forces and pressures experienced during the blast, providing valuable information for researchers to analyse and improve blast protection [41].

2.5.1 Mechanical Surrogate Legs

Mechanical surrogate legs are designed for specific applications such as evaluating protective clothing against landmine blast injuries, adaptation of crash test dummies for blast injury assessment, evaluating physical parameters and load changes in the lower leg, and capturing vertical forces and accelerations in the lower leg [13]. These surrogate legs incorporate various materials and features to mimic human leg properties and capture leg response to known input loads. Advantages of these surrogate legs include the ability to simulate soft tissue using materials like gelatine or urethane, as well as the use of sensors to monitor physical parameter changes under load. However, they also have limitations, such as the inability to accurately replicate the human knee joint or lower limb anatomy in some cases, and the potential mismatch between the force-time response and human corridors in certain designs [42]. The most used biomechanical surrogate legs in vehicle crash tests are Hybrid III and Thor-Lx. Biomechanical surrogates are designed to replicate the dimensions, weight, and response of the human body to blast or impact loading. A photograph of a common example of mechanical surrogate leg is shown in Figure 15.

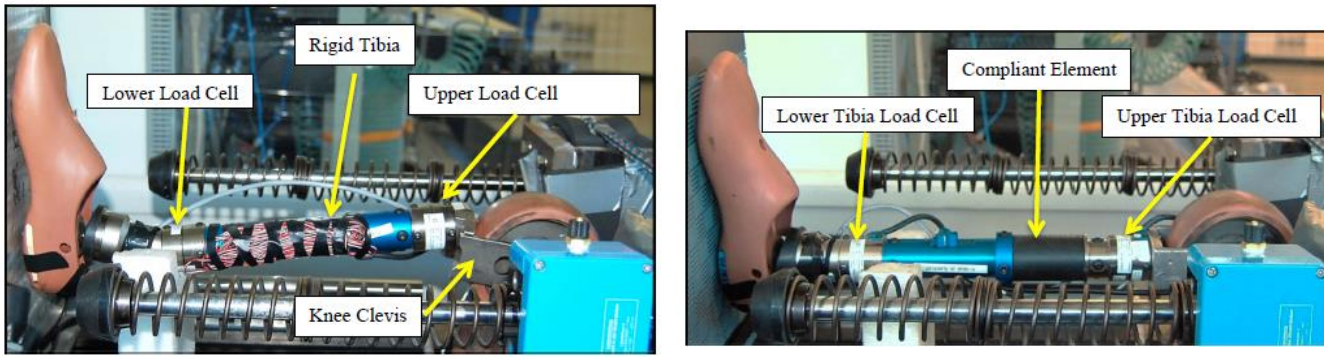

a) Hybrid III/Denton Leg b) Military Lower Extremity lower leg (MIL-Lx)

Figure 15 : Photographs of common examples of mechanical surrogate legs [13]

Hybrid III is a crash test dummy that enables full body evaluation of injury risks and kinematics in simulated automotive crashes. As a standardized platform, it allows repeatable testing but is limited in research-grade instrumentation. MIL-Lx is a linear impactor for controlled biomechanics research on lower extremity injuries. It allows precise replication of axial impact conditions but only on isolated leg segments. Hybrid III provides realistic crash scenarios but generalized injury metrics. MIL-Lx enables detailed injury mechanism research but lacks whole-body kinematics. In summary, Hybrid III is better for overall occupant safety evaluation while MIL-Lx provides targeted capabilities for understanding lower extremity injury biomechanics [13]. Their complementary strengths and limitations make them useful for trauma analysis from different perspectives.

The Warrior Injury Assessment Manikin (WIAMan) is one of the latest anthropomorphic test devices (ATD) that has been developed to assess injury risk to military vehicle occupants in under-body blast events[43]. The WIAMan generation 1 (Gen1) ATD consisted of a seated posture, with a vertical seat back, horizontal seat pan, and hip, knee, and varying posture angles as shown in Figure 16. The existing Hybrid III ATD lacks biofidelity and injury assessment capabilities for blast loading. WIAMan was intended to exhibit human-like biomechanics and measure data that correlates with blast-related injuries, enabling more accurate injury risk assessments to improve vehicle design and soldier protection. The Gen 1 WIAMan ATD prototype delivers improved durability, instrumentation, and biofidelity compared to Hybrid III PMHS across relaxed and semi-reclined postures, despite some biofidelity limitations[43].

Figure 16 : The anatomy of Warrior Injury Assessment Manikin (WIAMan)[43]

2.5.2 Frangible Surrogate Legs

Frangible surrogates aim to possess better biomimetic characteristics of the bone geometry of a 50th percentile male cadaver and load them until failure during experiments [44]. The surrogate legs incorporate details of the human lower leg, such as soft tissue materials and a more accurate geometric representation. They allow for physical measurements, X-ray imaging, and CT scans for clinical assessment purposes. Frangible surrogate legs have limitations that includes the lack of complete leg anatomical accuracy, simplified tissue simulation, and limited versatility in terms of representing surrounding tissues [45]. Photographs of common examples of frangible surrogate legs are shown in Figure 17.

a) Frangible Surrogate Leg (FSL)

b) Complex Lower Leg (CLL)

c) Simplified Surrogate Tibia (SSL)

Figure 17 : Photographs of common examples of frangible surrogate legs [44] [45]

2.5.3 Cadaver Surrogate Legs

Cadaver test devices are biological models used as test subjects to investigate the response of the human body to blast loading. They have been successfully used to assess the effectiveness of protective footwear used to mitigate the impact of an AP blast mine on the lower limb of a human being. Cadaver test devices proved to be close to accurate in mimicking the actual response to blast loading because they had actual leg geometry and material properties of a human bone. The cadaver test subjects were either used as whole-body cadavers or isolated human lower leg. However, the mechanical properties of the cadaver parts may vary slightly from one cadaver to another depending on the age and health of the donor.

The isolated human lower limb model consists of the lower limb only. The amputations can be either done below or above the knee for easy handling and experiments focusing on lower limb responses. The main advantage of this test subject is that the harvesting of the limb does not wait for the donor to die therefore the material properties of the bone and tissue are preserved. The results of the experimental tests on the subject can be evaluated by performing post-test autopsies of the limb. However, testing only an isolated lower leg segment may not accurately replicate the full stiffness and response of an intact leg. An intact leg has multiple structures spanning the entire limb that contribute to overall stiffness, including muscles, tendons, ligaments, and bones. Severing these connections to isolate the lower leg reduces the degrees of freedom and removes some sources of stiffness. Additionally, weightbearing forces and active muscle contraction in a living person further increase whole leg stiffness compared to a cadaver. Because an isolated cadaver lower leg has inherently less stiffness than an intact leg, it may show more damage than would occur in a live leg for a given force. To assess injury response most accurately, the whole leg should be evaluated to account for all the factors contributing to its stiffness and biomechanical behaviour. A photograph of an isolated human lower leg that may be used to conduct blast injury experimental investigations is as shown in Figure 18. Usually, the test subjects contain a load cell in the tibia, and sand train gauges on the knee and ankle as they go under blast tests as shown in Figure 19.

Figure 18 : A photograph of an Isolated lower leg of a human cadaver [46]

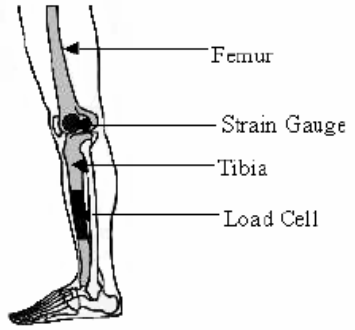

Figure 19 : A schematic diagram showing the instrumentation for an isolated human cadaver lower leg [44]

2.5.4 Experimental Approach

Experimental approach involves physically subjecting surrogate legs to blast pressures and recording the resulting data using sensors and other measurement tools. The surrogate leg may be mounted on a rigid platform or suspended in air, and the blast pressure may be applied using a shock tube, explosives, or other means. This method allows researchers to directly measure the response of the surrogate leg to the blast and can provide valuable insights into the effects of blast pressures on human legs. Each type of surrogate leg has its experimental test method.

Mechanical Surrogate Testing

The Test Rig for Occupant Safety System (TROSS) was designed by IAa BG, a German analysis and test engineering company. TROSS is currently the best test rig used to investigate the response of the human lower leg using Hybrid III Denton lower leg and MIL-Lx surrogates[41]. The TROSS system was used to simulate the AV landmine blasting conditions.

The Hybrid III with Denton lower leg and MIL-Lx are attached to the seat that is fixed to the base frame of the test rig. An explosive charge is attached underneath the footplate where the feet of the test subject rest. The test subject is attached in such a position that the blast load is transferred into the lower limb upon detonation. The footplate should not be attached to any part of the rig to avoid transfer of load onto it. Instrumentation such as accelerometers, high-speed cameras and strain gauges were used to measure the stress and movement induced in the lower leg. The TROSS system set-up is shown in Figure 20.

Figure 20 : An image showing Test Rig for Occupant Safety Systems (TROSS) set up with a Hybrid III surrogate [41]

The TROSS system was also implemented using a linear impactor method to apply the impulsive load to analyse the response of the THOR-Lx and Hybrid III anthropomorphic test devices (ATDs) to postmortem human subjects (PMHS) under simulated anti-vehicle (AV) land mine blast loading conditions. The standard Hybrid III lower limb and THOR-Lx surrogates were attached to the full body in such a way that the linear impactor applies axial loading through the lower limb as shown in Figure 21. At lower explosive charges, the THOR-Lx measured tibia forces closer to the PMHS, while the Hybrid III forces were much higher. At higher charges, both ATDs overpredicted the forces versus the PMHS. The deviations occurred due to the compressive element limits in the surrogates compared to the rate-dependent modulus of human bone. Although designed for biofidelic rate-dependent properties, the THOR-Lx lost biofidelity at severe blast levels. Overall, the THOR-Lx more closely matched PMHS tibia forces [31]. Hence, appropriate for assessing injury in either automotive vehicle collisions or low severity explosive loads.

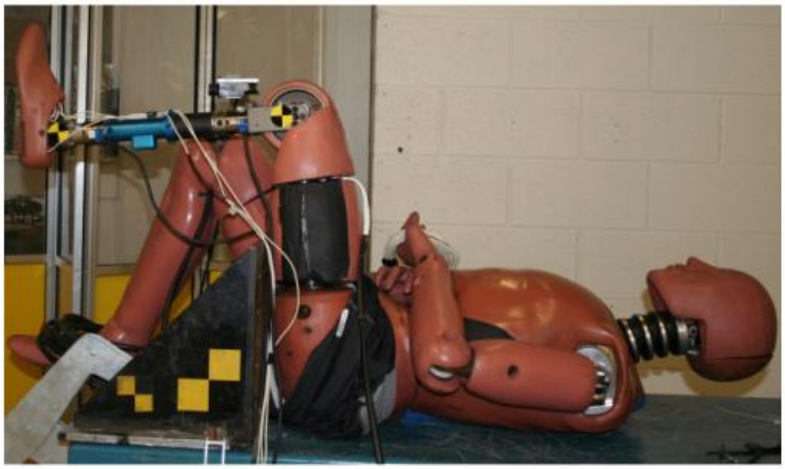

Figure 21 : The Linear impactor test set up[47]

Frangible Surrogates Testing

An experimental set-up was carried researchers form from Canadian Centre for Mine Action Technologies (CCMAT) to evaluate the effectiveness mine of protective footwear and assess the injury to the lower leg using a FSL surrogate subjected to blast loading. Three surrogate tubular structures were subjected to three distinct charges: PMA-3, 50g C4 and PMA-2. Instrumentation sus the strain gauges, high-speed cameras, load cells and flax-ray film cassette were used to monitor the blast event and the response of the test subject [44]. As shown in Figure 22, the FSL with a safety boot is set to support its own weight and a landmine was placed directly below the heel in a sand box. At the end of each test, pieces of the boot and FSL fragments were gathered. Thereafter an autopsy was carried out to determine the injury pattern. Figure 23 shows the correlation between the real blast photographs and an x-ray autopsy was carried out after each test.

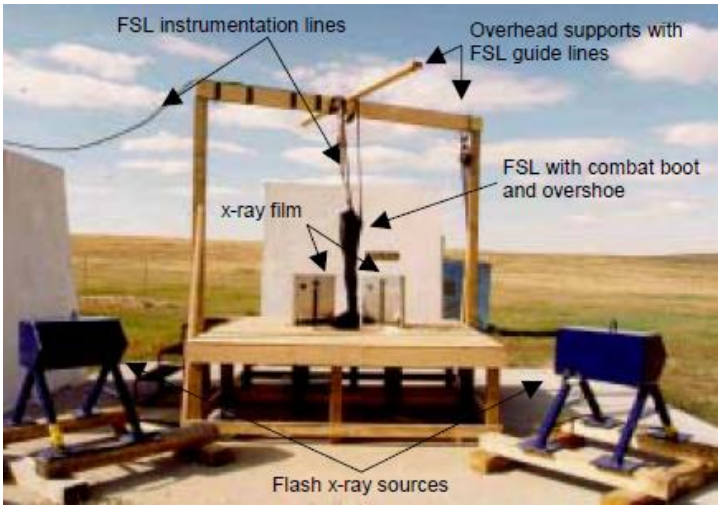

Figure 22 : A photograph showing the experiment set up of the FSL blast test, Canadian Centre for Mine Action Technologies (CCMAT) [48]

The results obtained were compared to the results obtained by Lower Extremity Assessment Procedure (LEAP) tests. The results concluded that FSL is an effective surrogate to use in assessing blast injury and validation of the mitigation strategies against blast loading [48]. As shown in Figure 30, the level of traumatic amputation increased as explosive mass increased from (a) to (c).

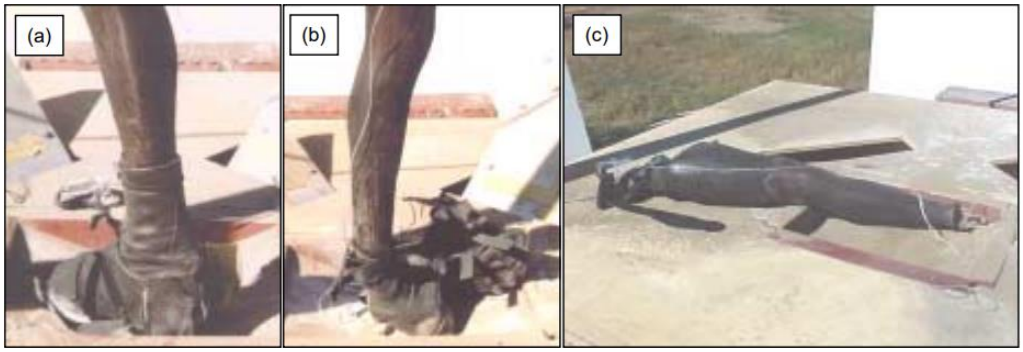

i. External damages

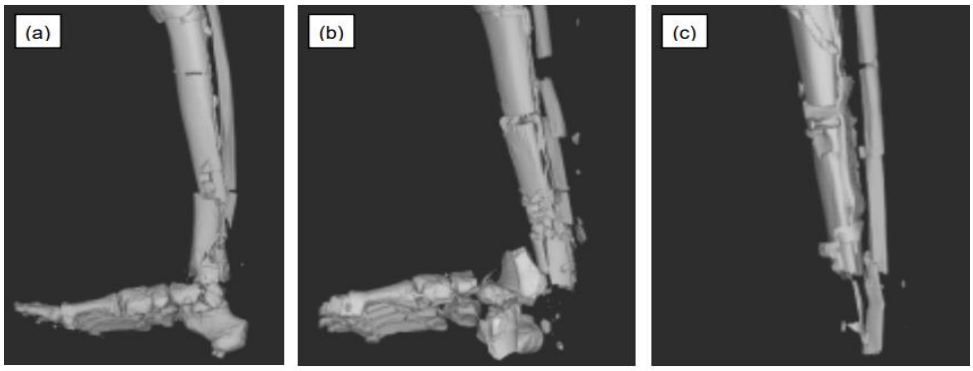

ii. Internal damages

Figure 23 : An image showing the correlation between the external (i) and internal (ii) damages of blasting of FSL with safety boot for the (a) PMA-3, (b) C4-50 and (c) PMA-2 landmine [48]

Testing Cadaver models

Testing cadaver models in blast scenarios has been an important area of biofidelic research to better understand and mitigate blast injuries. Several key studies have utilized cadavers to characterize the effects of blasts on different bodily systems and injury patterns.

Using the lower leg impactor approach, the researchers at the Medical College of Wisconsin examined how the cadaver lower leg and the Hybrid III lower limb responded. The dynamic stiffness of the cadaver lower limb as well as the ratio of axial force between the two test participants were determined. The test subject was able to slide when the impactor struck its base because a ballistic pendulum was utilized as the impactor. As seen in Figure 23, the test was run while adjusting the pendulum velocity. A pendulum acceleration and forces were measured using load cells and accelerometers.

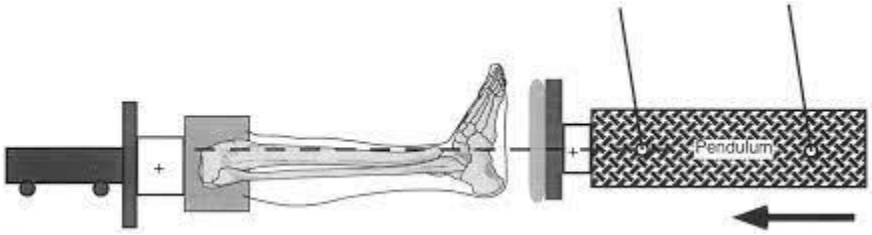

Figure 24 : Lower leg impactor test setup on a human lower leg cadaver [49]

Ramasamy utilized cadaveric lower limbs suspended vertically to simulate a standing posture near an explosion. They delivered controlled Claymore mine blasts to the limbs and analysed resulting trauma patterns through

dissection and x-rays. Strain gauges measured forces experienced during the blasts [14]. The dynamics of fluid or air flow around the head are fundamentally governed by its geometry, and this flow dynamics plays a crucial role in determining the mechanical load experienced by the head. Investigations have been carried on using the brain skull to investigate the traumatic brain injury using experimental and computational approaches. It was concluded that the head geometry significantly influences the dynamics of fluid flow around the head, impacting the mechanical load it experiences, hence the propagation of stress and localized in the occipital region [50]. Shock tubes were utilized by Masouros to deliver controlled underside blasts to cadaver lower limbs[51]. They positioned the limbs to simulate occupants in military vehicles. High-speed video captured limb kinematics during the blasts and fractures were assessed through dissection. A similar cadaver leg model was simulated military boots and used characterize injuries[52].

In summary, the studies show evolution in experimental methodology from basic limb loading to more sophisticated anatomical limb positioning. The use of sensors, high-speed video, and detailed trauma analysis provides in-depth understanding of lower extremity blast injuries for developing better protections.

2.5.5 Numerical Approach

The experimental methods have proved essential in assessment of landmine protective footwear and studying the physics behind the blast event. However, the process is complex, time consuming and difficult to monitor and obtained a detailed response of the test subject and the protective footwear. It is a costly process as well. Thus, numerical methods have been employed to provide a more detail to by understanding of the mine blast event on proximity and enabled a better response of complex structures subjected to blast loading.

Numerical modelling is a technique that is continuously evolving to better mimic the physics of mine blast and determine material of responses of structures at different times of the blast event. This method involves the use of Arbitrary Lagrange Eulerian-Lagrangian or Eulerian-Lagrangian analysis to model landmine detonation and the reciprocal action with structures. The numerical modelling technique are coupled together using power computers to develop material models that will imitate the response of complex structures such as the human leg with an increased accuracy to predict injury. Figure 25 shows the correlation between the real time landmine blasting and numerical modelling of landmine blast.

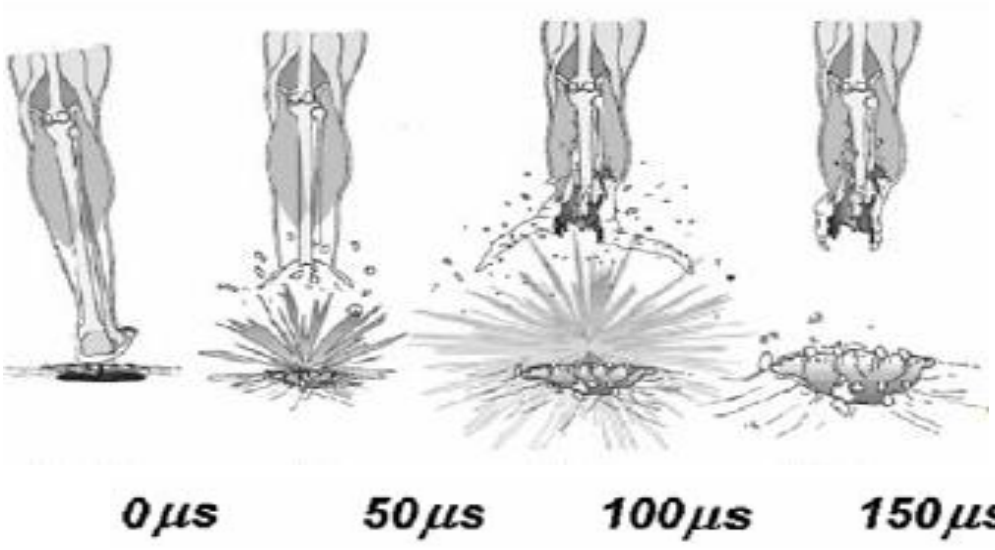

Numerical model of landmine blast test

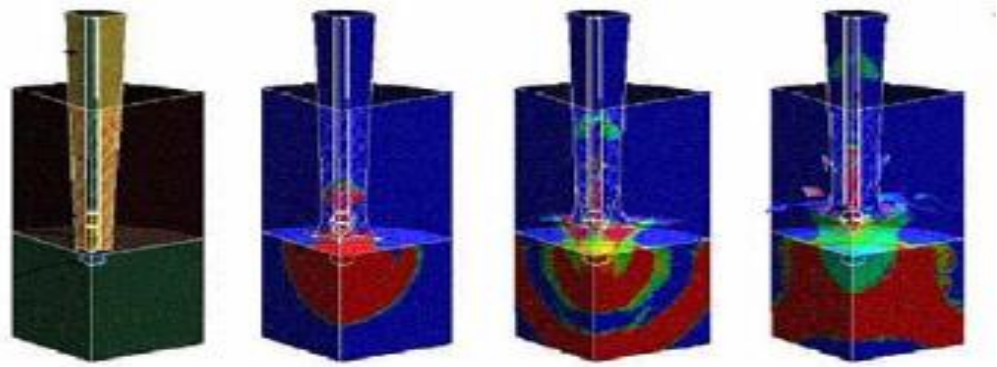

Figure 25 : Schematic diagram showing the correlation between real landmine blast and numerical simulations, of a surrogate tibia over a period of 150 μs [53]

Singh and Basri [44] developed a finite element computational framework utilizing a biofidelic human body lower limb model to simulate landmine blasts. The primary objective of this framework was to validate the model by comparing the tibia forces and injury patterns with data from Post-Mortem Human Subjects (PMHS) test models. The construction of the finite element model was accomplished using LS-Dyna software, and the model included buried M-14 mine detonations targeting the hind-foot, mid-foot, and front-foot, as depicted in Figure 26.

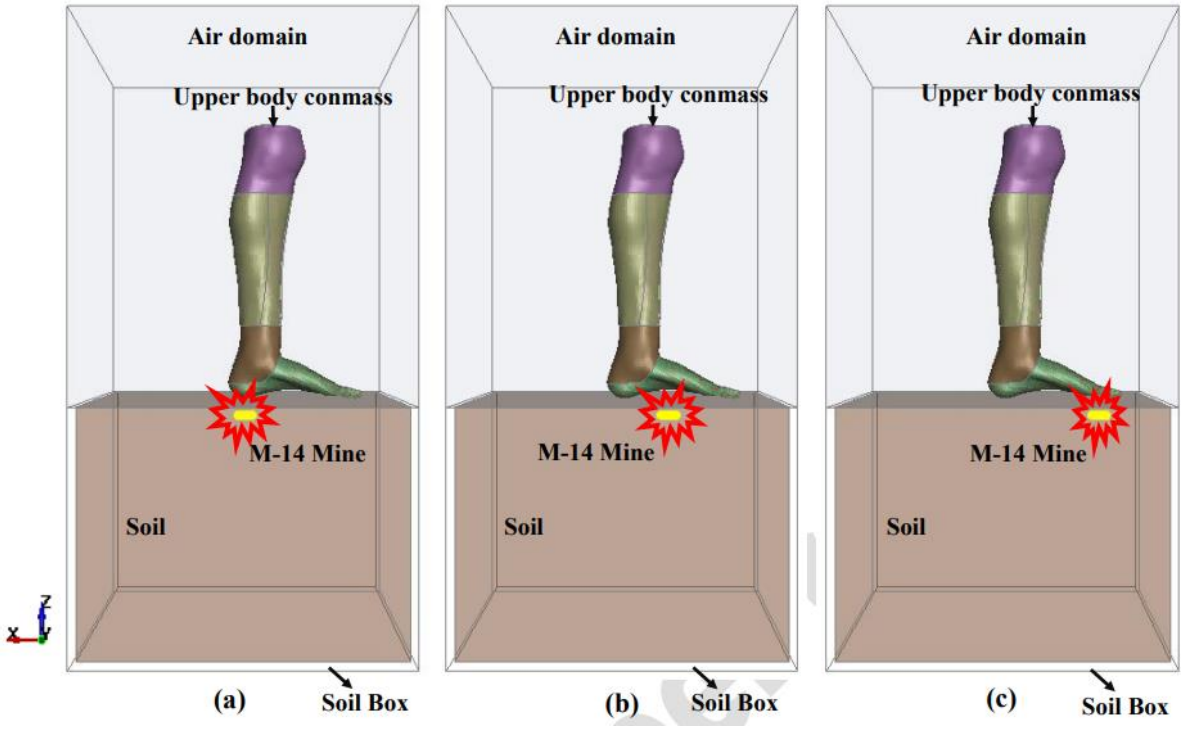

Figure 26 : Finite element model of (a) hind-foot, (b) mid-foot and (c) front-foot subjected to a M-14 landmine blast [54]

The finite element model successfully validated using the tibia forces and injury patterns based on the Post Mortem Human Subjects (PMHS) tests [55]. The numerical approach gave insights into the physics of landmine blasts for different mine threats and analysis of the pathophysiology of lower extremity trauma. However, limitations still existed due to simplified anatomy, unknown material properties, simplification of blast physics

which limits the simulation of complex human variability and behavioural effects. Hence, more data is needed to improve numerical blast models.

2.6 Summary

Landmines are a major cause of casualties and vehicle damage in military conflicts due to their low cost and ease of deployment. The detonation of landmines generates blast waves that induce severe injuries, with the lower limbs being the most vulnerable. Researchers employ a multifaceted approach combining clinical data, physical experiments, and computer simulations to investigate the complex injury mechanisms caused by landmines. This research has led to new strategies for mitigating landmine injuries through protective equipment and vehicle design modifications. Landmines are categorized as either anti-personnel (AP) or anti-vehicle (AV). AP mines like blast and fragmentation mines target individuals, while AV mines aim to immobilize vehicles using blast and penetrator effects. Detonations produce either idealized Friedlander-type or more complex blast waveforms, characterized by parameters such as peak pressure, impulse, and duration.

The lower limbs are highly exposed to landmine detonations and susceptible to severe trauma. The anatomy, geometry, and material properties of bones like the tibia influence their biomechanical response to blasts. Clinical evidence indicates primary blast effects on soft tissues and organs, while secondary effects cause penetrating wounds and fractures concentrated in the lower limbs. Researchers have developed surrogate legs, including mechanical, frangible, and cadaver models to experimentally study landmine blasts. These aim to mimic the anatomy and properties of actual human legs. The models are instrumented and subjected to controlled blast loads using shock tubes, explosives, or mechanical impactors to measure their responses. Computational methods using finite element analysis provides additional insights into injury mechanisms.

While studies have provided initial insights into the injury patterns through clinical data along with simplified experimental and computational biomechanical models, fundamental gaps persist in understanding localized damage mechanisms arising from blast wave interactions with lower limb tissues and bones. Key limitations include approximate surrogate anatomy, restricted visualization of internal damage progression, simplified computational models lacking anatomical heterogeneity and rate-dependent effects, limited injury metrics focused on overall trauma severity rather than localized tissue-level damage, and a lack of large statistical datasets capturing variability. There is a critical need for more systematic studies enabled by higher-fidelity experiments and simulations providing greater biological accuracy, along with real-time in-situ visualization capabilities to reveal the rapid evolution of injuries for developing timely treatments. A multidisciplinary approach addressing these gaps through more discerning injury metrics, biofidelic models, large datasets, and in-vivo imaging would provide deeper insights into the progression of blast injuries, transforming the ability to mitigate their devastating effects on lower limbs via targeted protective strategies and therapies.

Further research on the biomechanics of the tibia under blast loading is critical for a fundamental understanding the behaviour of tibia under dynamic blast loading may provide insights into the progression of traumatic lower limb injuries. Understanding the biomechanics of how blast waves induce injuries is critical, with a focus on the tibia bone. The tibia is the most exposed and strongest component of the lower limb, suffering the most complex damage as the foot is often ripped off during anti-personnel landmine blasts. Since the tibia is at the forefront of absorbing the intense impulsive loads from blasts, unravelling its mechanical response and failure modes is key. As a result, the result from this research forms an essential basis for developing enhanced protective strategies and therapeutic treatments to mitigate the devastating effects of landmine blasts on the lower extremities.

CHAPTER 3 – DESIGN OF EXPERIMENT

This chapter details the design of the blast experiment including the design and set-up of simplified tibia models, the modification and set-up of ballistic pendulums, and the arrangement and instrumentation of blast experiments. It also describes the process of capturing the stress response through the use data acquisition equipment.

3.1 Simplified Tibia Models

Due to complexity in shape and geometry of human tibia bone, the effect of the irregularities in tubular structure design was simplified using aluminium tubes machined in three different configurations; straight, stepped or tapered. Figure 27 depicts the different shapes and major dimensions of the aluminium tubes designed to represent a simplified tibia surrogate model. The length between the distal and proximal diaphysis of the tibia was used to evaluate the blast response and assessed the presence of developmental disorders, growth plate abnormalities, or fractures in the tibia [56]. The length of the models was kept at 450 mm which may not be the actual dimension of the human tibia since the tibia could vary because of a combination of genetic, environmental, and lifestyle factors. The dimensions of the surrogate tibia model were based on the easy accessibility of the Aluminium tube off the shelf with minimum machining requirements. The aluminium tube had dimensions of 25.04 x 3.18 x 19.04 mm and was cut into three 450 mm length tubes. Straight tube had similar dimensions as to the tube used. The second tube was machined to have a smaller external diameter of 23 mm for a length of 335 mm and a larger external diameter of 25.04 mm for a length of 115 mm to create a stepped tube. The third tube was machined into a tapered tube with external diameters of 23 mm and 25.04 mm at the two ends. The effects of muscles, tendons and skin attached to a human tibia were neglected, therefore there was no representation of these parts in the surrogate leg model design.

Although aluminium lacks the complex microstructure and rate-dependent properties of actual bone, it serves as a useful preliminary surrogate for controlled tibia blast experimentation to investigate stress wave propagation through a tubular structure with varying cross-sections. The homogeneous and isotropic aluminium provides more uniform and predictable responses compared to intricacies associated with bone. While aluminium results require careful interpretation, it provides initial control and consistency to demonstrate the basic experimental blast approach to use in numerical model validation. The response of bone is expected to be totally different.

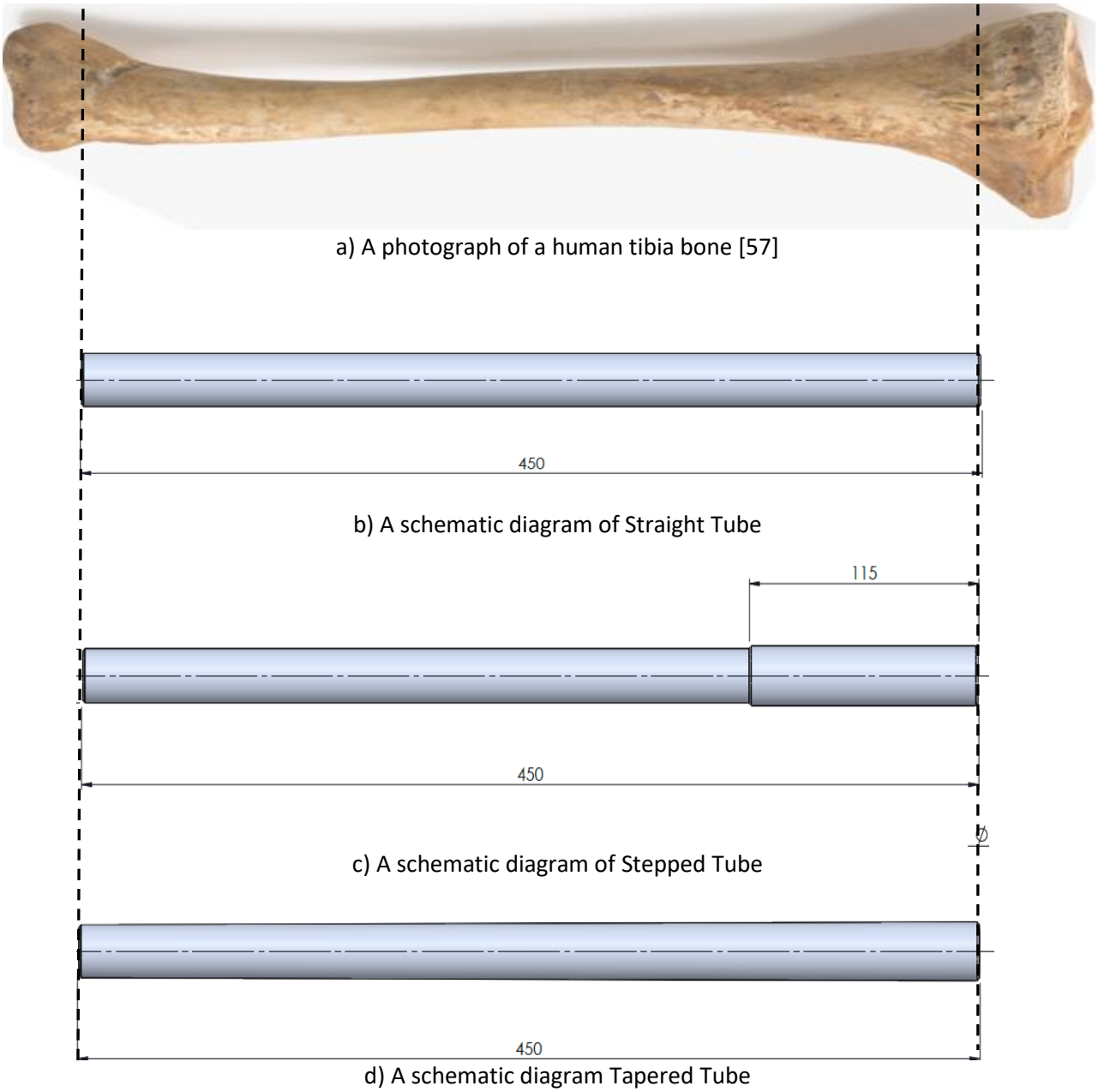

Figure 27 : Simplified surrogate tibia models

Split Hopkinson Pressure Bars (SHPBs) technique

The Split Hopkinson Pressure Bar (SHPB) is an experimental technique used to determine the dynamic mechanical properties of materials at high strain rates[58]. The SHPB consists of a striker bar, an incident bar, and a transmitted bar, usually made of an elastic material like steel or titanium. The test specimen placed between the incident and transmitted bars. A compressive stress pulse is generated by impacting the striker bar onto the incident bar and it propagates through and partially reflects through the specimen into the transmitted bar[58]. Strain gauges mounted on the bars allow measuring the strains caused by the stress pulses.

The different surrogate simplified tubular structures were used as Split Hopkinson Pressure Bars to capture the propagation of the blast-induced stress wave response when subjected to blast loading. The detonation of the explosive generated an incident wave that travelled to the tubular structure via a plate and thereafter propagated and reflected through the specimen. The transmitted and reflected stress waves were captured by the strain gauges mounted at the longitudinal centre of the tubular structure.

3.1.1 Strain Gauge Mounting

A set of two strain gauges were attached to each tubular structure opposite to each other using a special adhesive with the metal foil pattern lying parallel to the axis of the tubular structure to provide maximum sensitivity to axial stress. The set of strain gauges were mounted at the centre of each the tubular structure at 225 mm to capture the full signal as it travels through the centre of the tubular structure. This arrangement enabled a comprehensive and accurate assessment of stress distribution and deformation behaviour in the tubular structure. Figure 28 shows an image of the strain gauges mounted on the tubular structure. The specifications of the strain gauges used are listed in Table 4.

Figure 28 : A photograph showing the Strain Gauge mounted on the tubular structure [59]

Table 4 : Strain gauge specifications [48]

Make	TML Strain Gauges
Model	FLAB-2-23-1LJC-F
Gauge Factor	2.13
Gauge length	2 mm
Gauge Resistance	120 ± 0.5 Ω
Transverse Sensitivity	1.2 %
Lead wires	10/0.12 2W r=0.32 (Ω/m)

A Wheatstone bridge circuit and an amplifier were used to effectively capture and amplify the strain response from strain gauges. The strain gauge captures changes in resistance which are very small, therefore an amplifier magnified the change in resistance to visualize the signal output. The introduction of the Wheatstone bridge circuit and an amplifier enhanced the sensitivity and accuracy of the strain measurement thereby minimizing the noise and interference that could affect the accuracy of the strain measurements. All the circuits were connected to the PicoScope to collect the results and displaced onto a computer.

3.1.2 Strain Gauge Output Analysis

The output voltage from the strain gauges circuit was transformed into a stress history using the parameters presented in Table 5. The strain gauge factor specified for Aluminium, the amplifier gain and the bridge factor from the bridge circuit were obtained to facilitate the conversion process. The blast-induced stress, Equation 8, was calculated by multiplying the output voltage from the strain gauge with a conversion factor, K, in Equation 7 [59].

$$K = \frac{4E}{ABFV_{in}}$$

Equation 7

$$\sigma = \quad K\ x\ V_{out}$$

Equation 8

Table 5 : Strain gauge circuit parameters

Parameter	Definition	Value
E	Young modulus of the tubular structure material	68.9 GPa [60]
A	Gain Amplification	1000
B	Bridge Factor	2
F	Strain gauge factor for Aluminium	2.13 [48]
V_{in}	Bridge voltage supply	2 V
V_{out}	The output voltage from the test	Test result
σ	Stress-induced	Obtained from Equation 8

3.2 Ballistic Pendulum Design

The design modification of the horizontal ballistic pendulum, illustrated in Figure 29, was implemented to accommodate the varying cross-sections of the tubular structures. The original plate clamps and blast tubes were replaced with a witness plate, to which the explosive was attached. The front and middle plates were altered to suit tubular structures. The front and middle plates was divided into two parts, plate A and plate B, creating a central hole capable of accommodating various sizes of central bushings, as shown in Figure 30. Assembly of plates A and B was facilitated using two 6 x 6 mm dowel pins for alignment. The resulting assembly featured a 48 mm central hole, allowing for the insertion of an aluminium double-flanged central bushing.

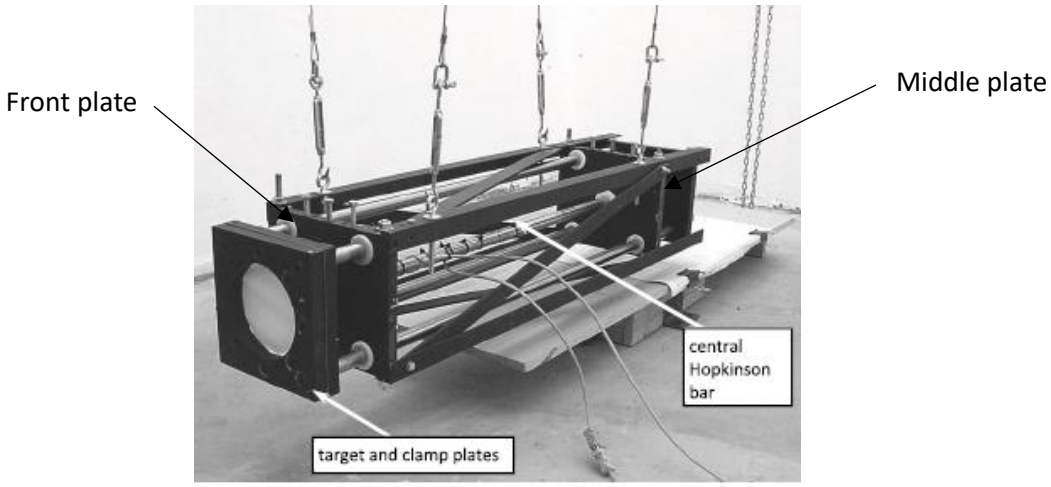

Figure 29 : An image of a horizontal ballistic pendulums initial design [61]

An aluminium double-flanged bushing was introduced into the central hole when the two plates were joined together to facilitate the insertion of single-flanged bushings of different shapes. Different single-flanged bushings were designed to accommodate the different geometries of the tubular structure. The tolerance between double-flanged bushing and single-flanged bushing allowed for easy interchangeability of the bushing when attaching a different tubular structure. A total of six single-flanged central bushings were manufactured to match specific geometry of the tubular structure. Single-flanged central bushings were attached to both the front and middle plate sub-assemblies to hold the tubular structure horizontally. The tubular structure and the single-flanged central bushings were designed with a sliding fit to allow for movement as it experienced the blast load. Figure 29 shows how the components were connected to the single flanged central bushing on the front and middle plate sub-assembly.

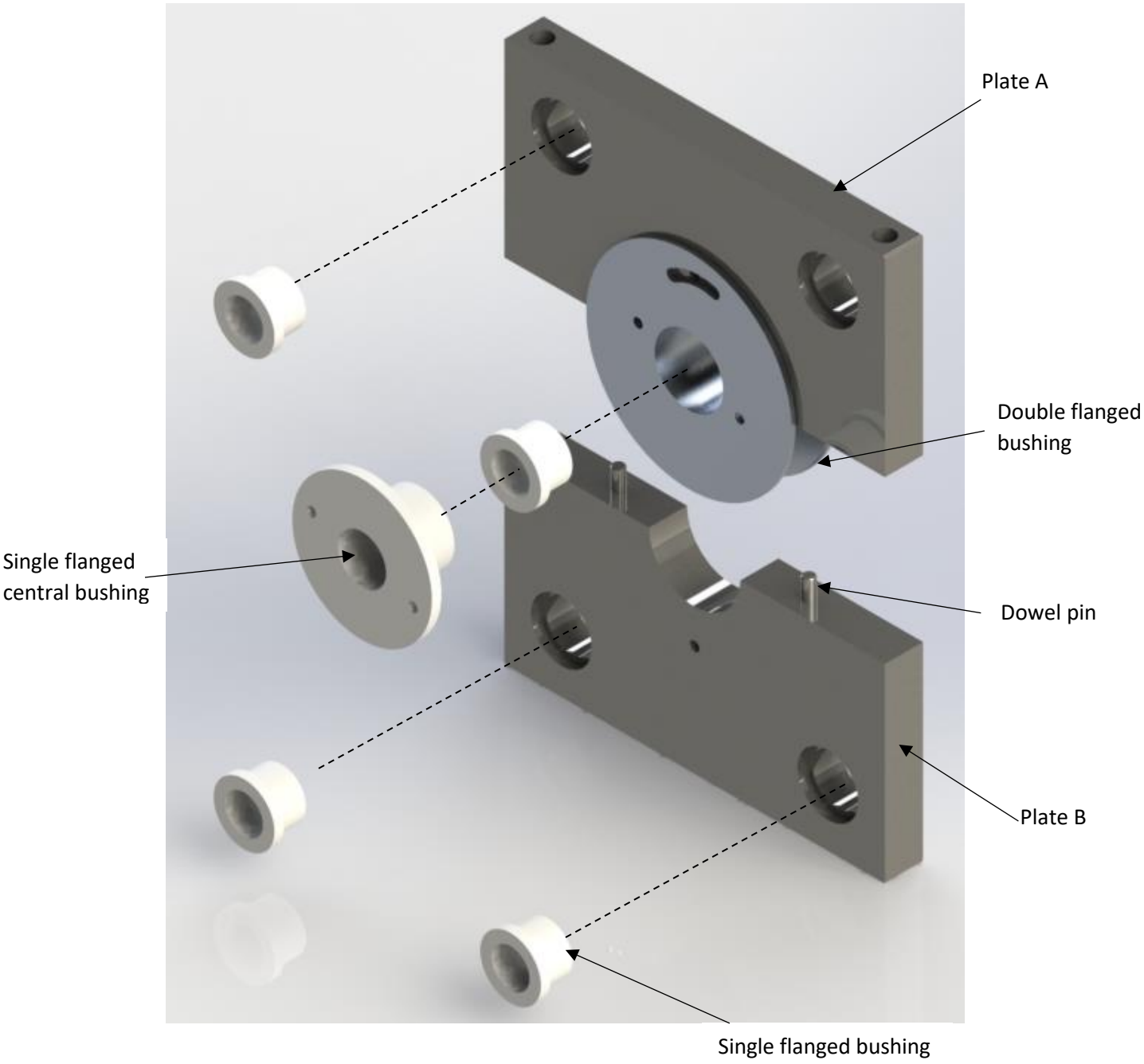

Figure 30 : A rendered image showing the exploded view of the Front/Middle plate sub-assembly.

Additionally, eight single flanged bushings were designed to fit the four solid shafts that hold the witness plate and the front and middle sub-assembly plates together. These single flanged bushings facilitated the sliding movement of the witness plate upon detonation. A slot was incorporated into the central double flanged bushing to enable vertical movement of the bushing between the gaps shown in

Figure 31. A 6 mm bolt was employed to guide the movement of the bushings along the slot, allowing for adjustment of the surrogate tibia model. Each tubular structure was adjusted using this mechanism to align its axis with the horizontal axis.

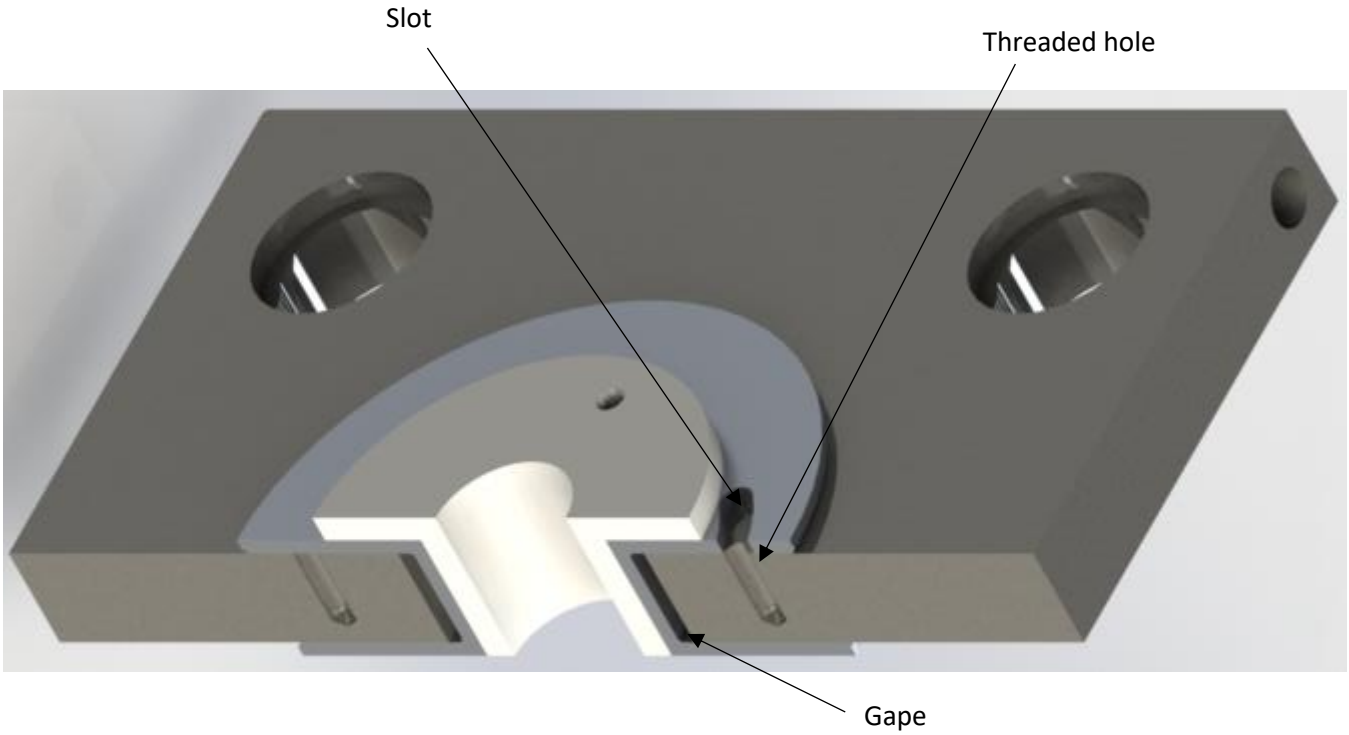

Figure 31 : A schematic diagram showing section view of the front/ middle plate sub-assembly.

The finalized arrangement of the horizontal ballistic pendulum, as illustrated in Figure 32, incorporated a mild steel witness plate (either 5 mm or 20 mm in thickness) to simulate the floor of a vehicle. A rigid 20 mm thick plate was utilized to represent the non-deformable witness plate, while a 5 mm thick plate was employed to represent the Deformable witness plate. A 20 mm mild steel back plate, and two 20 mm mild witness plates responsible for securing the central double flanged bushing used to position and hold the Teflon bushing connected to the surrogate tibia model. Dowel pins were utilized to align the two plates forming the front/middle sub-assembly, while four round solid bars held the witness plate and the front and middle sub-assembly together. The assembly was further reinforced by attaching four angle bars and flat bars to connect all the components of the horizontal ballistic pendulum. The overall length of the ballistic pendulum was adjusted to accommodate the dimensions of the surrogate leg model. For detailed information regarding the dimensions and geometries of all the components utilized in assembling the horizontal ballistic pendulum, please refer to APPENDIX A.

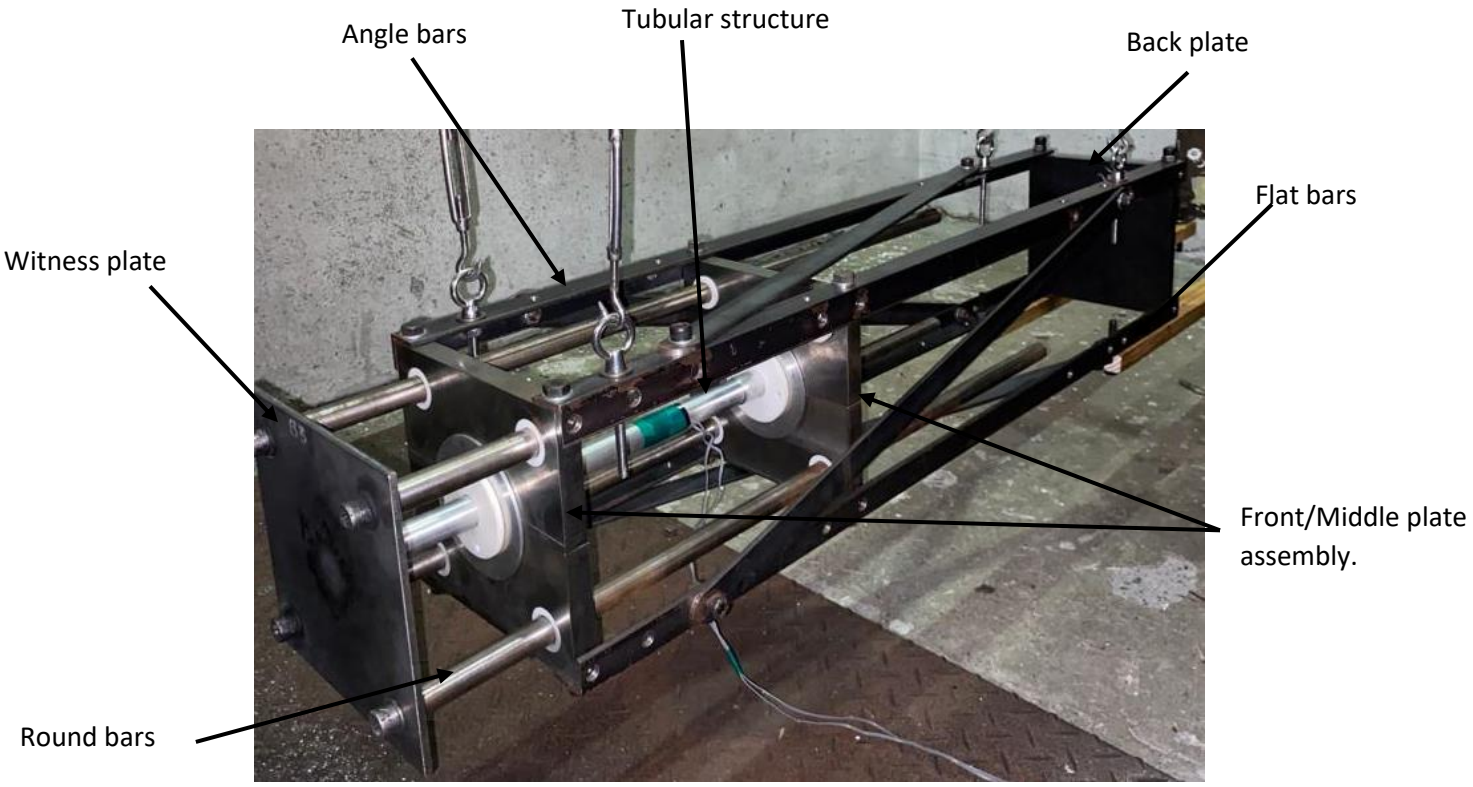

Figure 32 : Photograph of the horizontal ballistic pendulum with surrogate tibia Straight tube attached.

3.3 Ballistic Pendulum Set-up

The ballistic pendulum was suspended by four adjustable spring wire cables attached to the holding bars in the blast chamber as depicted in Figure 33. The adjustable 6 mm turnbuckle hooks were used to ensure that the ballistic pendulum was horizontal. The pendulum had a mass of 53.0 kg and 48.4 kg with non-deformable and deformable witness plate, respectively. A counter mass was placed at the back end of the pendulum to balance the masses at the front end so that the ballistic pendulum swung centrally. A laser displacement sensor mounted on the wall was used to measure the displacement of the ballistic pendulum and induced impulse upon the detonation of the explosive. The tubular structure, which was equipped with mounted strain gauges, was affixed to the ballistic pendulum in conjunction with the single flanged bushings designed specifically for that model.

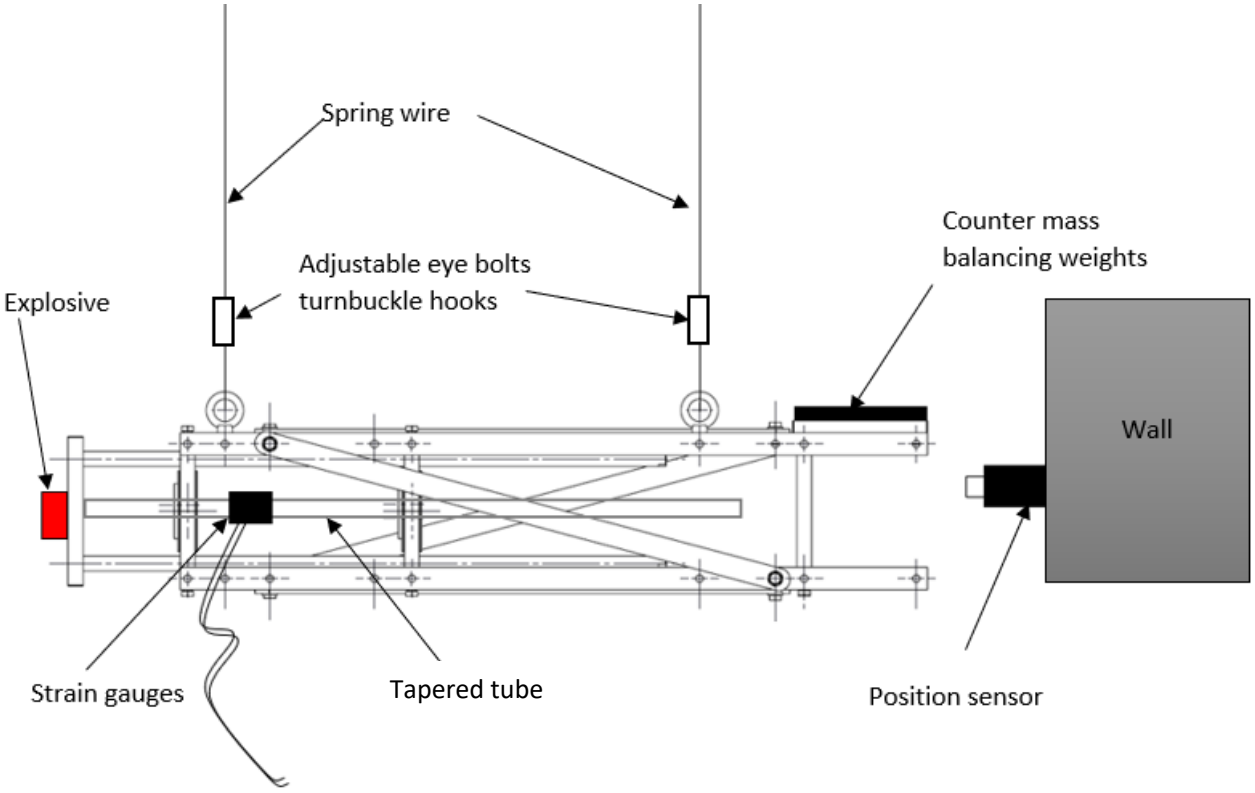

Figure 33 : A schematic diagram showing the ballistic pendulum test set up.

3.4 Explosive Charge Set-up

A 2.5 +1g cylindrical PE4 charge measuring 3 mm in height (H) and 20 mm in diameter (D) with an TNT equivalent weight of 4.62g [35], was attached to a cylindrical polystyrene foam with a thickness of 13 mm and a diameter of 100 mm. The purpose of using the polystyrene foam was to ensure consistent positioning of the charge. It was assumed that the polystyrene foam would burn upon detonation without significantly affecting the blast loading. Throughout all the tests, the parameters and geometry of the explosive was kept constant to maintain the magnitude of the impulse induced. Figure 34 provides an illustration of the setup with the explosive.

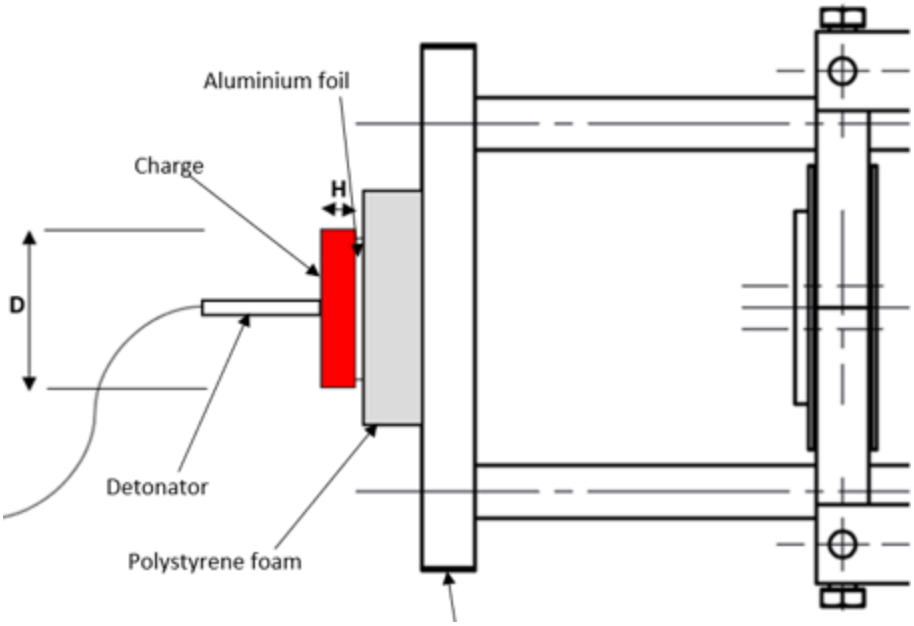

Figure 34 : A schematic diagram showing explosive charge set-up.

3.5 Instrumentation

A trigger circuit was incorporated to initiate the recording of voltage changes in both the strain gauge and trigger circuit when the charge detonated. An aluminium foil was affixed to the charge, which broke upon detonation, resulting in a voltage change within the trigger circuit. A detonator was positioned at the centre of the charge to initiate the explosion. The configuration of the trigger circuit is depicted in Figure 35.

Figure 36 illustrates the tubular structure attached to the ballistic pendulum along with the instrumentation in the blast chamber, before attaching the explosive to the polystyrene foam. The wiring connections extended outside the blast chamber and were directed to the control room, where the responses measured during the blast tests were captured by the data acquisition devices depicted in Figure 37. A PicoScope device was utilized to collect the responses from the trigger circuit, strain gauge circuit, and position sensor. The collected voltage responses were then displayed on a computer connected to the PicoScope.

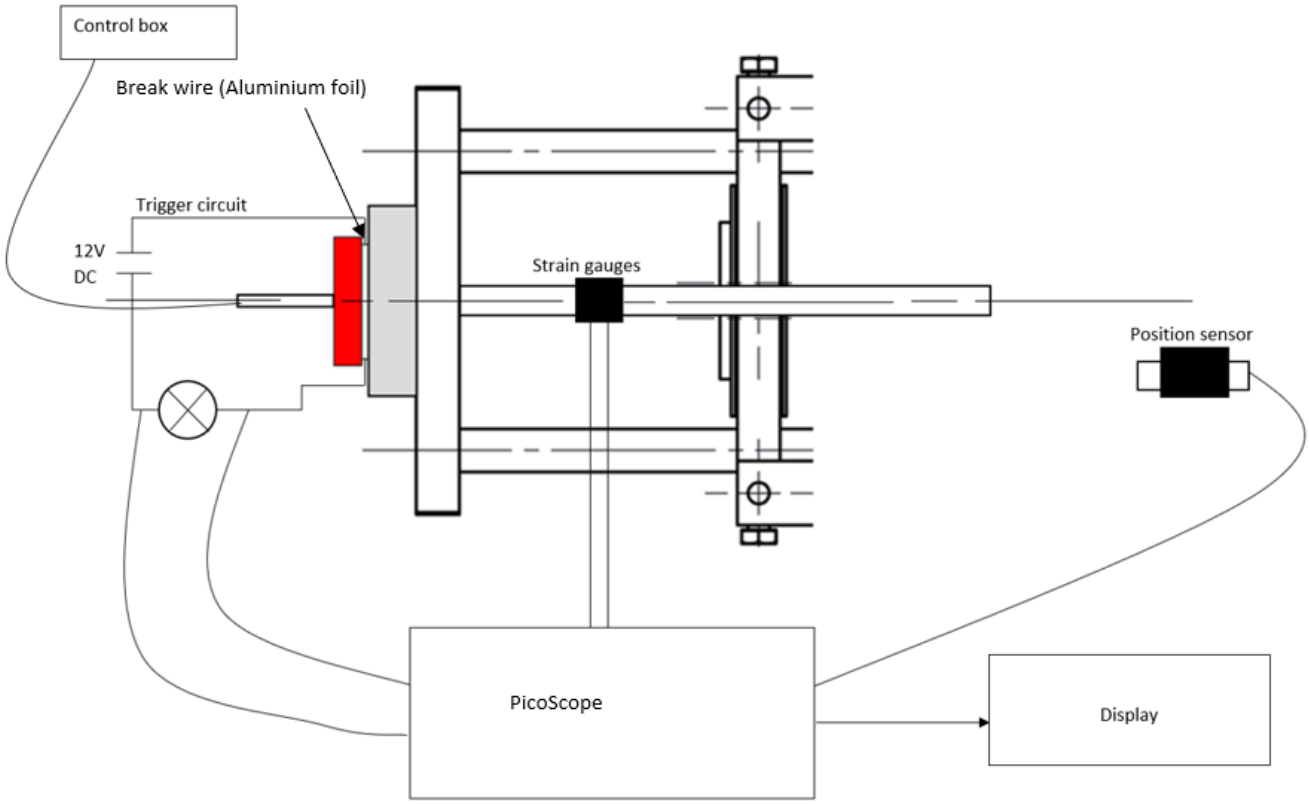

Figure 35 : A schematic diagram showing the instrumentation set up.

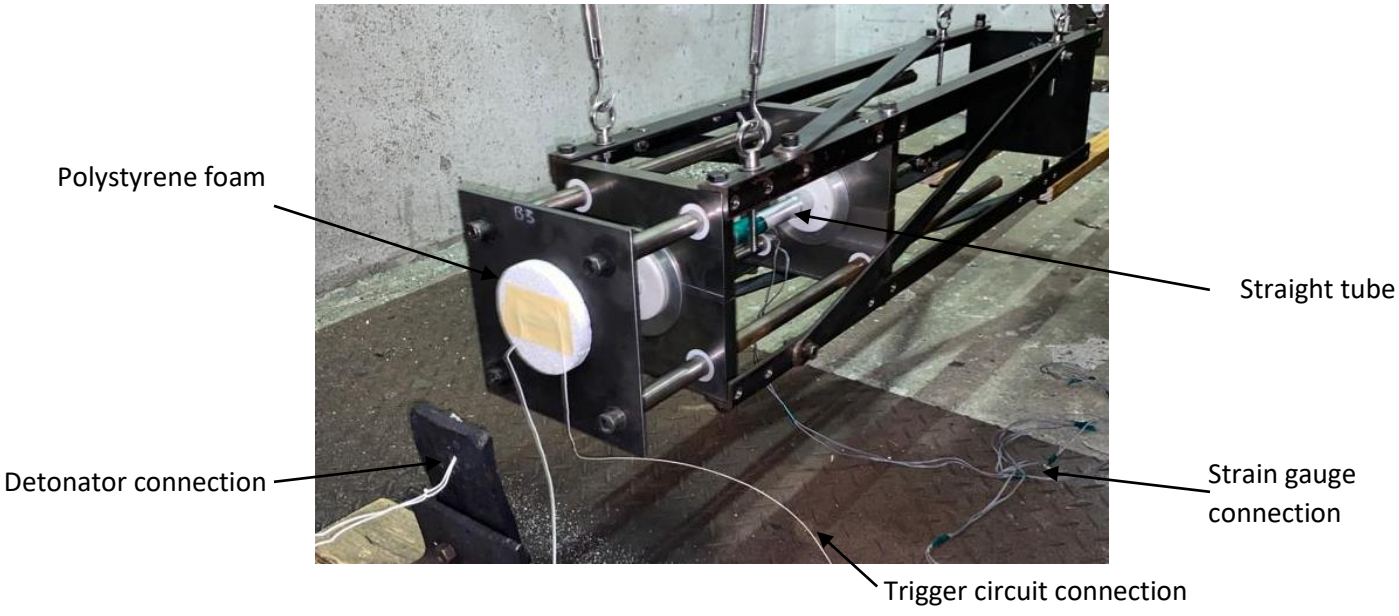

Figure 36 : Photograph of the test rig mounted in the blast chamber together with Straight Tube, strain gauge, trigger circuit connection and the detonator connection.

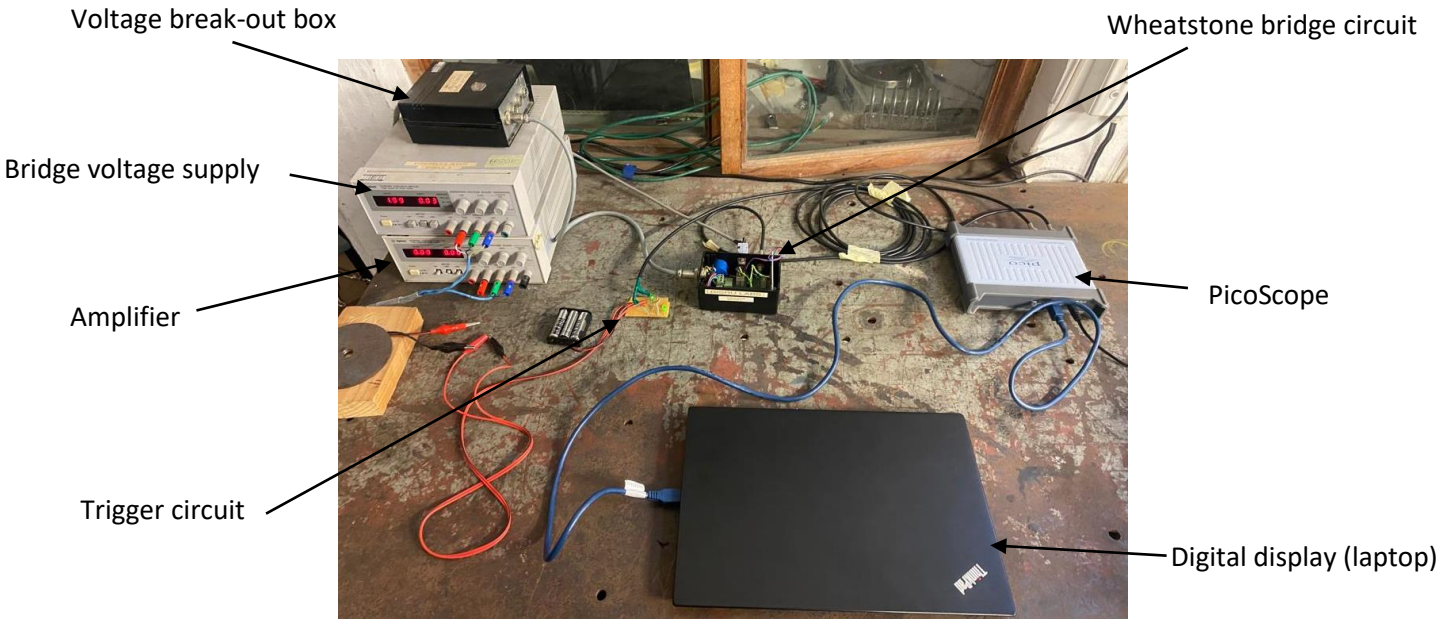

Figure 37 : A photograph of the data acquisition instruments set up used to capture the response of the tubular structure to blast loading.

3.6 Limitations and Constraints of the Experimental Approach

The experimental testing methodology utilizing a horizontal ballistic pendulum to study landmine blasts lacks the capability to fully replicate actual explosive events. The controlled laboratory conditions with standardized aluminium test materials for tibia model instead of bone material differ substantially from unpredictable real-world landmine explosions in irregular terrain with varying explosive forces and detonation locations. The experimental methodology approximates the complex parameters and variables in real world scenarios. Consequently, the accuracy of simulating the landmine blasts is limited. However, the experimental setup offers a valuable preliminary investigative tool for controlled examinations, furnishing foundational comprehension of stress wave dynamics. Initial insights gained can guide additional research using more advanced testing methods like field experiments or computational simulations to replicate real landmine blasts more precisely.

CHAPTER 4 – EXPERIMENTAL RESULTS

The Witness plate thickness was used to classify the testes conducted as deformable and non-deformable witness plate detonations. A naming convention was established, such as "S1/20_1" with S1 representing a test on straight tube and 20 representing a thickness witness plate and _1 representing the first test with the same set up. S2 represented a stepped tube and S3 representing the tapered tube.

4.1 Visual Observations

4.1.1 Non-deformable Witness Plate

The 20 mm thick plate showed no visible deformation, as shown in Figure 38 upon the detonation of the explosive. Localised abrasion of the surface in the central region where the charge was located were the only signed of damage on the thick plate. A visible circular burnt mark (black discolouration of the witness plate), like those reported by Nurick [61], was also evident on the blast sided of the plate.

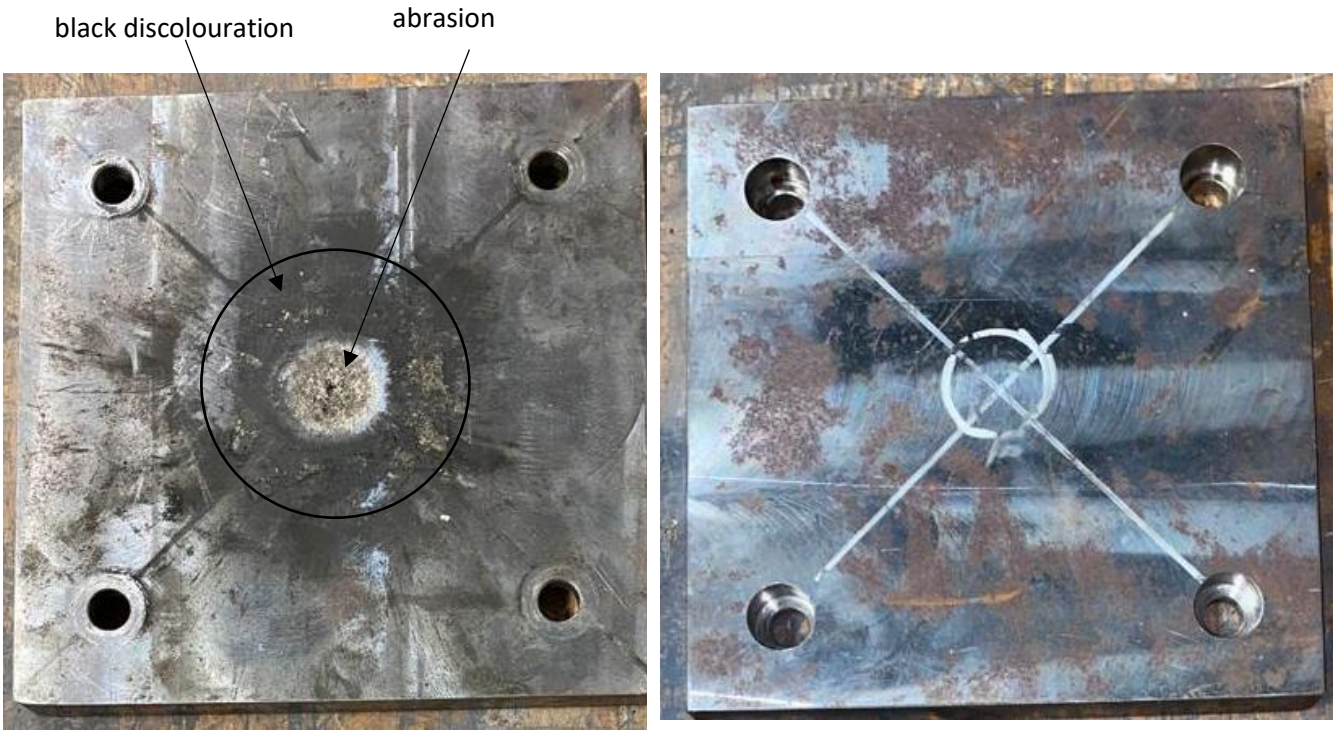

a) Blast loaded side b) Back face (non-loaded side)

Figure 38 : Photograph showing the damaged 20 mm thick witness plate.

All the tubular structures in contact with the 20 mm thick plate showed no visible deformation when the charge was detonated. The magnitude of the load transferred from the witness plate was not large enough to cause any plastic deformation at the point of contact.

4.1.2 Deformable Witness Plate

The 5 mm thick plate deformed in the central region upon the detonation of the charge. The localised abrasion of the surface and burnt marks, were also observed in the 5 mm thick witness plate as shown Figure 39. The tubular structures exhibited lateral deformation (bulging), as shown in Figure 40, on the surface that was in contact with the witness plate. The cross-sectional area of the tubular structures was distorted resulting in a flattened shape at the end of the tubes as shown in Figure 40 . The deformation was caused by the transferred stress induced by the blast load from the charge detonation.

a) Blast loaded side b) Back face (non-loaded side)

Figure 39 : Photograph showing the deformed 5 mm thick witness plate.

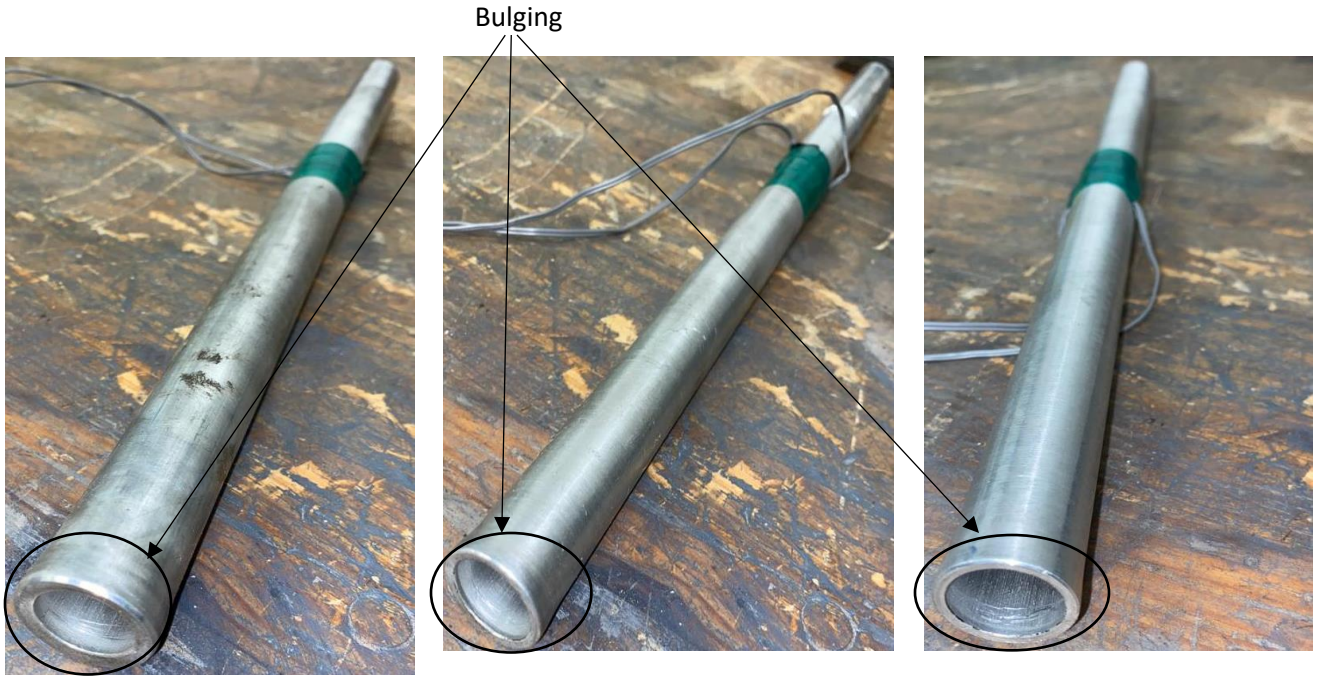

a) Straight Tube- Straight Tube b) Stepped Tube- Stepped Tube c) Tapered Tube- Tapered Tube

Figure 40 : Photographs showing the deformed tubular structures with deformable witness plate test.

4.2 Impulse Measurement

The displacement of the ballistic pendulum recorded as a voltage-time response. The voltage-time response was converted to displacement history, shown in Figure 41, by scaling the voltage by a factor of three, following the method described by Jacob [62]. The initial velocity of the ballistic pendulum as a function of time was then calculated by determining the slope of the displacement-time curve. The gradient of each curve was multiplied by the total mass of the pendulum to obtain the imparted impulse for each blast test. The displacement-time graphs from all the tests conducted were presented in APPENDIX B. Figure 41 depicts how the gradient was determined from the average displacement-time plot for all the experiments conducted. The average impulse exerted by the constant charge mass was found to be 4.6 Ns with less than 10 % variations suggesting good repeatability between experiments.

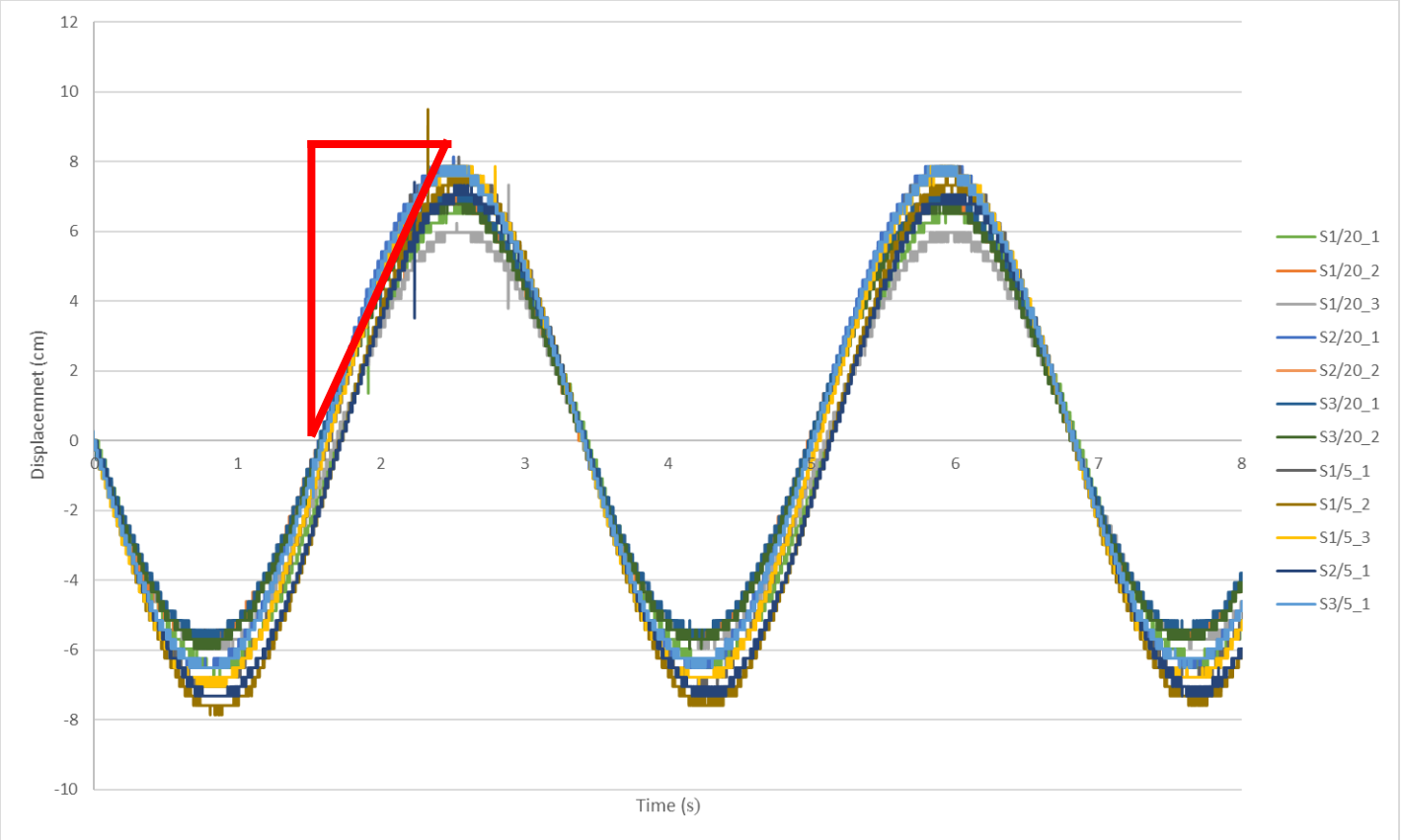

Figure 41 : The graph of the displacement time history of the ballistic pendulum displacement for each blast test

4.3 Stress Wave Propagation

The blast load generated a stress wave that was transmitted to the tubular structure through the witness plate. The blast-induced stress wave was monitored over a duration of 450 μs. The propagation of the stress wave within the tubular structures exhibited variations between compressive and tensile load cycles, aligning with the one-dimensional stress wave propagation theory proposed by Svensson [63]. The detailed description of the reflection of blast-induced stress waves upon encountering boundaries was omitted due to the complexities arising from continuous reflections and interactions with the tubular structures. As a result, the analysis focused only on the initial periods of the phenomenon.

In Figure 42 (a), region A-B represents the time taken for the stress wave to reach the strain gauges positioned at the centre of the tubular structure. It was expected that the stress-time response obtained from all the tests would exhibit consistency across both the tubular structure with non-deformable witness plates and those with deformable witness plates for the blast test.

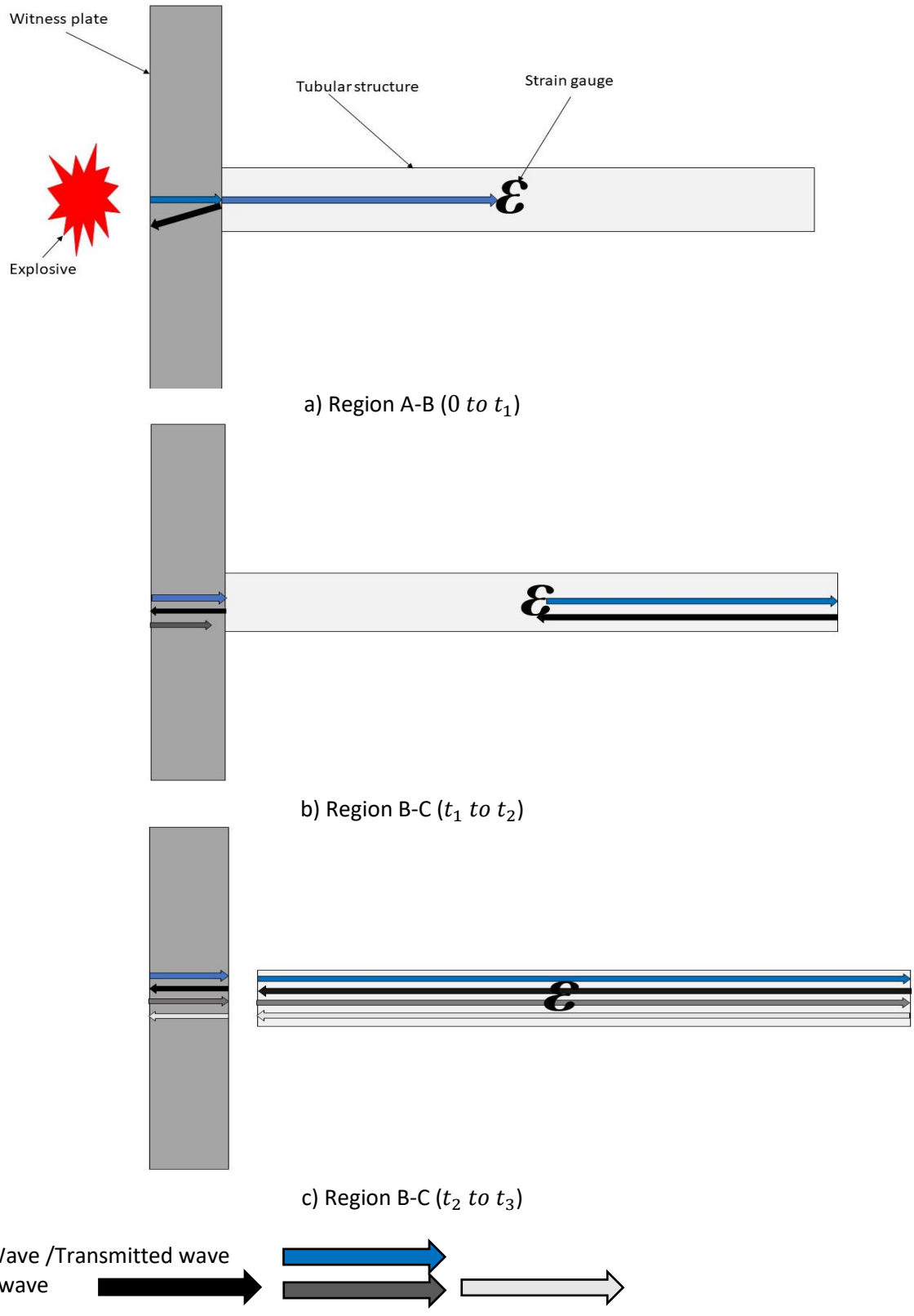

Figure 42 : An illustration of the stress wave one-dimensional wave propagation through a witness plate and tubular structure [51]

In Figure 42 (b), region B-C represents the period during which the stress wave travelled from the centre of the tubular structure towards the open end, where it encountered the free end boundary and reflected [63]. In this region, the tubular structure was expected to experience compressive loading as the induced stress wave propagated through it.

In Figure 42 (c), region C-D represented the period during which the reflected stress wave was expected to propagate back towards the witness plate. In this region, the stress wave would only be expected to continue interact with the tubular structure because of reflections as the stress waves encounter boundaries. Both the witness plate and the tubular structure would be expected to experience the continuous propagations of the stress wave as it weekends due to dispersion [63].

4.3.1 Processing Raw Data

Figure 43 depicts the voltage-time response obtained from data acquisition instruments during the blast experiment. Initially, the trigger circuit voltage was set at 2.2 V before the explosive detonation. When the circuit was disrupted, indicating the recording of the strain gauge voltage change, a subsequent voltage jump was observed. The variations across the strain gauge were recorded in Channel A of the PicoScope, while Channel B captured changes in the trigger voltage. Positive and negative voltage values were recorded after the trigger, as shown in Figure 43, indicating that the tubular structures experienced both compressive and tensile stresses as expected under the blast load. The positive and negative values of voltage was observed in all the tests as presented in APPENDIX B. Please note that only blast tests for straight tube blast tests were used to illustrate the processing of straight gauge voltage results capture by the PicoScope.

The PicoScope recorded the dynamic stress changes in the tubular structures as voltage-time signals during the detonations with non-deformable and deformable plates. These voltage profiles were converted to induced strain-time histories, depicted in Figure 44 and Figure 45. The non-deformable plate tests exhibited a maximum strain of 0.18 %, indicating that the tubular structures experienced minimal deformation based on visual inspection. In contrast, the deformable plate tests showed a peak strain of 0.60 %, suggesting that the tubular structures underwent small deformations greater than non-deformable plate tests, these were visibly noticeable upon inspection. The voltage out was later converted into a stress history by multiplying the strain gauge voltage magnitude by a conversion factor (K), from Equation 7 and Equation 8.

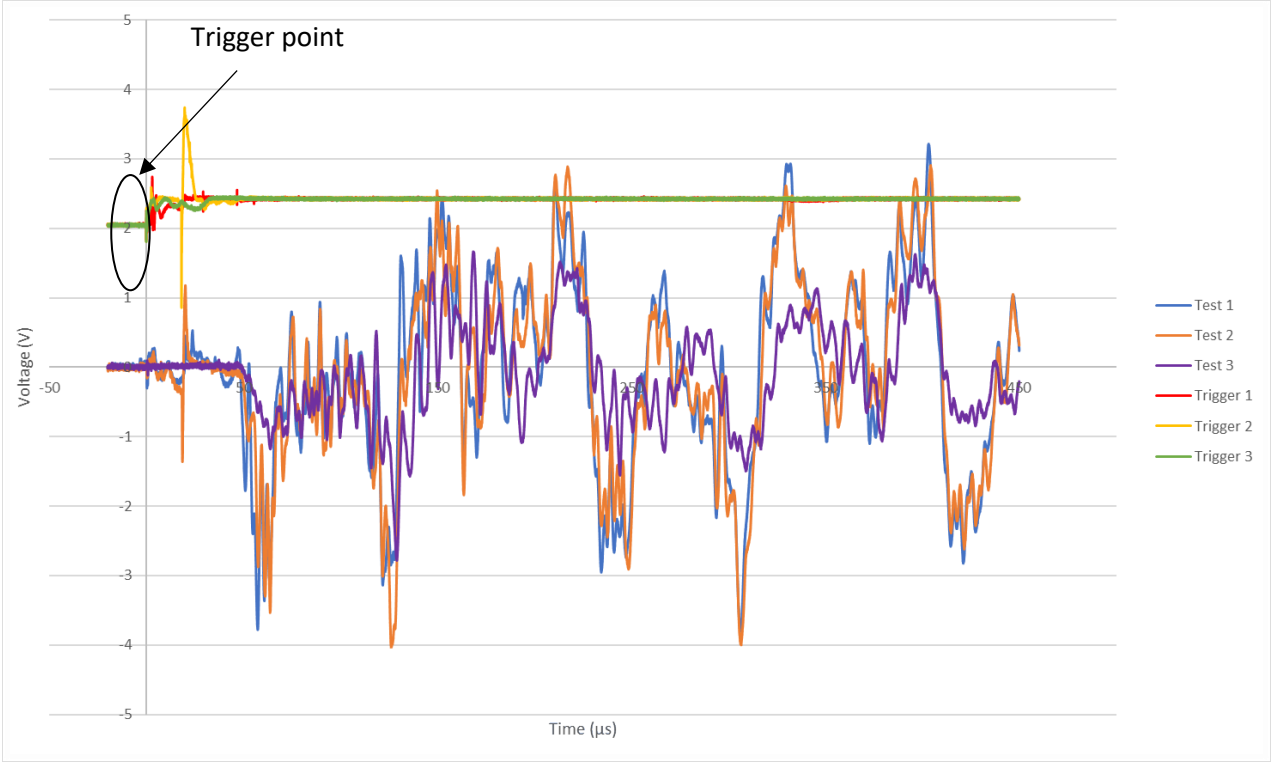

Figure 43 : Graph of voltage history recorded for the trigger circuit and strain gauge obtained from blast test of straight tube with non-deformable witness plate Test 1,2 and 3

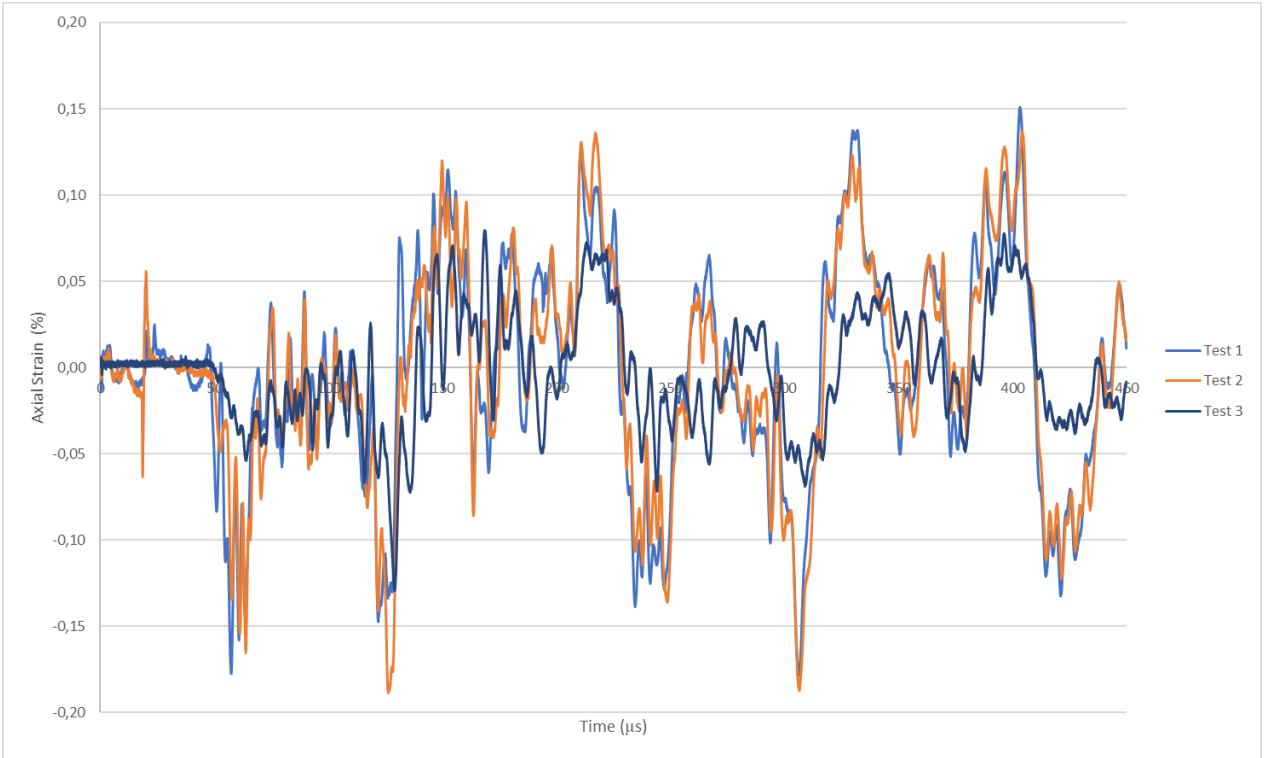

Figure 44 : The graph of the blast induced strain history recorded from the blast test of straight tube with non-deformable witness plate Test 1,2 and 3

Figure 45 : The graph of the blast induced strain history recorded from the blast test of straight tube with deformable witness plate Test 1,2 and 3

4.3.2 Non-deformable Witness Plate

Straight Tube

Figure 46 illustrates the stress-time response obtained from three tests using the straight tube in contact with a non-deformable witness plate. The time interval between Points A and B, averaging 50 μs, represented the duration it took for the induced stress wave to travel from the blast-loaded side of the witness plate to the centre of the straight tube, where the strain gauges were located. Within this region, there were sharp peaks caused by the breaking of the trigger circuit and interference from the detonator, resulting in voltage spikes captured by the PicoScope. Although these small spikes were present in all tests, they were considered insignificant since they were not caused by the blast load generated by the explosive.

The region from B to C indicated the period when the blast stress waves reached the strain gauge point on the straight tubular structure. The negative stresses observed in this region indicate compressive stresses resulting from the induced blast load. The overall shape of the stress wave resulting from the blast exhibited some similarities to the shape of the Friedlander pressure wave form an explosion as it propagates through air [32]. It displayed an abrupt increase in stress leading to the primary peak, followed by a rapid decline. This was noticed across all the stress response from all the tests. However, a notable difference was observed during the occurrence of the secondary peak, possibly due to the continued contact between the tubular structure and the witness plate during this period. This contact caused continuous transmission and interaction of the stress waves, resulting in the appearance of a secondary stress peak. When stress waves combined, constructive interference occurred, leading to a larger peak stress. Conversely, destructive interference caused a reduction in stress magnitude or

even cancellation. The peak stresses recorded were 121.8 MPa for Test 1 and 129.7 MPa for Test 2. Test 3 stress-time results exhibited a significant deviation from the observed trends in Tests 1 and 2 and was therefore disregarded for further analysis.

Region C to D showed positive stress, indicating that the tubular structure experienced a tensile load due to the reflection of the stress waves when they encountered the boundary of the tubular structure. In this region, both primary and secondary peaks, as observed in Region B to C, were present, indicating that the witness plate and tubular structure remained in contact during this period. The stress wave exhibited similar trend, as observed in region B-C. As the stress wave propagated through the tubular structure, a decrease in stress magnitude was noticed due to dispersion. The maximum positive peak stress of 80.4 MPa was recorded in Test 2.

Beyond point D, the stress waves exhibited increased complexity as they continuously interacted within the tubular structure, leading to the amplification and cancellation of stress waves in accordance with the principle of superposition. It should be noted that this section was not included in the scope of the present study, and therefore, the stress-time plots were only plotted up to 300 μs for the stress-time plots of other tests performed.

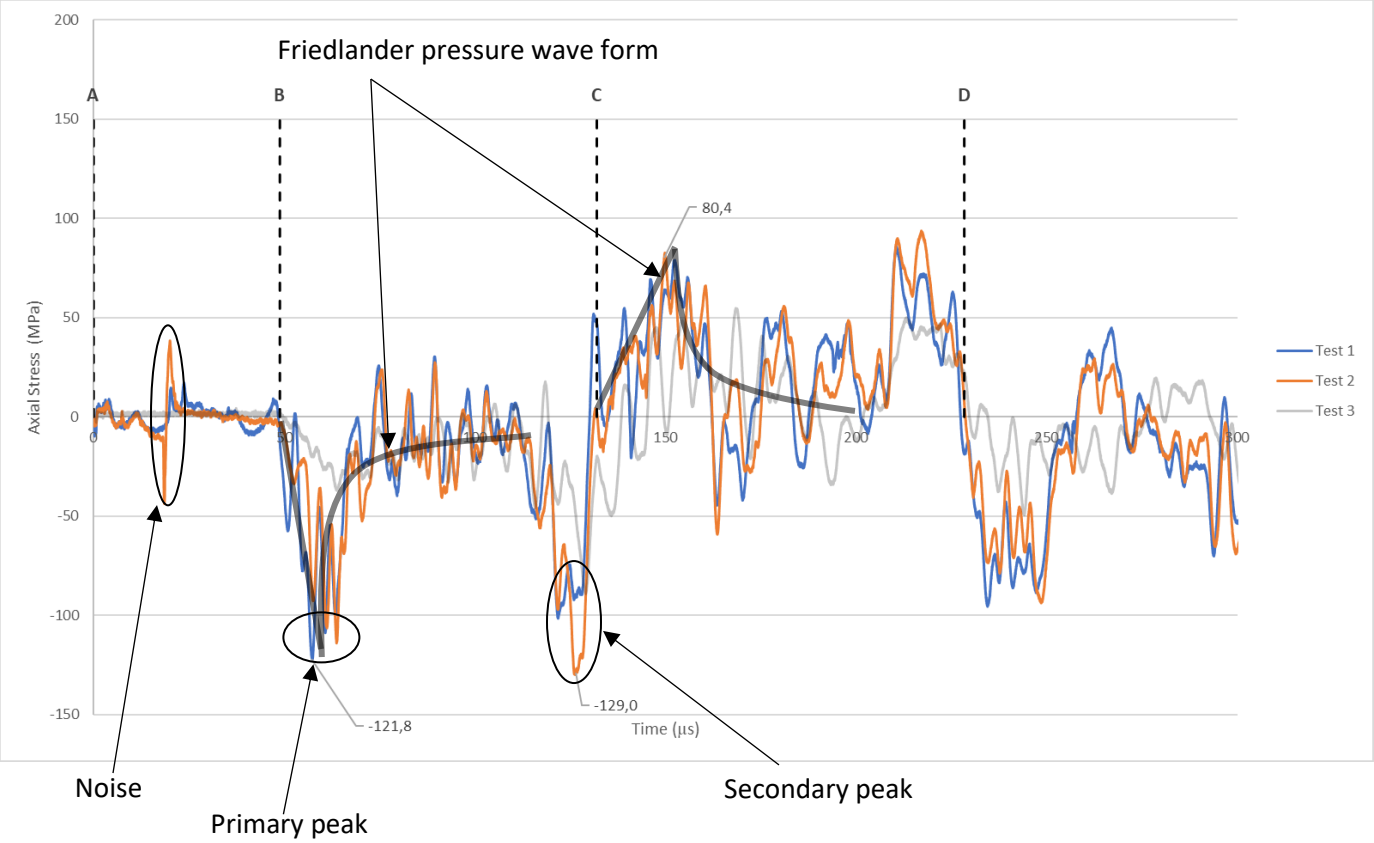

Figure 46 : Graph of stress history obtained from blast test 1, 2 and 3 of straight tube with non-deformable witness plate.

Stepped Tube

Two blast tests were conducted on stepped tube placed against a 20 mm witness plate, and the resulting stress-time responses are displayed in Figure 47. In region A-B, it took an average of 49 μs almost like the time it took the stress wave to travel from the witness plate to the location of the strain gauges of straight tube, as expected given that the distance was the same. The only difference was the change in cross-section of the tubular structure. The interference noise, as observed in the other tubular structure, was also present in this case.

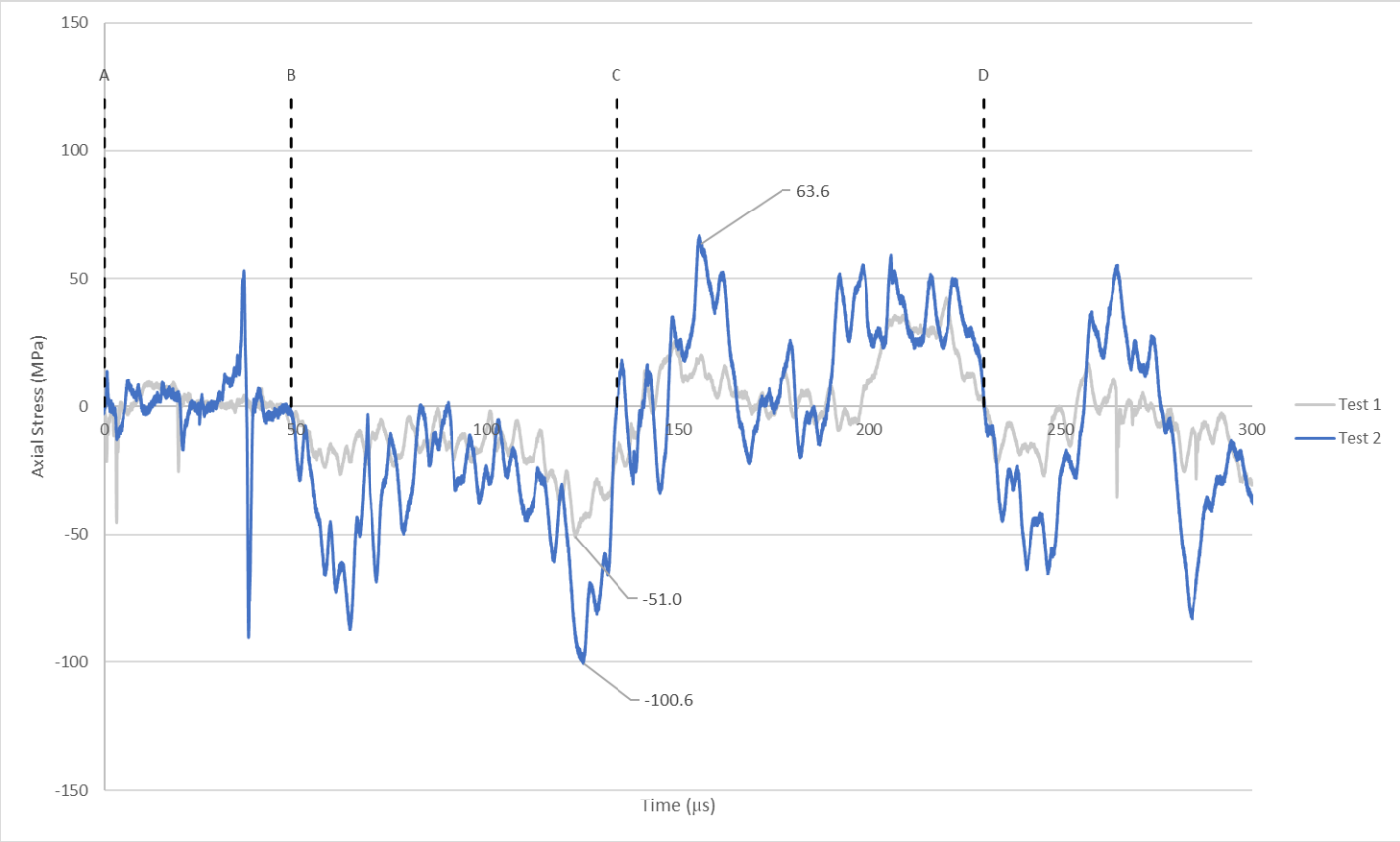

Figure 47 : The graph of stress history obtained from blast test 1 and 2 of Stepped tube with non-deformable witness plate.

Region B-C corresponds to the period when the blast stress waves initially interact with the stepped tube. Negative stress, like that observed in the straight tube test, indicates that the tubular structure experienced compressive stresses. Two significant stress peaks, resembling those seen in the straight tube test, were observed, suggesting that the witness plate and the tubular structure remained in contact during this region. Consequently, there was continuous transmission and interaction of the stress waves, resulting in the emergence of a secondary stress peak. The maximum negative stresses recorded were 51.0 MPa and 100.6 MPa for Test 1 and Test 2, respectively, which were lower than those observed in the straight tube test, indicating that the stepped tube experienced lower stress magnitudes. However, the results of Test 1 were disregarded since they were significantly lower than those observed in Test 2. Based on the peak stress magnitude observed in the straight tube test, the results of Test 2 exhibited a reasonable peak stress magnitude and were utilized. The overall shape of the stress wave resulting from the blast exhibited partial similarities to the shape of the Friedlander pressure wave, as observed in the straight tube test.

Region C to D exhibited positive stress, indicating that the tubular structure underwent a tensile load caused by the reflection of stress waves upon encountering the boundary of the tubular structure. In this region, both primary and secondary peaks, like those observed in Region B to C, were present, signifying that the witness plate and tubular structure remained in contact during this period. The stress wave displayed a comparable pattern to that observed in Region B to C. As the stress wave propagated through the tubular structure, a reduction in stress magnitude was observed due to dispersion. The maximum positive peak stress of 63.6 MPa was recorded in Test 2.

Tapered Tube

The stress-time responses depicted in Figure 48 were blast tests carried out on a tapered tube positioned adjacent to a 20 mm witness plate. In the A-B region, it took approximately 52.3 μs on average for the stress wave to travel from the witness plate to the location of the strain gauges, which is quite like the time required for the stress wave to travel in the case of the straight tube, as expected since the distance was the same. The only distinction was the alteration in the cross-section of the tubular structure. Additionally, like the other tubular structures, there was interference noise present in this instance as well.

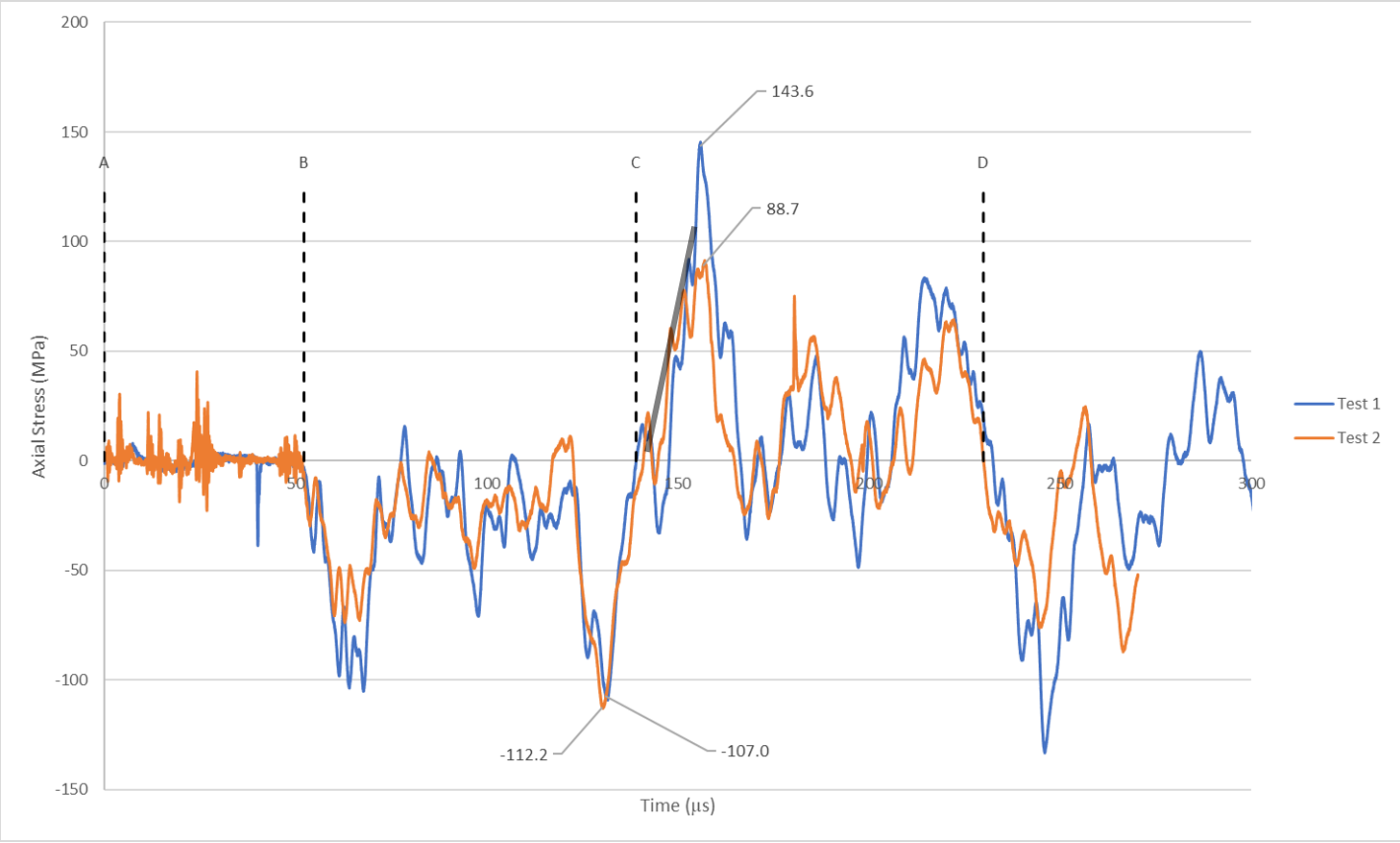

Figure 48 : The graph of stress history obtained from blast Test 1 and 2 of Tapered tube with non-deformable witness plate.

Region B-C corresponds to the interval when the blast stress waves initially interact with the tapered tube. The presence of negative stress, like that observed in the straight tube test, indicates that the tubular structure experienced compressive stresses. Two notable stress peaks, resembling those observed in the straight tube test, were identified, suggesting that the witness plate and the tapered tube remained in contact during this region. As

a result, there was a continuous transmission and interaction of the stress waves, leading to the emergence of a secondary stress peak. The maximum negative stresses recorded were 107.0 MPa for Test 1 and 112.2 MPa for Test 2, respectively. These values were lower than those observed in the straight tube test, indicating that the tapered tube experienced lower stress magnitudes. The overall shape of the stress wave resulting from the blast exhibited partial similarities to the shape of the Friedlander pressure wave, as observed in the straight tube test.

In Region C to D, positive stress was observed, indicating that the tubular structure underwent a tensile load due to the reflection of stress waves upon encountering the boundary of the tubular structure. Both primary and secondary peaks, like those observed in Region B to C, were present in this region, indicating that the witness plate and the tubular structure remained in contact during this period. The stress wave displayed a comparable pattern to that observed in Region B to C. As the stress wave propagated through the tubular structure, a reduction in stress magnitude was observed due to dispersion. The maximum positive peak stress of 143.6 MPa was recorded in Test 2.

4.3.3 Deformable Witness Plate

This section pertains to the interactions between stress waves and tubular structures using a 5 mm thick witness plate. Upon visual inspection, it was noted that both the witness plate and the tubular structures underwent plastic deformation, suggesting that the stress waves acted elastically until the witness plate and tubular structures began to yield. Greater stress magnitudes were observed across all tubular structures, indicating a transfer of greater magnitude of blast load from the witness plate to the tubular structures, as compared to non-deformable witness plate. The same approach used to convert the raw data for the blast test on straight tube with non-deformable witness plate test was used to derive the stress-time response for all the tubular structure blast tests that utilized a deformable witness plate.

Straight Tube

The blast test performed on straight tube with 5 mm witness plate yielded the stress-time responses shown in Figure 49. The time interval between Points A and B indicates the time it takes for the induced stress wave to travel from the blast loaded side of the witness plate to the centre of the tubular structure at the location of the strain gauges from the centre of detonation. The blast induced stress wave took an average of 47.1 μs to reach the centre of the tubular structure. Within this region, there were sharp peaks were observed caused by the trigger circuit breaking and the interference from the detonator causing spikes in the voltage captured by the PicoScope.

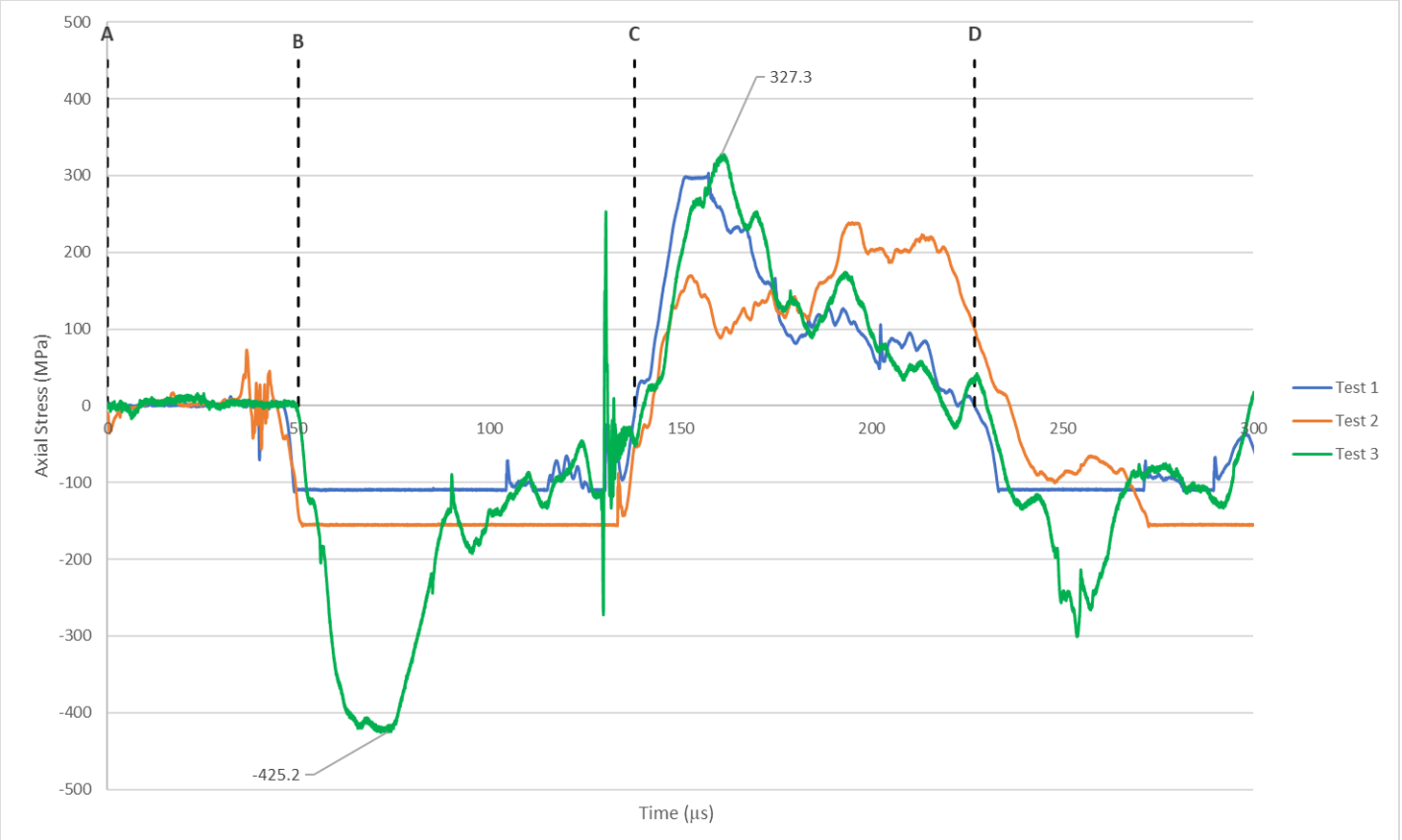

Figure 49 : Graph of stress history obtained from blast testing of Straight tube with Deformable witness plate.

In Region B-C, the stress signal from both Test 1 and Test 2 experienced the clipping of the voltage signal from the strain gauges. The clipping of the strain gauge signal was caused by amplifier saturation from the high bridge excitation voltage. The larger excitation increased the bridge output, overdriving the amplifier into saturation, which clipped the signal peaks. This was later rectified by calibrating the bridge circuit system voltage to accurately capture the maximum voltage corresponding to the stress induced by the blast load. However, the arrival time and overall pulse duration of the stress waves in Test 1 and 2 matched those measured in Test 3, which had no clipping. Therefore, while the peak magnitudes could not be compared, the general timing and duration of the stress waveforms were consistent between the three tests.

Test 3 exhibited a clear stress-time response signal after calibration, yielding a maximum compressive stress of 425.2 MPa, surpassing that observed in the non-deformable plate test. At 130 μs, a distinct sharp peak stress was observed in Test 3, which was caused by the noise picked up by the strain gauges due to interference in the connections leading to the data acquisition system. Unlike the non-deformable witness plate test, only one major peak stress was observed in all tests. The overall shape of the stress wave resulting from the blast displayed a similar pattern to that of the Friedlander pressure wave.

In Region C-D, a maximum tensile stress of 327.3 MPa was obtained from a clear signal in Test 3. The overall shape of the stress wave resulting from the blast exhibited a similar pattern to that of the Friedlander pressure wave, as observed in Region A-B. Beyond point D, the stress signal exhibited both compressive and tensile stresses, although the magnitude decreased due to the weakening of the stress signal as it interacted with the tubular structure. The stress waves became more complex beyond point D as they continuously interacted with the

tubular structure, leading to the amplification and cancellation of stress waves through the principle of superposition. Consequently, this section was not included in the scope of the present study.

Stepped Tube

The blast test performed on stepped tube with 5 mm witness plate yielded the stress-time responses shown in Figure 50. The blast induced stress wave took an average of 47.1 μs to reach the centre of the tubular structure as shown in region A-B. Within this region, there were sharp peaks caused by trigger circuit breaking and the interference from the detonator causing spikes in the voltage captured by the PicoScope as observed din all the tests.

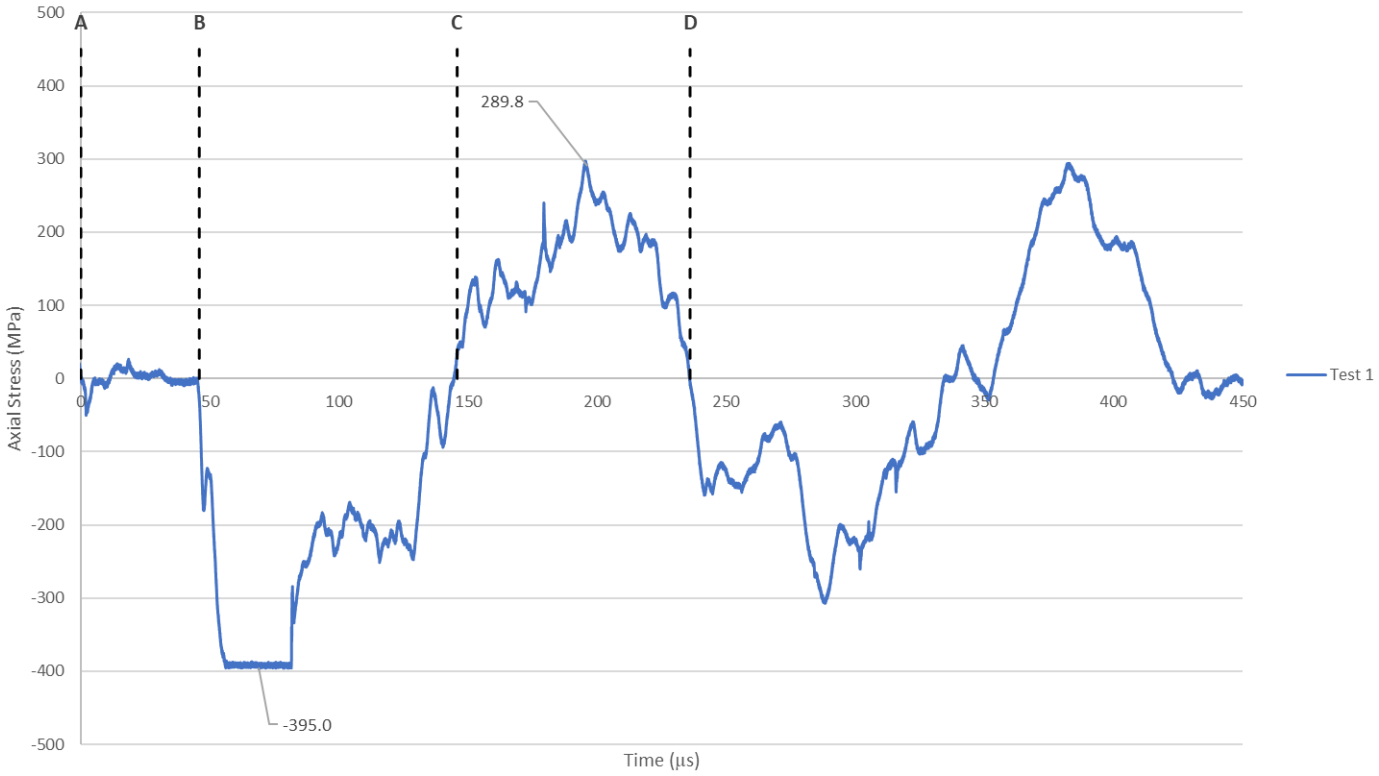

Figure 50 : The graph of stress history obtained from blast testing of Stepped tube with Deformable witness plate.

In Region B-C, the stepped tube experienced compressive stress, with a maximum negative stress of 395.0 MPa before plateauing which may be attributed to improper bonding, surface prep, or gauge alignment on the test structure. However, due to damage incurred during preliminary tests, only one successful test was performed. The distortion of the strain measurement signal may have resulted from the interference of the strain measurement with electromagnetic sources, such as power cables. In Region C-D, a maximum tensile stress of 289.8 MPa was recorded without any signal clipping. The overall shape of the stress wave displayed partial similarities to the shape of the Friedlander pressure wave, both during the compressive and tensile load cycles. A distinct stress-time trend was observed, attributed to the specific cross-sectional characteristics of the stepped tubular structure. Beyond point D, the stress waves became more complex as they continuously interacted with the tubular structure, leading to the amplification and cancellation of stress waves through the principle of superposition.

Tapered Tube

The stress-time responses obtained from the blast test conducted on a stepped tube with a 5 mm witness plate was depicted in Figure 51. It took an average of 52.0 μs for the blast-induced stress wave to propagate to the centre of the tubular structure, as indicated in region A-B. During this period, there were noticeable sharp peaks in the stress signal, resulting from the trigger circuit breaking and interference from the detonator as observed in all the conducted tests.

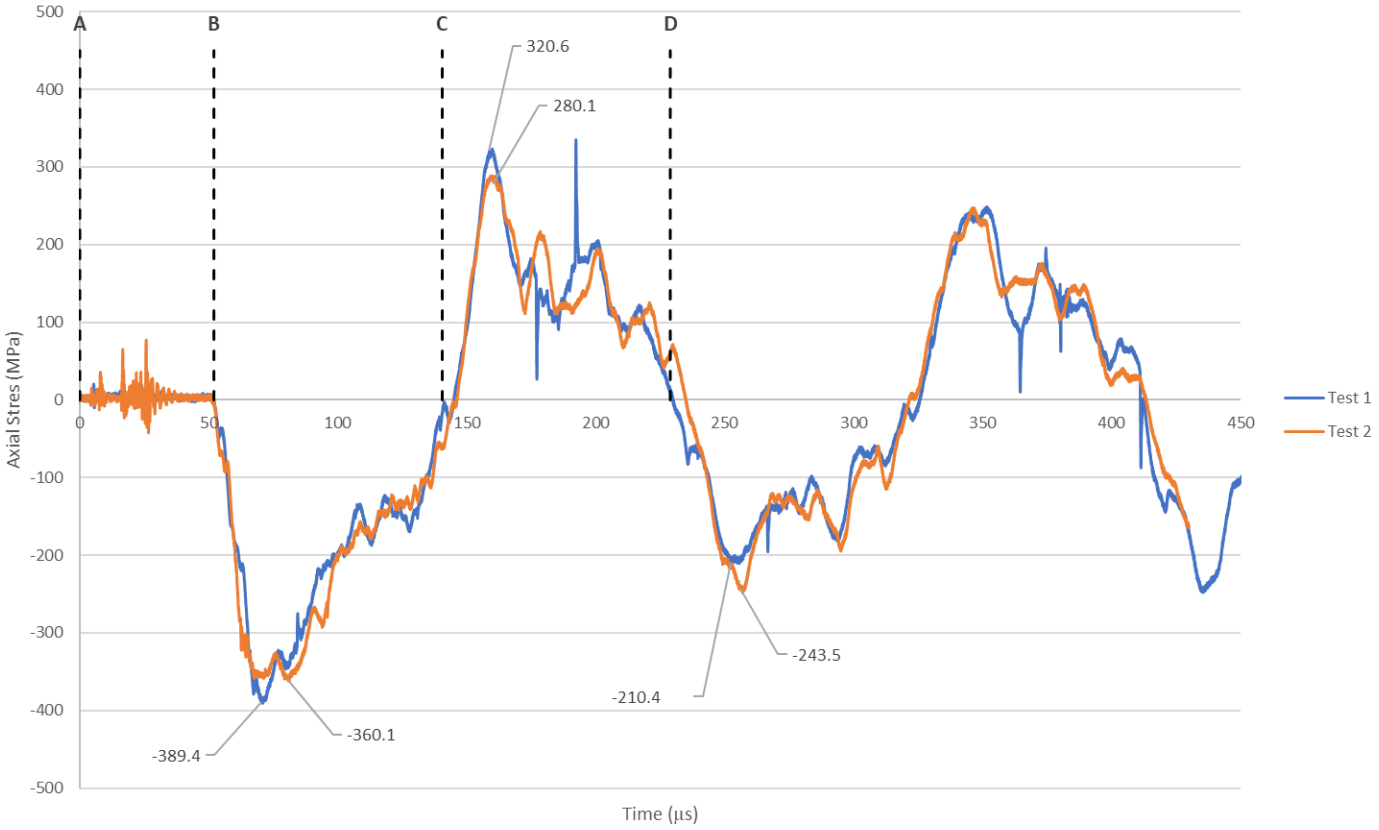

Figure 51 : Graph of stress history obtained from blast testing of Tapered tube with Deformable witness plate.

Region B-C indicates the period when the blast stress waves first interact with the tubular structure. The negative stresses are indicative of compressive stresses due to the induced blast load. Two major peaks are observed in all tests, with the highest magnitude of compressive stress occurring on either the first or second major peak stress. The maximum negative stresses observed were 389.4 MPa and 360.1 MPa for Test 1 and 2 respectively. The overall shape of the stress wave resulting from a blast exhibits partial similarities to the shape of the Friedlander pressure wave, wherein an abrupt stress increase leading to the primary peak is observed, followed by a rapid decline. However, a notable disparity is evident during the occurrence of the second major peak, primarily attributed to the specific cross-sectional characteristics of the tubular structure.

In Region C-D, the maximum tensile stress obtained were 320.6 MPa and 280.1 MPa, for Test 1 and 2 respectively. There was no stress plateauing for both Test 1 and 2 in this region because the maximum voltage changes captured were within the data acquisition system voltage range set. Beyond point D, the stress signal shows both compressive and tensile stress, but the magnitude decreased due to the stress signal weakening as it interacted with the specimen.

The stress waves exhibited increased complexity beyond point D, as they persistently interact with the tubular structure, leading to the amplification or cancellation of stress waves in accordance with the principle of superposition. It is worth noting that this section was not included in the scope of the present study.

4.4 Summary

Table 6 presents the results of blast tests conducted on various tubular structures with non-deformable and deformable witness plates. A subset of the tests, indicated by an asterisk (*), was omitted from the calculation of the average due to significant disparities in the obtained stress magnitudes when compared to the remaining tests. In the non-deformable witness plate tests, Straight tube with a 20 mm witness plate exhibited an average maximum negative stress of 125.8 MPa and an average maximum positive stress of 88.6 MPa. Stepped tube with the same plate size showed lower stress levels with an average maximum negative stress of 104.3 MPa and an average maximum positive stress of 64.3 MPa. Tapered Tube, again with a 20 mm witness plate, displayed an average maximum negative stress of 109.6 MPa and an average maximum positive stress of 116.2 MPa. The results indicated that the stress levels vary among the tubular structures, suggesting differences in their resistance to blast forces.

In the deformable witness plates tests, straight tube with a 5 mm witness plate showed higher stress levels compared to the non-deformable witness plates tests. It exhibited an average maximum negative stress of 230.3 MPa and an average maximum positive stress of 289.2 MPa. Stepped tube with the same plate size had an average maximum negative stress of 374.8 MPa and an average maximum positive stress of 300.4 MPa. The results indicated that the deformable witness plates configuration allowed for higher stress dissipation, resulting in increased stress levels within the tubular structures.

The time of arrival and impulse results provided additional insights into the blast tests conducted on the tubular structures. The average time of arrival for tubular structures with non-deformable witness plates ranged from 48.6 μs to 52.1 μs. The results indicated slight variations in the arrival times among the different tubular structures, suggesting slight differences in the propagation speed and distance from the explosion source due to the geometry of the tubular structure.

The average impulse values ranged from 4.3 Ns to 5.4 Ns for non-deformable witness plates tests and from 4.9 Ns to 5.5 Ns for deformable witness plates tests. Both the non-deformable and deformable witness plates exhibited relatively consistent impulse measurements. The small ranges and close average values indicated that the recorded impulses were within a narrow range across the tests. The consistency in impulse recorded suggests that the structures, regardless of plate type, experienced similar levels of momentum change due to the blast forces. The small variations in impulse values could be attributed to differences in the plate configuration and geometry of tubular structure, which affect the transfer and dissipation of forces during the blast.

Overall, the results indicated that the choice of plate configuration, whether non-deformable or deformable, significantly influences the stress levels experienced by the tubular structures during blast tests. Tubular structures with non-deformable witness plates generally exhibited lower stress levels, while those with deformable witness plates showed higher stress levels. The results highlighted the importance of selecting appropriate plate configurations and understanding their impact on stress distribution for effective blast resistance in various structural designs.

Table 6 : The results obtained from experimental blast tests.

Blast Test	Test Name	Maximum Negative Stress (MPa)	Maximum Positive Stress (MPa)	Time of Arrival (μs)	Impulse (Ns)
Non-deformable witness plate	S1/20_1	121.8	85.0	48.6	5.4
	S1/20_2	129.7	92.2	47.7	5.2
	S1/20 _3*	86.8	54.8	49.5	5.7
	Average	**125.8**	**88.6**	**48.6**	**5.4**
	S2/20_1*	50.3	41.9	49.0	4.5
	S2/20_2	100.4	64.3	49.2	4.1
	Average	**100.4**	**64.3**	**49.1**	**4.3**
	S3/20_1	107.0	143.6	52.0	5.0
	S3/20_2	112.2	88.7	52.3	5.6
	Average	**109.6**	**116.2**	**52.1**	**5.3**
Deformable witness plate	S1/5_1*	109.7	302.4	47.1	5.1
	S1/5_2*	156.0	237.8	46.0	4.9
	S1/5_3	425.2	327.3	49.4	5.5
	Average	**425.2**	**327.3**	**47.5**	**5.1**
	S2/5_1	396.0	289.8	46.0	5.0
	Average	**396.0**	**289.8**	**46.0**	**5.0**
	S3/5_1	389.4	320.6	51.0	4.7
	S3/5_2	360.1	280.1	51.8	5.0
	Average	**374.8**	**300.4**	**51.4**	**4.9**

NB: * data not included in average.

CHAPTER 5 - FORMULATION OF THE FINITE ELEMENT MODEL

Engineering tools, such as the Kingery and Bulmash semi-empirical method, along with equivalent single-degree-of-freedom methods, have been employed to evaluate blast load characteristics and the response of targeted structures [64]. In this study, the Finite Element Method (FEM) was used to simulate the conducted blast experiments. To achieve this, the LS-DYNA explicit solver (LS-DYNA V971 R8.10), an explicit finite elements software, was utilized to create a numerical model of the blast experiments. The numerical model involved simplifications and assumptions to represent only the air, explosive, witness plate, and surrogate tibia tubular structures, while ensuring appropriate boundary conditions were applied.

5.1 Material model and Equation of State

5.1.1 Air

The air domain material properties were defined using *MAT_NULL keyword card. The Null material model was chosen since it defined fluids without yield strength which best modelled the behaviour of air when load was applied [65]. The null material was accompanied by *EOS_LINEAR_POLYNOMIAL keyword card, which defined the equation-of-state of the air material. A small negative pressure cut off was defined to allow the material to numerically cavitate when material pressure went below the pressure cut-off set. The *EOS_LINEAR_POLYNOMIAL was the equation-of-state, Equation 9 [65], which related the pressure distribution of air. [53].

$$P = C_0 + C_1\mu + C_2\mu^2 + C_3\mu^3 + (C_4 + C_5\mu + C_6\mu^2)E$$

Equation 9

Where $C_0, C_1, C_2, C_3, C_4, C_5, C_6$ are constants, $\mu = \frac{\rho}{\rho_0} - 1$, ρ and ρ_0 are densities of air at the beginning and each instant of the explosion.E is the internal energy of air at atmospheric pressure (101 kPa). The material properties and parameters used to define the equation of state are summarized in Table 7**Error! Reference source not found.**.

Table 7 : Material properties and Equation of state defined for air model [66]

ALE Part	Material Definition	Equation of Sate
Air	*MAT_NULL $\rho_0 = 1.255\ \frac{kg^3}{m}$ $PC = -1.000e^{-6}\ Pa$	*EOS_LINEAR_POLYNOMIAL $C_0 = 0, C_1 = 0, C_2 = 0, C_3 = 0, C_4 = 0.4, C_5 = 0.4, C_6 = 0$ $E_0 = 253.4\ kPa$

5.1.2 Explosive

Material properties of the C4 explosive charge were used to model the PE4 explosive used in the experiments since they have similar energy [66]. The explosive charge was defined using the material parametersρ, D and P_{CJ}

defined as density, detonation velocity and Chapman Jouguet pressure respectively. The explosive charge material properties were defined using the *MAT_HIGH_EXPLOSIVE_BURN. The Jones-Wilkins-Lee equation-of-state (*EOS_JWL), was implemented to define the properties and behaviour of the charge when it detonated[67]. The pressure distribution of the charge is described using Equation 10 [65]. A summary of material properties and equation of state used to define C4 explosive material model, are summarized in Table 8.

$$P = A\left(1 - \frac{\omega}{R_1 V}\right)e^{-R_1 V} + B\left(1 - \frac{\omega}{R_2 V}\right)e^{-R_2 V} + \frac{\omega E}{V}$$

Equation 10

Where V is the volume and E is the internal energy. A, B, R_1, R_2 and ω are constants.

Table 8 : Material properties and Equation of states for the explosive model [66]

ALE Part	Material Definition	Equation of State
Explosive	*MAT_HIGH_EXPLOSIVE_BURN $\rho = 1601\ kg/m^3, D = 8193\ m/s$, $P_{CJ} = 28\ x\ 10^9\ Pa$	*EOS_JWL $A = 609.77x10^9\ Pa, B = 12.95x10^9\ Pa$ $R_1 = 4.5$,$R_2 = 1.4, \omega = 0.25$ $E_0 = 9x10^9\ Pa$

5.1.3 Mild Steel

Witness plate material, mild steel, was defined using the simplified Johnson-Cook (JC) material model. The material model chosen considered the strain rate effects due to high strain rate deformations induced by blast pressure waves by including the hardening law fundamentals [68]. The equivalent stress is related to the equivalent strain and strain rate using Equation 11 [68].

$$\sigma_{eq} = (A + B\epsilon_{eq}^{n})\dot{(}1 + Cln(\dot{\varepsilon_{eq}}/\dot{\varepsilon_0})$$

Equation 11

Where σ_{eq} equivalent stress

ε_{eq} equivalent strain

$\dot{\varepsilon_{eq}}$ equivalent strain rate

A, B, C, and n are Johnson-Cook (JC) material models associated with the material of the Lagrangian part. Constant B and exponent n indicate the strain-hardening effects of the material, whereas constant A represents the yield stress corresponding to a 0.2% offset strain [68]. The constant C defines the strain rate impact and constant A, is the flow stress at a strain rate of s^{-1}. The JC material parameters, obtained from Vedantam [68] , for the witness plate (both deformable and non-deformable witness plates), are shown in Table 9 [56]. It was not crucial in this investigation to conduct characterise the steel as the focus was on understanding the stress propagations through the tubular structures.

Table 9 : The summary of the material model and its parameters used for modelling the witness plate models [68]

Lagrangian Part	Material Definition
Witness plate	Mild Steel $\rho = 7700\ kg/m^3, \upsilon = 0.3, E = 205\ GPa$ *MAT_SIMPLIFIED_JOHNSON-COOK $A = 217\ MPa, B = 234\ MPa, n = 0.6428\ , C = 0.0756$

5.1.4 Aluminium

Aluminium, as use for the tubular structures, was also defined using the simplified Johnson-Cook (JC) material model witness plate. The JC material parameters, obtained from Akram [60]for the aluminium were presented in Table 10.

Table 10 : The summary of material model and its parameters used for modelling the tubular structure models [49]

Lagrangian Part	Material Definition
Tubular structure	Aluminium (6061 T6) $\rho = 2700\ kg/m^3, \upsilon = 0.33, E = 68.9\ GPa$ *MAT_SIMPLIFIED_JOHNSON-COOK $A = 250\ MPa, B = 79\ MPa, n = 0.499$ $C = 0.0249$

5.2 Geometric Modelling

5.2.1 Air and Explosive

Multi-Material Arbitrary Lagrangian-Eulerian (MMALE) method was employed to model the surrounding air and the explosive as two distinct parts. A 200 x 200 x 550 mm air mesh, as depicted in Figure 52, which covered clamping area the tubular structure and witness plate, made up of 1st-order 8-node cubic elements were created using the Shape Mesher in LS-Dyna. An *INITIAL_VOLUME_FRACTION_GEOMETRY keyword was used to insert and define the container that defined the shape of the explosive used in blast experiments. The combination of air and explosive formed a multilateral element referred to as the Arbitrary Lagrangian-Eulerian element (ALE)

which defined the ratio of the charge to air in each element of the ALE[67]. The air and explosive materials were defined using solid elements with a 1-point ALE multi-material element formulation.

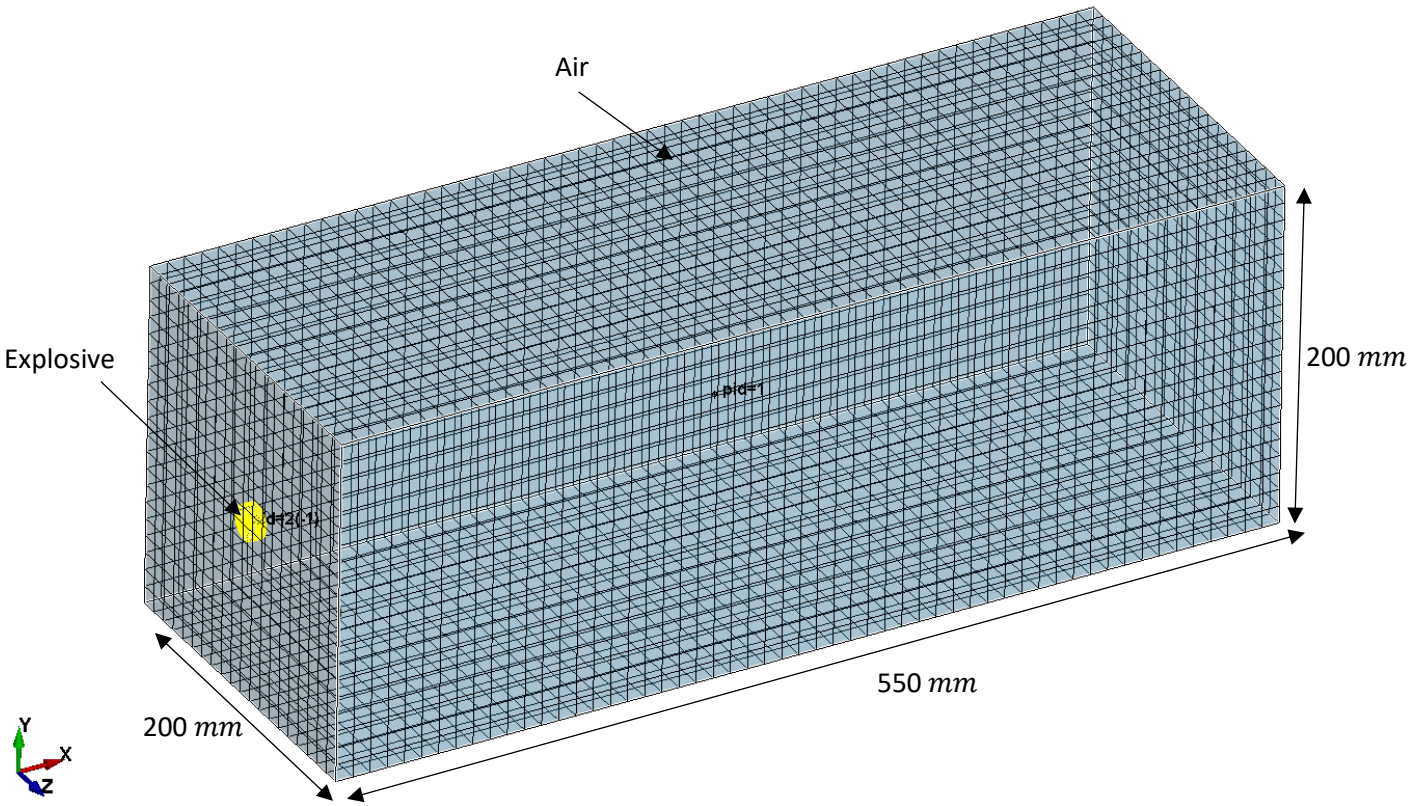

Figure 52 : A schematic diagram showing the Air and Explosive mesh.

5.2.2 Witness Plate and Tubular Structure

Witness Plate

The 200 x200 x 20 mm witness plate mesh witness plate was modelled as a Lagrangian part using the 1st-order 8-node cubic elements with a solid section formulation with reduced integration. The witness plate was modelled as a deformable witness plate with solid elements to capture its volumetric behaviour upon application of the blast load while maintaining the accuracy and computational efficiency of the model.

Tubular Structure

All the tubular structures were modelled as Lagrangian models. A 450 mm long tube mesh was generated using 1st order 8-node cubic elements with a solid section formulation and reduced integration [69]. The edge of the tubular structure was placed in contact with the face of the witness plate as illustrated in Figure 53.

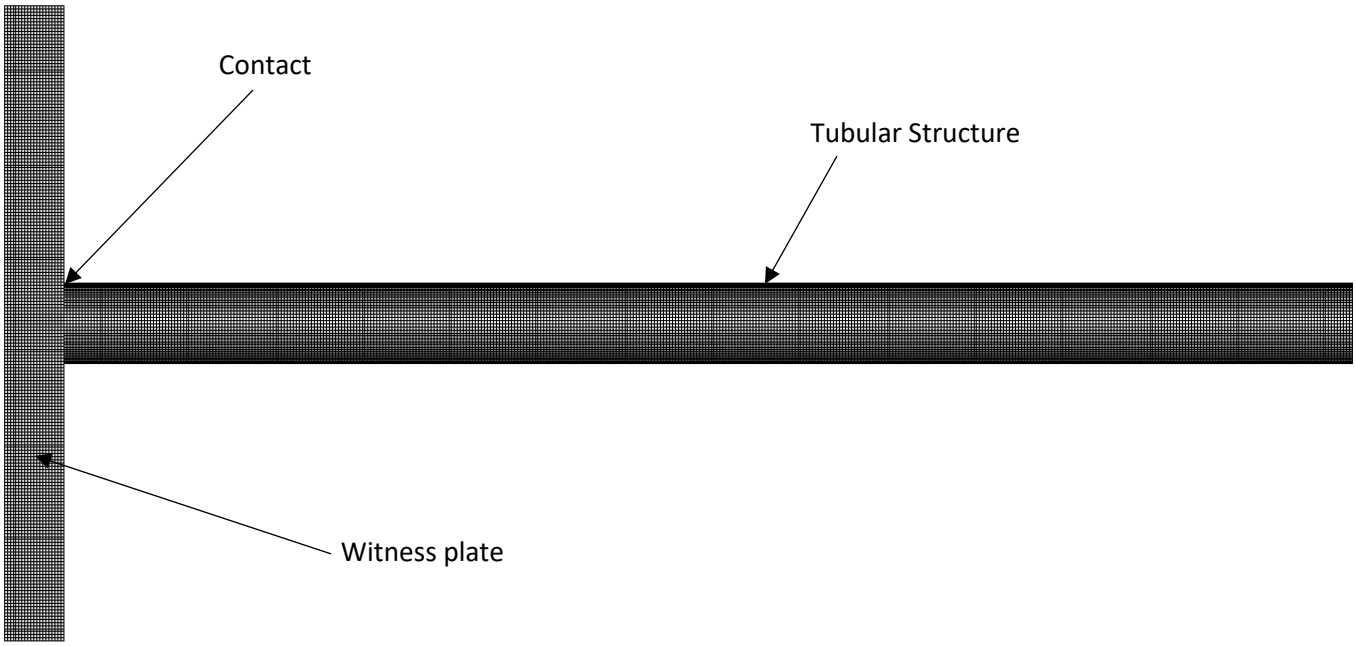

Figure 53 : A schematic diagram showing the 2D view of the tubular structure attached to the witness plate and the explosive.

Hourglass control of type 1 was employed on the Lagrangian elements and Hourglass control type 3 was implement ALE elements to mitigate the hourglass deformation that may lead to instability of the numerical model [69]. As a result, the accuracy of the model was increased with a reduction computation time.

5.3 Contact Modelling and Boundary Conditions

Contact Modelling

The contact between the surface of the witness plate and the tubular structure was defined using the *AUTOMATIC_SURFACE_TO_SURFACE keyword card. The selected penalty contact was selected to allow for automatic checking and identification of slave and master nodes, thereby preventing penetration between the two parts and ensuring smooth transfer of loads between the two components. The witness plate was defined as the Master part and the tubular structure as the Slave part. The values of static and dynamic coefficient of friction between the two Lagrangian parts used were μ_S= 0.61 and μ_D= 0.47 respectively[70]. The polystyrene foam attached used in the blast experiments was not modelled since it was assumed that it burned upon the detonation of the explosive with no significant impact on the stress wave propagation.

Boundary Conditions

Fixed boundary conditions were applied on all edges of the witness plate, restricting translation in all directions. This allowed transfer of the blast load onto the tubular structure. Translational boundary conditions were applied on circular surfaces of the tubular structure where bushings were located experimentally. This only permitted translation and rotation about the tube's axis, approximating the physical constraints. Non-reflective conditions on the air mesh surfaces prevented blast reflection. The boundary conditions, summarized in Figure 54, represented approximations necessary for mathematical solution, reducing complexity while enabling useful

comparative analysis. However, approximating the real physical system introduced limitations that needs further refinement.

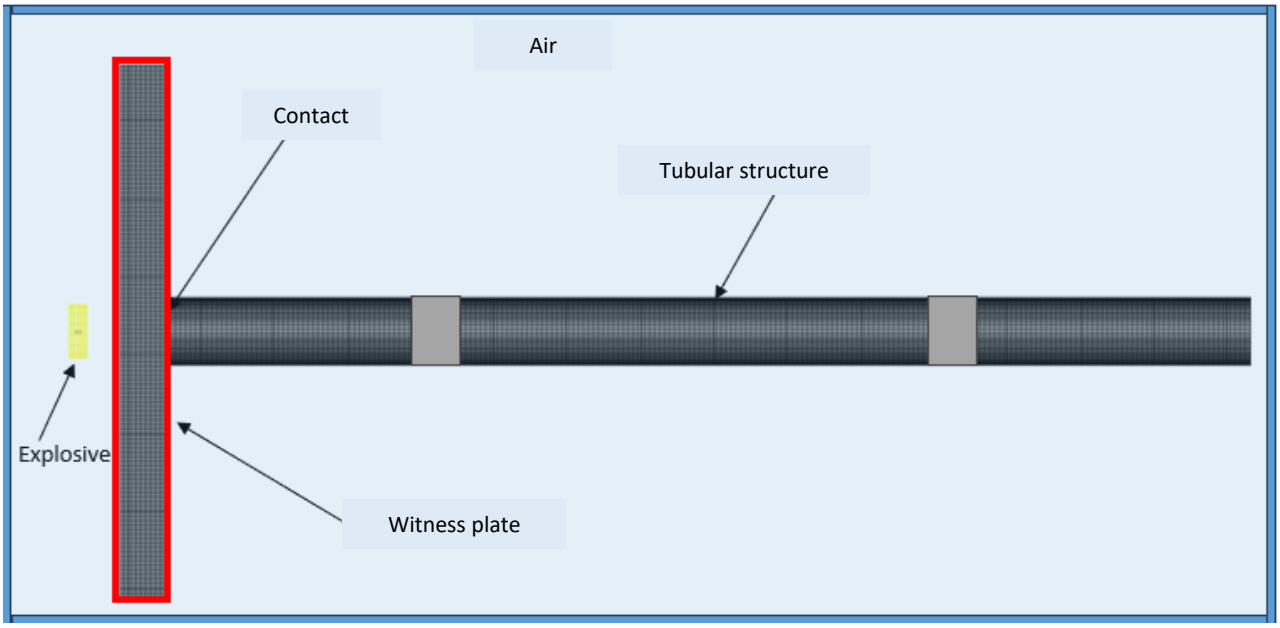

Figure 54 : A schematic diagram showing the 2D view of the Finite Element Model boundary conditions and contacts.

5.4 Loading the Lagrangian Models

The blast loading of the Lagrangian parts was achieved using fluid-structure interaction (FSI) to transfer the blast load from the ALE elements to the Lagrangian parts. The air and explosive were combined to form an Arbitrary Lagrangian-Eulerian (ALE) part set while the witness plate and the tubular structure formed a Lagrangian part-set. The *CONSTRAINED_LAGRANGE_IN_SOLID keyword card enabled the coupling of the blast load from the ALE parts to the Lagrangian parts [69]. A part-set containing the air and explosive was defined as the Master part ana a part-set containing the witness plate and tubular structure as the Slave part.

5.5 Symmetry and Mesh Sensitivity Analysis

5.5.1 Symmetry Analysis

Symmetry analysis was conducted to simplify the numerical model by exploiting the symmetrical properties of the finite element model. Geometric symmetries were identified to reduce the complexity of the simulations by

simplification of the geometry, reduction of computational time and modelling efforts. Full and quarter of the finite element model were studied, and the results were compared. The air and explosive mesh for both the full and quarter symmetry are shown in Figure 55. Translational boundary conditions were imposed on the planes of symmetry on the quarter finite element model to restrict translational displacement of element and nodes normal to the plane of symmetry. A *DATABSE_TRACER keyword was used to define three trace points in the air mesh that captured pressure when the explosive detonated. The coordinates of the trace points used were presented in Table 11. The trace points recorded the same pressure distribution across the full and quarter model as shown in Figure 56 Hence , a quarter model was employed for in the current study. Based on the outcome of this initial analysis, a quarter symmetry was applied to the whole Lagrangian parts (deformable and non-deformable witness plate and all tubular structures), as depicted in Figure 57. Therefore, the estimated maximum incident pressure at the coordinates (21, 20, 80) m from a 3.5 g C4 charge detonation was estimated to 0.147 MPa using the Kingery-Bulmash pressure equation [35].

Table 11 : The coordinates of the trace points used to capture the pressure distributions.

Trace Point	Coordinates (X, Y, Z)
T1	21,20,80
T2	21,40,60
T3	21,60,40

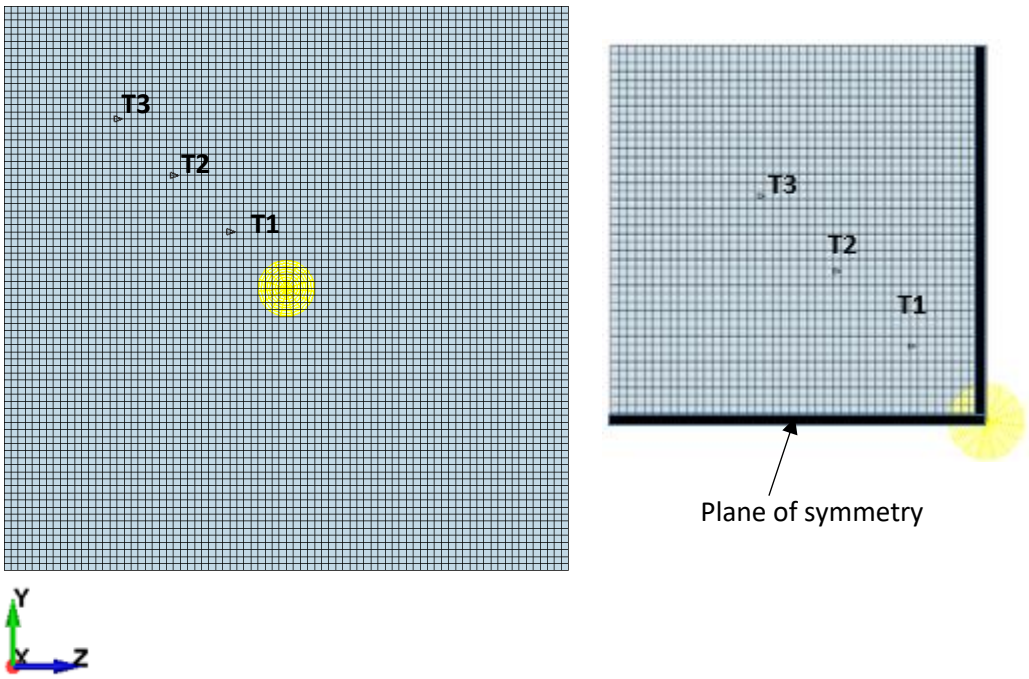

a) Full Model b) Quarter Model

Figure 55 : A 2D illustration of the trace points on the full and quarter finite element models

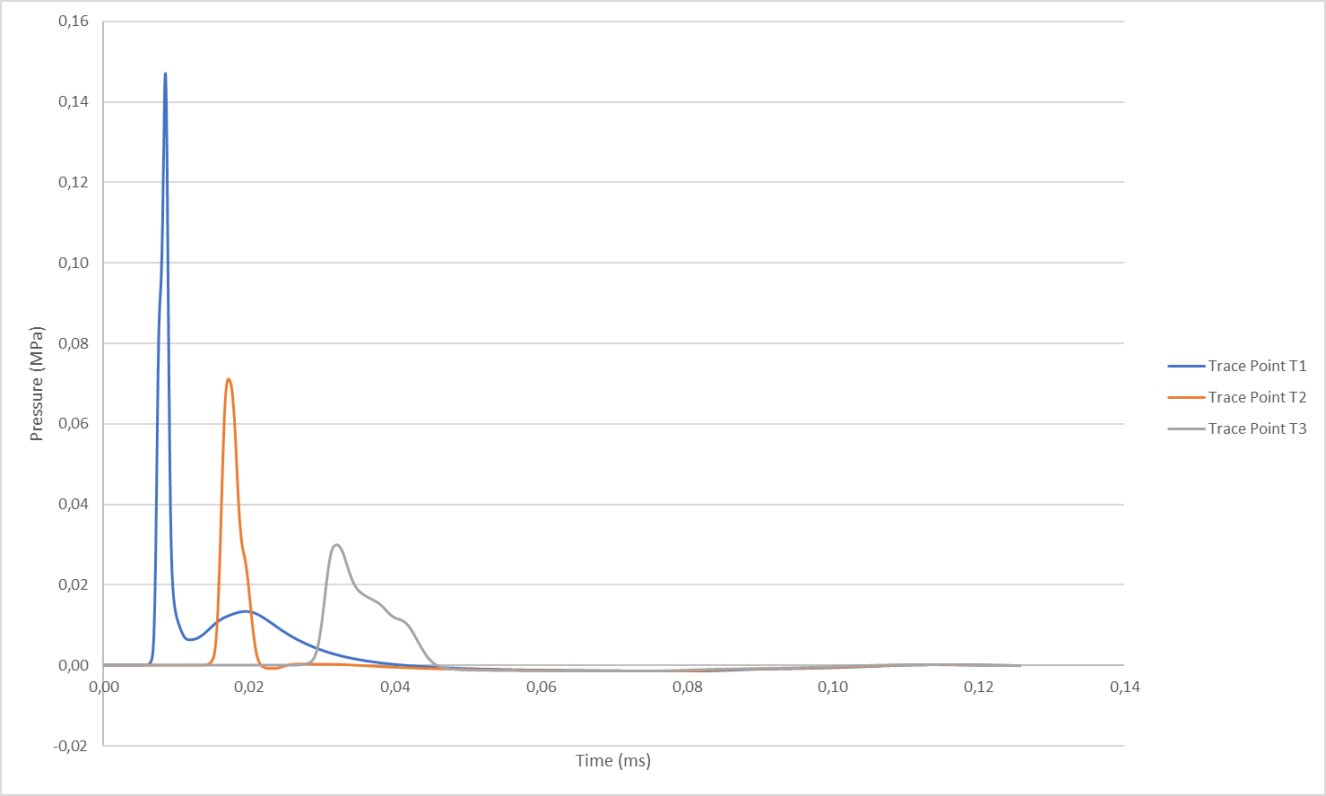

Figure 56 : The graph of pressure history for trace points in Full and Quarter FE Model

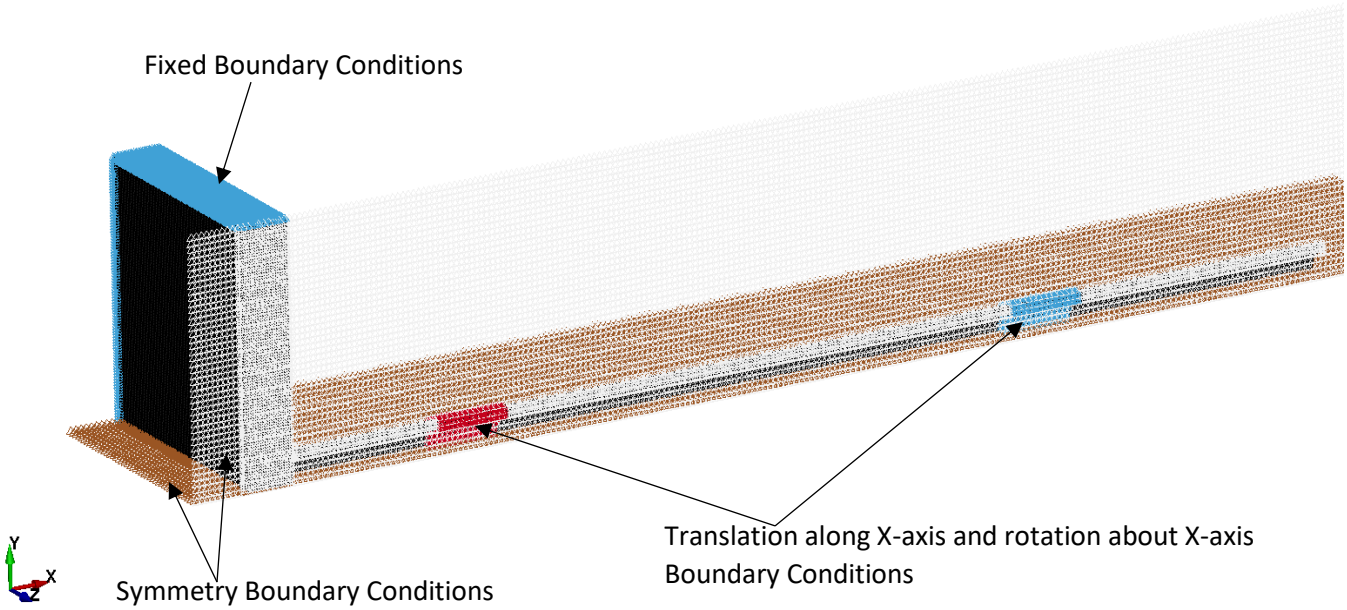

Figure 57 : A schematic diagram of the geometry and boundary conditions applied on the quarter symmetry of Lagrangian parts.

5.5.2 Mesh Sensitivity

Air and Explosive (ALE) Mesh

Mesh size refinement of the quarter ALE mesh was conducted to improve the accuracy of over-peak pressure recorded by trace point, T1, while maintaining the computational efficiency. The variation of mesh size led to different over-peak pressure values recorded for each case. The over-peak pressure, number of elements and the run time was recorded for each simulation and presented in Table 12. The solution was achieved by the convergence of over-peak pressure values, as shown in Figure 58.

Table 12 : The results obtained for ALE Mesh element size model simulations.

Cubic Element Size $(\boldsymbol{mm})$	**Over-peak Pressure** $(\boldsymbol{MPa})$	**Number of elements** $(\boldsymbol{x1000})$	**Run Time** $(\boldsymbol{Minutes})$
0	0	0	
10	59.6	0.688	1
5	91.1	5.5	1
2.5	98.2	44	9
2.25	98.7	352	19
2	98.78	483	32
1.75	98.79	1026	81

The results obtained were plotted on a graph as shown in Figure 58 and the magnitude of the over-peak pressure obtained increased with the decrease in mesh size (increase in number of elements). The over-peak pressure stabilized from 2.5 mm up to 2 mm element size. The run time doubled up from 9 minutes to 19 minutes between 2.5 mm and 2.25 mm element size with a small difference in the over-peak pressure recorded. Considering the small change in over-peak pressure and the run time of the simulation, 2.5 x 2.5 x 2.5 mm cubical elements were selected to model the ALE parts of the FE models. The selected ALE mesh size resulted in minimum run time of the ALE mesh simulations whilst maintaining accurate blast load generated by the explosive.

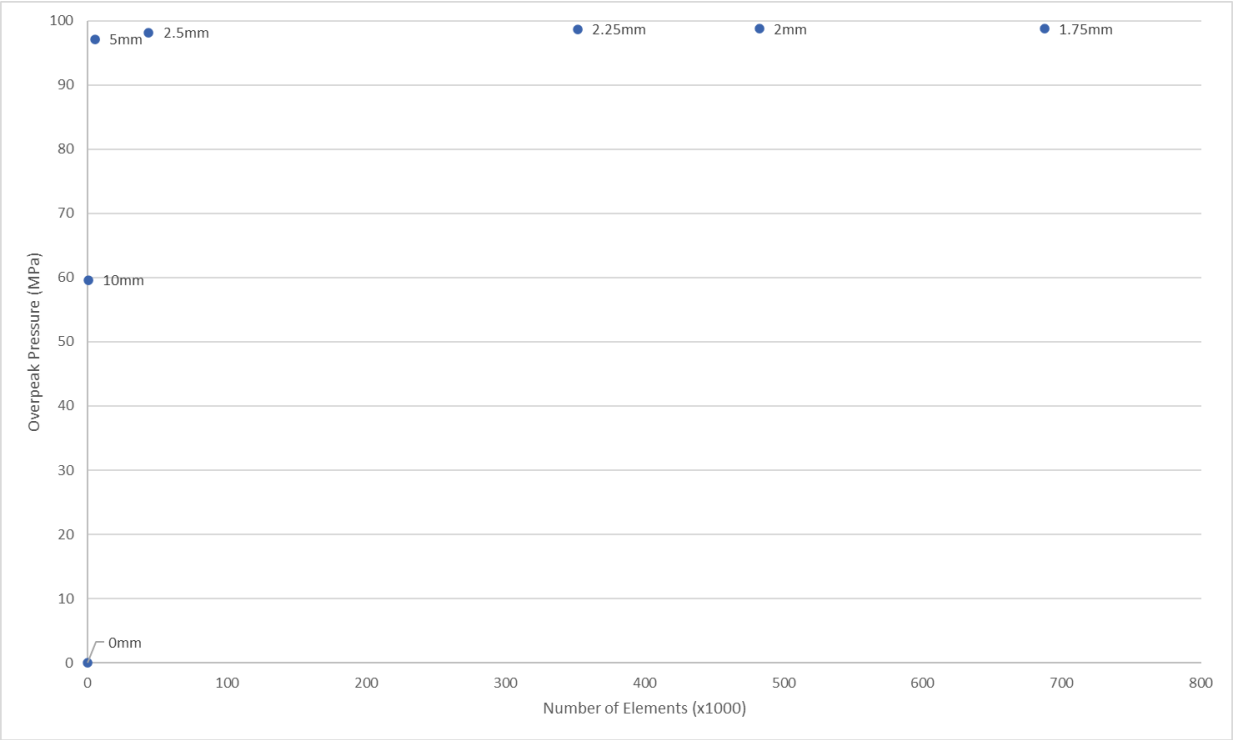

Figure 58 : The graph of over-peak pressure against the number of elements obtained from ALE mesh size variation.

Validation of the Over-Peak Pressure Prediction

The maximum pressure obtained at trace point T1, 98.7 MPa, was compared with the over peak pressure obtained from the Kingery & Bulmash (K-B) a proven prediction method for determining pressure load in free-field experiments [59] based on data obtained from explosive tests of less than 1 kg to over 400 $tonnes$. Using the values presented in Table 13, TNT equivalent weight and scaled distance, the analytical over-peak pressure was calculated.

Table 13 : Parameters for sailing blast wave from using PE4 charge [35]

Parameter	Definition	Value	Units
W_{exp}	Weight of the actual explosive	0.0035	kg
H_{exp}	Heat of detonation per 1 kg of the actual explosive	5.86	MJ/kg
H_{TNT}	Heat of detonation per 1 kg of TNT	4.325	MJ/kg
W_{eqv}	TNT equivalent weight	0.00474	kg
R	Distance from the centre of the explosive	0.00851	m
Z	Scaled distance from the centre of the explosive per $1kg$ of the TNT equivalent weight	0.0506	$m/kg\text{^ }(1/3)$
P_O	Ambient pressure	0.101	MPa
P_{SO}	Analytical over-peak pressure	96.1	MPa
P	Simulation over-peak pressure	98.7	MPa

From the results presented Table 13, the simulation over-peak pressure obtained at trace point T1 set was 98.7 MPa whereas using the empirical pressure equations by Kingery & Bulmash, yielded an over-peak pressure of 96.1 MPa. A variation of less than 5 % in pressure magnitude between the simulation and the analytical over pressure suggested that the numerical model showed very good correlation with existing empirical solution.

Witness Plate Mesh

A 200 x 200 x 5 mm witness plate was modelled at 13 mm away from the charge, with its centre in line with the centre of the explosive. The witness plate was modelled as a Deformable witness plate using a section solid formulation with reduced integration. The witness plate geometry was such that it deforms when the explosive detonates to capture the maximum central displacement obtained from each mesh size. A single node was set on the centre of the plate for each mesh size using *SET_NODE and *DATBASE_NODAL_HISTORY keywords to monitor its displacement history. A set of 5 cubical element sizes were selected to obtain the maximum deflection across each mesh size and the results were presented in Table 14.

Table 14 : The maximum central displacement results obtained for each witness plate mesh size.

Cubic Element Size (mm)	**Central Maximum Displacement** (mm)	**Number of elements**	**Run Time (minutes)**
5.0	5.0	400	1
2.0	10.8	7500	1
1.5	13.3	13467	7.2
1.2	16.2	27556	15.2
1.1	18.6	41405	25.6
1.0	19.2	50000	36.1
0.8	18.5	93750	64.8

The maximum deflection increased as the element size decreased, as depicted in Figure 59. As the number of elements increased, the maximum nodal deflection showed a trend of converging to 19.2 mm with a 1 mm element mesh size. However, when using a mesh size of 0.8 mm, the maximum deflection was slightly less than the peak displacement obtained with the run time increased by a scale factor of about 2 compared to the 1 mm element mesh size. Using an element size of 0.8 mm indicated that the simulation had already started to deviate from accurate displacement. The maximum displacement trend converged to a value of 19.2 mm when using a 1 x 1 x 1 mm element mesh size, which was close to the 21.7 mm obtained by Rigby [71] in the same finite element configuration.

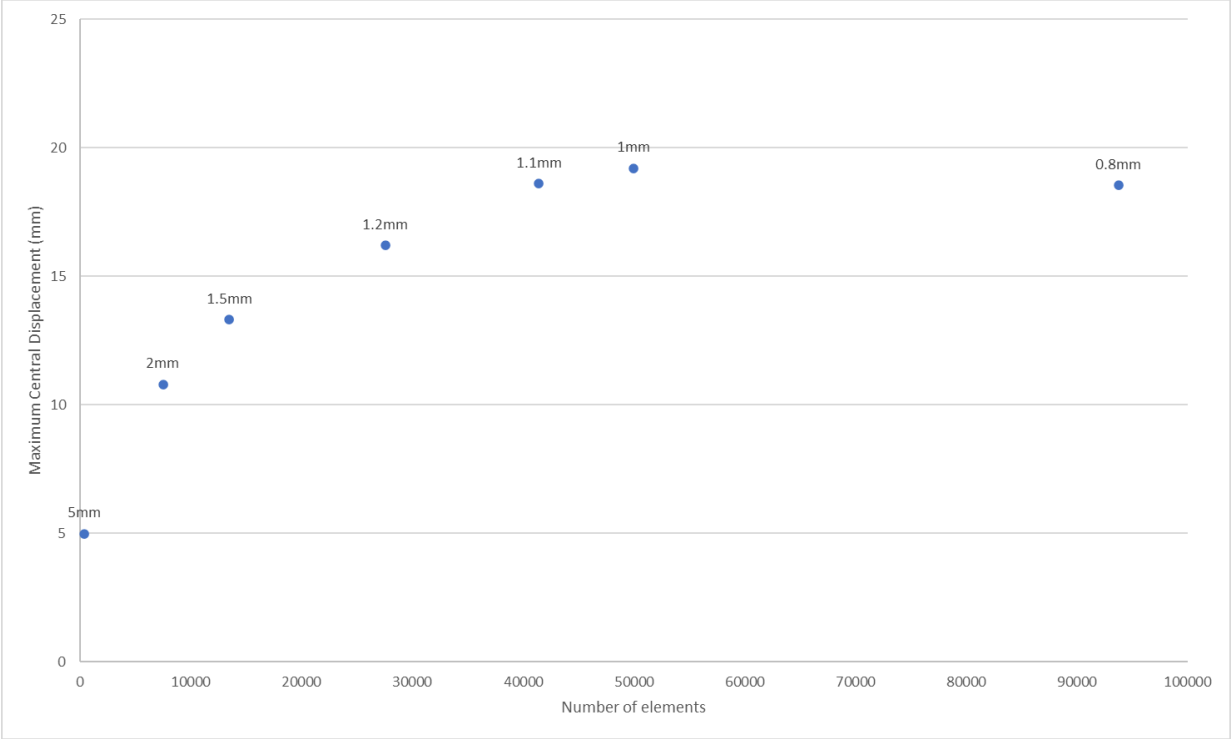

Figure 59: The graph of maximum central displacement against the number of elements obtained for each mesh size on witness plate.

Tubular Structure Mesh

The tubular structure mesh was selected to be the same as the witness plate which simplified the modelling process, ensuring accurate stress and strain representation at the interface, minimizing artificial stress concentrations and discontinuities leading to increased efficiency, consistency, and reduced chances of errors [72]. Maintaining the same element size resulted in deformation compatibility between the witness plate and tubular structure which improved the convergence behaviour and stability of the solution.

5.6 Final Numerical Model

In the study, the final numerical model included a quarter of the finite element model of the air, explosive, witness plate, and surrogate tibia tubular structures, as shown in Figure 60. Material properties and equations of state were defined for each component remained the same as described earlier. The geometric model included meshes for air, explosive, witness plate, and tubular structure using 1st-order 8-node cubic elements. The element mesh sizes used are presented in Table 15.

Table 15 : The mesh sizes used in finite element models.

Component	**Mesh size**
Air and Explosive (ALE parts)	2.5 x 2.5 x 2.5 mm
Witness plate	1 x 1 x 1 mm
Tubular structure tube	1 x 1 x 1 mm

An automatic-surface-to-surface contact was defined between the witness plate and the tubular structure tube. Fixed boundary conditions were applied to the witness plate edges, translational boundary conditions to the tubular structure at the bushing sections, and non-reflective boundary conditions to the air mesh surfaces. The blast loading of the Lagrangian parts was achieved through fluid-structure interaction (FSI) method. Hourglass control was applied to mitigate deformation and ensure model stability. The central elements were used to obtain the direct stress component due to blast loading.

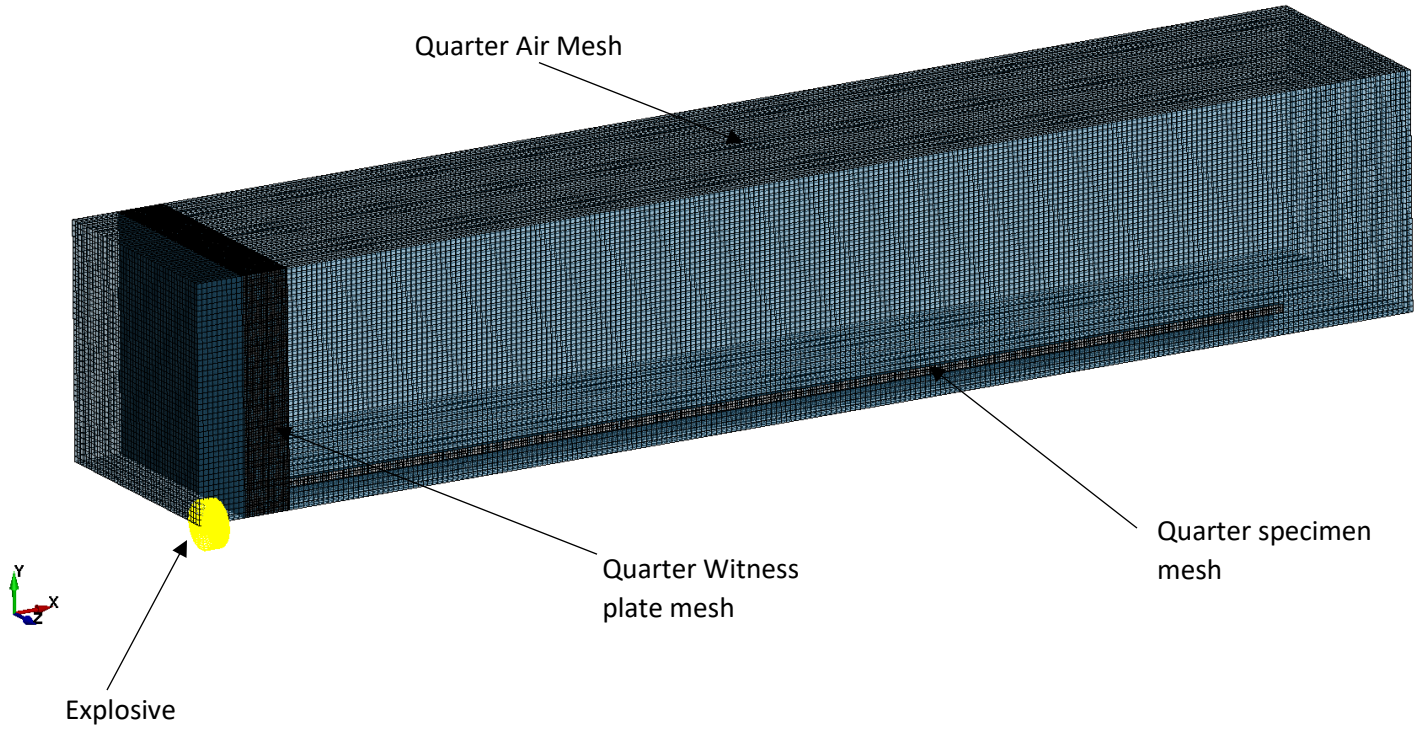

Figure 60 : A schematic diagram showing the Quarter Finite Element Model

CHAPTER 6 – NUMERICAL SIMULATION RESULTS

6.1 Visual Observations

The detonation of the explosive resulted in the stress wave that propagated through the witness plate into the tubular structure. The stress distribution plots for straight tube with non-deformable and deformable plate tests was plotted over 300 μs as shown in Figure 61 and Figure 62 respectively. The stress distribution plots used colour to indicate the intensity of stress in different tibia regions with warm hues like red and orange correspond to high stress, while cool hues like blue and green corresponded to lower stress. The stress distribution plots showed that movements of the region of high stress from the witness plate resulting in regions of high stress in both the witness plate and the tubular structure tube. Different stress distributions were observed for each test indicating that the geometry of the witness plate and the tubular structure affects the propagation of the stress waves.

As the propagating stress encountered boundaries, it was reflected as observed in the witness plate and the tubular structure tube. These reflected waves interacted with the incident stress waves, leading to complex stress interactions as they travelled back and forth within the witness plate and the tubular structure. As a result, high stress regions began to show as the wave got reflected at the free end of the tubular structure, as observed in Figure 61 and Figure 62.

In both the deformable witness plate and non-deformable witness plate detonations, it was observed that the witness plate and the tubular structure remained in contact until approximately 200 μs . As they remained in contact, stress waves were continuously transmitted through reflected stress waves between the two parts, resulting in complex stress interactions.

For non-deformable witness plate detonations, the witness plate underwent substantial stress which caused the plate to experience localized failure at the surface close to the explosive as shown Figure 61 . The tubular structure tubes experienced low magnitudes of blast-induced stresses as it exhibited no plastic deformation as observed in experimental blast tests.

For deformable witness plate detonations, the witness plate experienced plastic deformation as the blast-induced stresses propagated through it as shown in Figure 62. The stress magnitudes were high on the explosive side of the witness plate due to its proximity to the centre of detonation. A high stress region was also noticed on the interface with the tubular structure tube, as there was continuous transmission of the reflected stress waves between the two parts. The tubular structure tubes experienced substantial blast-induced stresses as it exhibited lateral deformation (bulging) due to the force exerted by stress wave as it propagated through.

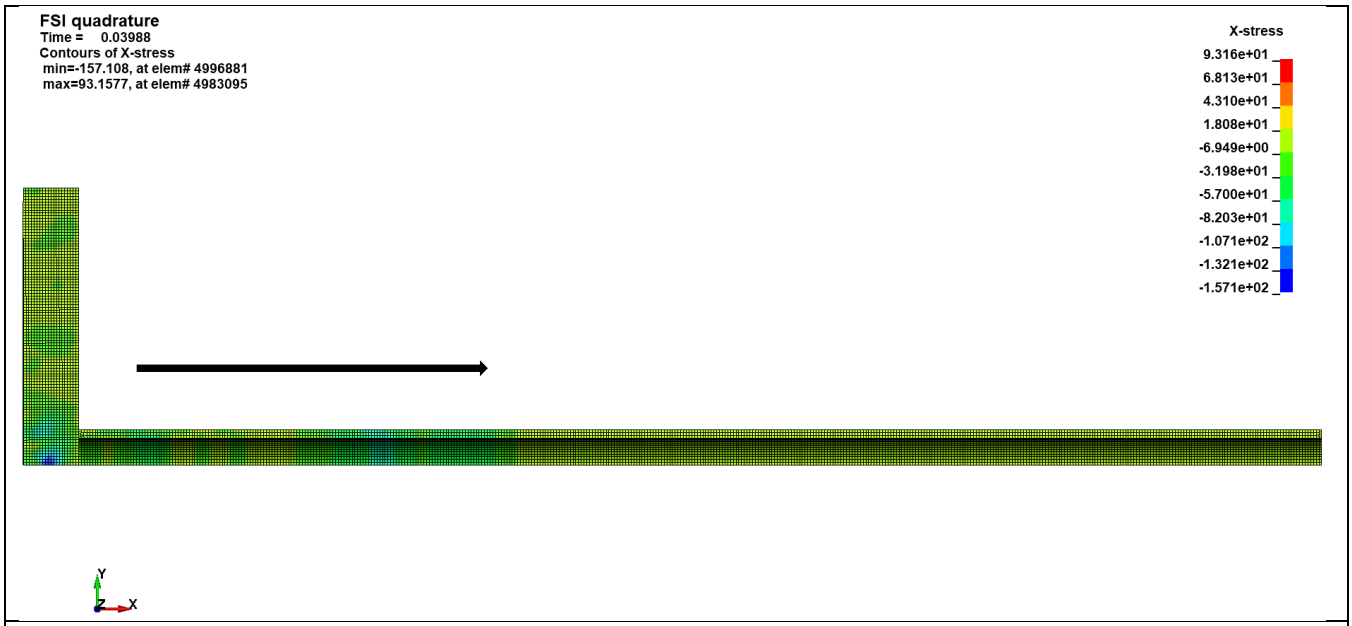
FSI quadrature
Time = 0.03988
Contours of X-stress
min=-157.108, at elem# 4996881
max=93.1577, at elem# 4983095
X-stress
9.316e+01
6.813e+01
4.310e+01
1.808e+01
-6.949e+00
-3.198e+01
-5.700e+01
-8.203e+01
-1.071e+02
-1.321e+02
-1.571e+02
Y
Z
X

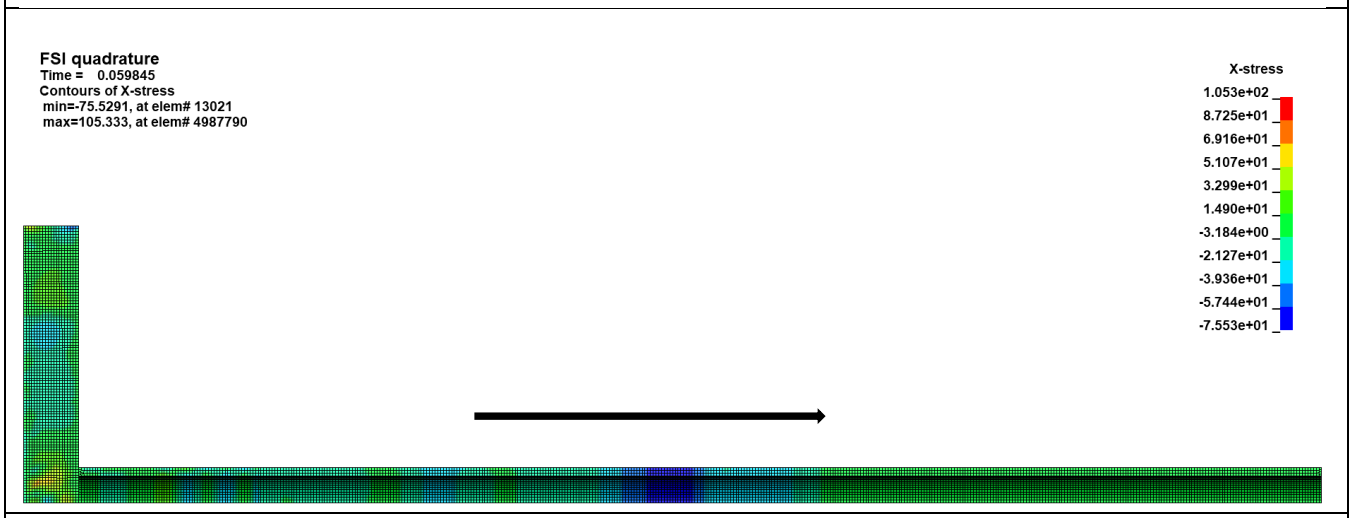
FSI quadrature
Time = 0.059845
Contours of X-stress
min=-75.5291, at elem# 13021
max=105.333, at elem# 4987790
X-stress
1.053e+02
8.725e+01
6.916e+01
5.107e+01
3.299e+01
1.490e+01
-3.184e+00
-2.127e+01
-3.936e+01
-5.744e+01
-7.553e+01

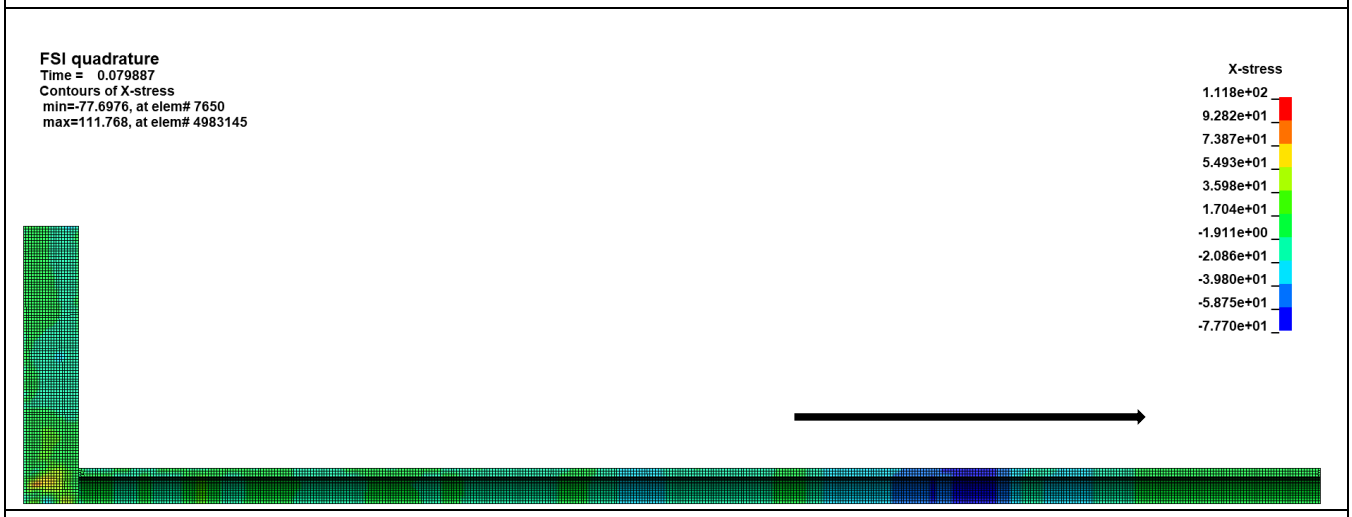
FSI quadrature
Time = 0.079887
Contours of X-stress
min=-77.6976, at elem# 7650
max=111.768, at elem# 4983145
X-stress
1.118e+02
9.282e+01
7.387e+01
5.493e+01
3.598e+01
1.704e+01
-1.911e+00
-2.086e+01
-3.980e+01
-5.875e+01
-7.770e+01

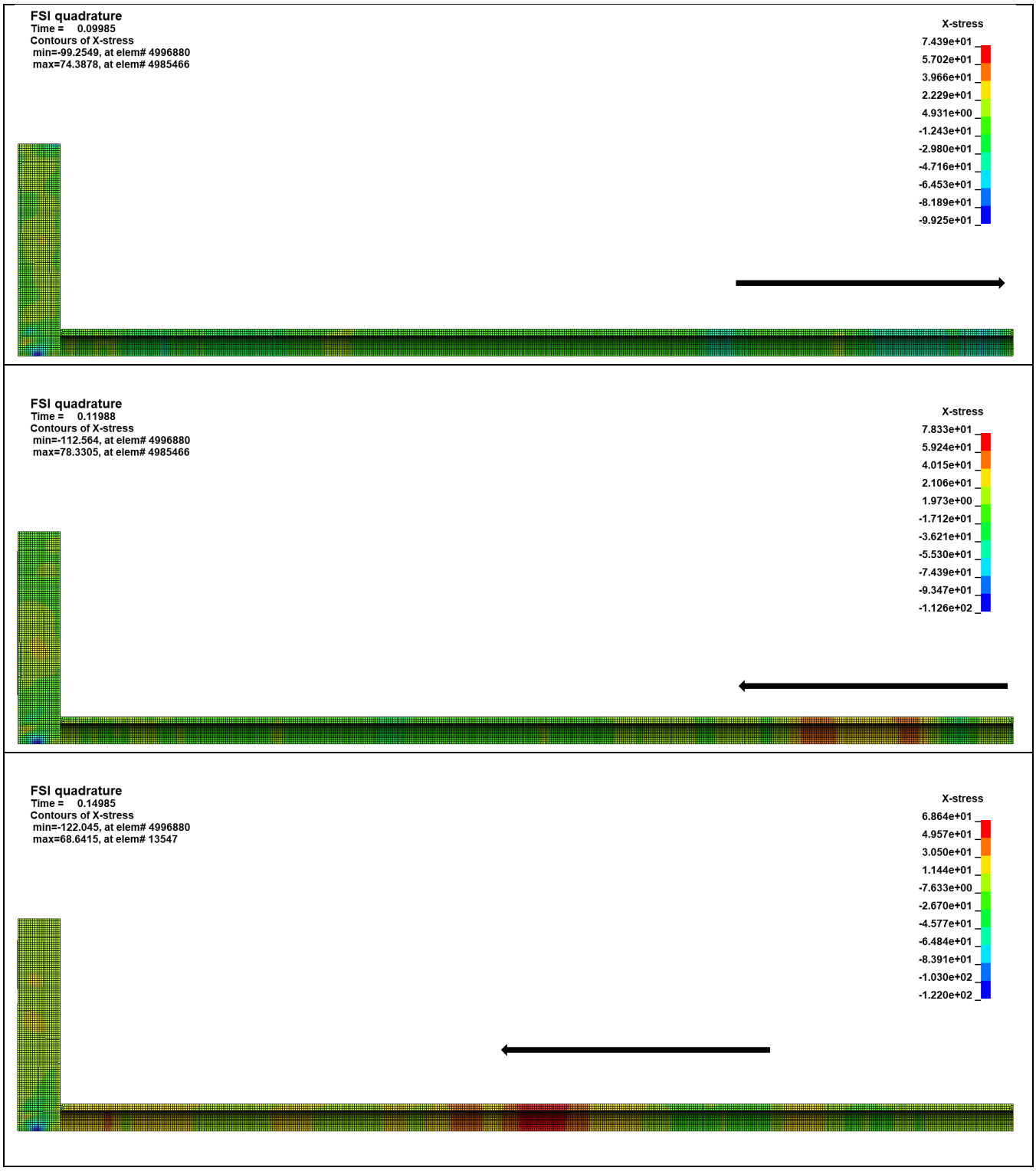

Figure 61 : The direct stress distribution of straight tube under non-deformable witness plate test

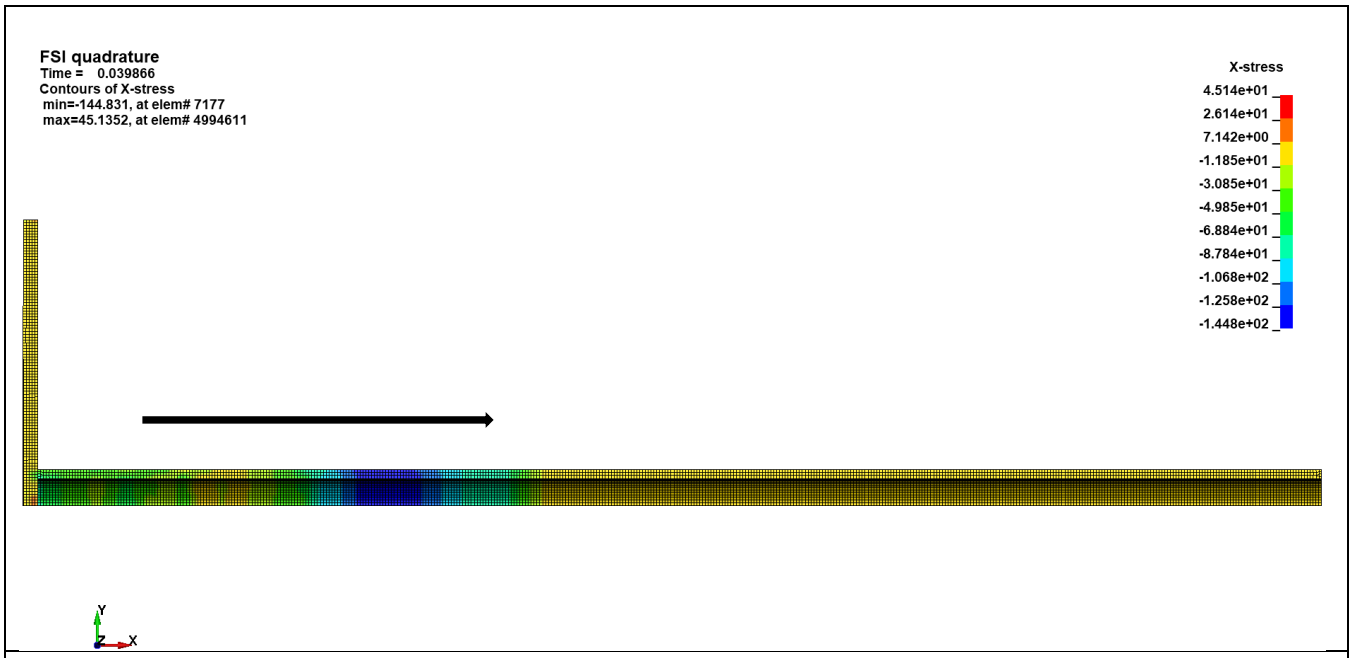
FSI quadrature
Time = 0.039866
Contours of X-stress
min=-144.831, at elem# 7177
max=45.1352, at elem# 4994611
X-stress
4.514e+01
2.614e+01
7.142e+00
-1.185e+01
-3.085e+01
-4.985e+01
-6.884e+01
-8.784e+01
-1.068e+02
-1.258e+02
-1.448e+02
Y
Z
X

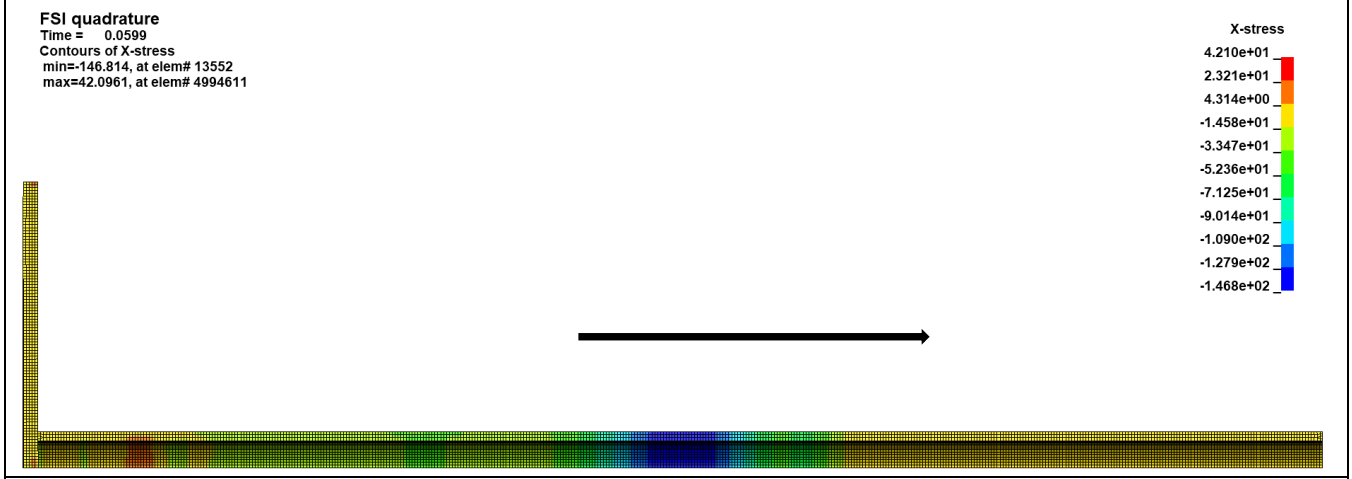
FSI quadrature
Time = 0.0599
Contours of X-stress
min=-146.814, at elem# 13552
max=42.0961, at elem# 4994611
X-stress
4.210e+01
2.321e+01
4.314e+00
-1.458e+01
-3.347e+01
-5.236e+01
-7.125e+01
-9.014e+01
-1.090e+02
-1.279e+02
-1.468e+02

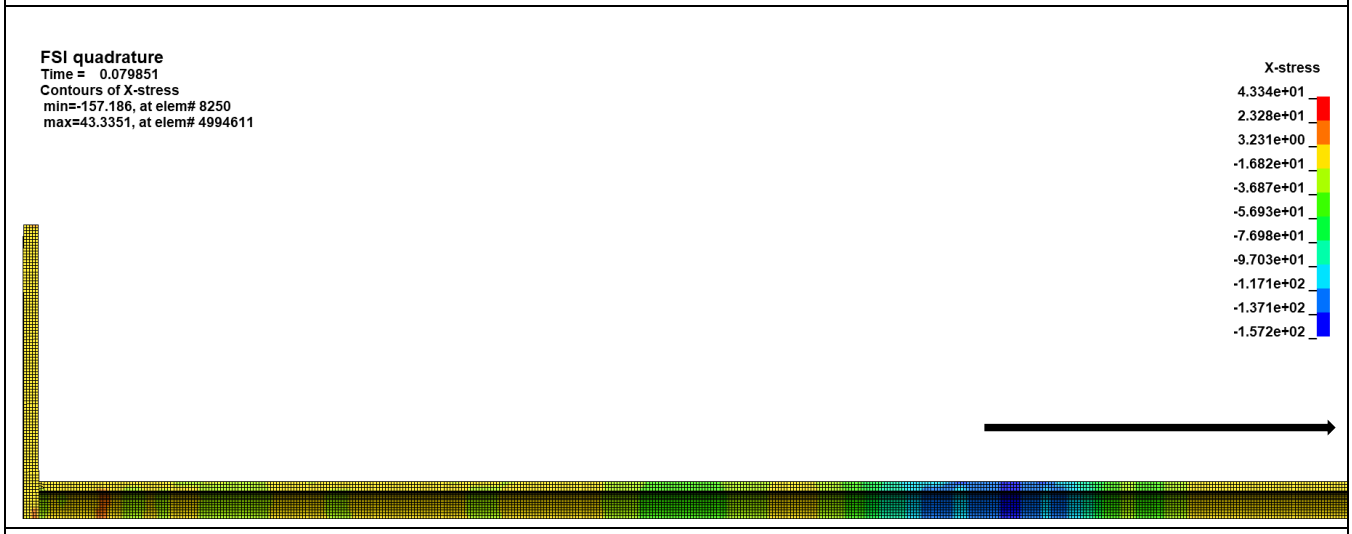
FSI quadrature
Time = 0.079851
Contours of X-stress
min=-157.186, at elem# 8250
max=43.3351, at elem# 4994611
X-stress
4.334e+01
2.328e+01
3.231e+00
-1.682e+01
-3.687e+01
-5.693e+01
-7.698e+01
-9.703e+01
-1.171e+02
-1.371e+02
-1.572e+02

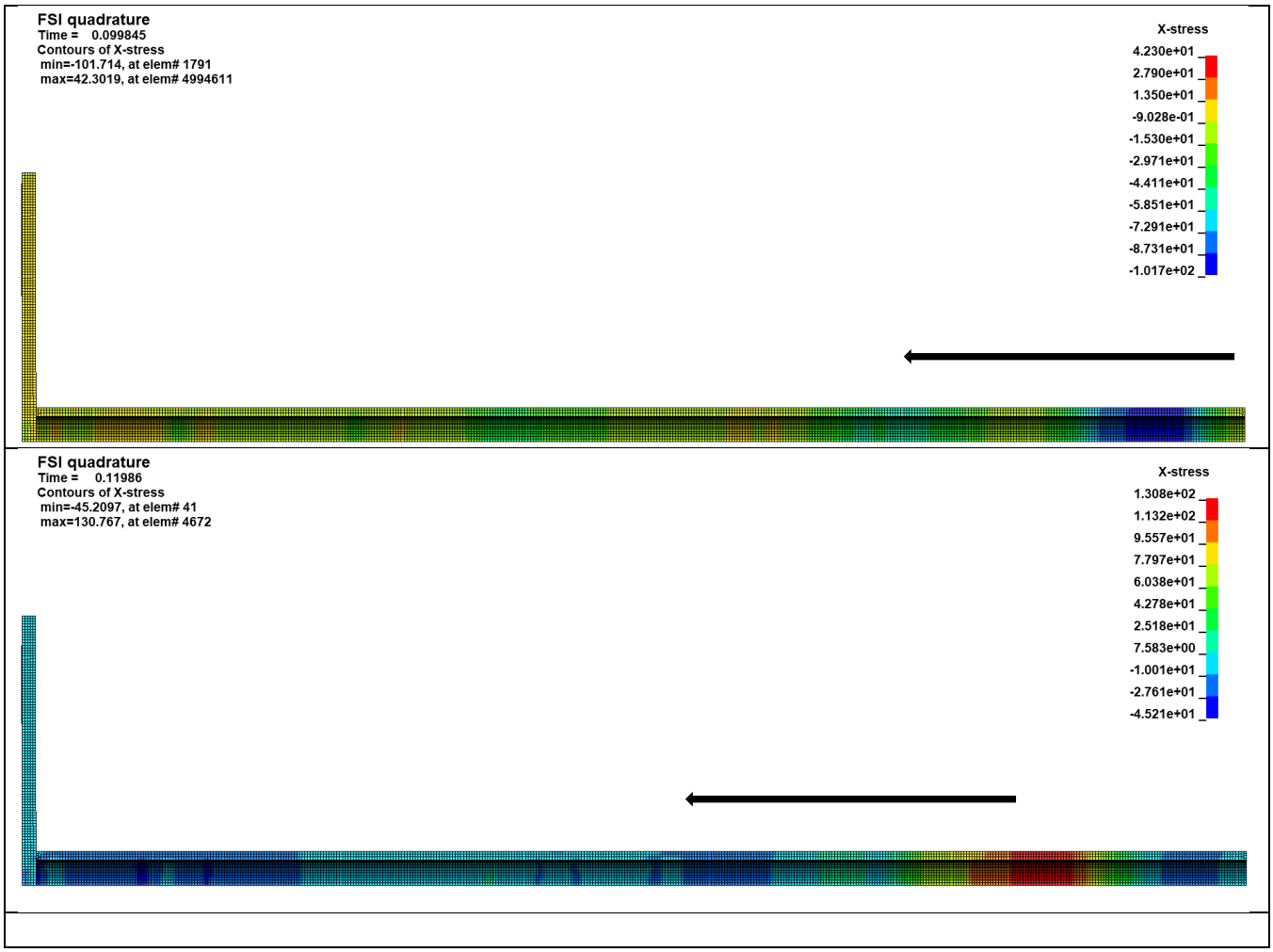

Figure 62 : The direct stress distribution of straight tube under deformable witness plate test

6.2 Stress Wave Propagation

The stress-time response from both the experimental blast tests and numerical blast tests were represented on a single graph for each conducted blast test. Region A-D was chosen to compare the stress response between the experimental and numerical blast tests because it exhibited a clearer signal before the stress waves underwent reflection and superposition, as they continued to interact with the tubular structure. By analysing this region, it was possible to determine the time at which the blast-induced stress signal arrived and ascertain the magnitudes of the peak stress for each test, including the initial impact of the reflected waves as the stress wave propagated through the tubular structure. The stress response was graphed over a duration of 0 μs to 250 μs.

6.2.1 Non-deformable Witness Plate Detonations

Straight tube

The stress-time plot, shown in Figure 50, compares the results of a finite element analysis conducted on Straight tube with a 20 mm witness plate with the experiments. In the A-B region, when the stress waves travel from the centre of detonation to the strain gauge point, the experimental blast tests showed the presence of noise in the experimental data, and none was present in the stress history plot from the simulation. This difference was due to the trigger circuit in experimental setup, while the numerical modelling did not have such noise-inducing factors.

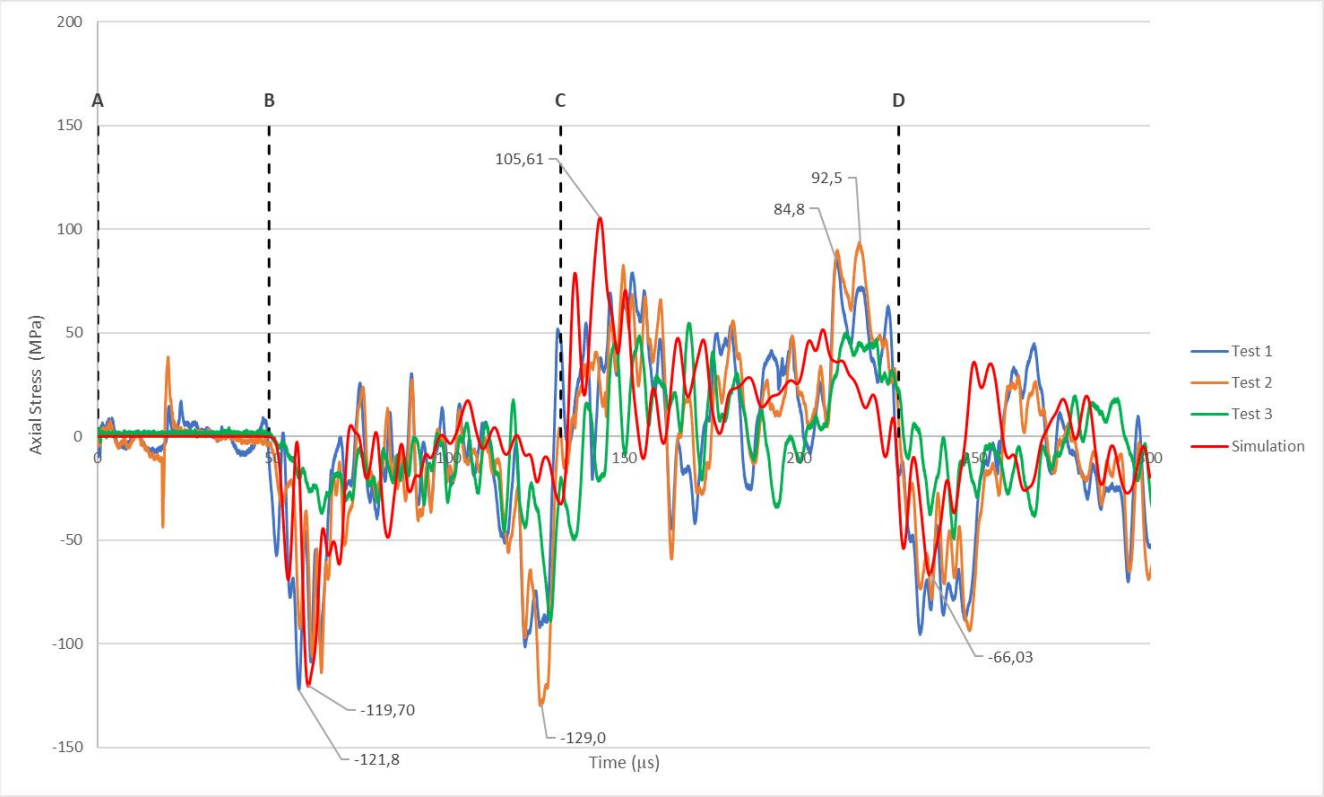

Figure 63: The graph showing the comparison between the experimental and numerical stress history obtained for Straight tube with 20mm Witness plate blast test.

Region B-C illustrates the interaction of stress waves with the tubular structure, resulting in compressive stresses as they propagate through it. The simulation recorded a peak negative stress of 119.7 MPa in this region. In comparison, the experimental blast tests recorded an average peak positive stress of 112.8 MPa. Although the there was some differences between the simulation and experiments peak stresses, the average stress from the experimental blast test shown a difference 6.1 %, indicating a good agreement between the simulations and experiments. The experimental blast tests exhibited secondary peaks in the measured compressive stress profiles of the tubular structures. The secondary stress peaks observed may be attributed to wave reflection/superposition effects as the witness plate remained in contact with the tubular structure for a short period and the variations in the material properties of the parts. Small gaps or compliance in experimental

boundary conditions can allow radial motion of the tube, inducing secondary hoop stresses whereases simplified fixed boundary conditions in models restricted the radial movements along the plane of symmetry.

In region C-D region, the stress wave travels from the end of the tubular structure towards the detonation point, resulting in tensile stresses. The simulations predicted tensile stresses of 105.6 MPa in this region. In comparison, the experimental blast tests recorded an average tensile stress of 77.0 MPa. The experimental average tensile stress was smaller compared to the simulation stresses recorded with a difference of 37.2 $\%$. The difference between the simulation and experimental results was due to reflection/superposition effects the blast induced stress wave as it continued to interact with the tubular structure and the strain gauge mounting. Also, the differences in material properties used and the boundary conditions applied in simulations may have affected stress distributions through wave reflections, interactions, focusing, and defocusing.

Overall, the stress distribution between simulations and experiments was generally the same, indicating that the numerical model captured the overall behaviour of the experimental blast test accurately.

Stepped tube

A finite element analysis of Stepped tube with 20 mm witness plate yielded the stress-time plot shown in Figure 51. In region A-B, the stress history plot from simulation indicated no noise compared to the experimental blast test since there was no trigger circuit required in the simulation of the blast test.

The interaction of the stress waves with the tubular structure as the waves propagated through the tubular structure resulted in compressive stress was shown by negative stress in Region B-C. A maximum compressive stress of 116.4 MPa was obtained from numerical modelling, while experimental blast test 1 and 2 yielded compressive stresses of 50.3 MPa and 100.4 MPa, respectively. The maximum stress obtained from experimental blast test 2 showed an anomaly due to the presence of errors in strain gauge and tubular structure set up, therefore this result was disregarded. The stress obtained from blast test 2 and simulation stress showed a percentage difference 14.8 $\%$, indicating a good agreement between the simulations and experiments.

In Region C-D, as the stress wave propagated to the end of the specimen, it was reflected backward resulting in tensile stresses within the specimen. The maximum tensile stresses of 79.3 MPa was obtained from simulation and an average of 64.3 MPa was obtained from the blast the experimental blast tests. Unlike the maximum stress from blast experiments, the maximum stress obtained from the simulation occurred on the first major peak. This discrepancy can be attributed to the interactions of the stress propagations with the reflections of stress waves and the strain gauge mounting. Also, the differences in material properties used and the boundary conditions applied in simulations may have affected stress distributions through wave reflections, interactions, focusing, and defocusing.

Figure 64 : The graph showing the comparison between the experimental and numerical stress history obtained for Stepped tube with 20mm Witness plate blast test.

Tapered Tube

A finite element analysis of Tapered tube with 20 mm witness plate yielded the stress-time plot shown in Figure 65. In region A-B, the stress history plot from simulation indicated no noise compared to the experimental blast test since there was no trigger circuit required in the simulation of the blast test.

The interaction of the stress waves with the tubular structure as the waves propagated through the tubular structure resulted in compressive stress was shown by negative stress in Region B-C. A maximum compressive stress of 90.2 MPa was obtained from numerical modelling, while experimental blast test yielded an average compressive stress of 109.6 MPa. Unlike the maximum stress from blast experiments, the maximum stress obtained from the simulation occurred on the first major peak. This discrepancy can be attributed to the interactions of the stress propagations with the reflections of pressure waves due to objects in the blast chamber. Although the there was some differences between the simulation and experiments peak stresses, the average stress from the experimental blast test shown a difference 19.4 %, indicating a good agreement between the simulations and experiments.

In Region C-D, as the stress wave propagated to the end of the specimen, it was reflected backward resulting in tensile stresses within the specimen. The maximum tensile stresses of 82.4 MPa was obtained from simulation and 116.2 MPa was obtained from the blast the experimental blast tests. Test 1 showed a maximum stress which was almost double than that obtained in Test 2. This may have been due to errors in the strain gauge mounting.

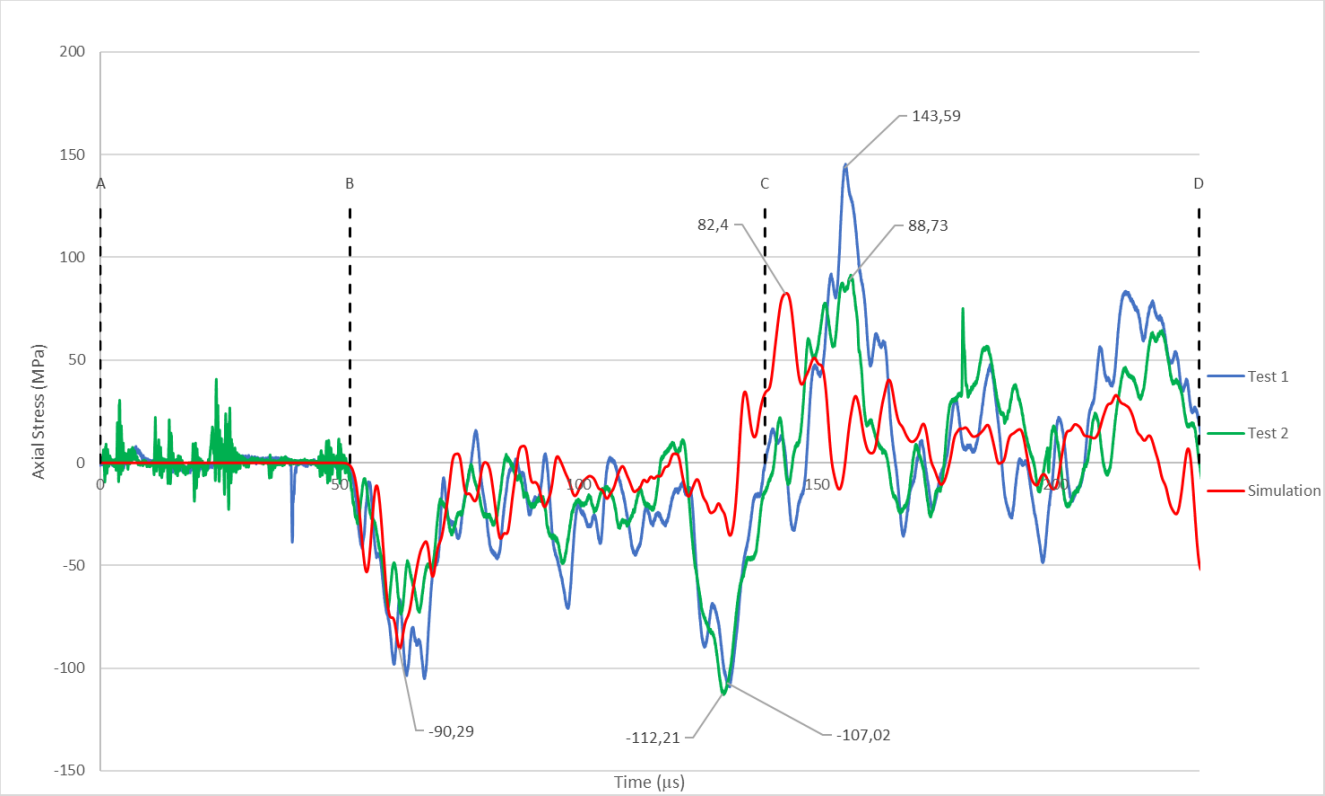

Figure 65 : The graph showing the comparison between the experimental and numerical stress history obtained for Tapered tube with 20mm Witness plate blast test.

6.2.2 Deformable witness plate Detonations

Straight tube

In Region A-B, several sharp peaks were noticed in the stress magnitude as the stress waves travelled from the detonation centre to the strain gauge point in experimental blast test and not the simulation as depicted in Figure 66. The presence of the trigger circuit in experimental blast tests attributed to the noise captured by strain gauges.

In Region B-C, the interaction of stress waves with the tubular structure was observed. The simulation and experimental tests yielded similar trends, as the stress waves propagated through the tubular structure causing compressive stresses. The magnitudes of the maximum compressive stresses were different, with 248.6 MPa from the simulations and 425.2 MPa from the experimental blast test. The percentage difference between the simulated stress and the experimental stress was approximately 70.9 % which may have been caused by variation in material properties used in the simulation and the uncertainties in the measurement of stress during the experimental blast test.

In Region C-D, both the simulation and experimental blast tests showed similar trends yielded tensile stresses of 327.3 MPa and 212.7 MPa respectively. A percentage difference of approximately 53.94 % was observed between the simulated stress and the experimental stress which may be attributed to material behaviour accuracy and measurement errors in the experimental blast tests.

Overall, the stress distribution between simulations and experiments was generally the same, indicating that the numerical model captured the overall behaviour of the experimental blast test accurately.

Figure 66 : The graph showing the comparison between the experimental and numerical stress history obtained for Straight tube with 5mm Witness plate blast test.

Stepped tube

In Region A-B, several sharp peaks were noticed in the stress magnitude as the stress waves travelled from the detonation centre to the strain gauge point in experimental blast test and not the simulation as depicted in Figure 67. The presence of the trigger circuit in experimental blast tests attributed to the noise captured by strain gauges.

In Region B-C, the interaction of stress waves with the tubular structure was observed. The simulation and experimental tests yielded similar trends, as the stress waves propagated through the tubular structure causing compressive stresses. The magnitudes of the maximum compressive stresses were different, with 271.0 MPa from the simulations and 395.0 MPa from the experimental blast test. The percentage difference between the simulated stress and the experimental stress was approximately 45.76 % which may have been caused by variation in material properties used in the simulation and the uncertainties in the measurement of stress during the experimental blast test.

In Region C-D, both the simulation and experimental blast tests showed similar trends yielded tensile stresses of 232.2 MPa and 289.8 MPa respectively. A percentage difference of approximately 24.5 % was observed between the simulated stress and the experimental stress which may be attributed to material behaviour accuracy and measurement errors in the experimental blast tests. Overall, the stress distribution between simulations and experiments was generally the same, indicating that the numerical model captured the overall behaviour of the experimental blast test accurately.

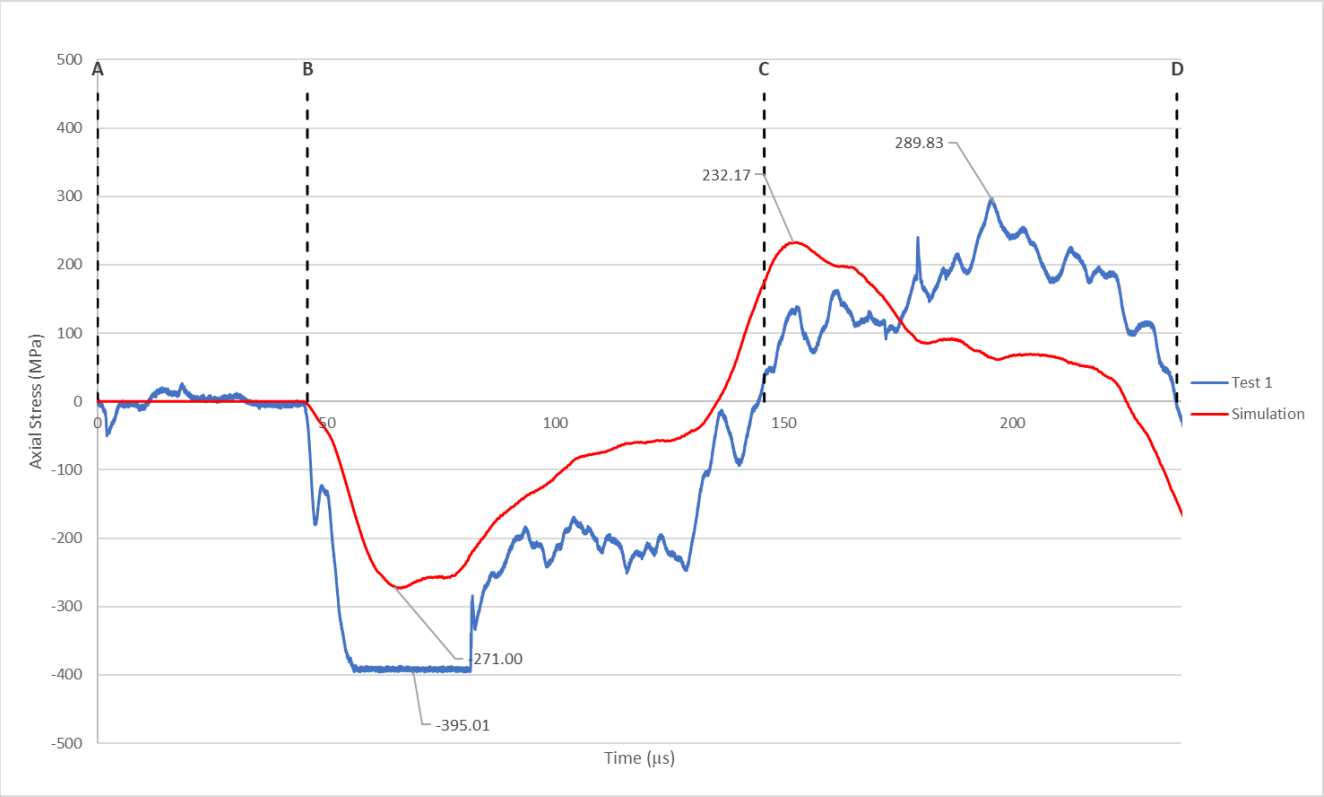

Figure 67 : Graph showing the comparison between the experimental and numerical stress history obtained for Stepped tube with 5mm Witness plate blast test.

Tapered tube

In Region A-B, several sharp peaks were noticed in the stress magnitude as the stress waves travelled from the detonation centre to the strain gauge point in experimental blast test and not the simulation as depicted in Figure 68. The presence of the trigger circuit in experimental blast tests attributed to the noise captured by strain gauges.

In Region B-C, the interaction of stress waves with the tubular structure was observed. The simulation and experimental tests yielded similar trends, as the stress waves propagated through the tubular structure causing compressive stresses. The magnitudes of the maximum compressive stresses were different, with 275.2 MPa from the simulations and an average of 374.8 MPa from the experimental blast test. The percentage difference between the simulated stress and the experimental stress was approximately 36.7 % which may have been caused by variation in material properties used in the simulation and the uncertainties in the measurement of stress during the experimental blast test.

In Region C-D, both the simulation and experimental blast tests showed similar trends yielded tensile stresses of 233.1 MPa and an average of 300.35 MPa respectively. A percentage difference of approximately 28.9 % was observed between the simulated stress and the experimental stress which may be attributed to material behaviour accuracy and measurement errors in the experimental blast tests. Overall, the stress distribution

between simulations and experiments was generally the same, indicating that the numerical model captured the overall behaviour of the experimental blast test accurately.

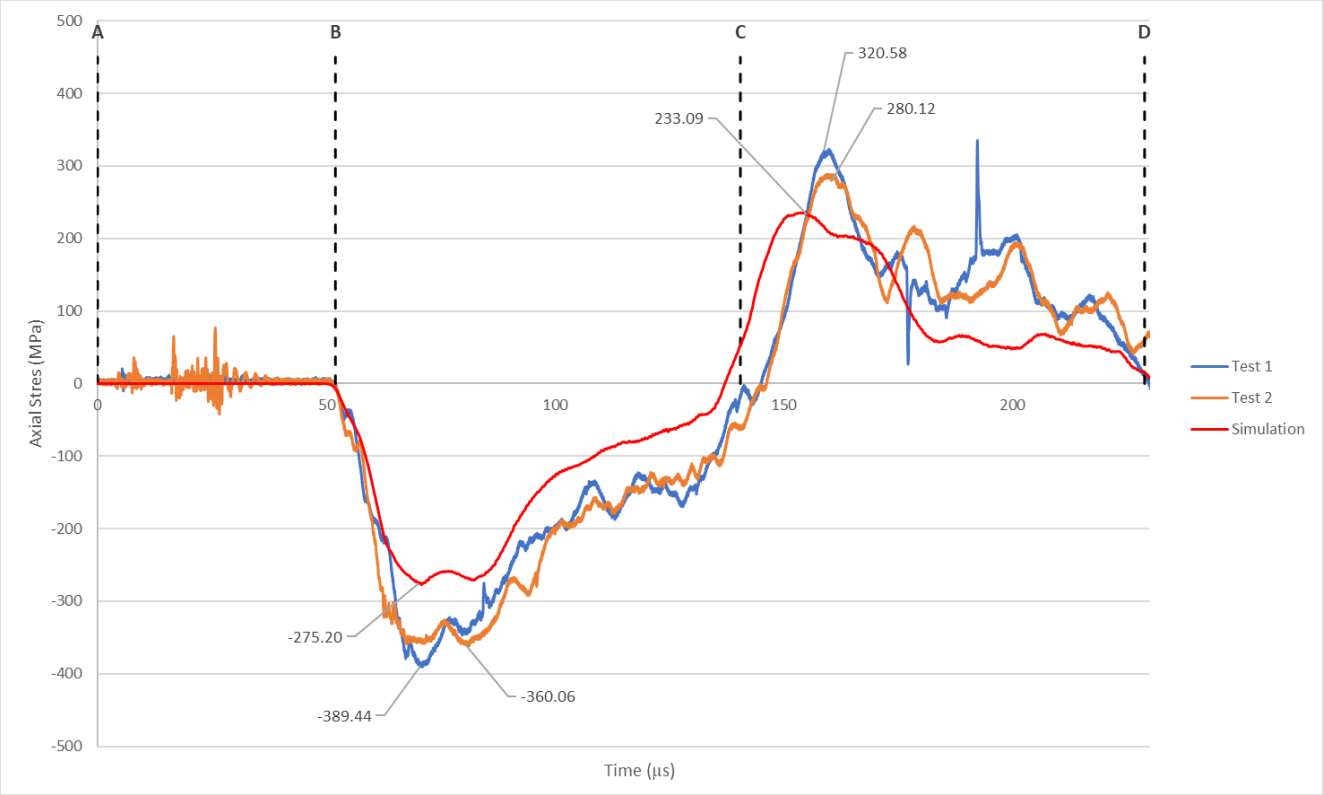

Figure 68 : Graph showing the comparison between the experimental and numerical stress history obtained for Tapered tube with 5mm Witness plate blast test.

6.3 Summary

The direct stress criterion was used to obtain the distribution of the resultant stress induced by the blast load in the numerical modelling of the blast tests. Direct stress was the strain gauge element at the centre of the tubular structure and validated using the stress-time data obtained from the blast experiments. The tubular structure experienced compressive stress as indicated by the negative stress values. The compressive load was caused by the propagation of the stress wave away from the detonation point. The wave continued until it reached the end of the tubular structure and was then reflected, resulting in a tensile load in the specimen. The blast experimental results and numerical modelling results, the maximum compressive and tensile stress values from each test simulation were presented in Table 16. The percentage difference between the two values was used to assess the level of agreement between the tests, with lower percentage values being more acceptable.

For the non-deformable witness plate tests, excluding data that deviated from the average, the percentage difference between the experimental and simulated maximum negative stress values ranged from 1.8 % to 31.8 %, indicating a reasonable agreement between the two tests. The percentage difference between the experimental and simulated maximum positive stress values ranged from 7.4 % to 63.4 %. For the Deformable witness plate tests, excluding data that deviates from the average, the percentage difference between the experimental and simulated maximum negative stress values was from 26.7 % to 52.4 %, indicating a larger

variation compared to the non-deformable witness plate tests. The percentage difference between the experimental and simulated maximum positive stress values was from 11.2 % to 42.5 %.

The tests marked with "*" indicated in Table 16 showed a higher deviation from the average stress magnitude therefore they were regarded as outliers in the experimental blast tests. The errors were because of inconsistency in experimental set up of tubular structure tubes and mounting of strain gauges. Both non-deformable and Deformable witness plate tests, show relatively small percentage differences ranging from 0.0 % to 5.7 % for non-deformable witness plates and from 0.1 % to 1.4 % for Deformable witness plates regarding the time of arrival.

Excluding experimental data that deviated from the average, the deformable witness plate tests exhibited a better correlation between the experimental and simulation stress magnitude. The Deformable witness plate tests showed generally smaller variations in the stress magnitudes as compared to the non-deformable witness plate tests. However, there was no universally defined threshold for an allowed percentage difference in stress magnitudes between experimental and simulation results since the aim of the study was to understand stress wave propagation through the tibia under blast loading and provide insights into the behaviour and response of the tibia in such scenarios.

In summary, the stress distribution between simulations and experiments was generally the same, indicating that the numerical model captured the overall behaviour of the experimental blast test. The numerical model showed a good agreement with the experiments in capturing the general trends and presence of compressive and tensile stresses and the influence of surrounding objects on the stress distribution and magnitudes. The numerical model set was further developed by replacing the tubular structure with a 3D tibia CAD model which better represents the geometry of the human tibia.

Table 16 : The comparison of results obtained from numerical modelling and experimental blast tests.

Blast Test	Test Name	Experimental Maximum Negative Stress (MPa)	Simulation Maximum Negative Stress (MPa)	Percentage Difference (%)	Experimental Maximum Positive Stress (MPa)	Simulation Maximum Positive Stress (MPa)	Percentage Difference (%)	Experimental Time of Arrival (μs)	Experimental Time of Arrival (μs)	Percentage Difference (%)
Non-deformable witness plate	S1/20_1	121.8	119.7	1.8	85.0	105.6	21.6	48.6	50.2	3.3
	S1/20_2	129.7	119.7	8.0	92.2	105.6	13.6	47.7	50.2	5.1
	S1/20 _3	86.8	119.7	31.8	54.8	105.6	63.3*	49.5	50.2	1.4
	Average	**112.8**	**119.7**	**6.0**	**77.3**	**105.6**	**30.9**	**48.6**	**50.2**	**3.2**
	S2/20_1	50.3	116.4	79.3*	41.9	79.3	61.8	49.0	49.1	0.2
	S2/20_2	100.4	116.4	14.8	64.3	79.3	20.8	49.2	49.1	0.2
	Average	**75.4**	**116.4**	**42.8**	**53.1**	**79.3**	**39.6**	**49.1**	**49.1**	**0.0**
	S3/20_1	107.0	90.3	16.9	143.6	82.3	54.3*	52.0	52.3	0.6
	S3/20_2	112.2	90.3	21.6	88.7	82.3	7.5	52.3	52.3	0.0
	Average	**109.6**	**90.3**	**19.3**	**116.2**	**82.3**	**34.1**	**52.1**	**52.3**	**0.3**
Deformable witness plate	S1/5_1	109.7	248.6	77.5*	302.4	212.7	34.8	47.1	49.8	5.7
	S1/5_2	156.0	248.6	45.8	237.8	212.7	11.1	46.0	49.8	8.0
	S1/5_3	425.2	248.6	52.4*	327.3	212.7	42.5	49.4	49.8	0.8
	Average	**230.3**	**248.6**	**7.6**	**289.2**	**212.7**	**30.5**	**47.5**	**49.8**	**4.8**
	S2/5_1	**396.0**	**271.0**	**37.5**	**289.8**	**232.2**	**22.1**	**46.0**	**46.3**	**0.8**
	Average	**396.0**	**271.0**	**37.5**	**289.8**	**232.2**	**22.1**	**46.0**	**46.3**	**0.8**
	S3/5_1	389.4	275.2	34.4	320.6	233.1	31.6	51.0	51.7	1.4
	S3/5_2	360.1	275.2	26.7	280.1	233.1	18.3	51.8	51.7	0.1
	Average	**374.8**	**275.2**	**30.6**	**300.4**	**233.1**	25.2	**51.4**	**51.7**	**0.6**
Overall Percentage Difference				**24.0**			**30**			**1.6**

NB: * data regraded as outliers.

CHAPTER 7 – PARAMETRIC STUDY

The validated Finite Element Model (FEM) was further improved by substituting the tubular structure with the complete 3D tibia Computer-Aided Design (CAD) model developed by Ardatov [58]. A comprehensive numerical model consisting of the air, explosive, explosion plate, and tibia model was utilized, as shown in Figure 71. Due to the absence of symmetry in the tibia model, a full finite element model was employed to capture the overall behaviour of the tibia structure.

7.1 Geometric Modelling

Figure 69 shows the geometry and the overall dimensions used of the 3D tibia model. The major dimensions, summarized in Table 17 were used in modelling the tibia are distal and proximal diaphysis diameters and the total length of the tibia. The dimension of the tibia model was based on a study conducted by Sume [73]. The two ends of the tibia were flat which facilitated the definition of the contact between the witness plate and the tibia for uniform transfer of the blast load into the tibia model. The tibia model included medullary cavity which was modelled as open space. The length of the tibia was scaled to investigate different tibiae, with the short tibia representing a tibia for a woman and the long tibia representing tibia for a Men. The distal diaphysis and proximal diaphysis diameters were based on the 3D tibia model used and the tibial length was altered leading to variation in the cross-sectional area between the man and woman tibia models.

The tibia model was further simplified by modelling it with shell elements with a shell thickness of 3 mm because the tibia model was only available in shell form. The tibial finite element model consisted of 4-node quadrilateral elements of size 1 x 1 mm with a low integration to minimise the run time. The tibia bone has a relatively thin and curved geometry compared to its length and width therefore using shell elements would accurately capture the behaviour of the stress propagations on the surface of the tibia model. The objective of the study was more focused on the propagation of the stress waves rather than the intricate local details of model response.

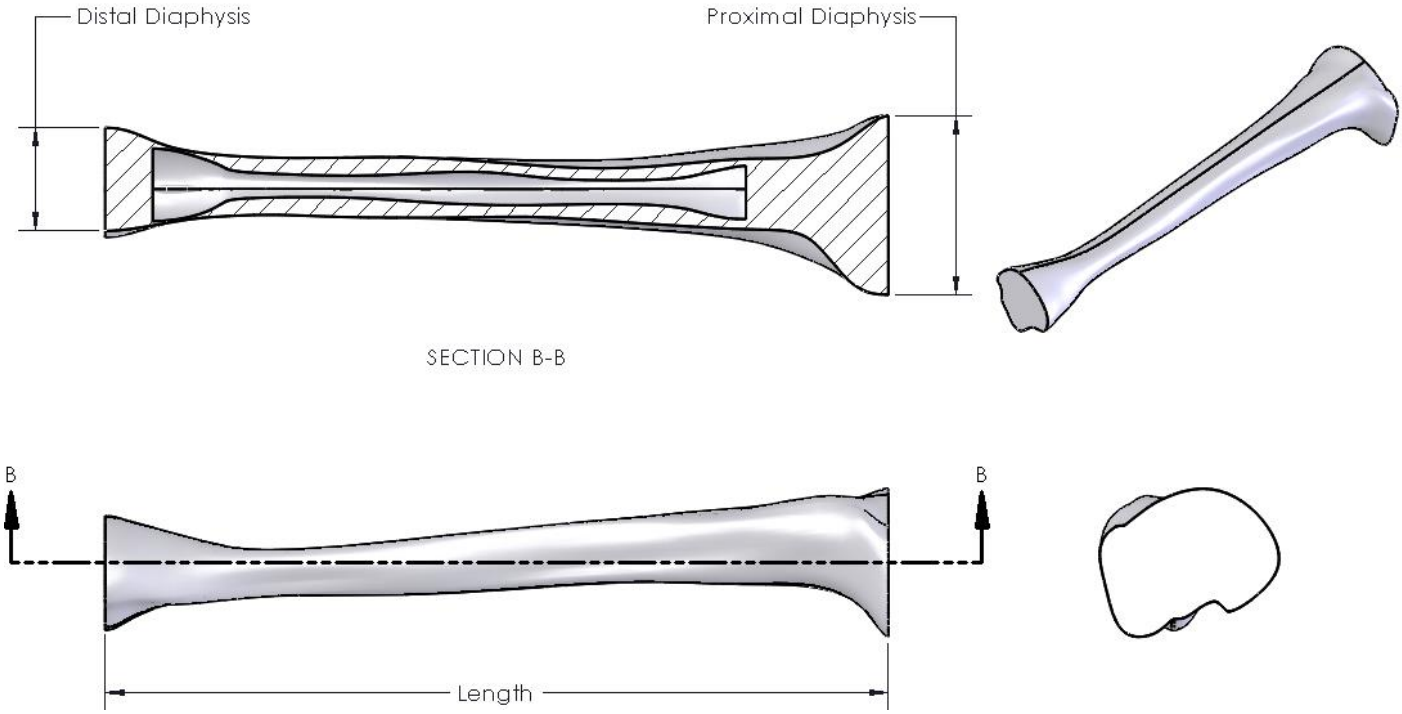

Figure 69 : Schematic diagram of the Tibia 3D CAD Model used for simulations.

Table 17 : Tibia dimensions [60]

Tibia Model	Length (mm)	Distal diaphysis diameter (mm)	Proximal diaphysis diameter (mm)
Men	450	46	80
Women	350	46	80

a) 3D CAD Tibia b) 3D Finite Element Tibia

Figure 70 : Schematic diagram showing (a) 3D CAD Model b) 3D Finite Element Model

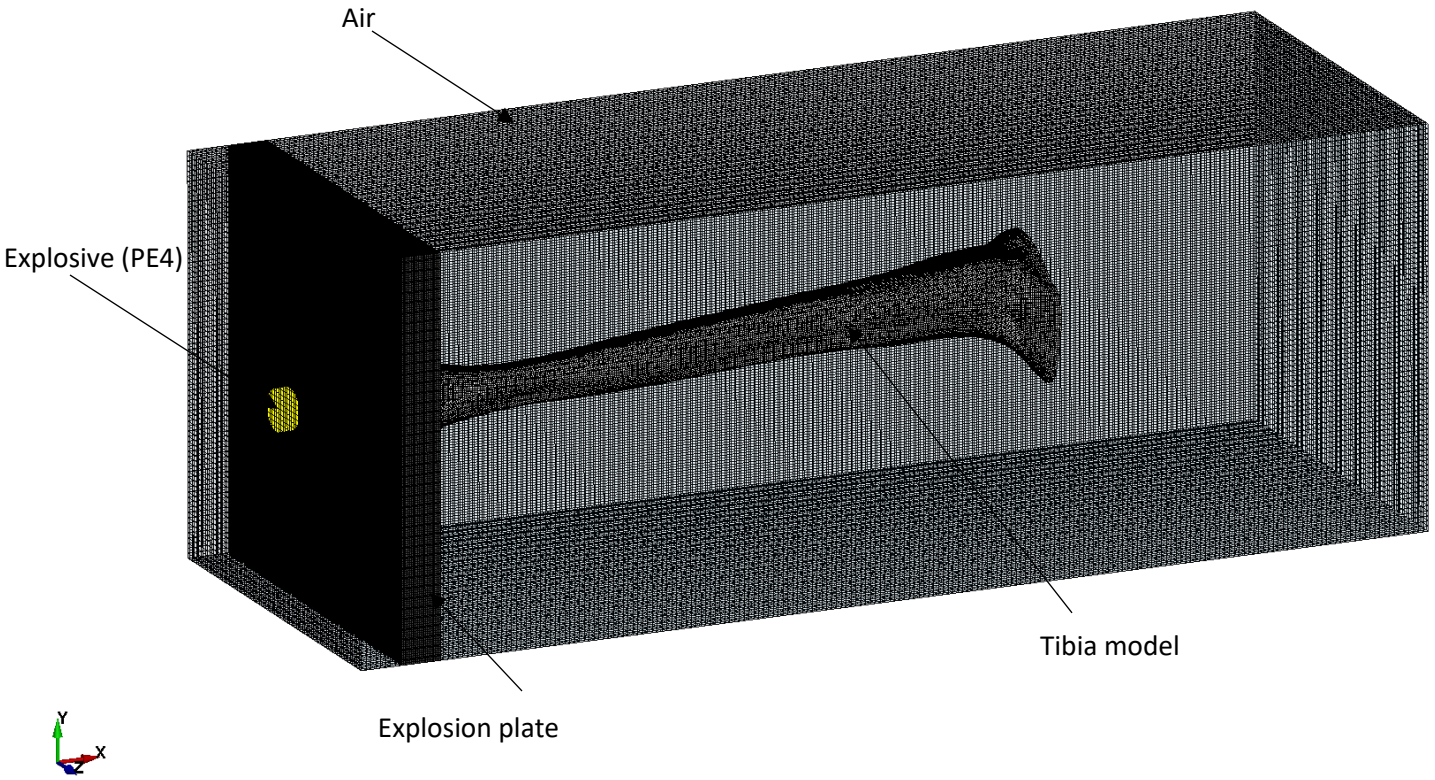

Figure 71 : Image of the Full Finite Element Model with the tibia model

7.2 Material Modelling

The mechanical properties of Aluminium material were employed to represent the tibia in the model, instead of using bone material. The simplification of the material was made because the aluminium material exhibits relatively isotropic and homogeneous mechanical properties which makes it easier to use in numerical simulations [60]. The bone is a complex composite material that is highly anisotropic and has heterogeneous mechanical properties which may pose a great challenge in material modelling [74]. Using Aluminium material would provide insights into the stress wave propagation through the tibia under blast loading.

7.3 Results of the Parametric Study

7.3.1 Visual Observations

The distributions of the blast induced stress across the tibia was obtained using the direct stress form 0 up to 0.299 ms, as shown in Figure 72 and Figure 73 for non-deformable plate detonations of man and woman tibia respectively. Areas of high stress concentrations were observed as the blast-induced stress wave propagated through the tibia structure. The same phenomenon of the stress attributions as the stress wave propagated through the tibia structure was observed for deformable plate detonations, refer to APPENDIX D. As a result, areas with high stress concentrations may be potential injury locations. Stress concentrations variations across all the

tibia models were observed which indicated that there was localized structural weaknesses due to variations in geometry and the loading conditions along the axis of the tibia structure.

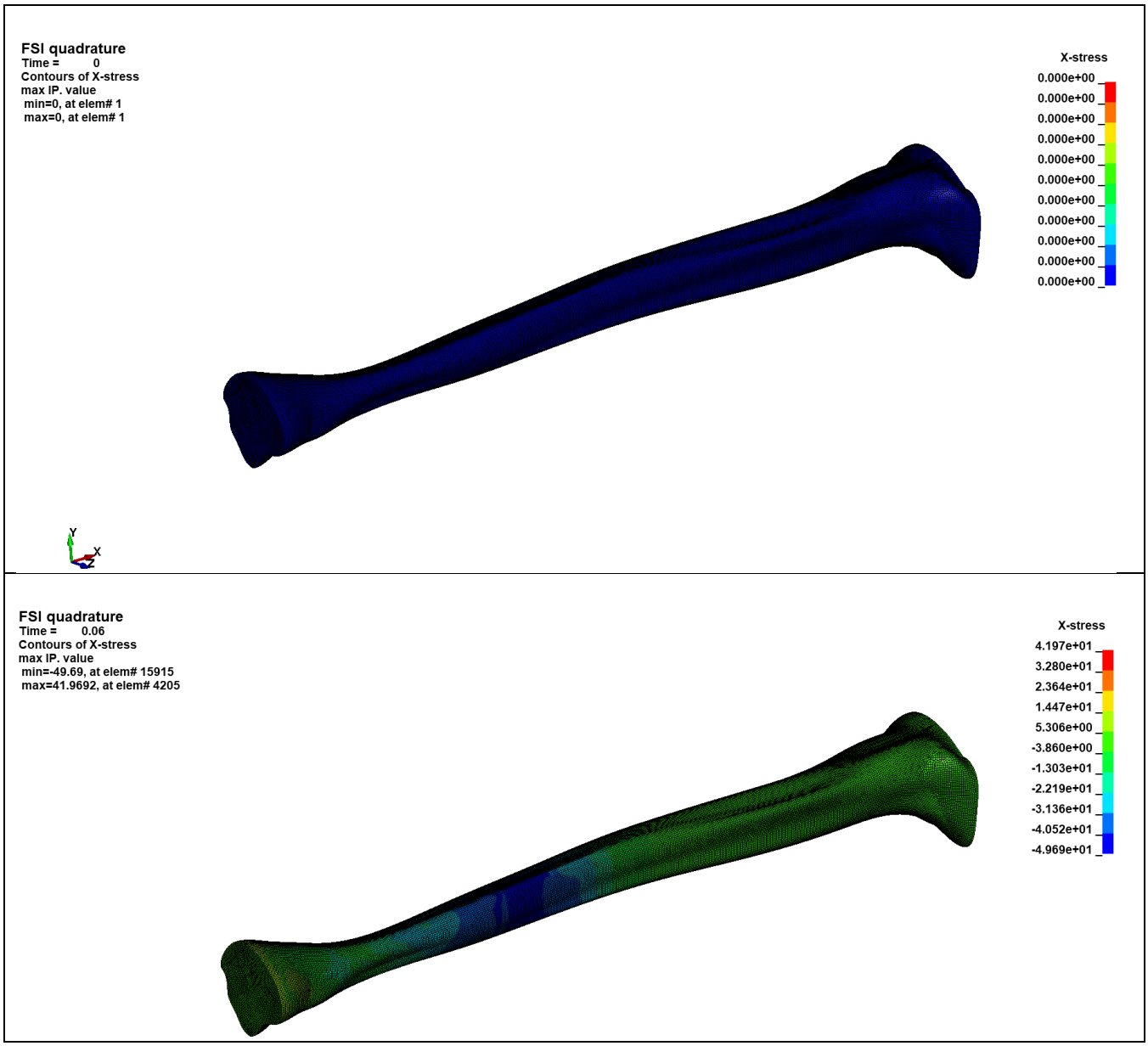

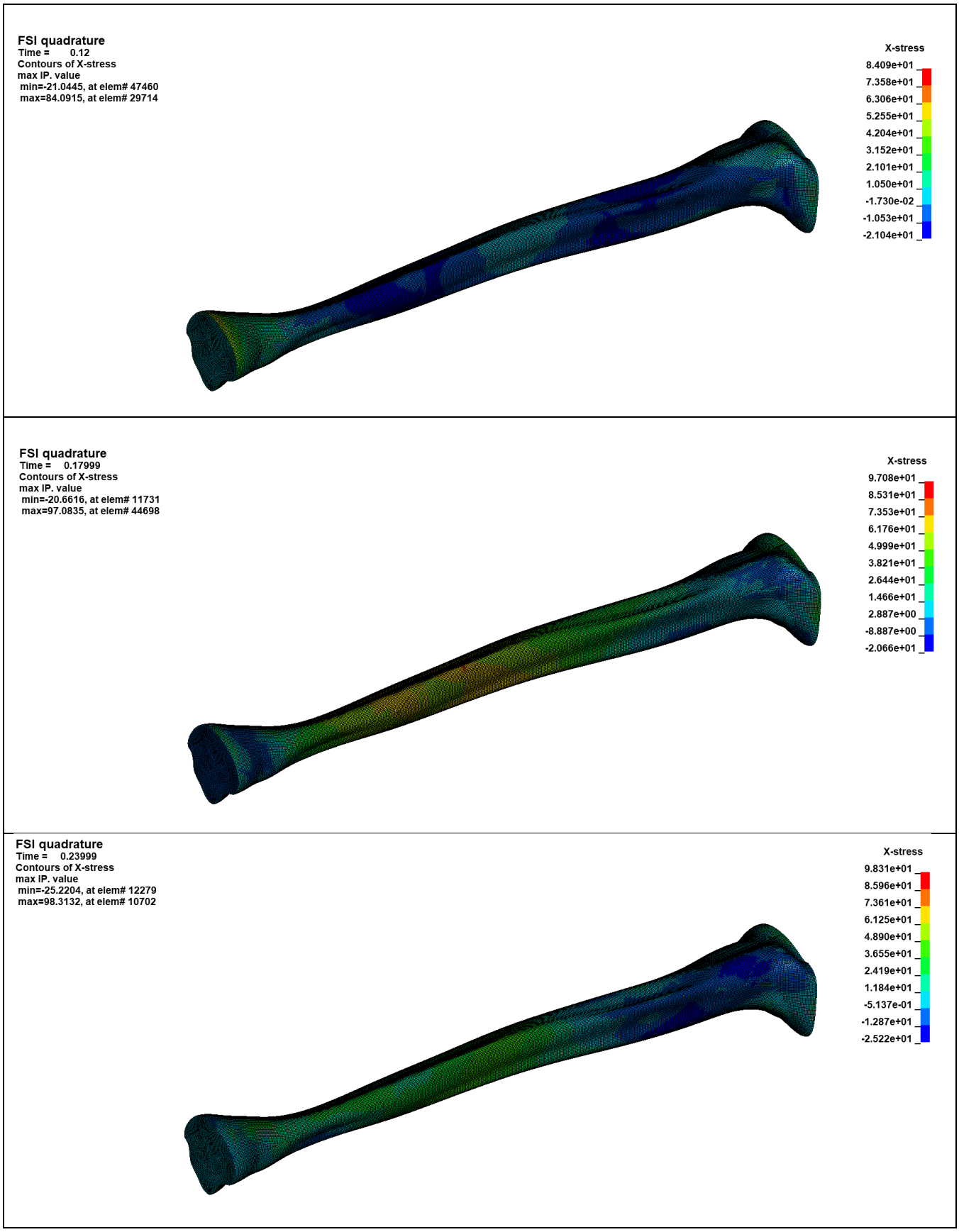
FSI quadrature
Time = 0.12
Contours of X-stress
max IP. value
min=-21.0445, at elem# 47460
max=84.0915, at elem# 29714
X-stress
8.409e+01
7.358e+01
6.306e+01
5.255e+01
4.204e+01
3.152e+01
2.101e+01
1.050e+01
-1.730e-02
-1.053e+01
-2.104e+01
FSI quadrature
Time = 0.17999
Contours of X-stress
max IP. value
min=-20.6616, at elem# 11731
max=97.0835, at elem# 44698
X-stress
9.708e+01
8.531e+01
7.353e+01
6.176e+01
4.999e+01
3.821e+01
2.644e+01
1.466e+01
2.887e+00
-8.887e+00
-2.066e+01
FSI quadrature
Time = 0.23999
Contours of X-stress
max IP. value
min=-25.2204, at elem# 12279
max=98.3132, at elem# 10702
X-stress
9.831e+01
8.596e+01
7.361e+01
6.125e+01
4.890e+01
3.655e+01
2.419e+01
1.184e+01
-5.137e-01
-1.287e+01
-2.522e+01

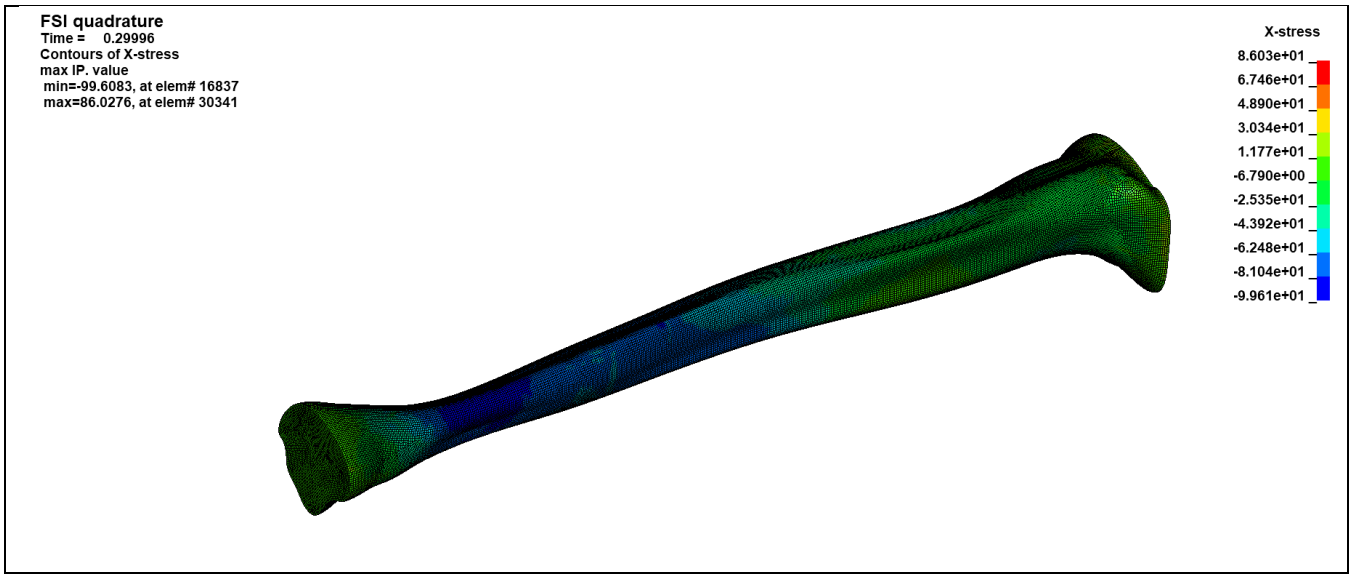

Figure 72 : The axial stress distribution of man Tibia under non-Deformable plate detonations

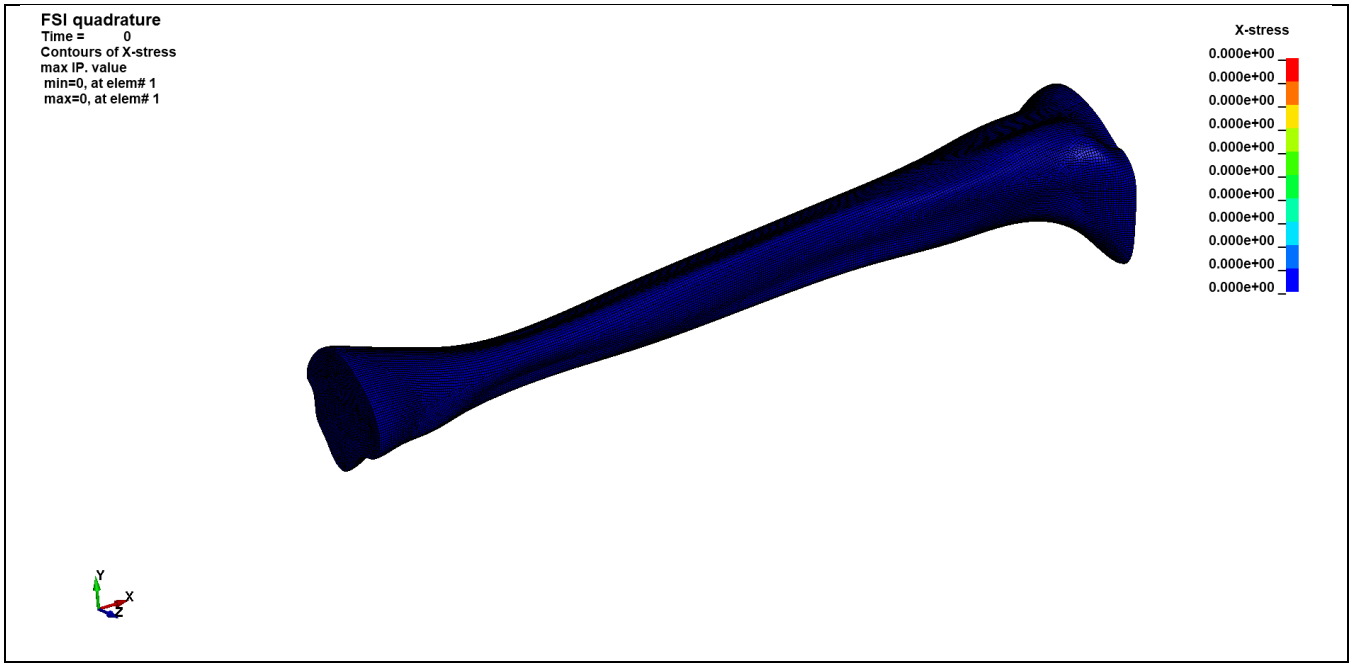

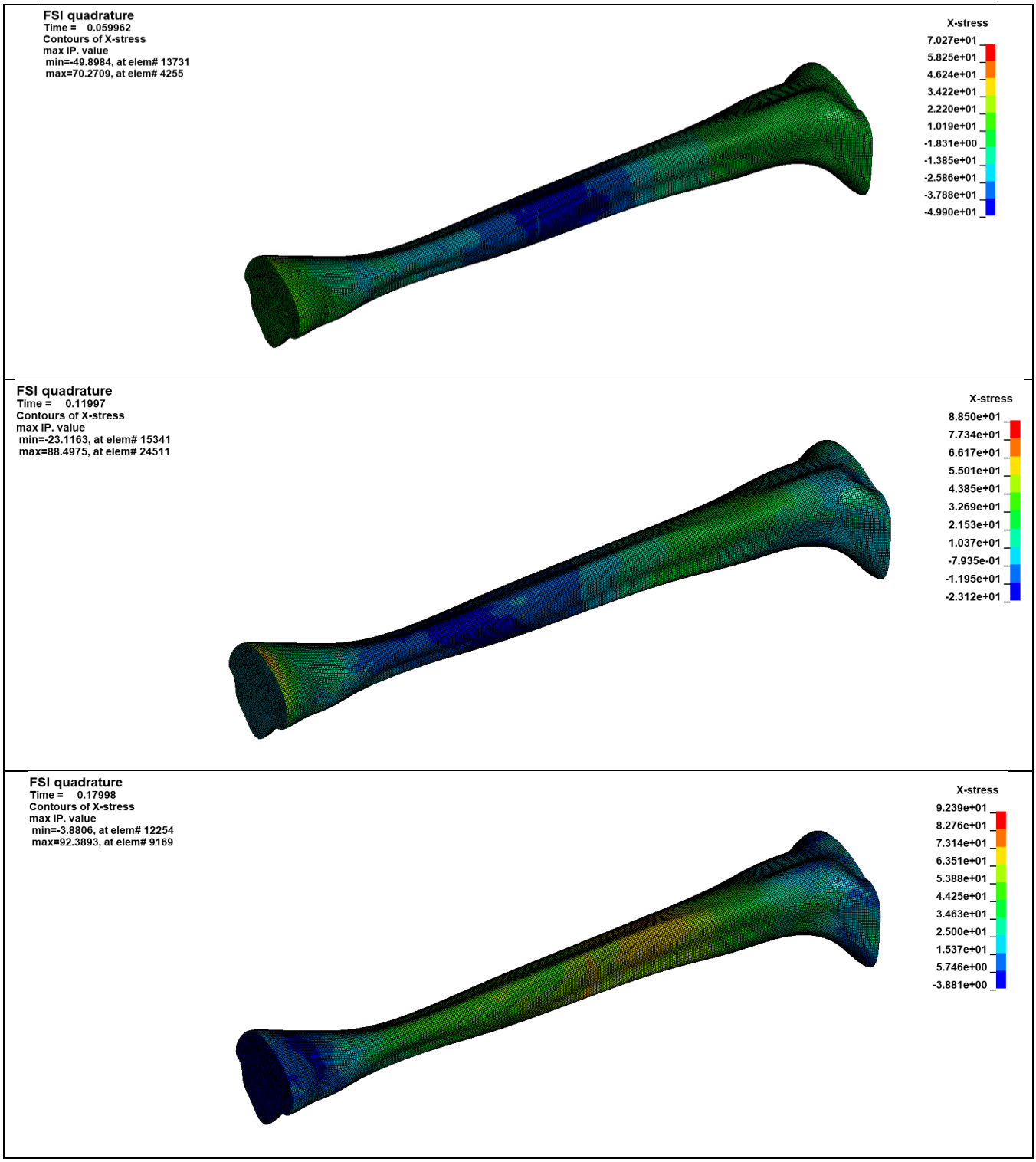
FSI quadrature
Time = 0.059962
Contours of X-stress
max IP. value
min=-49.8984, at elem# 13731
max=70.2709, at elem# 4255
X-stress
7.027e+01
5.825e+01
4.624e+01
3.422e+01
2.220e+01
1.019e+01
-1.831e+00
-1.385e+01
-2.586e+01
-3.788e+01
-4.990e+01
FSI quadrature
Time = 0.11997
Contours of X-stress
max IP. value
min=-23.1163, at elem# 15341
max=88.4975, at elem# 24511
X-stress
8.850e+01
7.734e+01
6.617e+01
5.501e+01
4.385e+01
3.269e+01
2.153e+01
1.037e+01
-7.935e-01
-1.195e+01
-2.312e+01
FSI quadrature
Time = 0.17998
Contours of X-stress
max IP. value
min=-3.8806, at elem# 12254
max=92.3893, at elem# 9169
X-stress
9.239e+01
8.276e+01
7.314e+01
6.351e+01
5.388e+01
4.425e+01
3.463e+01
2.500e+01
1.537e+01
5.746e+00
-3.881e+00

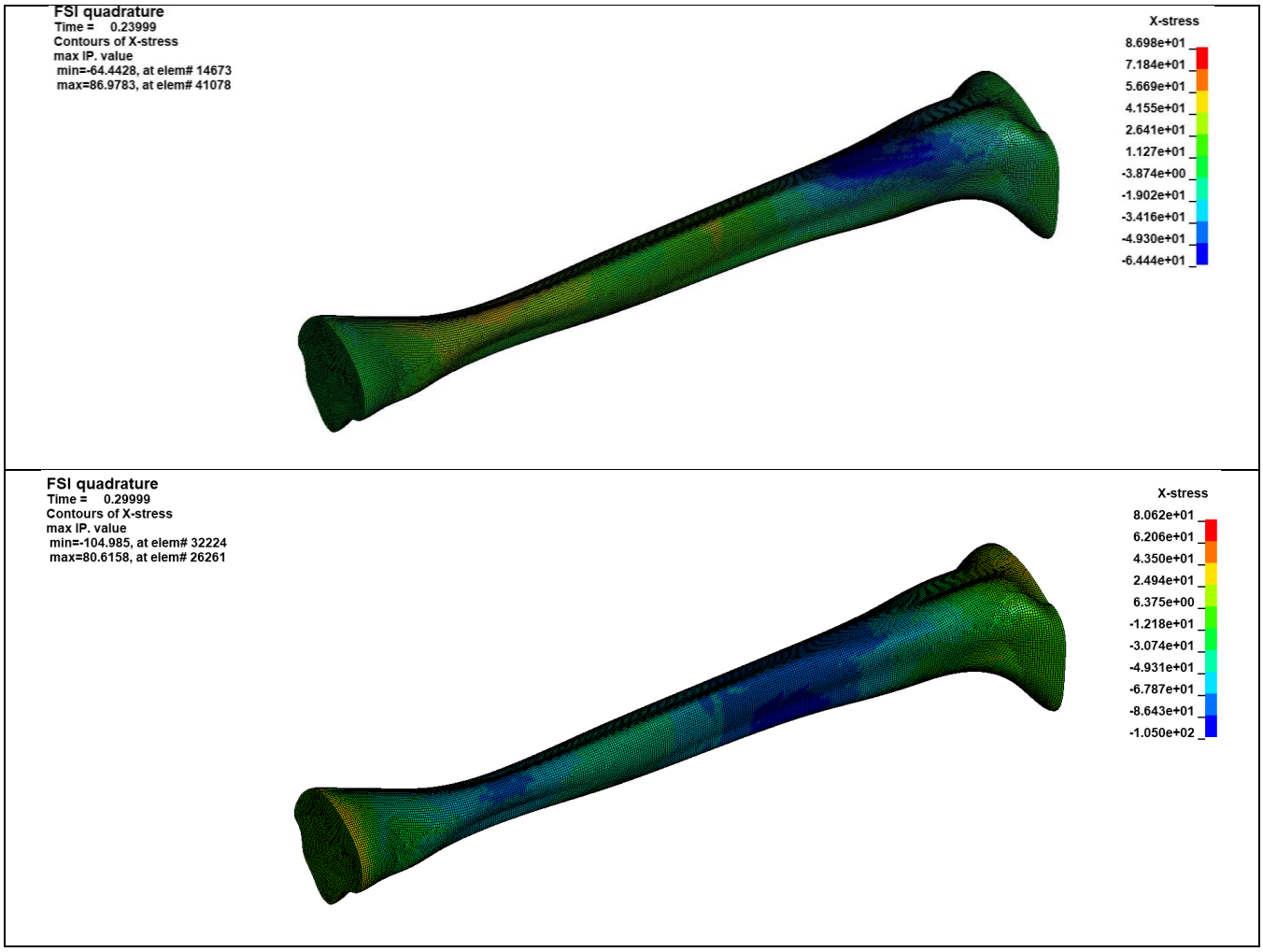

Figure 73 : The axial stress distribution of woman Tibia under non-Deformable plate detonations

7.3.2 Stress Wave Propagation

The direct stress history plots were plotted for each tibial model with deformable and non-deformable plate detonation from point A, B and C, as shown in Figure 74. Points A, B, and C were located at approximate distances of one-quarter, one-half, and three-quarters of the length, respectively, from the surface in contact with the witness plate. The mean diameters of the man and woman tibiae at each point (A, B and C) were presented in Table 18.

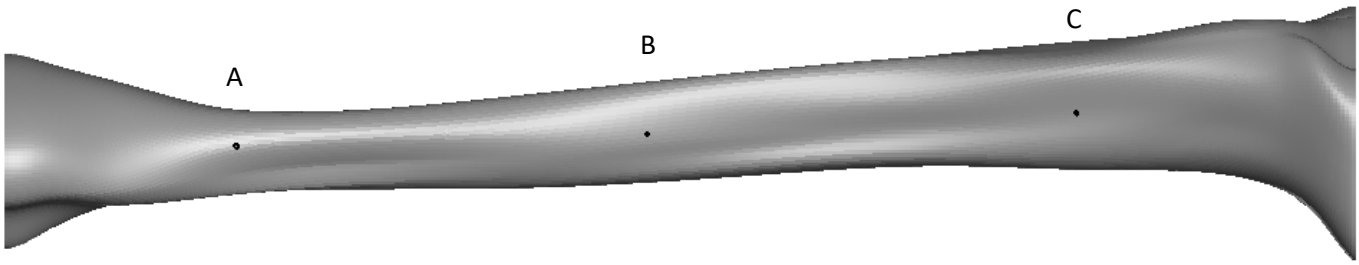

Figure 74 : Schematic diagram showing Points A, B and C used as strain gauge points.

Table 18 : The average dimeters of points A, B and C across the length of the tibiae structures

Tibia	**Average Diameter (mm)**		
	A	**B**	**C**
Men	21.7	28.8	33.1
Women	19.2	26.0	33.8

The results showed the different stress distribution across the entire tibia model. It was evident that the cross-sectional shape of the tibia models affected the stress wave propagations as the cross-sectional area varied from point A to C. The distribution of stress in the tibia structure was shown by the variations of stress response obtained at each point due to variations in the cross-sectional area. All the plots showed that high stress magnitudes are observed at point A as compared to point B and C for all the tests conducted. Point A has the smallest cross-sectional area compared to other parts therefore it has less resistance to deformation and plastic yielding, hence yields the maximum magnitude of stress induced by the blast load.

In the stress history plots of the blast simulations conducted, it was observed that both man and woman experienced higher tensile stress than compressive stress in tibial non-deformable plate detonations. This was because the non-deformable witness plate resisted deformation as it remained in contact with the tibia. Consequently, the reflected in the witness plate were continuously transmitted to the tibia structure, with a relatively minor decrease in magnitude. Hence, the transmitted stress waves superimposed with the reflected waves in the tibia structure leading to higher tensile stress than the initial compressive stress observed. Conversely, deformable plate detonations induced higher compressive stress than tensile stress, linked to the deformation of the witness plate transmitting reflected stress waves of lower magnitude. Hence, the interaction of the transmitted stress waves with the reflected stress waves in tibia structure resulted in lower tensile stress than the initial compressive stress.

The magnitude of the positive stress and time of arrival of the blast stress wave observed from point A on both man and woman tibia blast simulations were presented in Table 19. Blast testing of both tibia models indicated that the stress induced in deformable plate detonations is much higher than the stress induced in non-deformable plate detonations, as observed in the blast experiments on the tubular structures. The observed stress magnitudes in the tibia of a woman were greater than that in the tibia of a man, indicating that the stress experienced by the model was influenced by the variation in geometry and dimensions. The difference in stress levels could be attributed to the aspect ratio, as both the man and woman tibia had the same length but different diameters along the axis. The tibia of a woman had overall smaller diameter compared to the tibia of a man which led to the noted variation in stress levels. The smaller diameter of the tibia of a woman resulted in a reduced resistance to deformation, allowing for higher stress levels to be experienced in response to the same applied load.

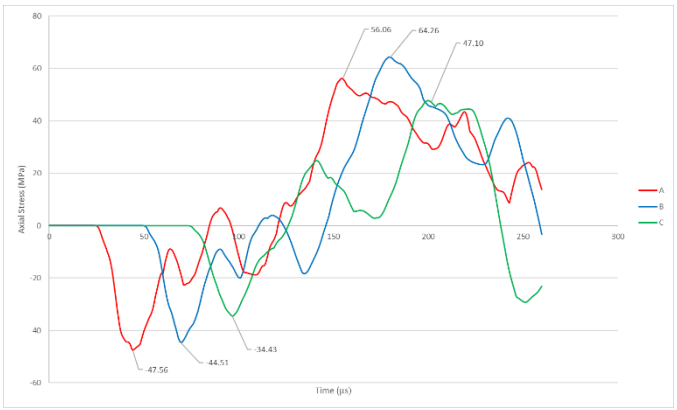

Figure 75 : The graph of stress history plots obtained from points A, B and C for man Tibia Non-Deformable Plate Detonations

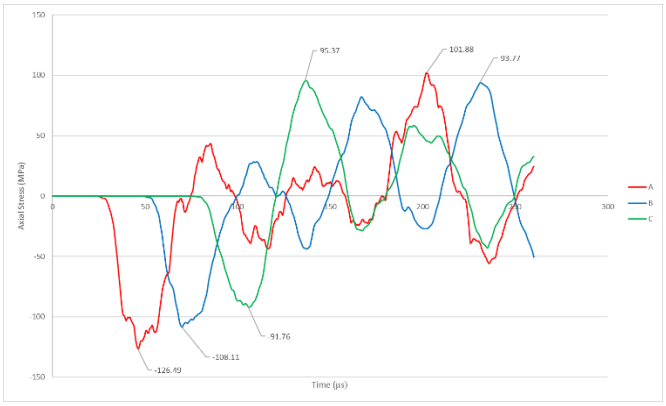

Figure 76 : The graph of stress history plots obtained from points A, B and C for man Tibia Deformable Plate Detonations

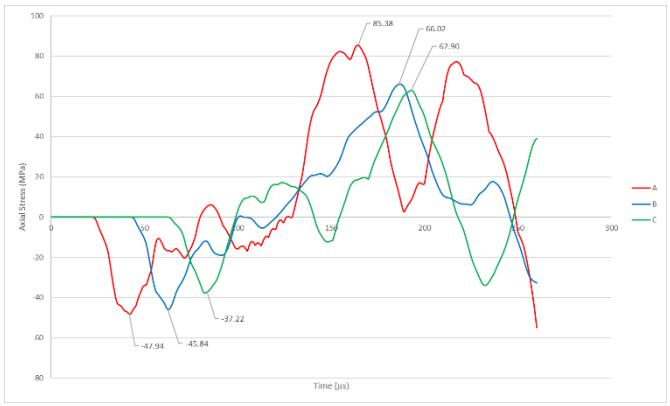

Figure 77 : The graph of stress history plots obtained from points A, B and C for woman Tibia Non-Deformable Plate Detonations

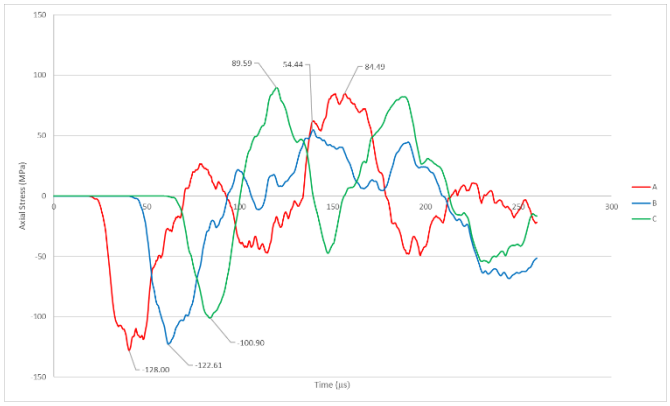

Figure 78 : The graph of stress history plots obtained from points A, B and C for woman Tibia Deformable Plate Detonations

Table 19 : The results on the maximum compressive and tensile stress response of tibia models and the time of arrival of blast stress wave

Tibia Model	Non-Deformable Plate Detonations			Deformable Plate Detonations		
	Compressive Stress $(\boldsymbol{MPa})$	Tensile Stress $(\boldsymbol{MPa})$	Time of Arrival (μs)	Compressive Stress $(\boldsymbol{MPa})$	Tensile Stress $(\boldsymbol{MPa})$	Time of Arrival (μs)
Man	47.6	56.1	27.0	126.5	101.9	26.0
Woman	47.9	85.4	23.0	128.0	84.5	21.0

The time of arrival of the blast wave to the strain gauge point was 27 μs for non-deformable plate blast test and 26 μs deformable plate blast test for the man tibia model. The time of arrival of the blast wave was 23 μs for non-deformable plate detonations and 21μs for deformable plate detonations on the woman tibia model.

CHAPTER 8 – DISCUSSIONS

Effect of Witness Plate on the Stress Wave Propagation

The stress-time response from non-deformable and deformable plate detonations for man and woman tibia were plotted on the same graph to analyse the effect of witness plate yielding on the stress wave propagations through the tibia model. Figure 79 and Figure 76 shows the stress history plots for man and woman non-deformable and deformable plate detonations respectively. The period of positive stress was almost the same for both deformable and non-deformable plate detonations for each tibia model stress response. The period observed on the negative stress wave showed a significate difference between the deformable and non-deformable plate detonations for each tibial test.

The expected axial stress-time responses obtained from both experimental and numerical model, the tibia/tubular structure experienced higher stress magnitudes for deformable plate than non-deformable plate detonations. This may be attributed to the bending and deformation of the deformable plate and the budging of the tubular structures resulting in stress concentrations at the interface between the plate and the tibia with high deflection or bending moments. The bending of the plate causes some regions to experience higher axial stresses than others. The tibia structure in contact with the deformable plate experienced higher axial stresses due to redistribution of the absorbed and the transmitted forces from the witness plate. Unlike non-deformable plate which does not undergo significant deformation. As a result, the stress distribution is relatively uniform across the surface of the plate thus transmitting stresses to the coincident tibia/tubular structure in a more direct and evenly distributed behaviour. Consequently, the axial stresses in the tibia structure adjacent to the non-deformable plate were less severe compared to those near the deformable plate.

As observed from the stress-time plots in Figure 79 and Figure 80 non-deformable plate generated a stress wave with a shorter period than that generated by deformable plate detonations. In the case of a non-deformable plate, the inertia of the plate resists the impulse generated by the blast wave causing instantaneous transmission of the load to the adjacent tibia/tubular structure hence generate a faster and shorter-duration stress wave compared to deformable plate. For deformable plate, the plate undergoes deflection and deformation, before transmitting the load to adjacent tibia/tubular structures.

The duration of the stress wave determines a duration of interaction of the stress wave with the structure which may cause more damage to the component, as it applies a sustained force for a longer period. In this study the deformable plate detonation caused a high magnitude of blast induced stress but for shorter period whereas the non-deformable plate detonations had low magnitude of stress for longer periods. This indicated that both the surrogate tibia models in each case would suffer different forms of injury. The non-deformable plate displayed more pronounced stress perturbations compared to the deformable plate due to elastic stress wave interactions that may be attributed to the resistance to deformation of the witness plate and particle vibrations. The deformable plate, on the other hand, undergoes rapid deformation and plastic flow, resulting in less prominent stress perturbations.

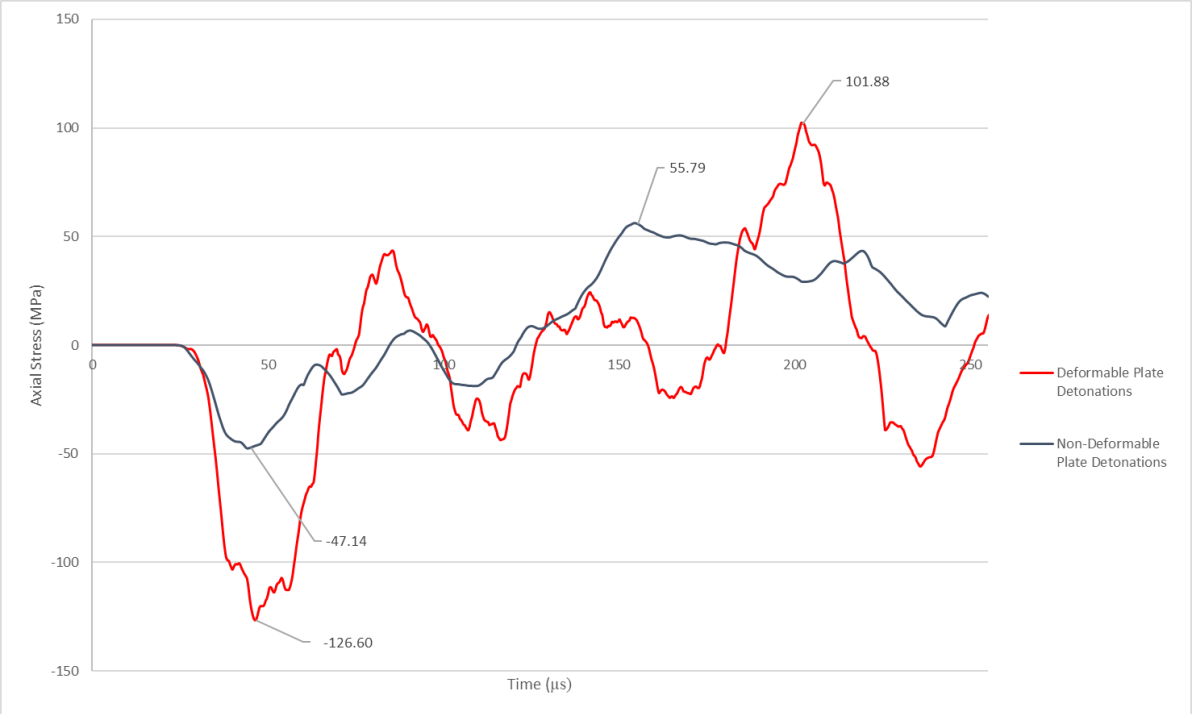

Figure 79 : The graph showing the stress history of man tibia under non-deformable and deformable plate blast tests.

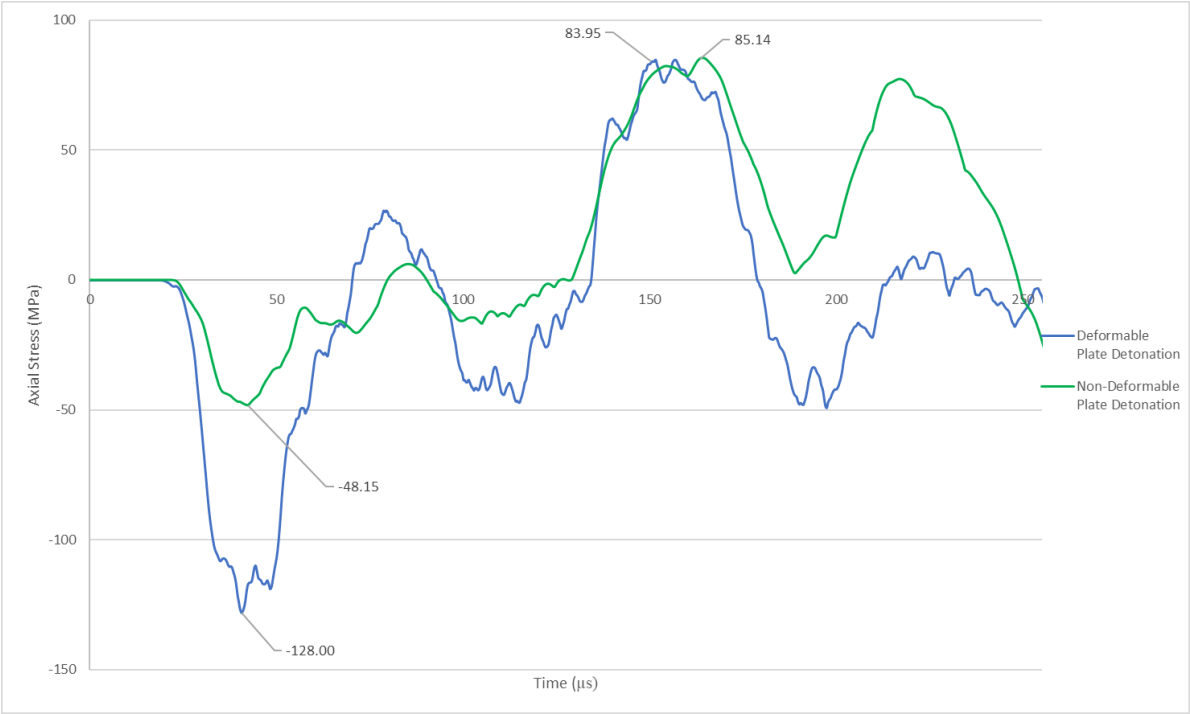

Figure 80 : The graph showing the stress history of woman tibia under non-deformable and deformable plate blast tests.

Effect of Geometry on the Stress Wave Propagation

The stress-time response obtained from the numerical modelling of deformable and non-deformable plate detonations on tubular structures and tibia structures were plotted on the same axis as shown in Figure 81 and Figure 82. The stress response obtained from tibial specimens of different cross sections were compared to conclude on the effect of cross section to blast loading. The variations of stress-time response observed on each structure showed that the blast wave propagated differently within each specimen. The different cross-sections offer various resistance to deformation and plastic yielding, which affects the stress distribution and magnitudes. As a result, the arrival time and intensity of the wave was affected, and the blast wave reflections and amplifications may have occurred in certain directions on the cross-section.

The cross-sectional shape and size of each structure determined how the blast energy was distributed and dissipated. Tibia structures with more material absorb and dissipate more blast energy, resulting in a lower peak stress compared to a tubular structure with less material [75]. Tibia specimens with irregular or complex cross-sectional shapes experience local areas of stress concentration or deformation, leading to failure in those regions.

From the stress history plots in Figure 81 and Figure 82, all the other specimens seem to follow almost a similar trend except for straight tube. Straight tube had a constant cross section across the axis of the tubular structure unlike other specimens. Therefore, the choice of cross-sectional shape and size affects the accuracy and reliability of the results obtained from the surrogate tibia model under blast loading. A straight tube is not a good tubular structure to use for investigating the response of tibia under blast loading since it showed much deviation in the stress-time trend compared to other tubular structures.

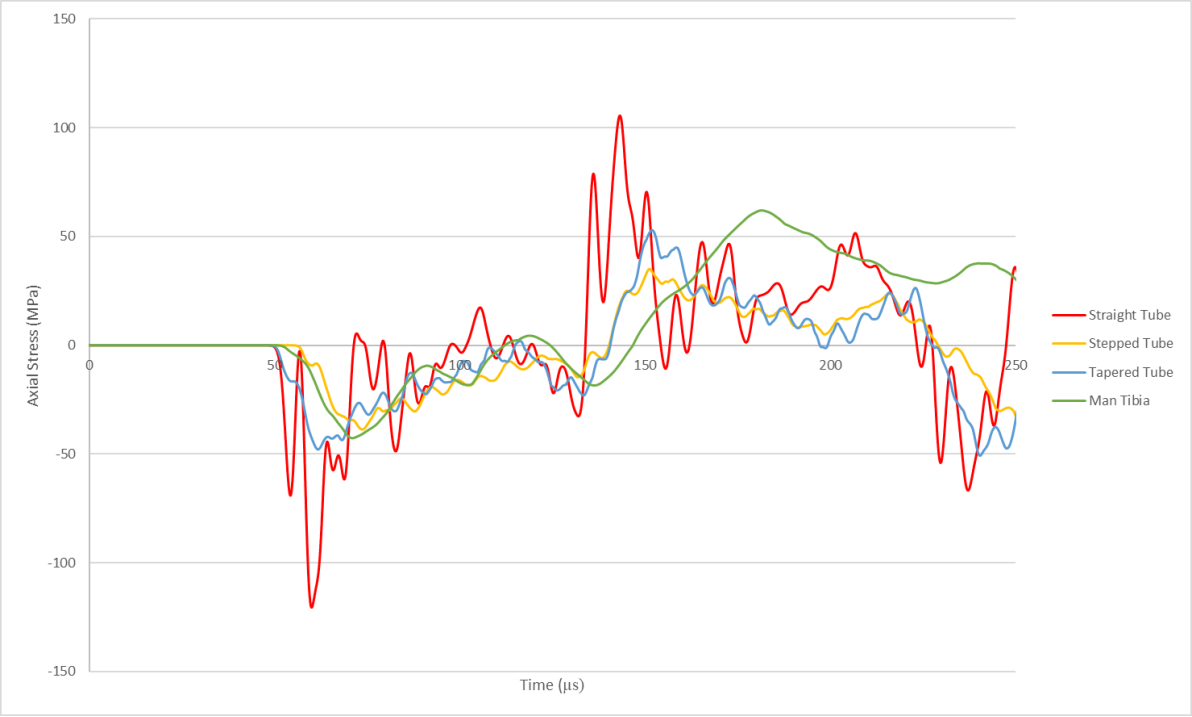

Figure 81 : The graph showing the comparison of stress response obtained from Non-Deformable Plate Detonations

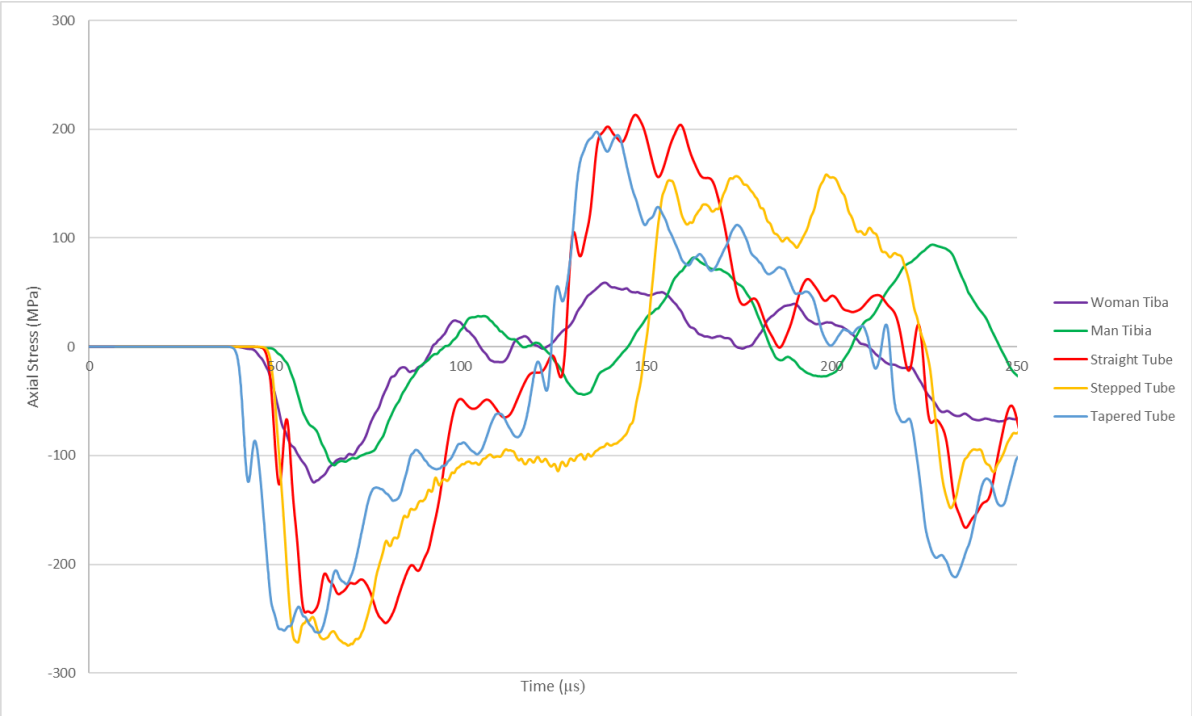

Figure 82 : The graph showing the comparison of stress response obtained from each tubular structure under Deformable Plate Detonation

Injury Pattern Prediction

The numerical model successfully gave valuable insights into the stress wave propagations and magnitude that could be used to approximate damage on a tibia model based on the stress experienced and the injuries associated with anti-vehicle landmines. The differences in material properties between the aluminium tibia structure and bone tibia were assessed to predict the failure mechanism and patterns of the tibia models. The failure criteria of the tibia models were considered for the blast load generated by detonating a 3.5 g of cylindrical PE4 charge at 13 mm stand-off distance. The differences in material properties between the two materials affects the blast loading and the resulting deformation and stress in the specimen, therefore, it was important to consider these differences in material properties when interpreting the results [76]. These properties include density, elastic modulus, yield strength, fracture toughness, and strain rate sensitivity. The average material properties of aluminium and human femoral cortical bone used to assess the expected failure criteria were presented in Table 20.

Table 20 : The average material properties of Aluminium and Bone material [60][77]

Material Property	**Density** $(\frac{kg}{m^3})$	**Elastic modulus** (MPa)	**Tensile yield strength** (MPa)	**Compressive yield strength** (MPa)	**Fracture toughness (tensile loading)** $(MPaM^{\frac{1}{2}})$
Aluminium	2700	68.9	276	386.0	29
Bone	1850-2000	17.9	71.6	115.1	2 - 6

Both male and female tibial non-deformable plate detonations produced higher tensile stress than compressive stress. As a result, failure of the tibia model was likely to occur due to tensile load at the selected points. Conversely, the tibia model was more likely to fail due to compressive load since the compressive stress yield was greater than the tensile stress yield for deformable plate detonations. However, the magnitudes of the peak stress for both compressive and tensile load was compared to predict the failure criteria. The results of peak stresses obtained from the man and woman tibia under non-deformable and deformable plate detonations and the predicted injury pattern was presented in Table 22.

Table 21 : The maximum stress results and prediction of the injury mechanism and injury pattern associated with each blast test [78]

Tibia Model	**Test**	**Compressive Stress** $(\boldsymbol{MPa})$	**Tensile Stress** $(\boldsymbol{MPa})$	**Time of Arrival** (μs)	**Injury Mechanism**	**Injury Pattern**
Man	Non-Deformable Plate	47.6	56.1	27.0	None	None
Man	Deformable Plate	126.5	101.9	26.0	Compressive and tensile load	fractures or cracks and avulsion fractures
Woman	Non-Deformable Plate	47.9	85.4	23.0	Tensile load	avulsion fractures
Woman	Deformable Plate	128.0	84.5	21.0	Compressive load	fractures or cracks

From deformable plate detonation tests on a man tibia, compressive and tensile stress magnitudes of 126.5 MPa and 101.9 MPa, respectively. Meanwhile, under non-deformable detonations, 56.1 MPa of tensile stress and 47.6 MPa of compressive stress. Notably, both the peak compressive and tensile stress values exceeded the yield strength of bone, suggesting that using bone material in deformable plate detonations would result in plastic yielding. However, non-deformable plate detonations posed no risk of failure, as the stress values were below the tensile and compressive strengths of both bone and aluminium.

For woman tibia, the peak stress magnitudes were 128.0 MPa in compression and 84.5 MPa in tension under deformable plate detonations. In non-deformable detonations, stress of 85.4 MPa in tension and 47.6 MPa in compression were recorded. The compressive stress exceeded the strength of the bone, implying potential plastic yielding due to compressive loading with bone material in deformable plate detonations. Similarly, the tensile stress surpassed the tensile strength of the bone, suggesting plastic yielding under non-deformable plate detonations. In contrast, aluminium in deformable plate detonation simulations showed no signs of failure, as the stress remained within its strength properties.

As observed in both experimental and numerical modelling of the blast test, both compressive and tensile stresses occur simultaneously as the stress propagates through the tibia, as observed in the stress response data. This combination can result in a variety of fractures and avulsion injuries [78]. Compressive stress may lead to fractures or cracks when the bone is compressed or crushed, potentially causing the tibia to break into multiple pieces. Tensile stress, on the other hand, may cause avulsion fractures, where a piece of bone is forcibly pulled away from the rest. However, these external manifestations way not observed in the tests as there were no muscles included

in the numerical model. The results in Table 21 detail the expected injury mechanisms and patterns for tibia models that may be observed in the event of a full lower limb being subjected to blast loading.

Injury severity, as per AIS 2005 guidelines, predicted the severity of the injuries predicted. Compressive fractures were classified as AIS 2 minor injuries, while tensile avulsion fractures are considered AIS 3 serious injuries. A combination of fracture patterns could have resulted in an AIS 4 severe injury [79]. The period which the plate remained in contact with the tibia resulted in complex stress waves which have may lead to multiple fractures or mixed injury types. The timing of blast-induced stress waves plays a pivotal role in injury prediction as it influences the magnitude, duration, distribution, and nature of stress experienced by the tibia structure.

Effect of using Aluminium Material instead of Bone Material

It was important to note that relying solely on material yield strength may not have accurately predicted failure mechanisms and criteria for tibia models in blast loading scenarios as the anisotropic nature of bone could have introduced complexities in predicting stress propagation and injury outcomes when compared to isotropic aluminium [74]. The bone material may have had different stiffness or strength during axial loading whereas aluminium had uniform properties in all directions affecting the distribution of induced stress. The anisotropic nature of bone meant that the tibia may have been more prone to specific types of injuries in certain loading scenarios and aluminium may have been less accurate due to its isotropy. This was evident from the stress distribution where areas of high and low stress concentrations were spread around the surface of the tibia. Also, the bone may have exhibited plastic deformation or failure under stresses that aluminium, with its isotropic properties, would not have failed. Factors such as density, elastic modulus, and fracture toughness also played crucial roles in determining the stress response of the tibia.

Propagation of stress wave through the tibia caused the material to undergo deformation and stress owing to the compression of the material particles. Low density materials offered less resistance to deformation and were more easily compressed by the shock wave. From the material densities in Table 20, aluminium material used was denser than the human bone material. As a result, it was expected that aluminium resisted deformation as compared to human bone. Therefore, the stress magnitude yielded by using the aluminium tibial structure was less than that which would have been obtained from using bone tibia specimen. This may have resulted in different failure criteria and mechanism as compared to a human bone tibia.

Aluminium had a higher elastic modulus, as shown in Table 20, which made it stiffer and less susceptible to deformation under an equivalent load. When subjected to blast loading, an aluminium tibia structure was expected to undergo less deformation and absorb less energy than a bone specimen, as bone material was more pliable and likely to have deformed under stress. Consequently, the stress magnitude produced in the aluminium tibia structure may potentially have been greater than that which could have been observed in the bone tibia structure.

CHAPTER 9 – CONCLUSIONS

The stress waves propagation through a simplified tibia subjected to blast loading was successfully investigated using the experimental and numerical approach. An experiment was successfully developed to perform blast tests on tubular structures of various cross sections and results from the blast induced stress history validated the numerical model using LS-Dyna explicit dynamics software. The validated numerical model was updated by replacing the tubular structure with more complex and realistic tibia structures. Two tibia structures, short and long, represented a woman and man tibia were subjected to blast loading through deformable and non-deformable witness plate using the numerical model. A parametric study was successfully conducted to comprehend the effect of geometry, plate thickness on the stress wave propagations leading to injury pattern prediction. The stress-time plots were obtained and analysed based on each set test scenario. Based on the findings from the analysis and discussions of the stress-time responses obtained, the following conclusions were drawn:

Effect of Witness Plate on the Stress Wave Propagation

The tibia structures in contact with the deformable witness plate experienced higher axial stresses due to stress concentrations resulting from plate bending and deformation. Conversely, the non-deformable witness plate resisted deformation and transmitted stresses instantaneously to the adjacent tibia/tubular structure, which were of lesser magnitude. Furthermore, the stress-time plots revealed that the non-deformable witness plate generated a faster and shorter-duration stress wave compared to the deformable witness plate, as the deformation of the witness plate caused a delay in the transmission of the blast load. Hence, it is imperative to consider the characteristics of the witness plate in the analysis of blast-induced stress wave propagation, as they play a pivotal role in predicting injury patterns and assessing the structural response of complex structures under blast loading conditions.

Effect of Reflections on Stress Wave Propagation

As observed in both numerical and experimental blast tests, the witness plate and the tubular structure remained in contact with each other for a short period. As the stress waves propagated through each component it got reflected upon encountering boundaries leading to continuous transmission of stress waves between the witness plate and the tubular structure. The interaction of these reflected waves led to formation of secondary stress peak with higher magnitudes of stress when constructive or destructive interference. It is crucial to consider the contact period and potential secondary peaks when assessing the maximum blast induced stress as it leads to complex injuries.

Effect of Geometry on the Stress Wave Propagation

Variations in stress-time response was observed for each tibia structure which indicated that the blast wave propagated differently within each structure. The cross-sectional shape and size played a critical role in distributing and dissipating blast energy, resulting in varying peak stress magnitudes and stress distribution. The tibia structures, with irregular or complex cross-sectional shapes, exhibited localized stress concentration and deformation, which are susceptible to injury. The analysis showed that the choice of cross-sectional shape and size significantly influenced the accuracy and reliability of results obtained from tibia models under blast loading. The parametric study reviewed that a smaller diameter female tibia experienced higher stresses overall than a

male variant, indicating greater susceptibility to deformation and injury due to its lower resistance to equivalent blast impulses.

Injury Pattern Prediction

The numerical model proved to be effective in approximating damage on the tibia models based on stress wave propagations and magnitudes experienced during detonations through deformable and non-deformable witness plate. A critical consideration was made regarding the differences in material properties between the aluminium tibia structure and bone tibia on how they influence stress-time response in the blast loading in prediction of the injury pattern. Particularly the difference in density between aluminium and bone could have impacted the predicted injury patterns since the bone has lower fracture toughness may be more susceptible to crack propagation and failure, leading to higher stress magnitudes compared to aluminium. The analysis of injury patterns resulting from compressive and tensile stress revealed potential fractures, cracks, and avulsion fractures in the tibia structures subjected to detonations.

The time of arrival of the blast-induced stress wave was also identified as a critical factor in injury prediction since it influences the magnitude, duration, distribution, and nature of the stress experienced by the tibia structure. Non-deformable witness plate generated a faster and shorter-duration stress wave that may cause immediate fractures due to high impulsive loading whereas deformable witness plate results in more progressive damage since it generates slower and longer-duration stress waves. Also, complex injury patterns may be observed as the witness plate and the tibia structure remains in contact for a short period. As a result, multiple fractures or a combination of different injury patterns may be observed due to complex stress wave observed.

Limitations and Contributions of the Study

While this study offered important fundamental insights into tibia biomechanics under blast loading, there were some limitations largely stemming from solely relying on the tibia without incorporating other lower limb bones and soft tissue representations. The complex material properties of actual bone were simplified with the use of aluminium in the tibia models. Characteristics such as localized density, porosity and modulus variations were, therefore, not accounted for. The reliance on simulated blast scenarios under idealized conditions meant that real-world complexities were not fully captured by the numerical model. The injury predictions relied primarily on basic material yield strengths, without fully accounting for the anisotropic nature of bone versus the isotropy of aluminium. As a result, capturing the differences between the materials restricted the accuracy of the simulated tibia stress response.

The model only includes the tibia bone and does not account for energy absorption and wave propagation effects from surrounding soft tissue like muscles, skin, and fat. This may lead to higher predicted bone stresses than would occur affecting fracture patterns or damage that may be associated with. The isolated tibia segment may not accurately replicate the full stiffness and response compared to intact leg. An intact leg has multiple structures spanning the entire limb that contribute to overall stiffness, including muscles, tendons, ligaments, and bones. Additionally, weightbearing forces and active muscle contraction in a living person further increase whole leg stiffness compared to a cadaver. To assess injury response most accurately, the whole leg should be evaluated to account for all the factors contributing to its stiffness and biomechanical behaviour.

However, the core emphasis on comprehending the interactions and propagation effects of stress waves in the tibia provided significant fundamental contributions to the understanding of blast injury biomechanics. The combined experimental and computational approach enabled systematic quantification of factors influencing

stress distribution and potential injury mechanisms. Fundamental knowledge was gained through modelling tibia response and validating simulations via controlled blast experiments on tubular structures. This study offered an in-depth analysis of stress wave propagations in the tibia under blast loading, laying the groundwork for developing enhanced protective systems and treatments. While refinements in model biofidelity and validation are still needed, the platform established, and insights gained constitute important steps forward in comprehending the blast injury mechanisms in the vulnerable lower extremities.

CHAPTER 10 – RECOMMENDATIONS

Based on the findings and conclusions of the study on effect of stress wave propagation in a simplified tibia the following recommendations were made:

- Additional research to explore the effect on using bone as compared to aluminium material on the stress wave propagation through the tibia structure.
- Further refinement on the numerical models with more extensive experimental studies using real-world tibia specimens and surrogate materials to enhance the accuracy and reliability of the predictions.
- Investigation of how using different plate hull geometries affect the blast induced stress wave through the lower limb.
- Incorporate soft tissue effects to simulate a more realistic tibia response to blast loading.
- Investigate and analyse different blast mitigation techniques and materials that can be used to reduce the effects of blast loading on the tibia structures.

By implementing these recommendations, the study can contribute significantly to advancing the understanding of stress wave propagations, injury patterns, and blast mitigation strategies, ultimately enhancing the safety and well-being of individuals in blast-prone environments.

REFERENCES

[1] K. Anderson, “The Ottawa Convention banning landmines, the role of international non-governmental organizations and the idea of International Civil Society,” European Journal of International Law, vol. 11, no. 1, pp. 91–120, 2000. Doi: 10.1093/ejil/11.1.91

[2] United Nations Office for Disarmament Affairs (UNODA), “Anti-Personnel Landmines Convention,” Accessed on: Mar. 22, 2023. [Online]. Available: https://www.un.org/disarmament/anti-personnel-landmines-convention/

[3] NORTH ATLANTIC TREATY ORGANISATION RESEARCH AND TECHNOLOGY ORGANISATION, “Test Methodologies for Personal Protective Equipment Against Anti-Personnel Mine Blast (Méthodologies d’essais pour le matériel de protection personnel centre le souffle product par les mines antipersonnel) Final Report of the RTO Human Factors and Medicine Panel (HFM),” RTO-TR-HFM-090, 2004. [Online]. Available: https://apps.dtic.mil/sti/pdfs/ADA424297.pdf

[4] Canadian Centre for Mine Action Technologies, Accessed on: Oct. 24, 2023. [Online]. Available: https://commons.lib.jmu.edu/cisr-journal/vol7/iss1/35/

[5] R. M. Coupland and A. Korver, “Injuries from antipersonnel mines: the experience of the International Committee of the Red Cross,” BMJ, vol. 303, no. 6816, pp. 1509–1512, 1991.

[6] T. Melcer, V. F. Sechriest, J. Walker, and M. Galarneau, “A comparison of health outcomes for combat amputee and limb salvage patients injured in Iraq and Afghanistan wars,” Journal of Trauma and Acute Care Surgery, vol. 75, no. 2, 2013. doi:10.1097/ta.0b013e318299d95e

[7] “Explosive violence in July 2023 - Ukraine”, Accessed on: Oct. 24, 2023. [Online]. Available: https://reliefweb.int/report/ukraine/explosive-violence-july-2023

[8] Landmine and Cluster Munition Monitor, “Landmine Monitor 2020,” Nov. 2020. [Online]. Available: http://www.the-monitor.org/en-gb/reports/2020/landmine-monitor-2020.aspx

[9] B. J. Eastridge, J. Brian, Hardin, Mark, Cantrell, Joyce; Oetjen-Gerdes, Lynne, Zubko, Tamara,Mallak, Craig, Wade, E. Charles, Simmons, John, Mace, James, Mabry, Robert, Bolenbaucher, Rose, Blackbourne and H. Lorne, “Died of wounds on the battlefield: Causation and implications for improving combat casualty care,” Journal of Trauma: Injury, Infection & Critical Care, vol. 71, no. 1, 2011. doi:10.1097/ta.0b013e318221147b

[10] N. Jacobs, K. Rourke, J. Rutherford, A Hicks, S. R. C. Smith, P. Templeton, S.A. Adams, J. O. Jansen, “Lower limb injuries caused by improvised explosive devices: Proposed ‘bastion classification’ and prospective validation,” Injury, vol. 45, no. 9, pp. 1422–1428, 2014. Doi: 10.1016/j.injury.2012.05.001

[11] H. A. Pietsch, K. E. Bosch, D. R. Weyland, E. M. Spratley, K. A. Henderson, R. S. Salzar, T. A. Smith, B. M Sagara, C. K. Demetropoulos, C. J. Dooley, and A. C. Merkle, “Evaluation of WIAMAN technology demonstrator Biofidelity relative to sub-injurious PMHS response in simulated under-body blast events,” *SAE Technical Paper Series*, 2016. Doi:10.4271/2016-22-0009

[12] “Landmine Monitor 2021,” Monitor, Accessed: Oct. 17, 2022. [Online]. Available: http://www.the-monitor.org/en-gb/reports/2021/landmine-monitor-2021.aspx

[13] N. Shewchenko, E. Fournier, and C. Quenneville, “ATD Lower Leg Surrogate Selection and the Effects on the Evaluation of Blast Energy Attenuating Floor Mats.”

[14] A. Ramasamy, S. D. Masouros, N. Newell, A. M. Hill, W. G. Proud, K. A. Brown, A. M. J. Bull and J. C. Clasper, “In-vehicle extremity injuries from Improvised Explosive Devices: Current and future foci,” Philosophical Transactions of the Royal Society B: Biological Sciences, vol. 366, no. 1562, pp. 160–170, 2011. Doi:10.1098/rstb.2010.0219

[15] T. Enke and M. Crone, “THE UNITED NATIONS AND CONTRIBUTING ORGANIZATIONS SHALL NOT BE HELD RESPONSIBLE FOR DEATHS OR INJURIES TO PERSONNEL AND/OR DAMAGE TO PROPERTY THAT MAY RESULT FROM THE USE OF THIS HANDBOOK. A manual for people working in environments contaminated by landmines and other explosive hazards including improvised explosive devices. UNITED NATIONS LANDMINES, EXPLOSIVE REMNANTS of WAR and IMPROVISED EXPLOSIVE DEVICES SAFETY HANDBOOK 2,” 2015.

[16] J. Baldeschwieler and H. J. Hatch, Alternative Technologies to Replace Antipersonnel Landmines. Washington, DC, USA: National Academies Press, 2001. Doi: 10.17226/10071

[17] R. Keeley, “Understanding landmines and mine action,” Journal of Mine Action, vol. 7, no. 3, pp. 2–7, 2003.

[18] S. Chatterjee, U. Deb, S. Datta, C. Walther, and D. K. Gupta, “Common explosives (TNT, RDX, HMX) and their fate in the environment: Emphasizing bioremediation,” Chemosphere, vol. 184, pp. 438–451, 2017. Doi: 10.1016/j.chemosphere.2017.06.008

[19] J. Akhavan, *Chemistry of Explosives*. Cambridge: Royal Society of Chemistry, 2004.

[20] K. Trimble and J. Clasper, “Anti-Personnel Mine Injury: Mechanism and Medical Management,” Journal of the Royal Army Medical Corps, vol. 147, no. 1, pp. 07-12, 2001. Doi: 10.1136/jramc-147-01-07

[21] A. Smith, “Mines PMN,” Accessed on: Jul. 15, 2021. [Online]. Available: https://www.nolandmines.com/explosive_hazards/minesPMN.htm

[22] Landmine Alert, "Landmines," Accessed on: Oct. 24, 2023. [Online]. Available: https://landminealert.com/en/landmines/

[23] K. Trimble and J. Clasper, “Anti-Personnel Mine Injury: Mechanism and Medical Management,” Journal of the Royal Army Medical Corps, vol. 147, no. 1, pp. 07-12, 2001. Doi: 10.1136/jramc-147-01-07

[24] K. Bonsor, “How Landmines Work,” Accessed on: Jul. 15, 2021. [Online]. Available: https://science.howstuffworks.com/landmine.htm#pt2

[25] Imperial War Museums, “PMR 2A Anti-Personnel Fragmentation Stake Mine,” Accessed on: Jul. 15, 2021. [Online]. Available: https://www.iwm.org.uk/collections/item/object/30021731

[26] SJH Projects, “Landmines - All You Never Wanted to Know,” Accessed on: Jul. 15, 2021. [Online]. Available: https://www.sjhprojects.com/landmines-all-you-never-wanted-to-know

[27] D. R. Sory, H. D. Amin, D. J. Chapman, W. G. Proud, and S. M. Rankin, “Replicating landmine blast loading in cellular in vitro models,” *Physical Biology*, vol. 17, no. 5, p. 056001, 2020. doi:10.1088/1478-3975/ab7d1c

[28] SJH Projects, “Landmines - All You Never Wanted to Know,” Accessed on: Jul. 15, 2021. [Online]. Available: https://www.sjhprojects.com/landmines-all-you-never-wanted-to-know

[29] T. C. Dougherty, Weapons effects, and parachute injuries - emergency war surgery: The survivalist's medical desk reference, Accessed on: Jul. 15, 2021. [Online]. Available: https://doctorlib.info/surgery/emergency-war-surgery/1.html

[30] G. Grigoriadis, D. Carpanen, C. E. Webster, A. Ramasamy, N. Newell and S. D. Masouro, "Lower limb posture affects the mechanism of injury in under-body blast," Annals of Biomedical Engineering, vol. 47, no. 1, pp. 306–316, 2018. doi:10.1007/s10439-018-02138-4

[31] C. Bir, A. Barbir, F. Dosquet, M. Wilhelm, M. van der Horst and G. Wolfe, "Validation of lower limb surrogates as injury assessment tools in floor impacts due to anti-vehicular land mines," Military Medicine, vol. 173, no. 12, pp. 1180–1184, 2008. doi:10.7205/milmed.173.12.1180

[32] T. Pandelani, Z. Schutte and E. Wium, "Experimental and Numerical Validation of a Simplified Rigid Torso Surrogate used for Investigating the Fluid-Structure Interaction of Air Blast Waves," in 26th International Symposium on Ballistics, pp. 17–19, 2018.

[33] P. A. Shirbhate and M. D. Goel, "A Critical Review of Blast Wave Parameters and Approaches for Blast Load Mitigation," Archives of Computational Methods in Engineering, vol. 28, no. 3, pp. 1713–1730, 2021. Doi: 10.1007/s11831-020-09436-y

[34] P. F. Acosta, "Overview of UFC 3-340-02 structures to resist the effects of accidental explosions," Structures Congress 2011, 2011. doi:10.1061/41171(401)127

[35] V. Karlos, G. Solomos, and B. Viaccoz, "Calculation of blast loads for application to structural components.", Luxembourg: Publications Office of the European Union, 2013.

[36] Lecturio Medical, "Pelvis: Anatomy [+ labelled diagram]: Concise medical knowledge," Accessed on: Jul. 16, 2021. [Online]. Available: https://www.lecturio.com/magazine/lower-extremity-bones/

[37] These Bones of Mine, "Skeletal Series Part 10: The Human Leg," Accessed on: Jul. 19, 2021. [Online]. Available: https://thesebonesofmine.wordpress.com/category/femur/

[38] S. M. Tommasini, P. Nasser, M. B. Schaffler, and K. J. Jepsen, "Relationship between bone morphology and bone quality in male tibias: Implications for stress fracture risk," *Journal of Bone and Mineral Research*, vol. 20, no. 8, pp. 1372–1380, 2005. doi:10.1359/jbmr.050326

[39] A. Ramasamy, A. M. Hill, S. Masouros, I. Gibb, A. M. J. Bull and J. C. Clasper, "Blast-related fracture patterns: A forensic biomechanical approach," Journal of The Royal Society Interface, vol. 8, no. 58, pp. 689–698, 2010. Doi:10.1098/rsif.2010.0476

[40] R. M. Harris, M. S. Rountree, L. V. Griffin, R. A. Hayda, and T. Bice, "Final report of the Lower Extremity Assessment Program (LEAP 99-2)". volume 2, 2000. doi:10.21236/ada409059.

[41] "Test Methodology for Protection of Vehicle Occupants against Anti-Vehicular Landmine Effects (Méthodologie d'essais pour la protection des occupants de véhicules contre les effets des mines terrestres anti-véhicules) Final Report of HFM-090 Task Group 25. Distribution and Availability on Back Cover," 2007. [Online]. Available: https://apps.dtic.mil/sti/pdfs/ADA473218.pdf

[42] J.D. Reinecke, I.N. Snyman, R. Ahmed, F. J, Beetge, A safe and secure South Africa Vehicle landmine protection validation testing, CSIR Defence Peace Safety and Security, South Africa, November 2008.. [Online]. Available: http://playpen.meraka.csir.co.za/~acdc/education/CSIR%20conference%202008/Proceedings/CPO-0074.pdf

[43] J. D. Rupp, C. Miller, A. Bonifas, K. A. Ott, C. K. Demetropoulos, J. M. Gipple, D. Sherman, J. M. Cavanaugh, D. R. Barnes, and K. L. Loftis, "Warrior injury assessment manikin (WIAMan) generation 1 anthropomorphic test device (ATD) positioning in highly reclined and other alternative postures," DTIC, Accessed Oct. 25, 2023, [Online]. Available: https://apps.dtic.mil/sti/citations/AD1131250

[44] D. S. Cronin, K. Williams, C. R.D Bass, P Magnan, F. Dosquet, D.M. Bergeron and J.L.M.J van Bree, "Test Methods for Protective Footwear Against AP Mine Blast". [Online]. Available: https://www.researchgate.net/publication/228975300_Test_Methods_for_Protective_Footwear_Against_AP_Mine_Blast

[45] M. S. Rountree, "Final Report of the RTO Human Factors and Medicine Panel (HFM), Task Group TG-024: Test Methodologies for Personal Protective Equipment Against Anti-Personnel Mine Blast", RTO-TR-HFM-024, Mar. 2004.

[46] F. Wei, E. G. Meyer, J. E. Braman, J. W. Powell, and R. C. Haut, "Rotational stiffness of football shoes influences talus motion during external rotation of the foot," Journal of Biomechanical Engineering, vol. 134, no. 4, 2012. Doi: 10.1115/1.4005695

[47] R. E. Tannous, J. L. Serres, D. V. Jones, N. Dau, and C. A. Bir, "APPLICATION OF THE MIL-LX IN INVESTIGATING THE RISK OF LOWER LIMB INJURY FOR MILITARY PURPOSES," July 2011.

[48] D. M. Bergeron, G. G. Coley, M. S. Rountree, I. B. Anderson, and R. M. Harris, "Assessment of foot protection against anti-personnel landmine blast using a frangible surrogate leg," UXO Forum 2001, 9-12 April 2001 Page 1 of 8.

[49] D. Ungerer, "INVESTIGATING THE USE OF RUBBER TO ATTENUATE THE EFFECT OF BLAST LOAD APPLIED TO A SRROGATE LOWER LEG," MSc dissertation, University of Cape Town, South Africa, 2008.

[50] S. Ganpule, A. Alai, E. Plougonven, and N. Chandra, "Mechanics of blast loading on the head models in the study of traumatic brain injury using experimental and computational approaches," Biomechanics and Modeling in Mechanobiology, vol. 12, no. 3, pp. 511–531, 2012. doi:10.1007/s10237-012-0421-8

[51] S. Datta, N. R. Guntur, B. S. T. Jolly, R. Arun, W. Anderton, C. J. C. Ramasamy, and B. A. M. Masouros, "A further insight into primary blast injury criteria," *Proc Inst Mech Eng H*, vol. [Volume Number], no. [Issue Number], pp. 365–383, 2008.

[52] I. Emma, H. Nancy, B. A. Moothedath, and C. J. C. Gibb, "The influence of military boots on load attenuation in an experimental model of under-vehicle blast injury," *vol. 168*, no. 1, pp. 64-68, 2022.

[53] D. S. Cronin, "Numerical Modelling of a Simplified Human Leg to Characterize Landmine Threats," MSc dissertation, University of Maryland, College Park, 2009.

[54] B. Singh and M. A. Basri, "Numerical Simulation of Anti-personnel landmine explosions on human lower extremity: Injury assessment and mitigation strategies," SSRN Electronic Journal, 2022. Accessed Oct. 25, 2023, [Online]. Available: https://ssrn.com/abstract=4057664

[55] C. K. Demetropoulos, K. A. Ott, D. G. Drewry III, M. Montoya, J. M. Cavanaugh, J. J. Rupp, D. R. Barnes, and K. L. Loftis “Whole-Body Postmortem Human Subject (PMHS) Injury Outcome Technical Report,” JHU-APL, 2020.

[56] B. Scannell and S. L. Frick, “1 - Skeletal Growth, Development, and Healing as Related to Pediatric Trauma,” in Pediatric Orthopedic Trauma, S. L. Frick, Ed. Elsevier, 2020, pp. 1-26. Doi: 10.1016/B978-0-323-61336-1.00001-7

[57] Tornado Studio, “Real Human Tibia Bone 01 3D Model,” Accessed on: Oct. 24, 2023. [Online]. Available: https://www.tornado-studios.com/stock-3d-models/3d-human-tibia-bone-01-model

[58] P. Church, R. Cornish, I. Cullis, P. Gould, and I. Lewtas, “Using the split Hopkinson pressure bar to validate material models,” Philosophical Transactions of the Royal Society A: Mathematical, Physical and Engineering Sciences, vol. 372, no. 2023, 2014, Art. no. 20130191. Doi: 10.1098/rsta.2013.0191

[59] TML, “Strain Gauges,” Accessed on: Oct. 24, 2023. [Online]. Available: https://www.tml.jp/e/product/strain_gauges/pdf/Catalog_Gages.pdf

[60] S. Akram, S. H. I. Jaffery, M. Khan, M. Fahad, A. Mubashar, and L. Ali, “Numerical and experimental investigation of Johnson–Cook material models for aluminum (AL 6061-t6) alloy using orthogonal machining approach,” Advances in Mechanical Engineering, vol. 10, no. 9, pp. 1-14, 2018. Doi: 10.1177/1687814018797794

[61] T. J. Cloete and G. N. Nurick, “Blast characterization using a ballistic pendulum with a centrally mounted Hopkinson bar,” International Journal of Protective Structures, vol. 7, no. 3, pp. 367-388, 2016. Doi: 10.1177/2041419616663535

[62] N. Jacob, G. N. Nurick, and G. S. Langdon, "The effect of stand-off distance on the failure of fully clamped circular mild steel plates subjected to blast loads," Engineering Structures, vol. 29, no. 10, pp. 2723-2736, October 2007. Doi: 10.1016/j.engstruct.2007.01.021

[63] T. Svensson and F. Tell, "Stress Wave Propagation Between Different Materials," Master's thesis, Chalmers University of Technology, Göteborg, Sweden, 2020.

[64] V. Karlos, G. Solomos, and M. Larcher, "Analysis of the blast wave decay coefficient using the Kingery–Bulmash data," International Journal of Protective Structures, vol. 7, no. 3, pp. 409-429, September 2016. Doi: 10.1177/2041419616659572

[65] Z. Liang Wang, Y. Chi Li, and J. G. Wang, "Numerical analysis of blast-induced wave propagation and spalling damage in a rock plate," International Journal of Rock Mechanics and Mining Sciences, vol. 45, no. 4, pp. 600-608, 2008. Doi: 10.1016/j.ijrmms.2007.08.002

[66] S. E. Rigby and P. W. Sielicki, "An Investigation of TNT Equivalence of Hemispherical PE4 Charges," Defence Science and Technology Organisation, Edinburgh, Australia, Report DSTO-TR-2888, 2014.

[67] C. Bisyk, I. Chepkov, M. Vaskivsky, L. Davidovsky, O. Slyvinsky and O. Aristarkhov “Methods for modelling air blast on structures in LS-Dyna. comparison and analysis,” Weapons and Military Equipment, vol. 21, no. 1, pp. 22–31, 2019. doi:10.34169/2414-0651.2019.1(21).22-31

[68] K. Vedantam, D. Bajaj, N. S. Brar, and S. Hill, “Johnson-Cook strength models for mild and DP 590 steels,” AIP Conference Proceedings, vol. 845, no. 1, pp. 775-778, 2006. Doi: 10.1063/1.2263437

[69] "LS-DYNA User's Manual," Livermore Software Technology Corporation, Livermore, CA, USA, 1992. [Online]. Available: www.lstc.com

[70] "Friction Coefficients," The Engineering ToolBox. Accessed Jul. 18, 2023, [Online]. Available: https://www.engineeringtoolbox.com/friction-coefficients-d_778.html.

[71] S. E. Rigby, O.I. Akintaro, B. J Fuller, A. Tyas, R. Curry, G. Langdon, and D. J. Pope, "Predicting the response of plates subjected to near-field explosions using an energy equivalent impulse," International Journal of Impact Engineering, vol. 128, pp. 24–36, 2019. Doi: 10.1016/j.ijimpeng.2019.01.014

[72] M. Cremonesi, A. Franci, S. Idelsohn, and E. Oñate, "A State-of-the-Art Review of the Particle Finite Element Method (PFEM)," Archives of Computational Methods in Engineering, vol. 27, no. 5, pp. 1709–1735, November 2020. Doi: 10.1007/s11831-020-09468-4

[73] B. W. Sume, "Estimation of body height from percutaneous length of tibia in Debre Markos University students, Northwest Ethiopia," Egyptian Journal of Forensic Sciences, vol. 9, no. 1, p. 30, December 2019. Doi: 10.1186/s41935-019-0157-z

[74] S. K. Parashar and J. K. Sharma, "A review on application of finite element modelling in bone biomechanics," Perspectives in Science, vol. 8, pp. 696-698, September 2016. Doi: 10.1016/j.pisc.2016.06.062

[75] A. Gargano and A. P. Mouritz, "Comparative Study of the Explosive Blast Resistance of Metal and Composite Materials Used in Defence Platforms," Composites Part C: Open Access, vol. 10, p. 100345, March 2023. Doi: 10.1016/j.jcomc.2023.100345

[76] G. Lu and T. X. Yu, "Energy Absorption of Structures and Materials.", Boca Raton, FL, USA: CRC Press, 2003.

[77] E. F. Morgan, G. U. Unnikrisnan, and A. I. Hussein, "Bone Mechanical Properties in Healthy and Diseased States," Annual Review of Biomedical Engineering, vol. 20, no. 1, pp. 119-143, 2018. Doi: 10.1146/annurev-bioeng-062117-121139

[78] M. M. Harjai, D. C. Agarwal, P. Dave, S. S. Jog, and P. Arora, "Mine blast injuries - Our experience," Medical Journal Armed Forces India, vol. 61, no. 2, pp. 143-147, 2005. Doi: 10.1016/S0377-1237(05)80010-3

[79] "2015 DATA DICTIONARY M•TQIP," American College of Surgeons, Chicago, IL, USA, 2015.

APPENDIX A – BALLISTIC PENDULUMN PART DRAWINGS

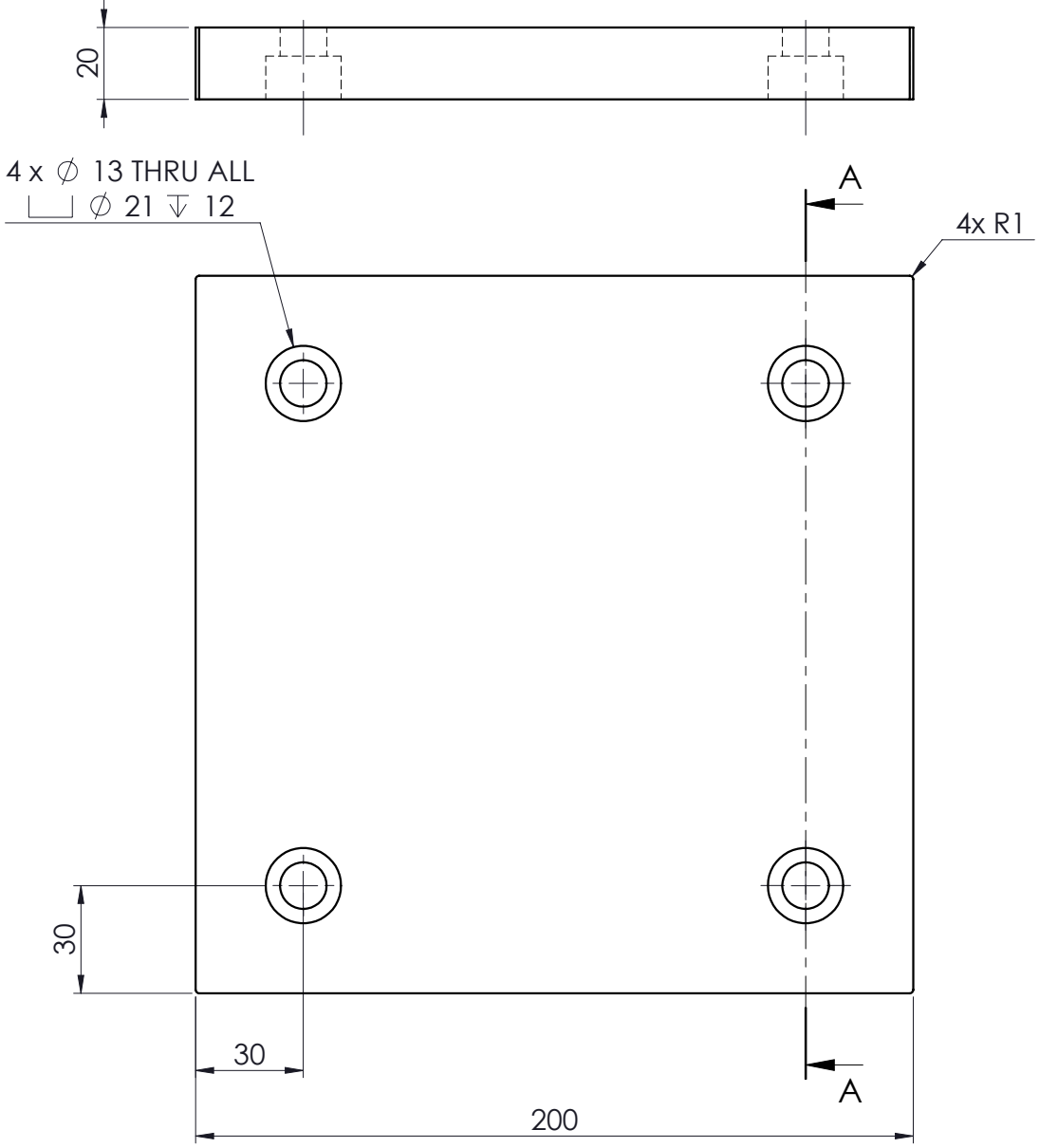

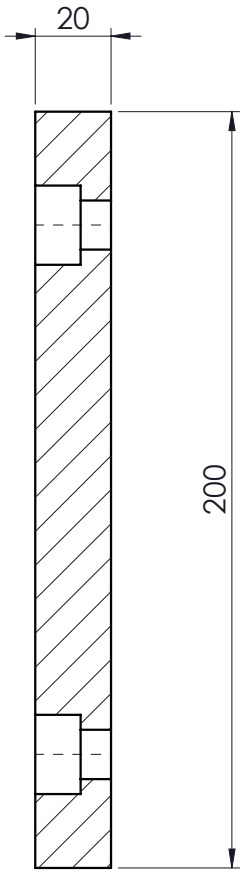

SECTION A-A

Scale: 1:2 on A4	University of Cape Town Department of Mechanical Engineering			
Drawn By: Davison .T Seenzayi	All un-toleranced dimensions to adhere to ISO 2768-m	Title: Non-Deformable Witness Plate		
Checked :	Assembly Drawing	Drawing Number : 1-1	Rev. : A	Sheet : 1 of 1

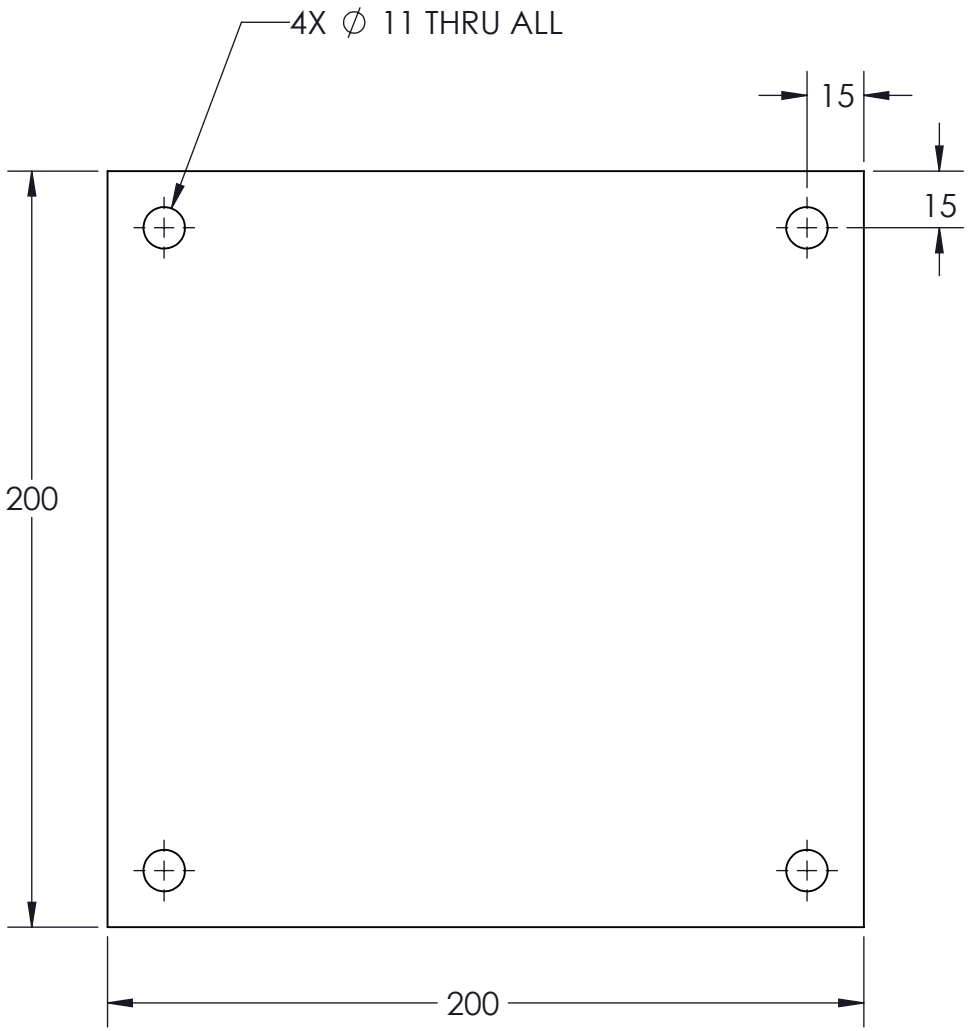

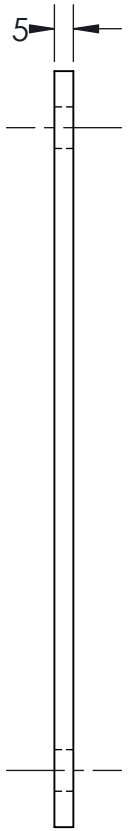

A4 Landscape	University of Cape Town Department of Mechanical Engineering				
	Title: Deformable Witness Plate				
Quantity: 6	Part Finish	Date: 2023/07/21	Scale: 1:2	Sheet1	of 1
Material: Mild Steel	Drawn By: Davison Seenzayi			Drawing Number 1-B	

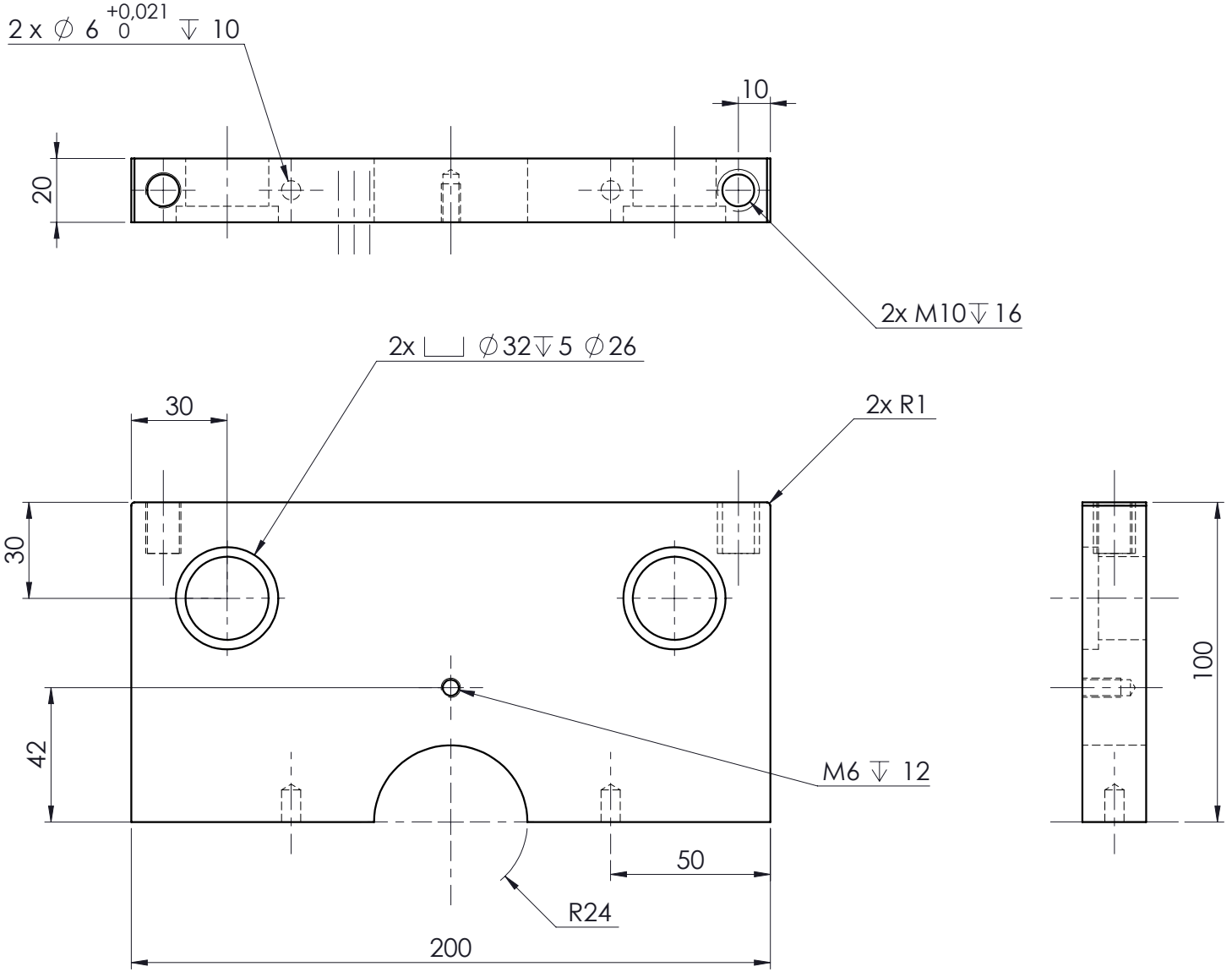

Note: QTY x 4

Scale: 1:2 on A4	University of Cape Town Department of Mechanical Engineering			
Drawn By: Davison .T Seenzayi	All un-toleranced dimensions to adhere to ISO 2768-m	Title: Front plate (A/B)		
Checked :	Material : AISI 1020	Drawing Number : 1-2	Rev. : A	Sheet : 1 of 1

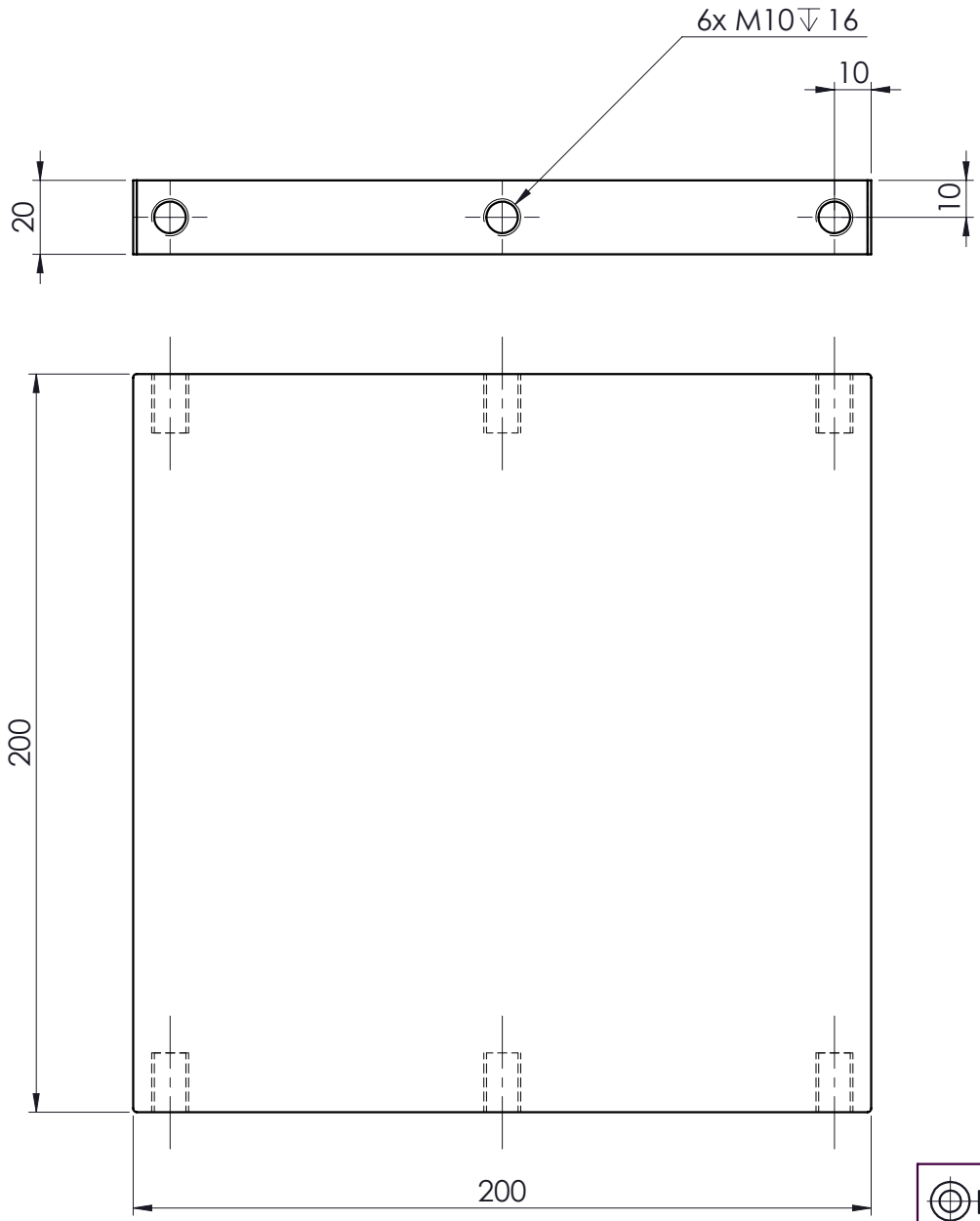

Scale: 1:2 on A4	University of Cape Town Department of Mechanical Engineering			
Drawn By: Davison T. Seenzayi	All un-toleranced dimensions to adhere to ISO 2768-m	Title: Back plate		
Checked :	Material : AISI 1020	Drawing Number : 1-3	Rev. : A	Sheet : 1 of 1

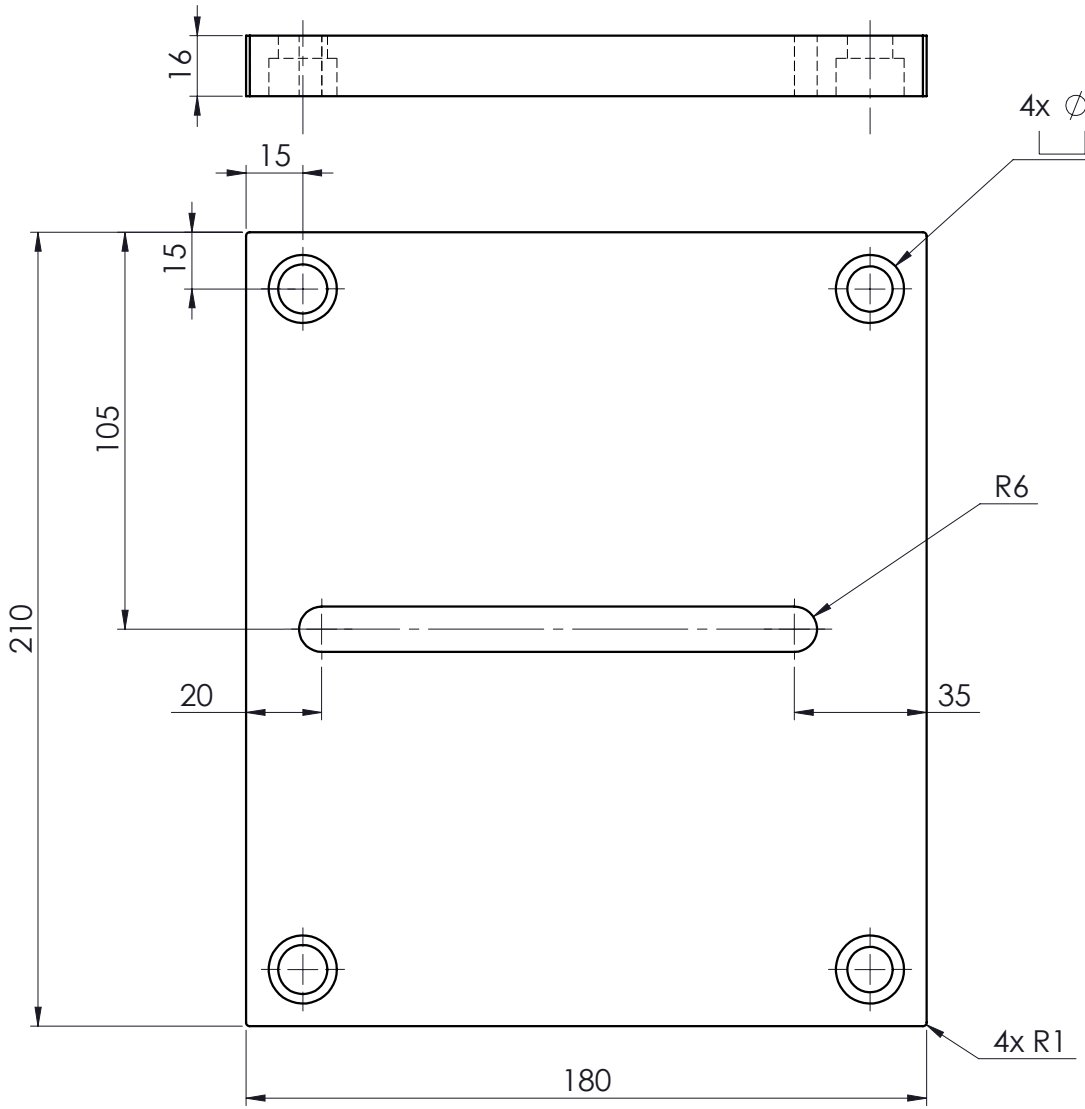

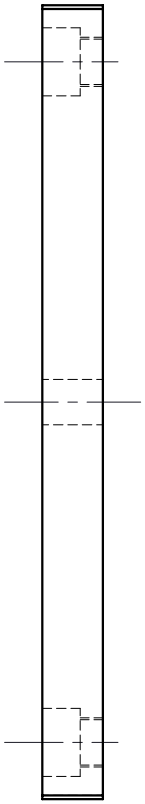

Scale: 1:2 on A4	University of Cape Town Department of Mechanical Engineering			
Drawn By: Davison T. Seenzayi	All un-toleranced dimensions to adhere to ISO 2768-m	Title: Top plate		
Checked :	Material : Steel	Drawing Number : 1-4	Rev. : A	Sheet : 1 of 1

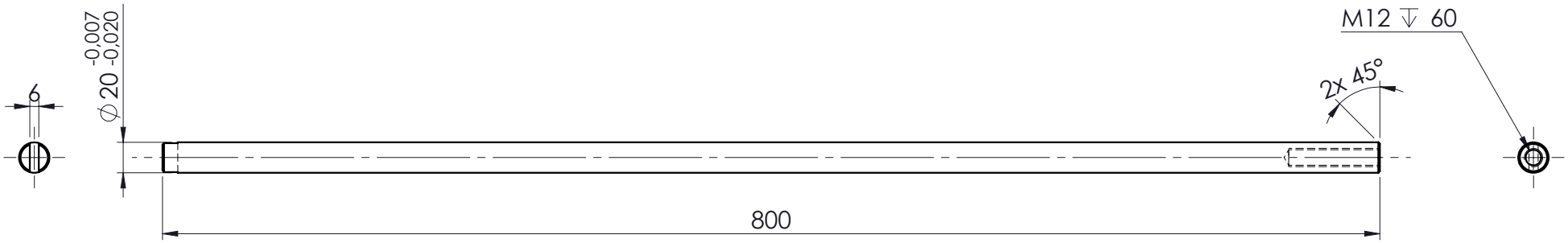

Note: Qty x 4

Scale: 1:10 on A4	University of Cape Town Department of Mechanical Engineering			
Drawn By: Davison. T Seenzayi	All un-toleranced dimensions to adhere to ISO 2768-m	Title: Steel rod		
Checked :	Material : AISI 1010 Steel, hot rolled bar	Drawing Number : 1-5	Rev. : A	Sheet : 1 of 1

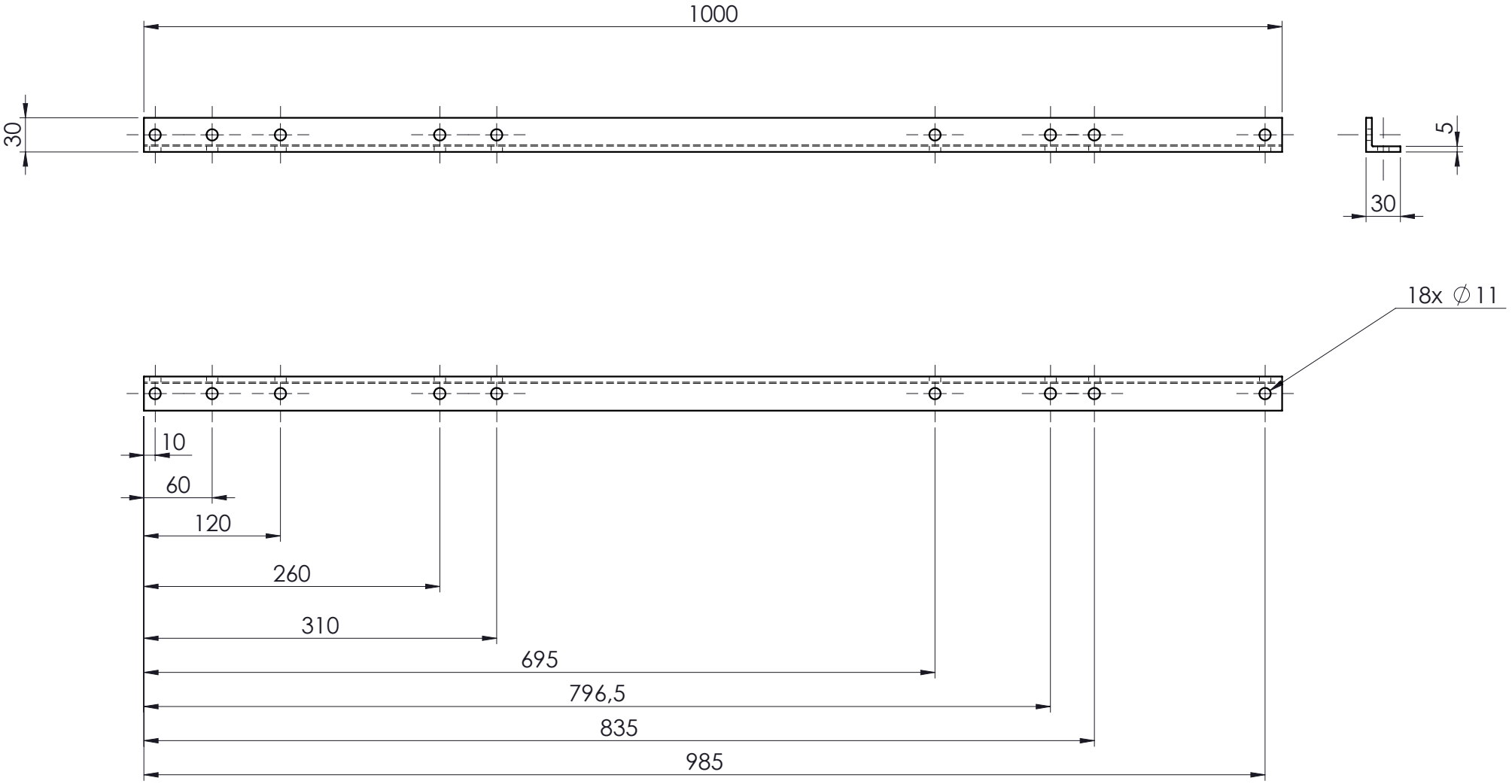

Note: Qty x 4

Scale: 1:10 on A4	University of Cape Town Department of Mechanical Engineering			
Drawn By: Davison. T Seenzayi	All un-toleranced dimensions to adhere to ISO 2768-m	Title: Angle bar		
Checked :	Material : Gray Cast Iron	Drawing Number : 1-6	Rev. : A	Sheet : 1 of 1

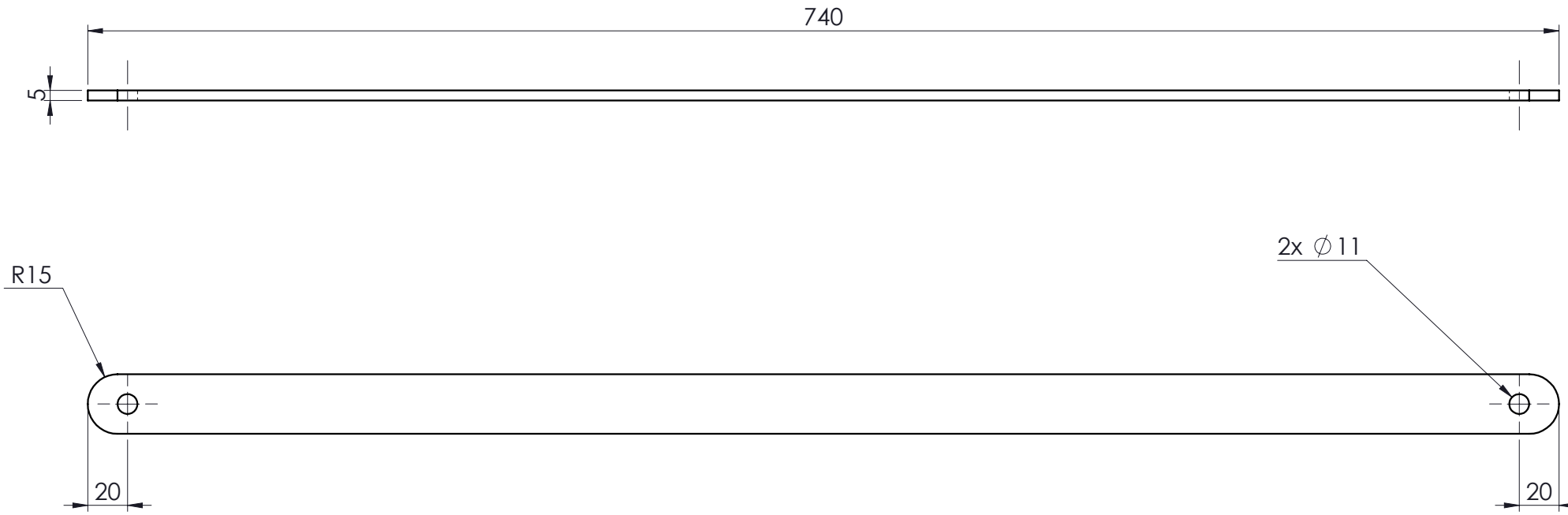

Note: Qty x4

Scale: 1:5 on A4	University of Cape Town Department of Mechanical Engineering			
Drawn By: Davison . T Seenzayi	All un-toleranced dimensions to adhere to ISO 2768-m	Title: Brace bar		
Checked :	Material : Gray Cast Iron	Drawing Number : 1-7	Rev. : A	Sheet : 1 of 1

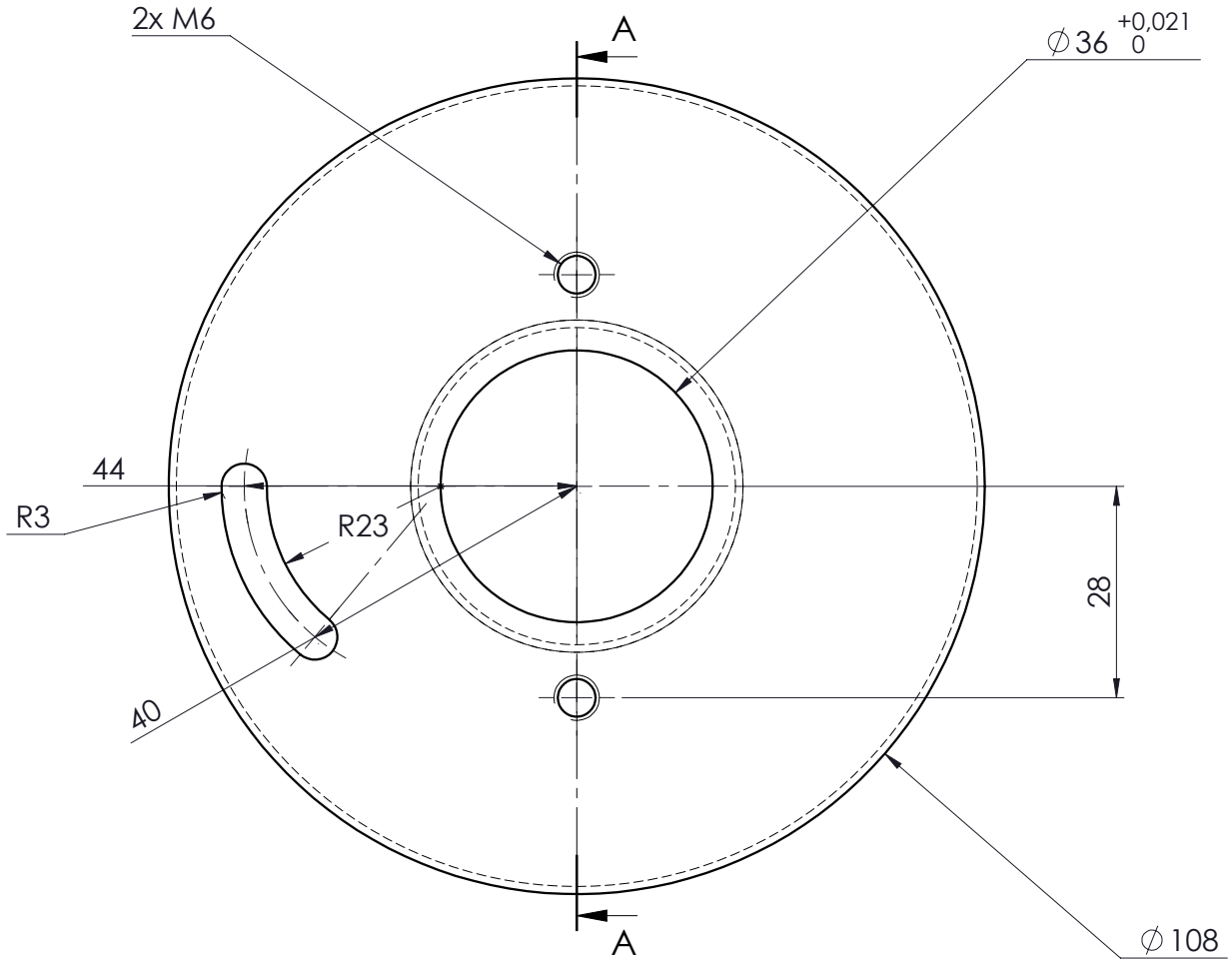

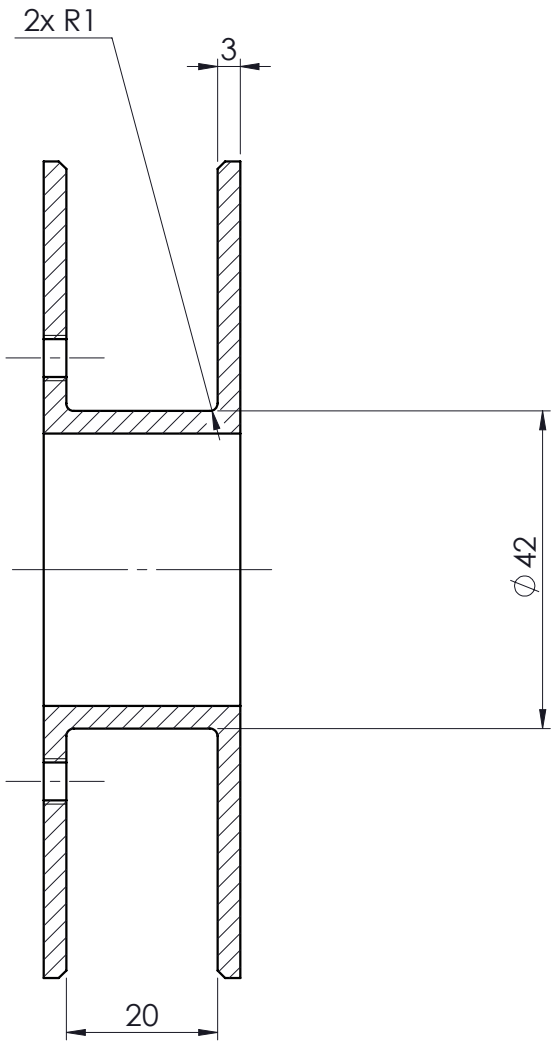

SECTION A-A
SCALE 1 : 1

Note: Qty x 2

Scale: 1:2 on A4	University of Cape Town Department of Mechanical Engineering			
Drawn By: Davison . T Seenzayi	All un-toleranced dimensions to adhere to ISO 2768-m	Title: Double flanged bushing		
Checked :	Material : Al 1060 Alloy	Drawing Number : 1-8	Rev. : A	Sheet : 1 of 1

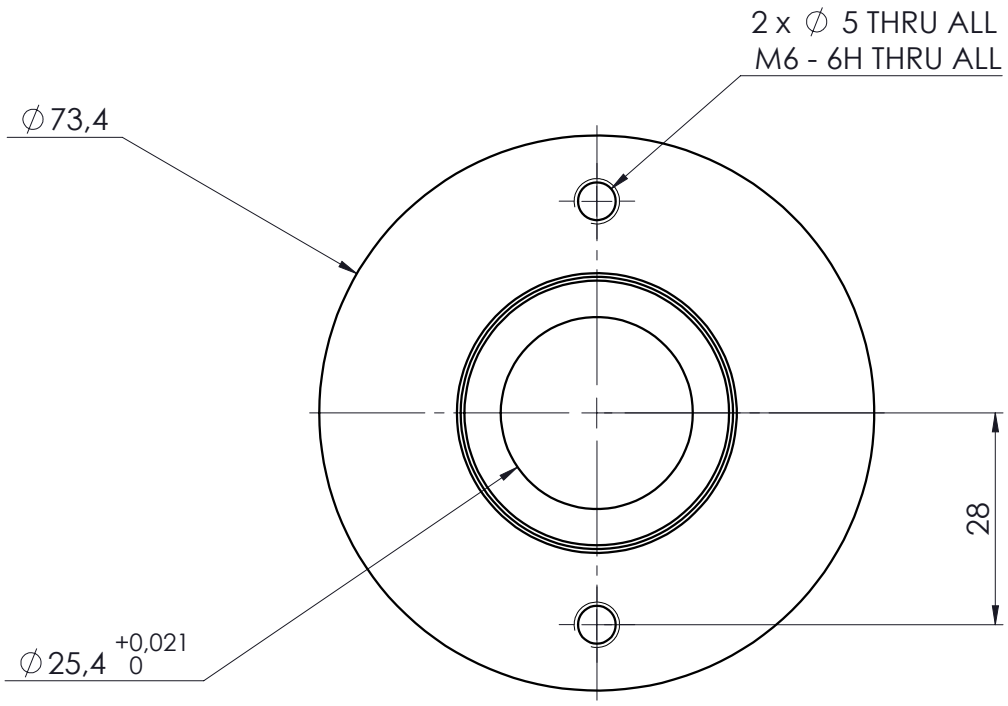

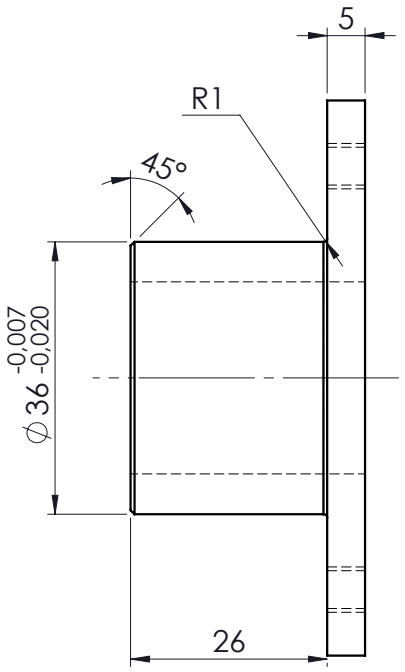

Note: Qty x3

Scale: 1:2 on A4	University of Cape Town Department of Mechanical Engineering			
Drawn By: Davison. T Seenzayi	All un-toleranced dimensions to adhere to ISO 2768-m	Title: Bushing B1.1/B1.2/B3.1		
Checked :	Material : PTFE (general)	Drawing Number : 1-9	Rev. : A	Sheet : 1 of 1

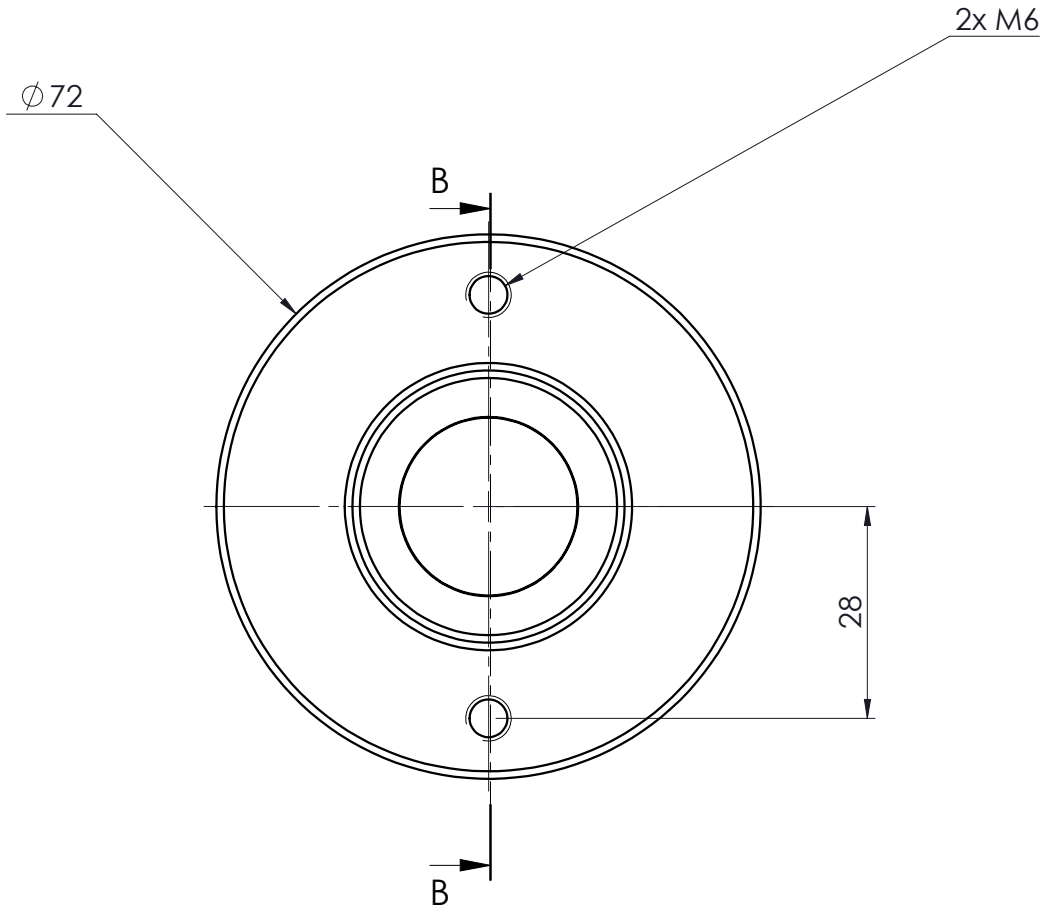

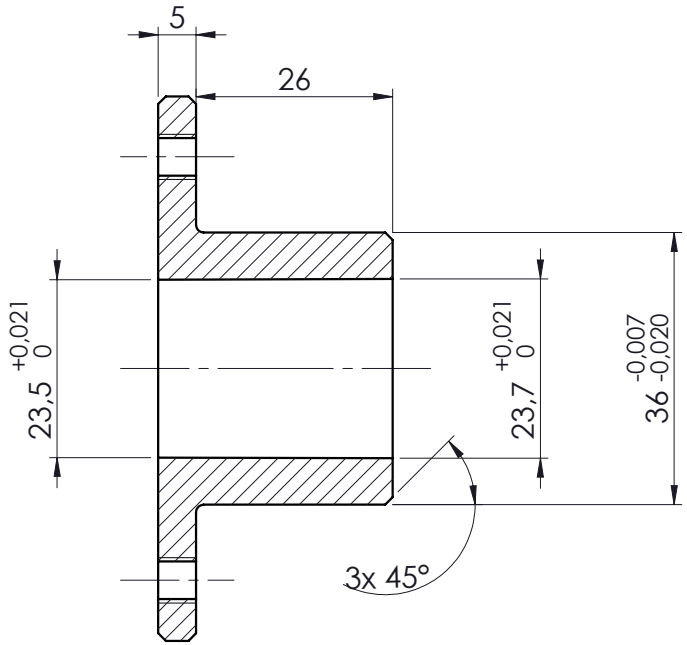

SECTION B-B
SCALE 1 : 1

Scale: 1:2 on A4	University of Cape Town Department of Mechanical Engineering			
Drawn By: Davison. T Seenzayi	All un-toleranced dimensions to adhere to ISO 2768-m	Title: Bushing B2.1		
Checked :	Material : PTFE (general)	Drawing Number : 1-10	Rev. : A	Sheet : 1 of 1

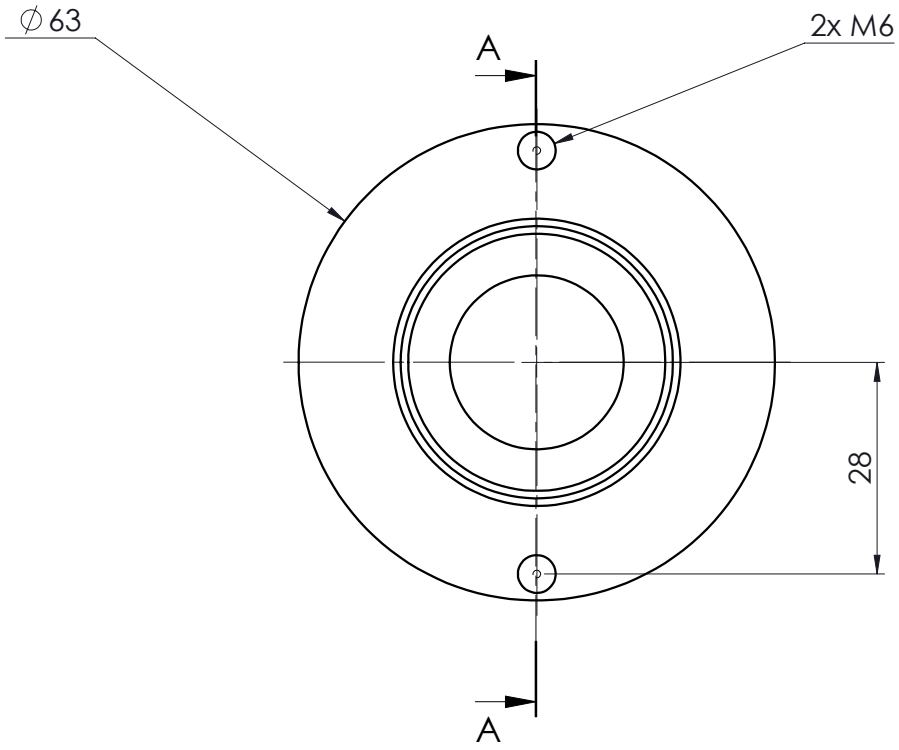

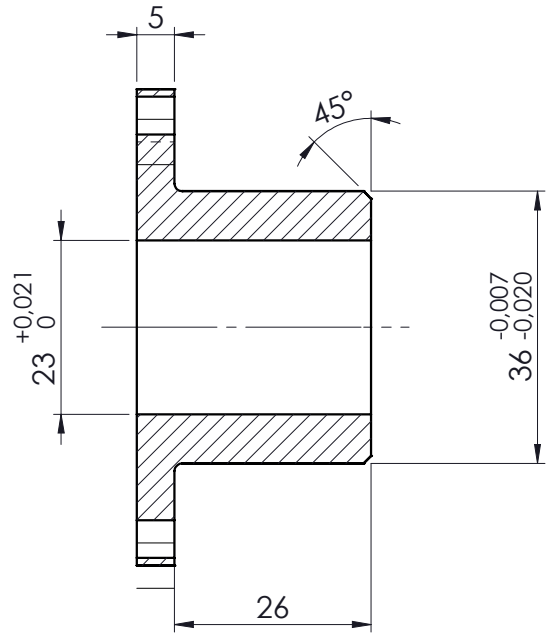

SECTION A-A
SCALE 1 : 1

Scale: 1:2 on A4	University of Cape Town Department of Mechanical Engineering			
Drawn By: Davison. T Seenzayi	All un-toleranced dimensions to adhere to ISO 2768-m	Title: Bushing B3.2		
Checked :	Material : PTFE (general)	Drawing Number : 1-12	Rev. : A	Sheet : 1 of 1

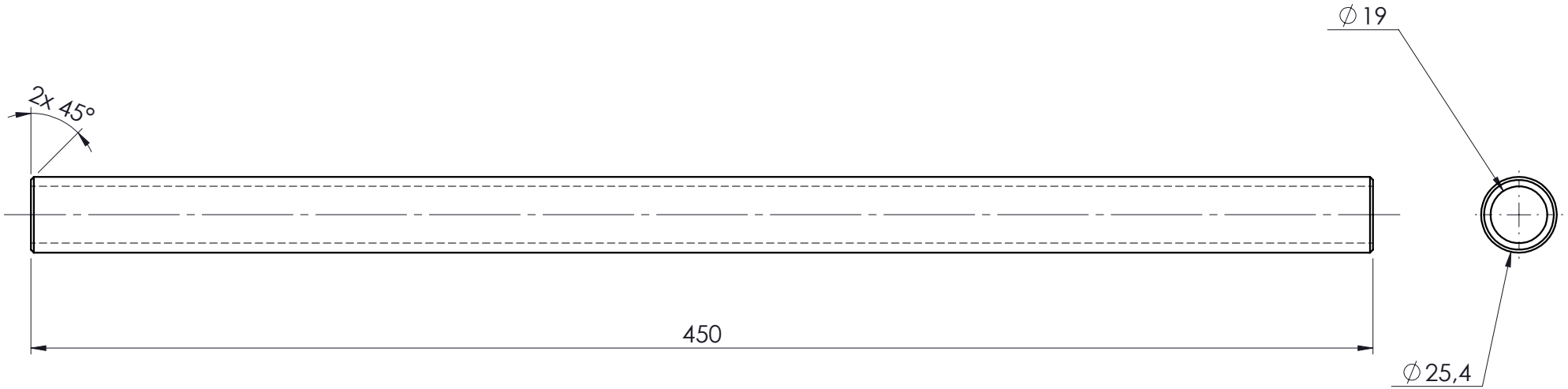

Scale: 1:5 on A4	University of Cape Town Department of Mechanical Engineering			
Drawn By: Davison. T Seenzayi	All un-toleranced dimensions to adhere to ISO 2768-m	Title: Straight Tube		
Checked :	Material : Aluminium	Drawing Number : 1-13	Rev. : A	Sheet : 1 of 1

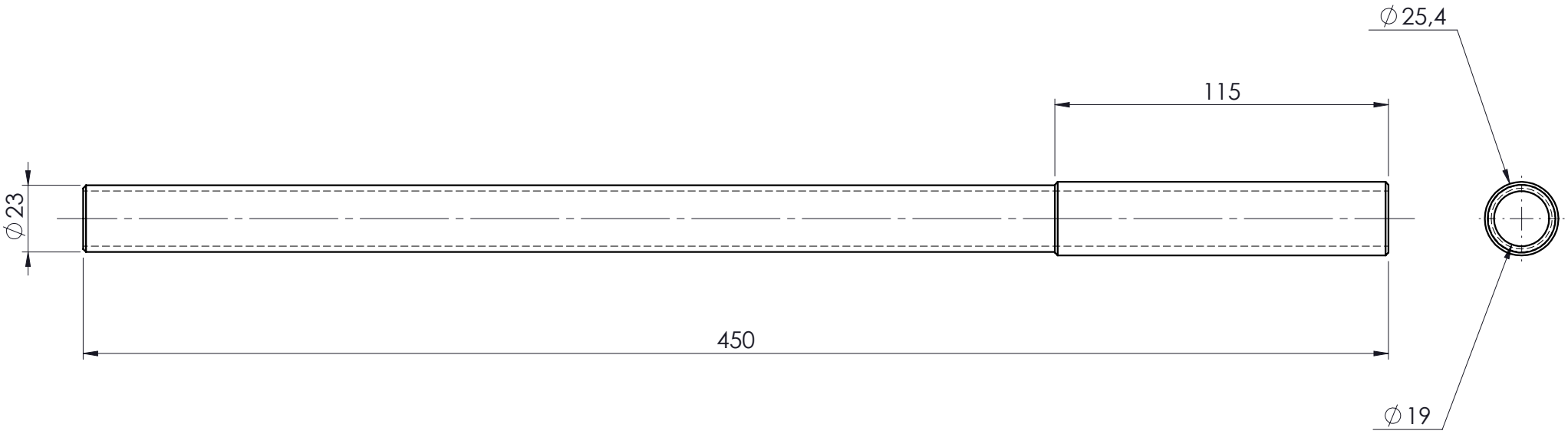

Scale: 1:5 on A4	University of Cape Town Department of Mechanical Engineering			
Drawn By: Davison T Seenzayi	All un-toleranced dimensions to adhere to ISO 2768-m	Title: Stepped Tube		
Checked :	Material : Aluminium	Drawing Number : 1-15	Rev. : A	Sheet : 1 of 1

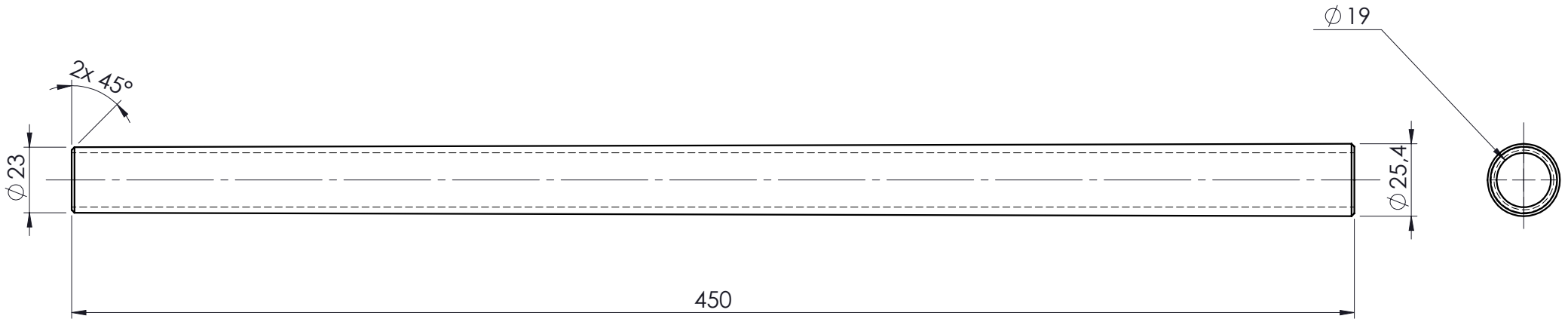

Scale: 1:5 on A4	University of Cape Town Department of Mechanical Engineering			
Drawn By: Davison. T Seenzayi	All un-toleranced dimensions to adhere to ISO 2768-m	Title: Tapered Tube		
Checked :	Material : Aluminium	Drawing Number : 1-14	Rev. : A	Sheet : 1 of 1

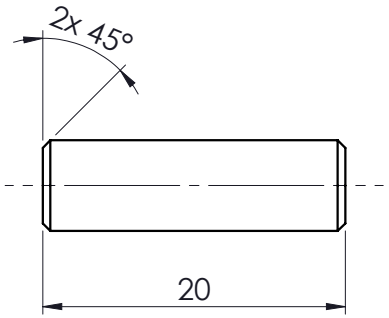

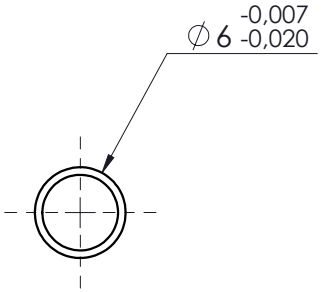

Note: Qty x4

Scale: 2:1 on A4	University of Cape Town Department of Mechanical Engineering			
Drawn By: Davison. T Seenzayi	All un-toleranced dimensions to adhere to ISO 2768-m	Title: Dowel Pin		
Checked :	Material : AISI 1020	Drawing Number : 1-16	Rev. : A	Sheet : 1 of 1

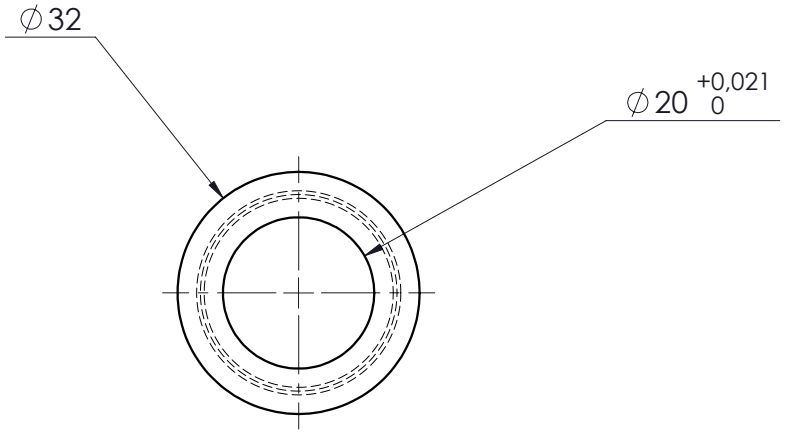

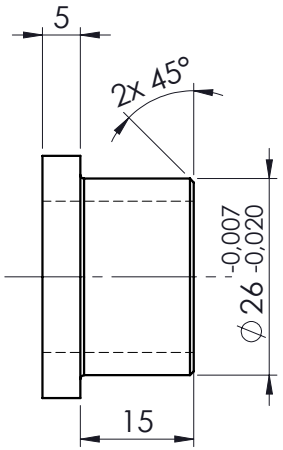

NOTE: QTY x8

Scale: 1:1 on A4	University of Cape Town Department of Mechanical Engineering			
Drawn By: Davison T. Seenzayi	All un-toleranced dimensions to adhere to ISO 2768-m	Title: Single Flange Bushing		
Checked :	Material : PTFE (general)	Drawing Number : 1-17	Rev. : A	Sheet : 1 of 1

APPENDIX B - EXPERIMENTAL BLAST TEST RESULTS

Impulse

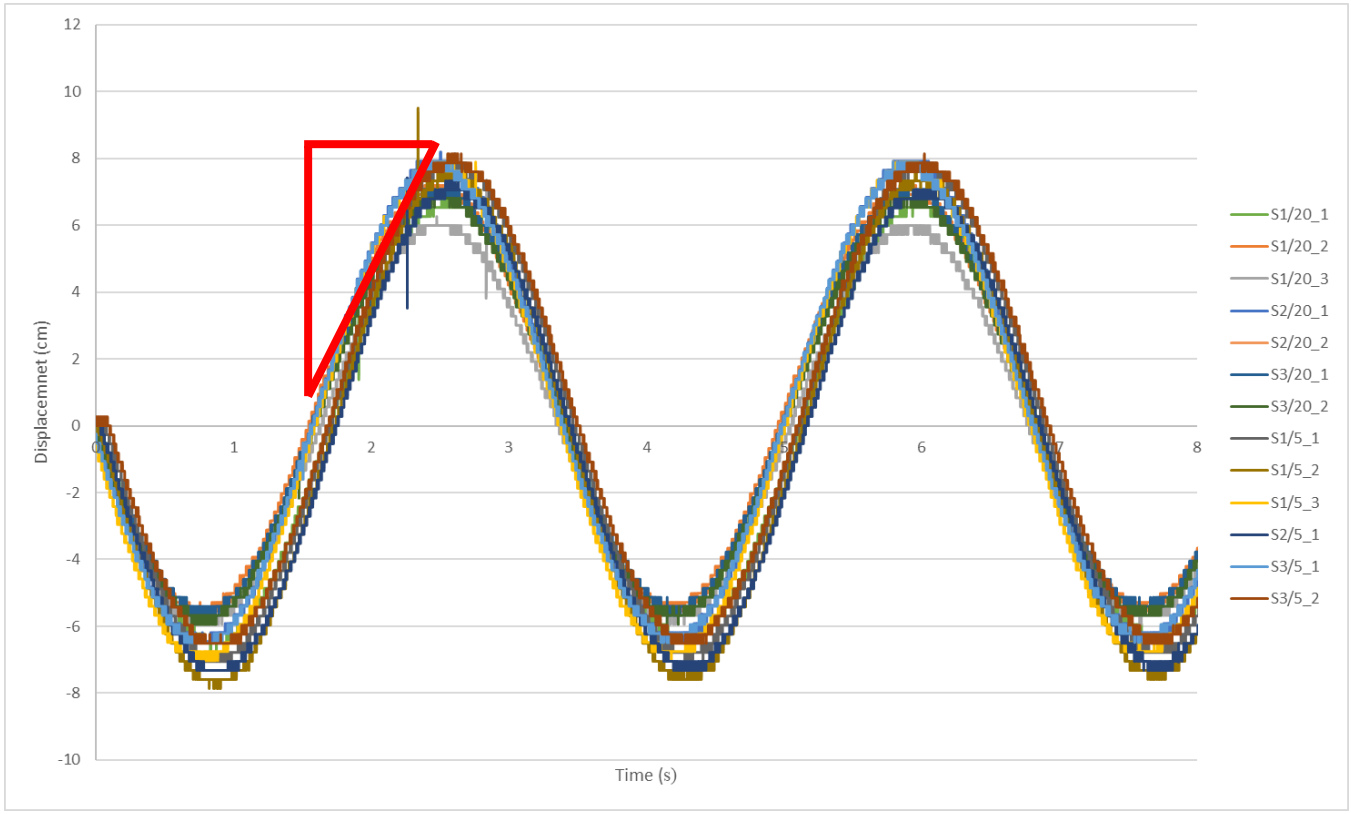

Non-deformable witness plate Detonations

Straight tube – Straight tube

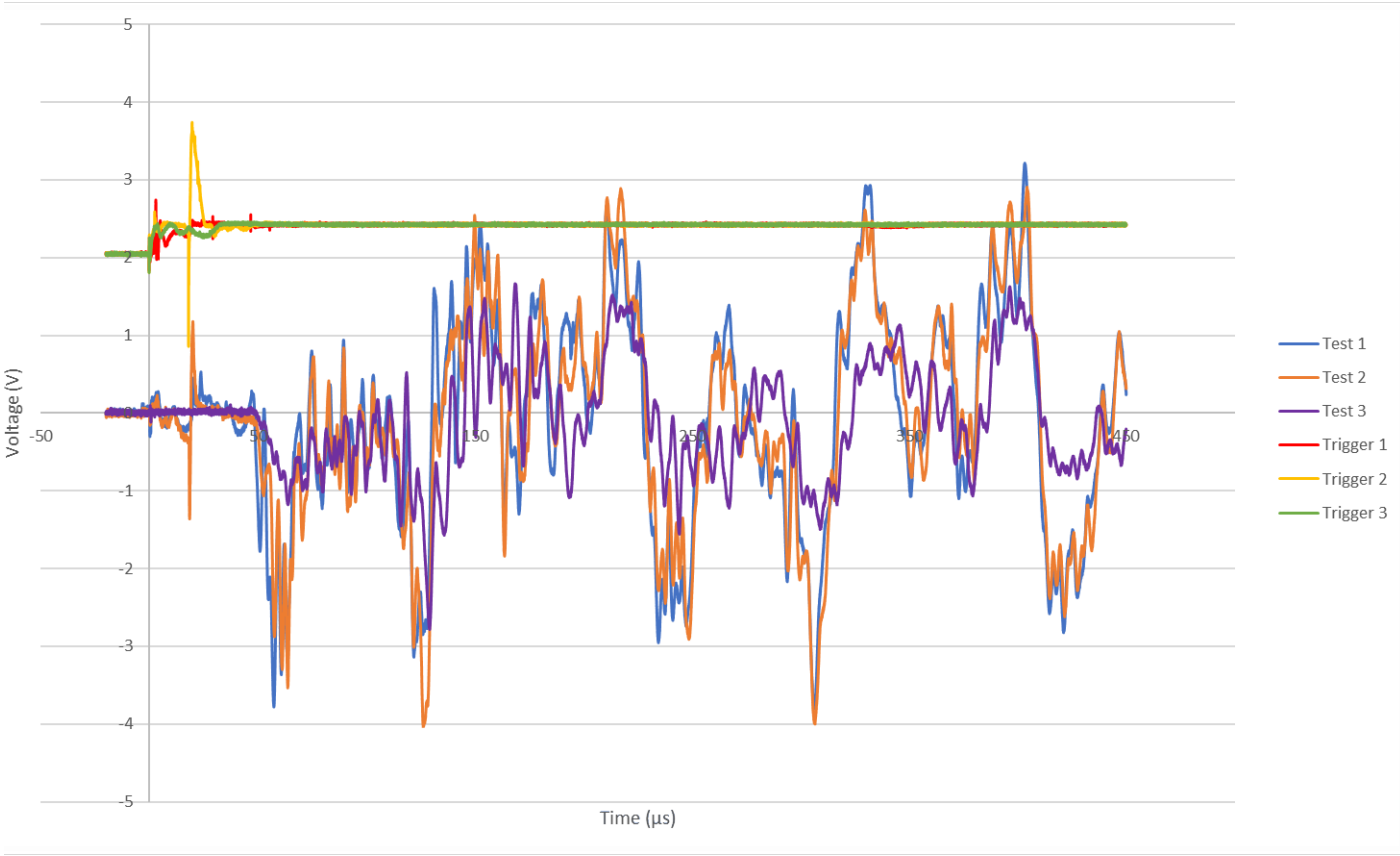

Stepped tube – Stepped tube

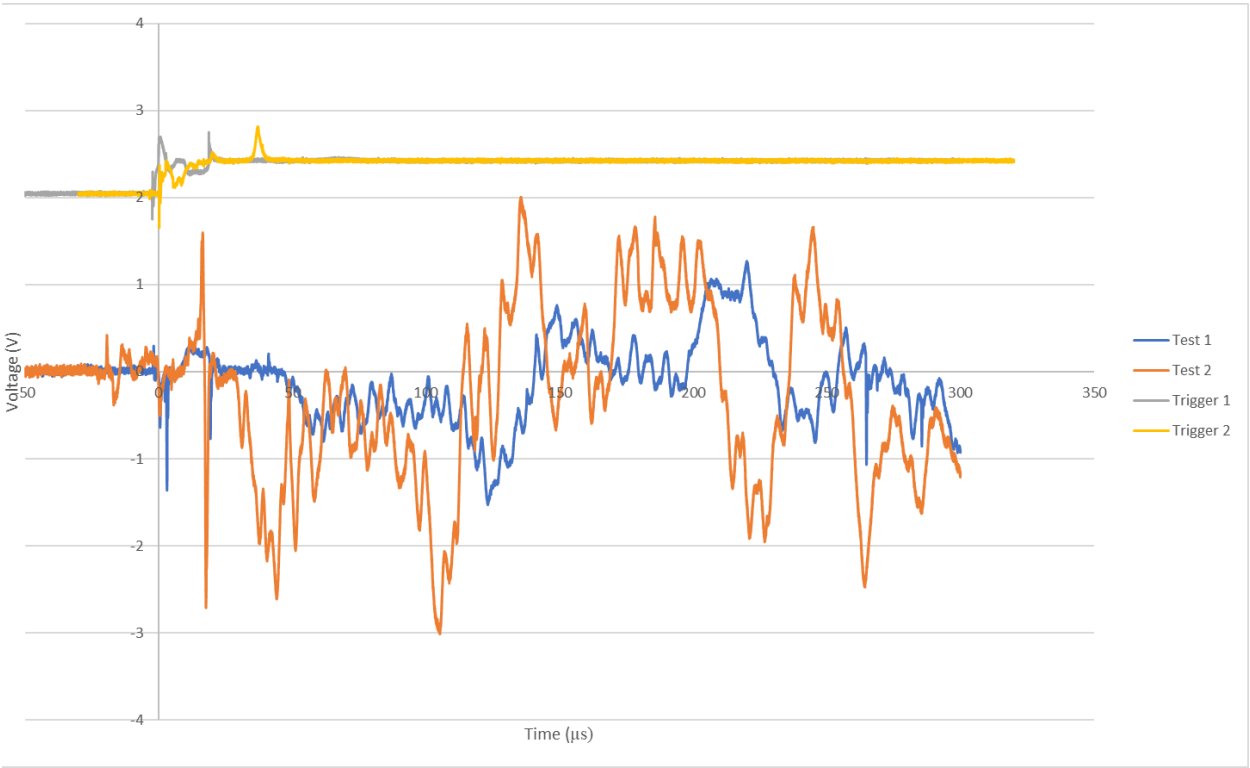

Tapered tube – Tapered tube

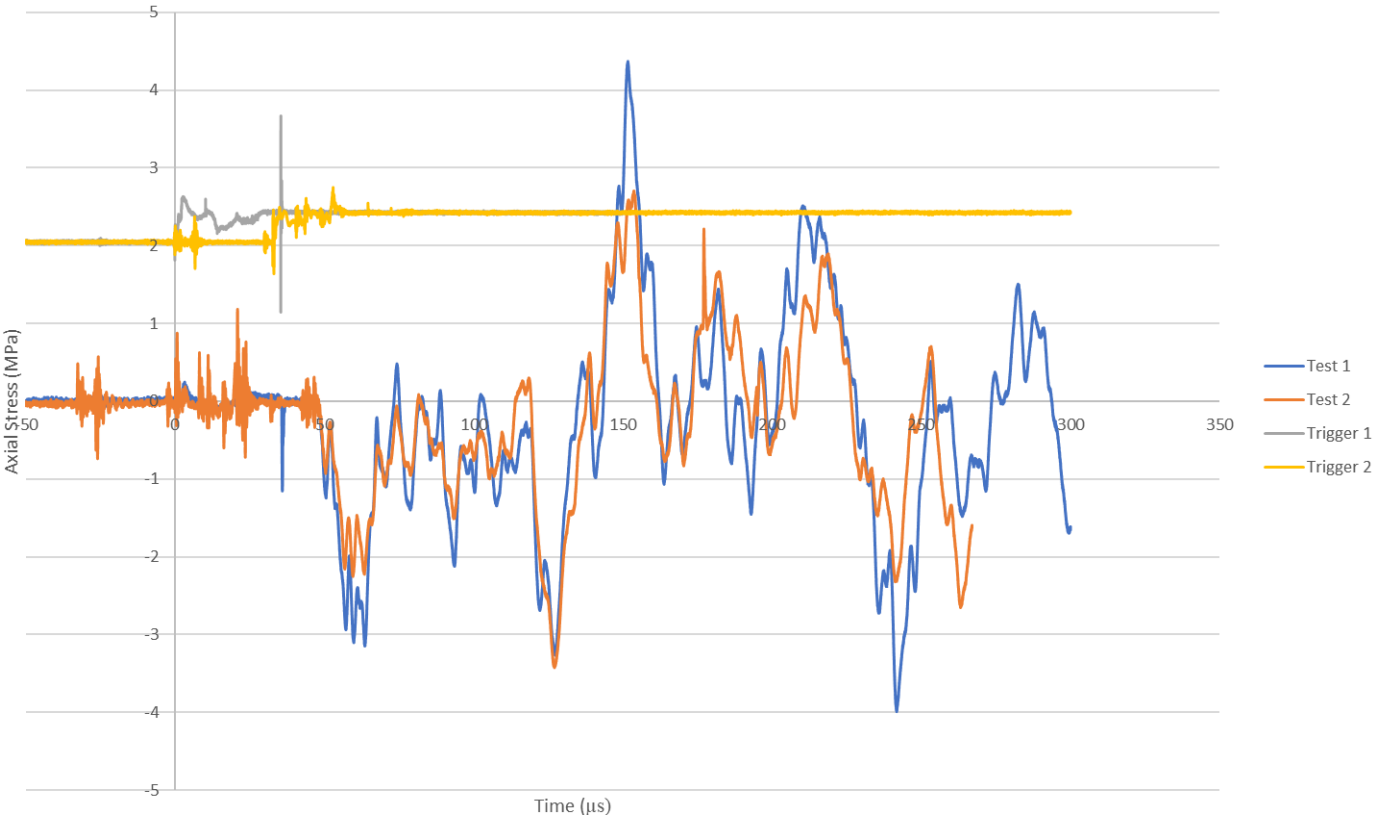

Deformable witness plate Detonations

Straight tube – Straight tube

Stepped tube – Stepped tube

Tapered tube – Tapered tube

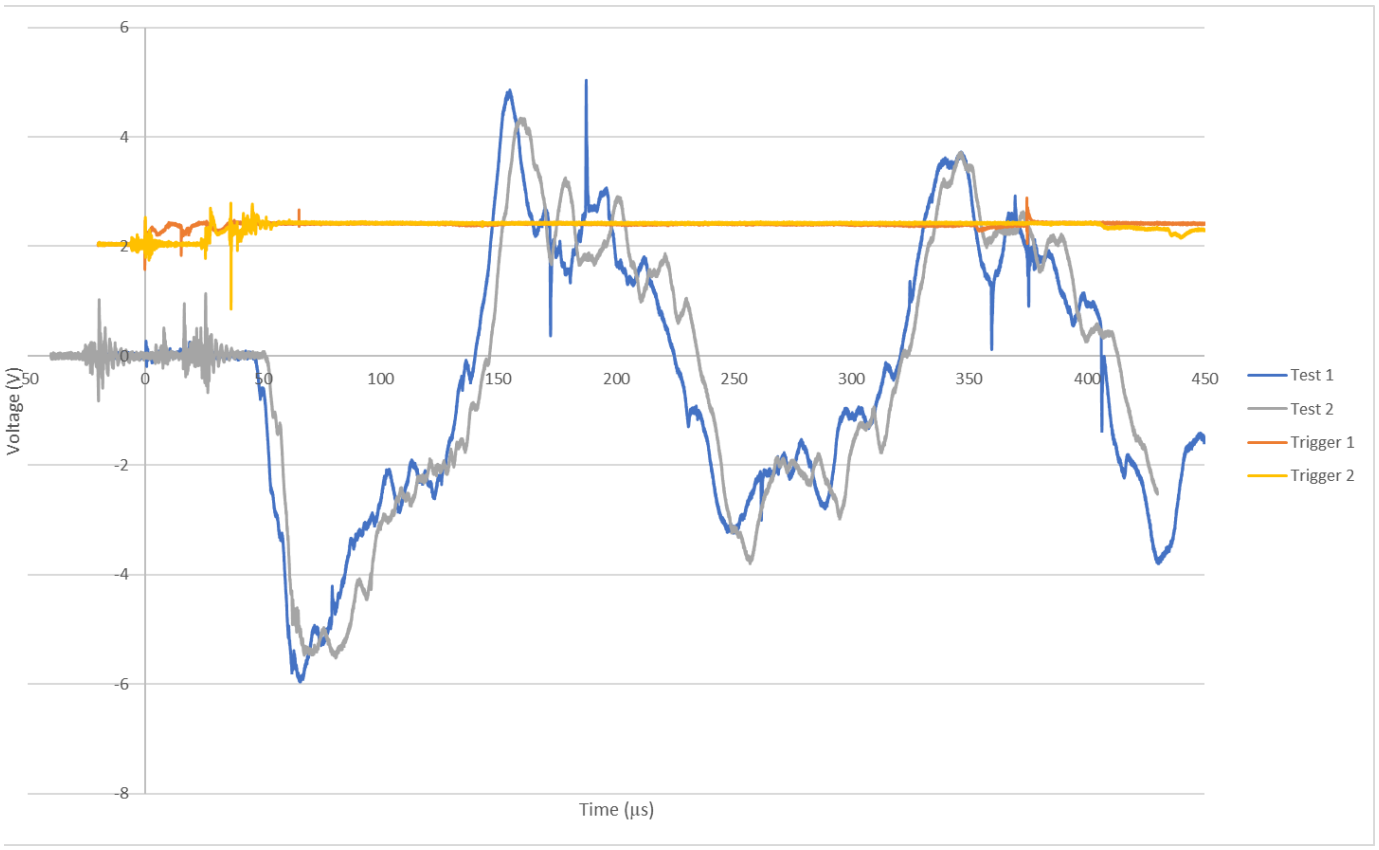

APPENDIX C- BLAST-INDUCED STRESS DISTRIBUTION PLOTS

Non-deformable witness plate Detonations

Straight tube – Straight tube

FSI quadrature
Time = 0.13784
Contours of Effective Stress (v-m)
min=0.117036, at elem# 12307
max=221.3, at elem# 4992415

Effective Stress (v-m)
2.213e+02
1.992e+02
1.771e+02
1.549e+02
1.328e+02
1.107e+02
8.859e+01
6.647e+01
4.435e+01
2.224e+01
1.170e-01

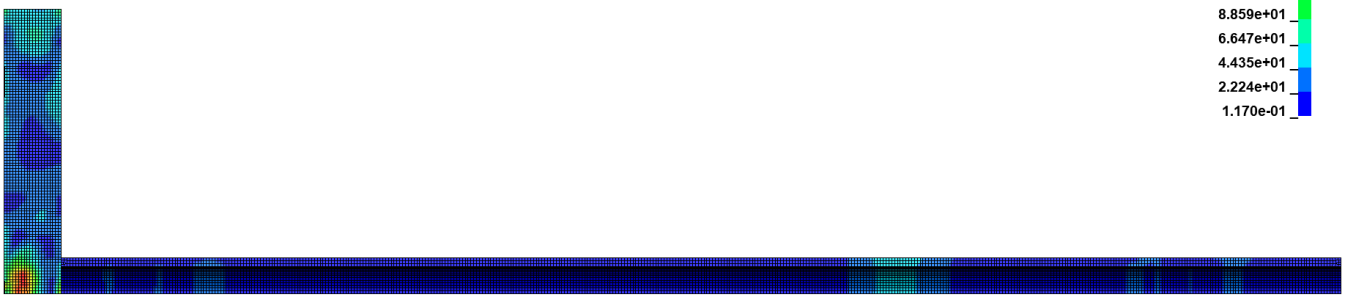

FSI quadrature
Time = 0.08828
Contours of Effective Stress (v-m)
min=0.000399026, at elem# 57
max=284.952, at elem# 4996875

Effective Stress (v-m)
2.850e+02
2.565e+02
2.280e+02
1.995e+02
1.710e+02
1.425e+02
1.140e+02
8.549e+01
5.699e+01
2.850e+01
3.990e-04

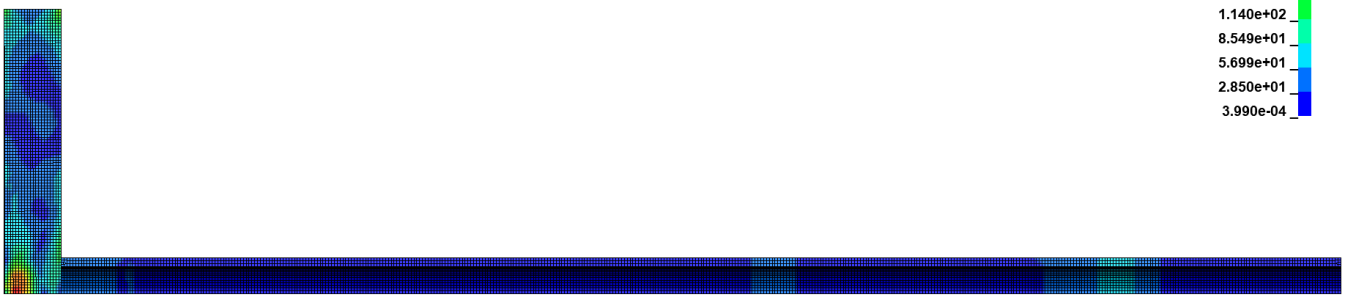

FSI quadrature
Time = 0.0644
Contours of Effective Stress (v-m)
min=2.3884e-07, at elem# 7126
max=233.767, at elem# 4969268

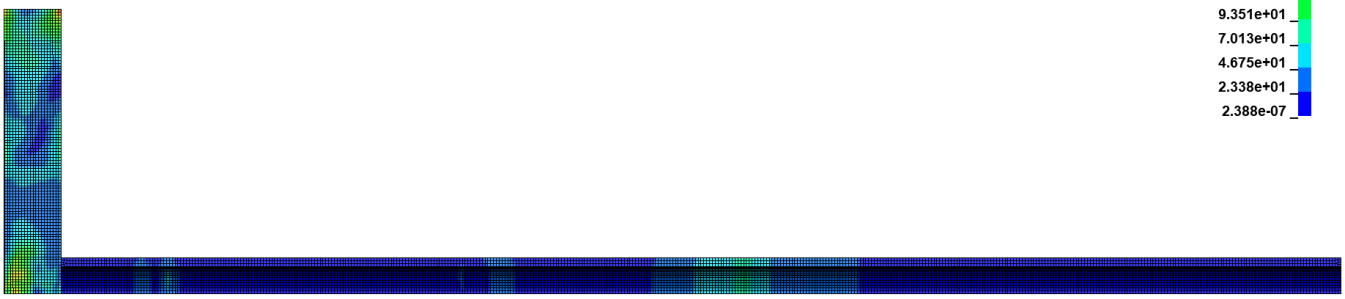

FSI quadrature
Time = 0.051859
Contours of Effective Stress (v-m)
min=6.79554e-08, at elem# 7463
max=224.243, at elem# 4999168

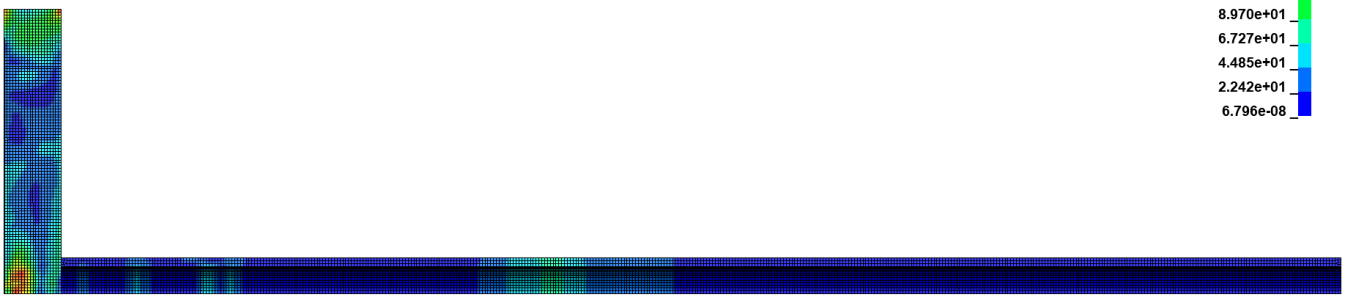


FSI quadrature
Time = 0
Contours of Effective Stress (v-m)
min=0, at elem# 4769172
max=0, at elem# 4769172
Effective Stress (v-m)
0.000e+00
0.000e+00
0.000e+00
0.000e+00
0.000e+00
0.000e+00
0.000e+00
0.000e+00
0.000e+00
0.000e+00
Y
Z
X

Stepped tube – Stepped tube

FSI quadrature
Time = 0.09886
Contours of Effective Stress (v-m)
min=0.175171, at elem# 4774468
max=269.981, at elem# 4409252

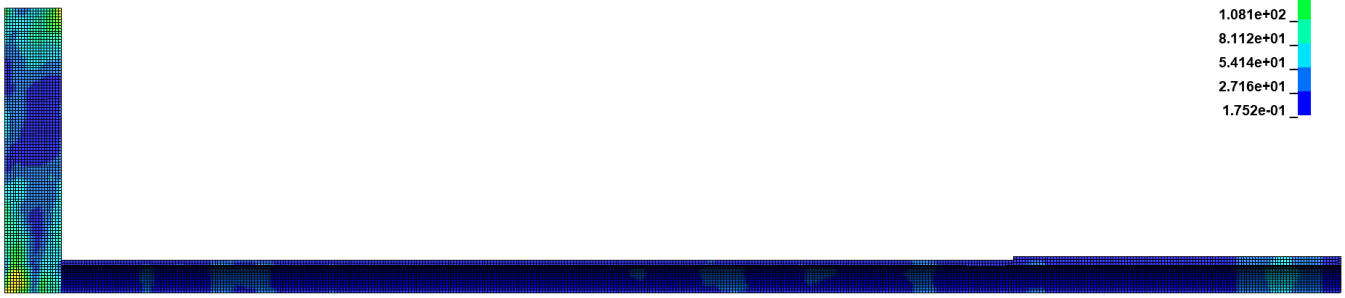

FSI quadrature
Time = 0.059578
Contours of Effective Stress (v-m)
min=0, at elem# 4769184
max=243.194, at elem# 4409273

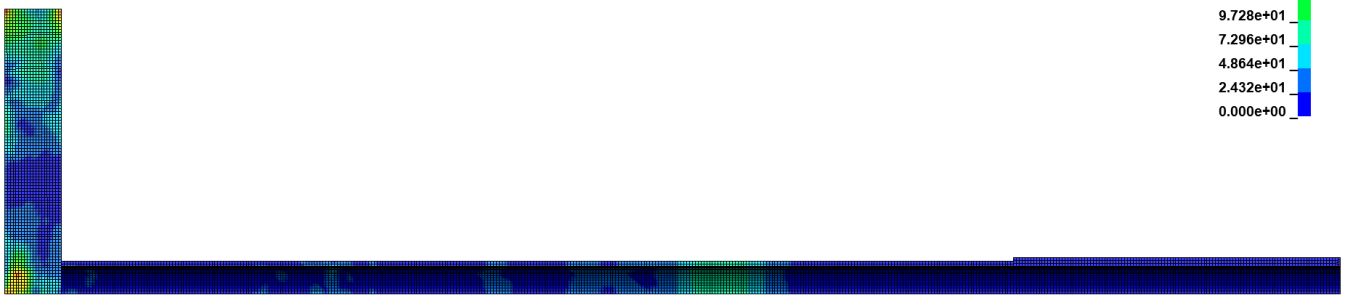

FSI quadrature
Time = 0.051787
Contours of Effective Stress (v-m)
min=0, at elem# 4769169
max=269.512, at elem# 4217188

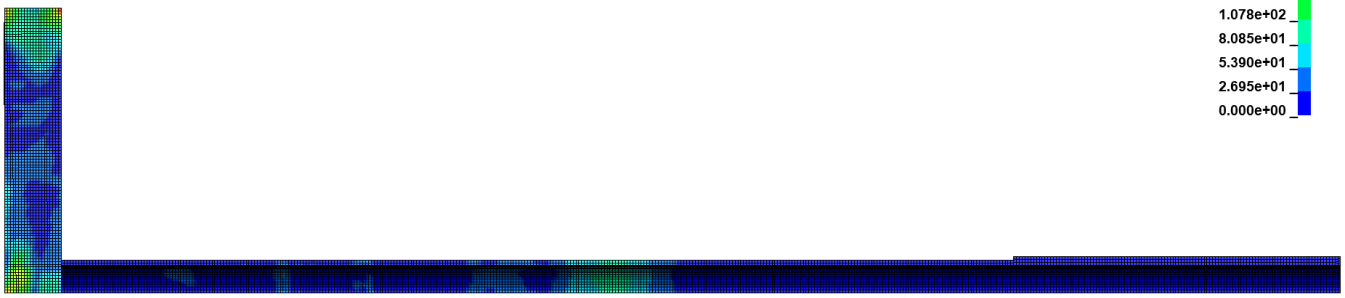

FSI quadrature
Time = 0
Contours of Effective Stress (v-m)
min=0, at elem# 4217169
max=0, at elem# 4217169

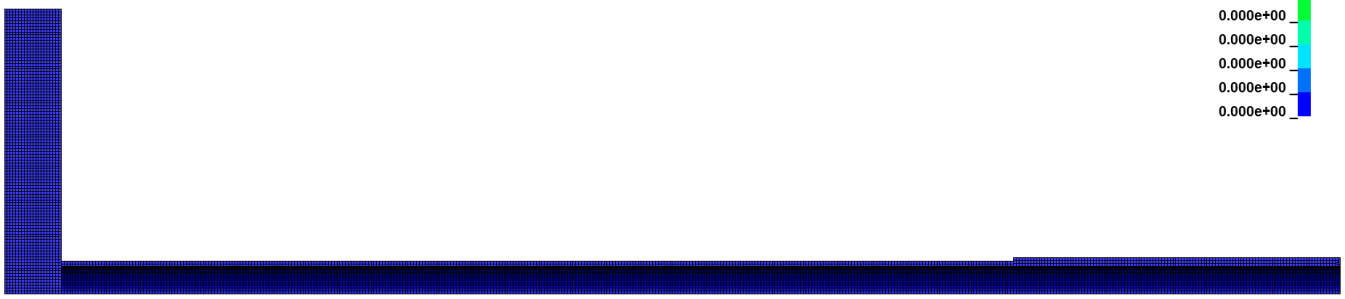

FSI quadrature
Time = 0.20888
Contours of Effective Stress (v-m)
min=0.0898002, at elem# 4780780
max=202.941, at elem# 4403328

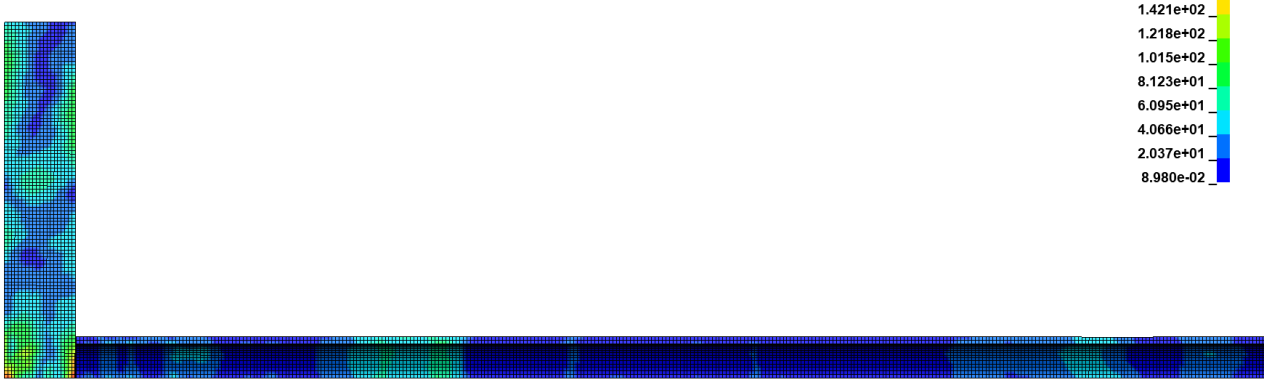

FSI quadrature
Time = 0.18786
Contours of Effective Stress (v-m)
min=0.379825, at elem# 4774891
max=257.153, at elem# 4217389

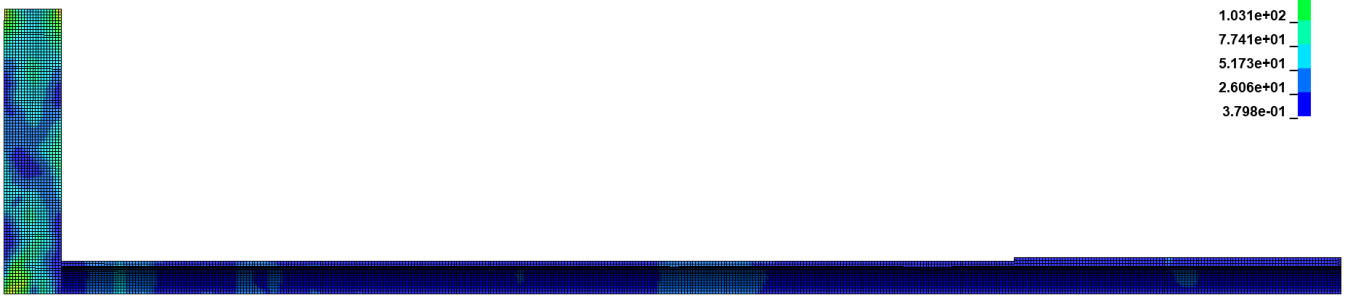

Tapered tube – Tapered tube

FSI quadrature
Time = 0.14989
Contours of Effective Stress (v-m)
min=0.0365404, at elem# 4793784
max=177.347, at elem# 4415170

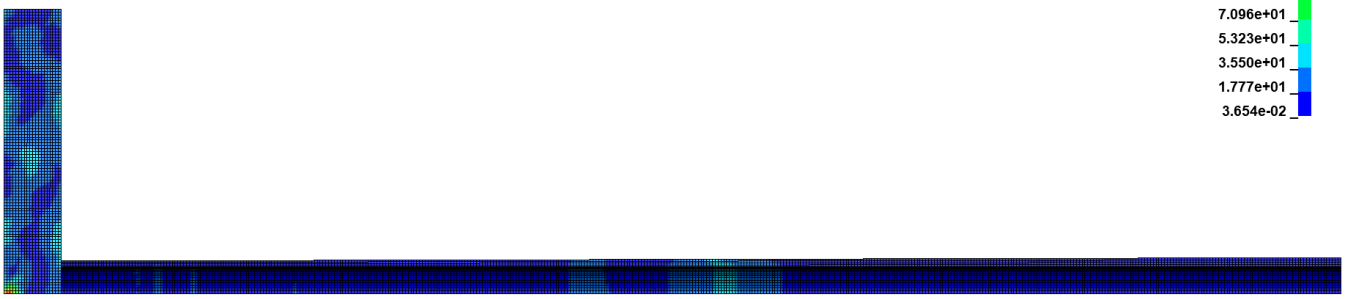

FSI quadrature
Time = 0.13587
Contours of Effective Stress (v-m)
min=0.0386521, at elem# 4773545
max=189.239, at elem# 4415170

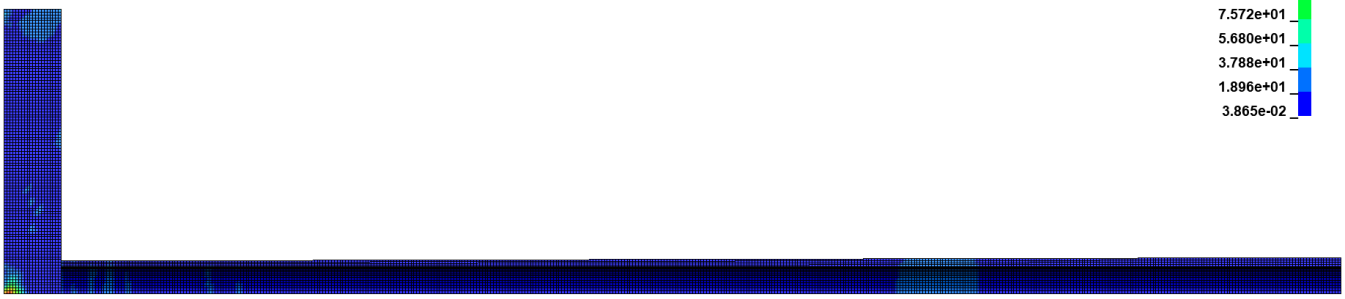

FSI quadrature
Time = 0.13287
Contours of Effective Stress (v-m)
min=0.134282, at elem# 4773852
max=190.474, at elem# 4415170

Effective Stress (v-m)
1.905e+02
1.714e+02
1.524e+02
1.334e+02
1.143e+02
9.530e+01
7.627e+01
5.724e+01
3.820e+01
1.917e+01
1.343e-01

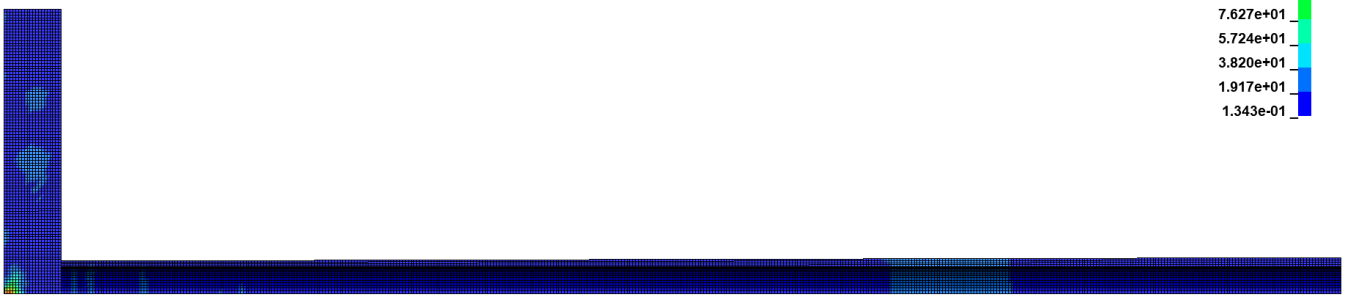

FSI quadrature
Time = 0.062093
Contours of Effective Stress (v-m)
min=0, at elem# 4769169
max=205.535, at elem# 4415170

Effective Stress (v-m)
2.055e+02
1.850e+02
1.644e+02
1.439e+02
1.233e+02
1.028e+02
8.221e+01
6.166e+01
4.111e+01
2.055e+01
0.000e+00

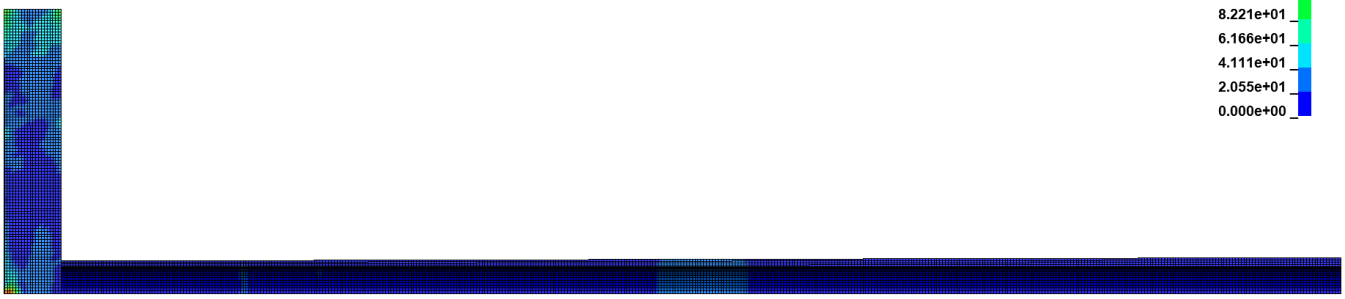

Deformable witness plate Detonations

Straight tube – Straight tube

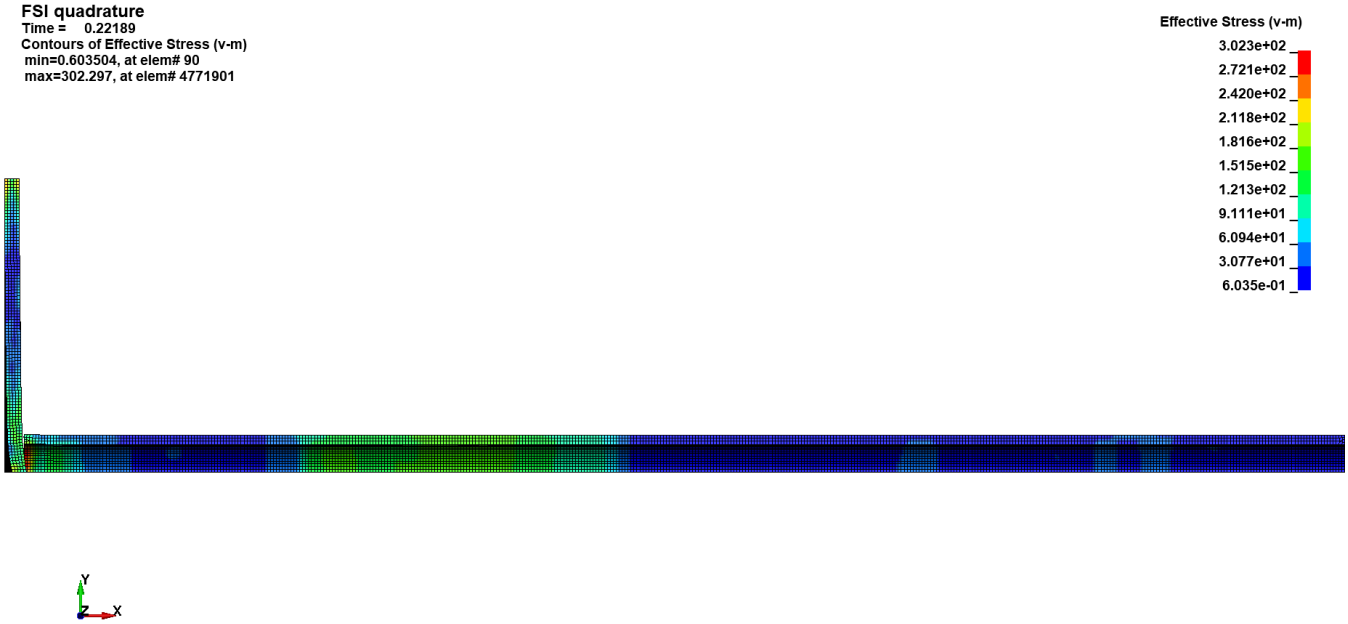

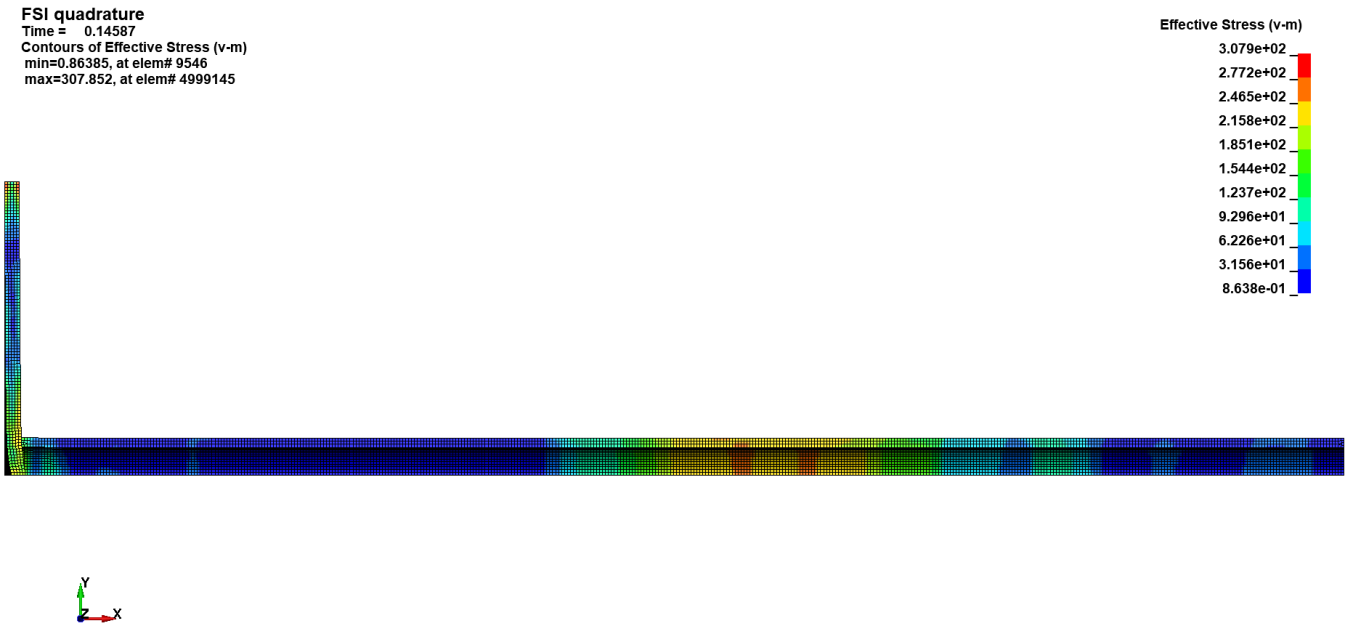

FSI quadrature
Time = 0.13389
Contours of Effective Stress (v-m)
min=0.584749, at elem# 9490
max=298.145, at elem# 4994568

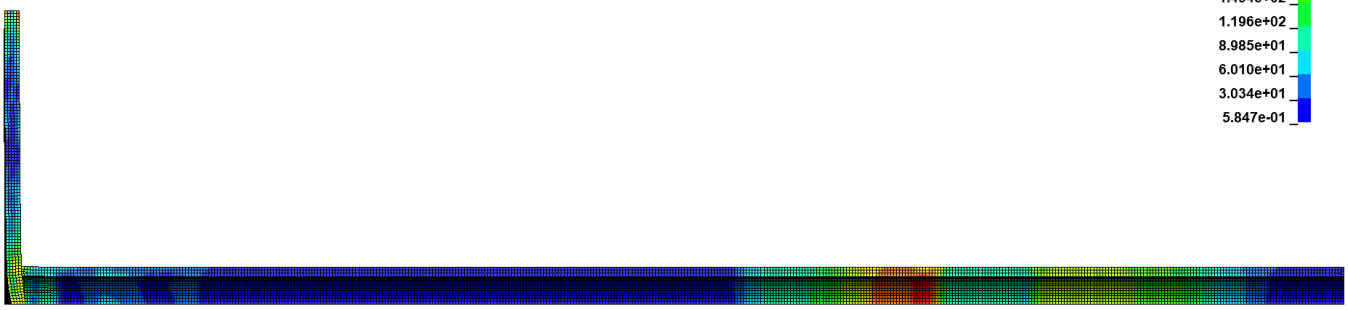

FSI quadrature
Time = 0.060856
Contours of Effective Stress (v-m)
min=2.80016e-06, at elem# 622
max=404.837, at elem# 4994637

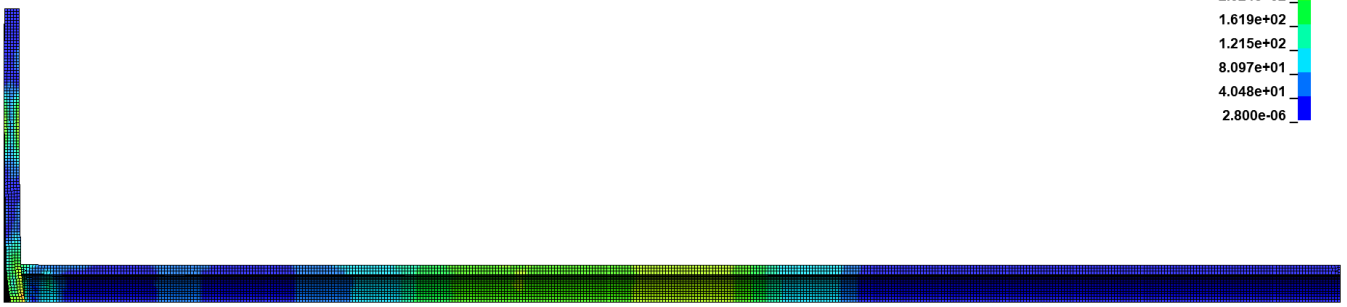

FSI quadrature
Time = 0.050561
Contours of Effective Stress (v-m)
min=3.04401e-08, at elem# 7282
max=414.662, at elem# 4992314

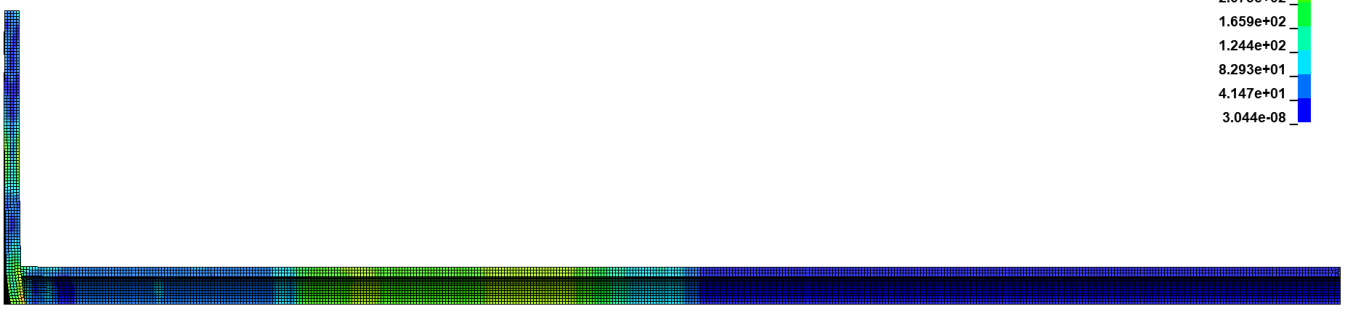

FSI quadrature
Time = 0
Contours of Effective Stress (v-m)
min=0, at elem# 4769187
max=0, at elem# 4769187

Stepped tube – Stepped tube

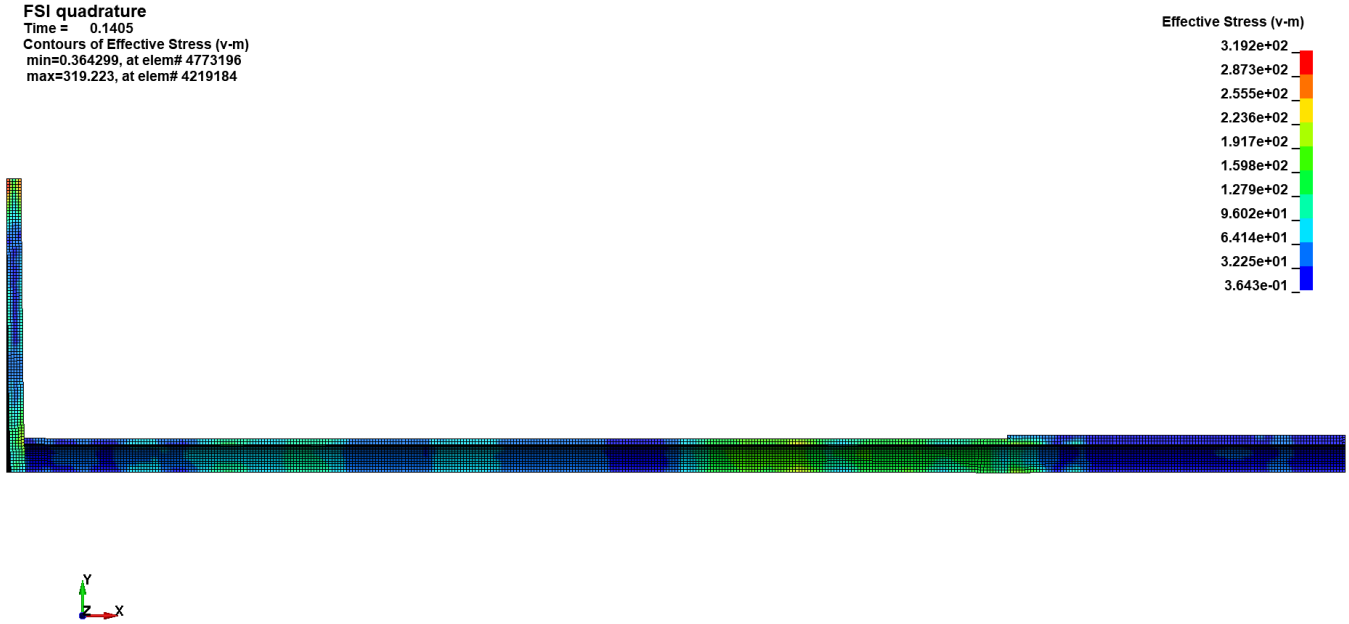

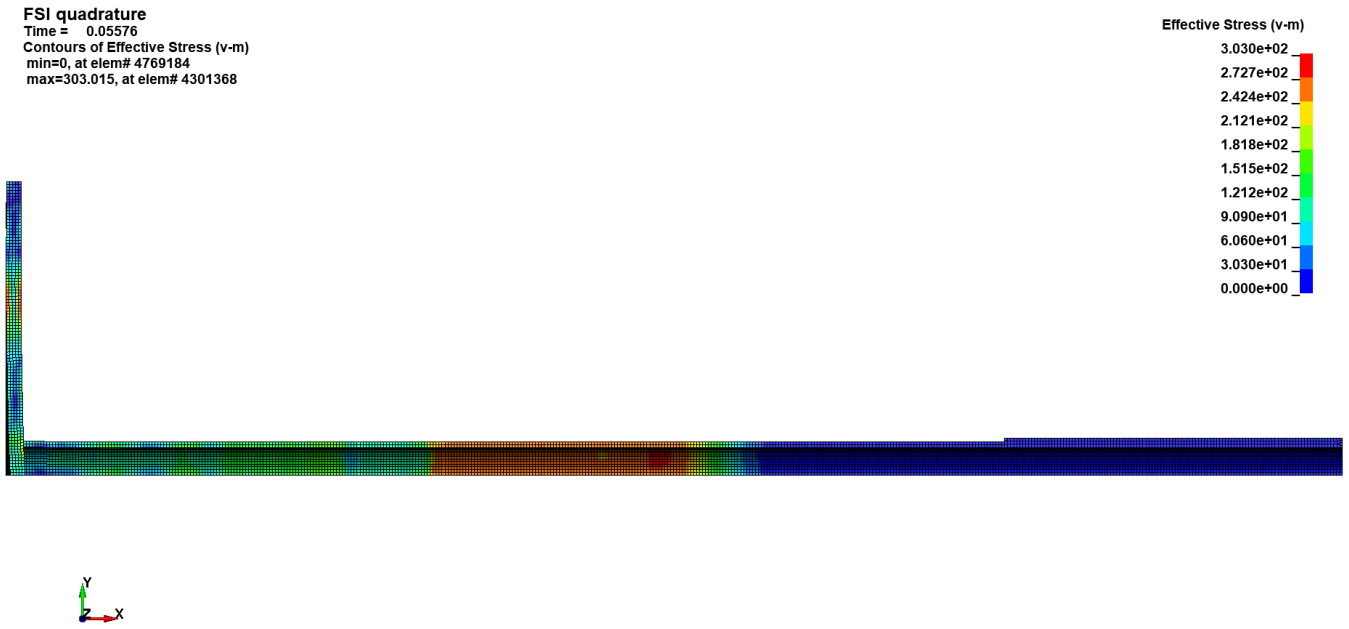

FSI quadrature
Time = 0.044049
Contours of Effective Stress (v-m)
min=0, at elem# 4769169
max=304.47, at elem# 4365204

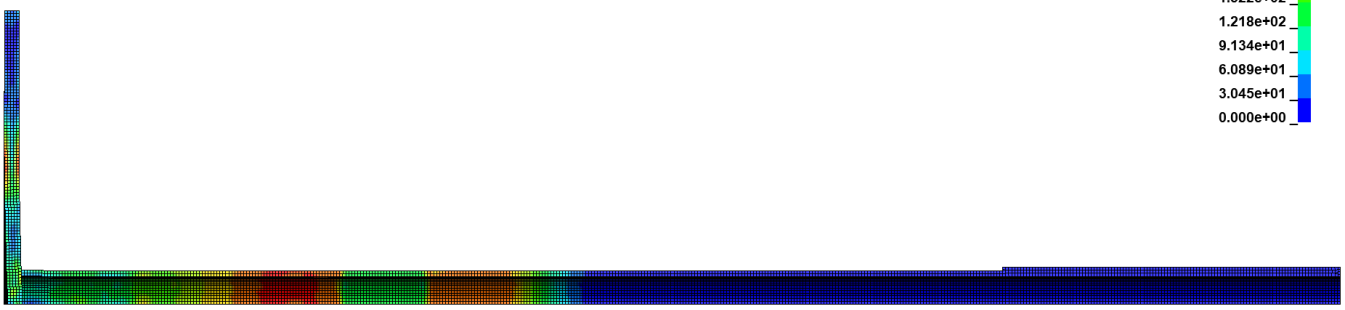

FSI quadrature
Time = 0
Contours of Effective Stress (v-m)
min=0, at elem# 4217184
max=0, at elem# 4217184

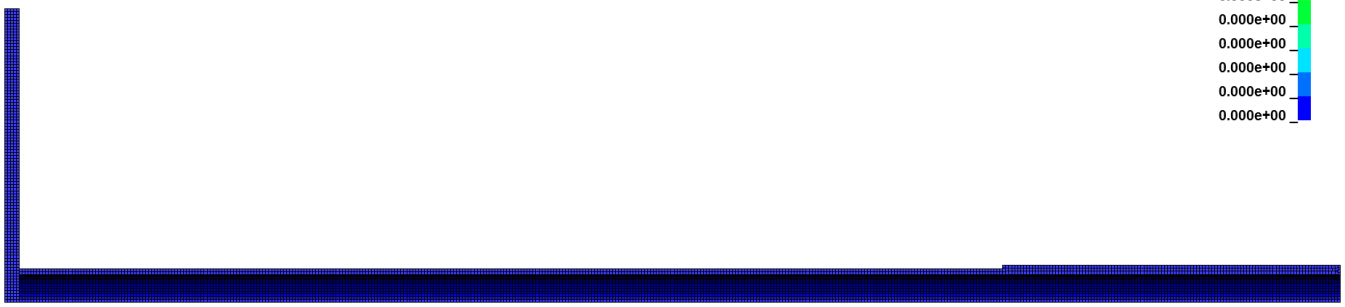

FSI quadrature
Time = 0.25557
Contours of Effective Stress (v-m)
min=0.500213, at elem# 4782751
max=312.877, at elem# 4411628

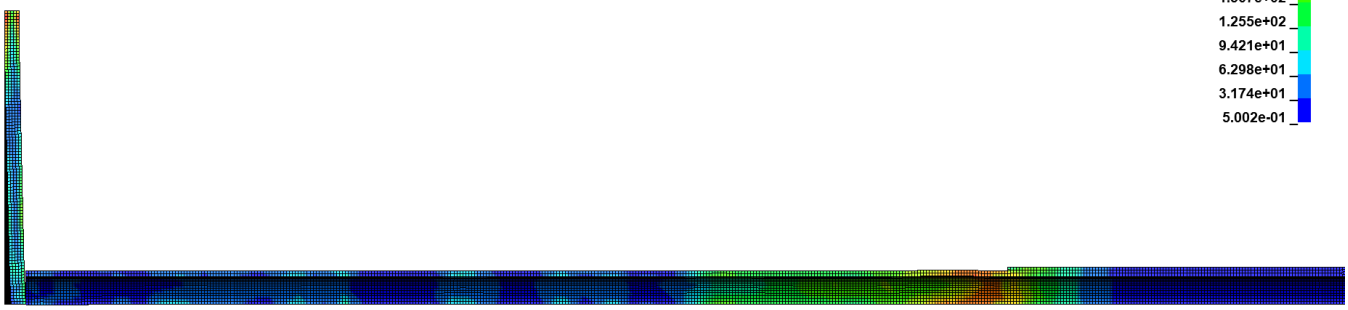

FSI quadrature
Time = 0.14809
Contours of Effective Stress (v-m)
min=0.2384, at elem# 4772497
max=303.754, at elem# 4417148

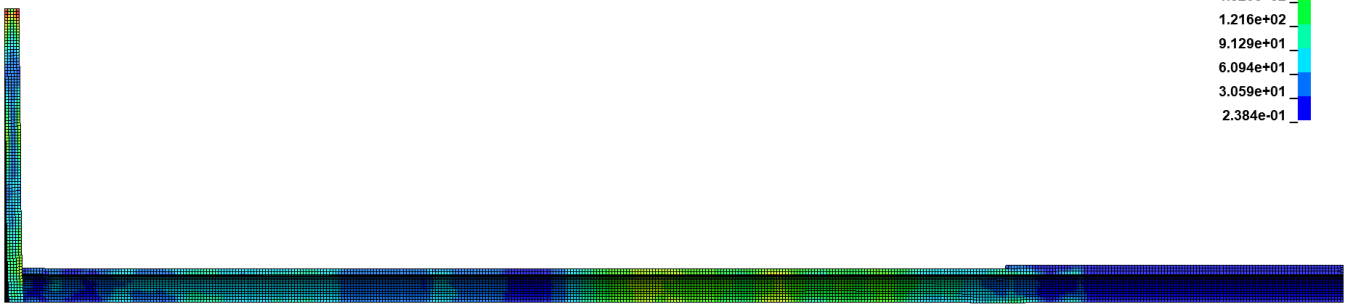

Tapered tube – Tapered tube

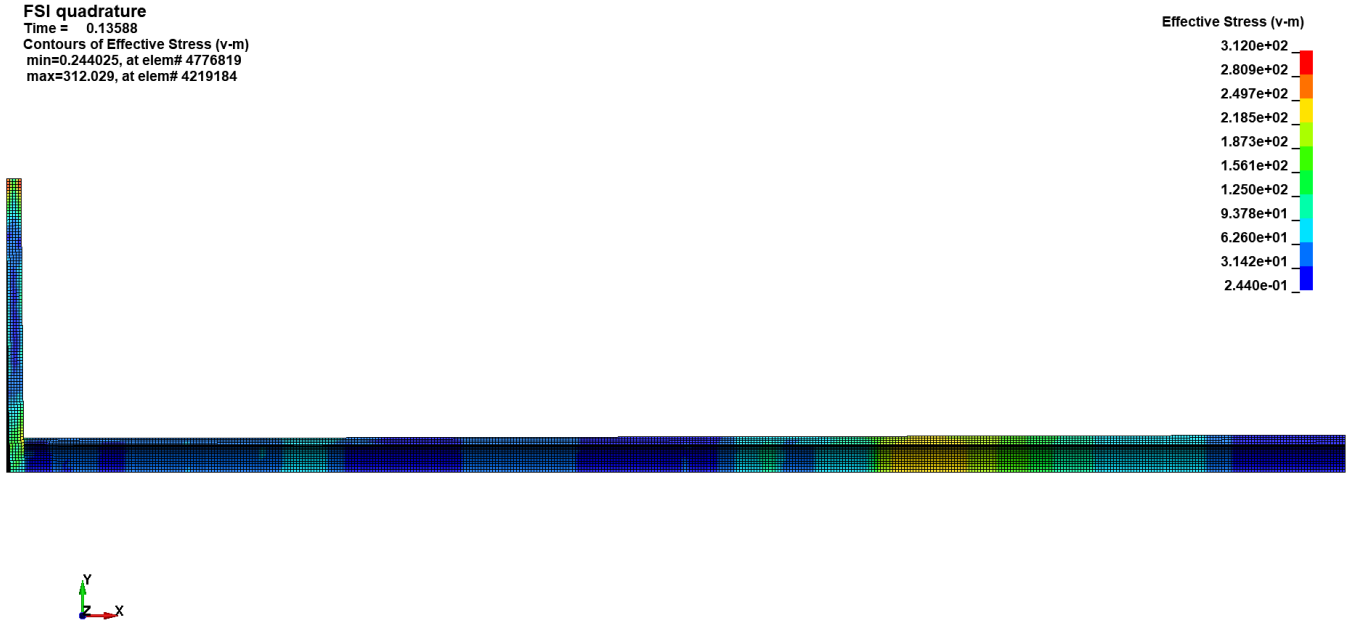

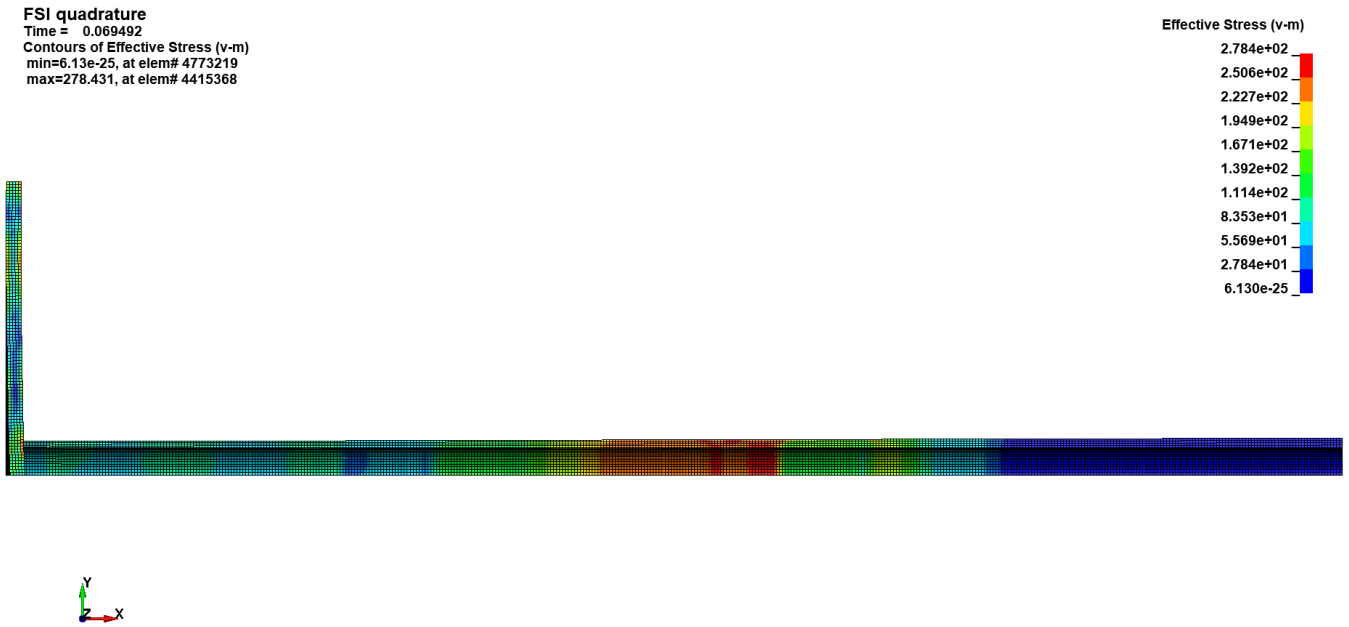

FSI quadrature
Time = 0.04897
Contours of Effective Stress (v-m)
min=0, at elem# 4769169
max=304.582, at elem# 4305184

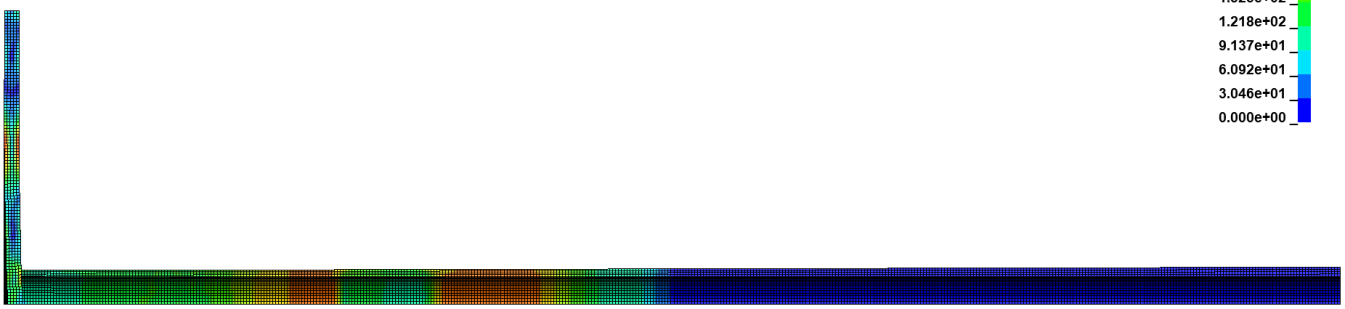

FSI quadrature
Time = 0
Contours of Effective Stress (v-m)
min=0, at elem# 4217184
max=0, at elem# 4217184

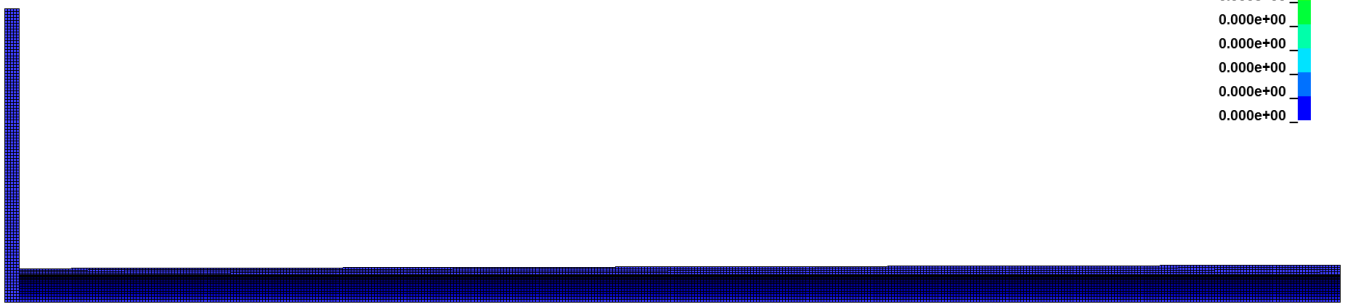

FSI quadrature
Time = 0.2239
Contours of Effective Stress (v-m)
min=0.480349, at elem# 4784019
max=276.381, at elem# 4385144

Effective Stress (v-m)
2.764e+02
2.488e+02
2.212e+02
1.936e+02
1.660e+02
1.384e+02
1.108e+02
8.325e+01
5.566e+01
2.807e+01
4.803e-01

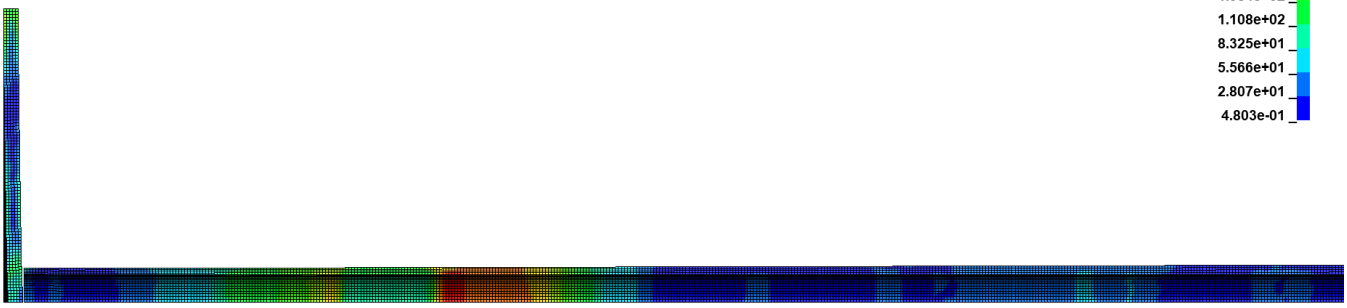

FSI quadrature
Time = 0.1519
Contours of Effective Stress (v-m)
min=2.34714, at elem# 4331166
max=301.346, at elem# 4299184

Effective Stress (v-m)
3.013e+02
2.714e+02
2.415e+02
2.116e+02
1.817e+02
1.518e+02
1.219e+02
9.205e+01
6.215e+01
3.225e+01
2.347e+00

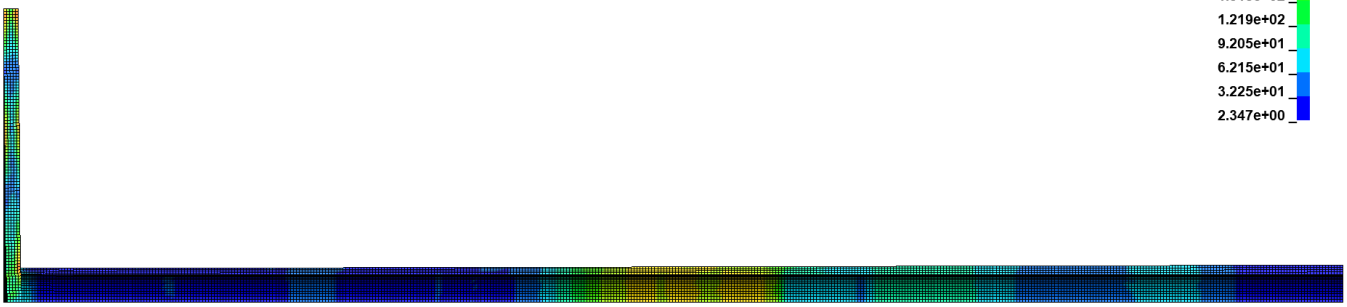

APPENDIX D- TIBIA BLAST-INDUCED STRESS DISTRIBUTION PLOTS

Non-deformable Plate Detonations

Men Tibia

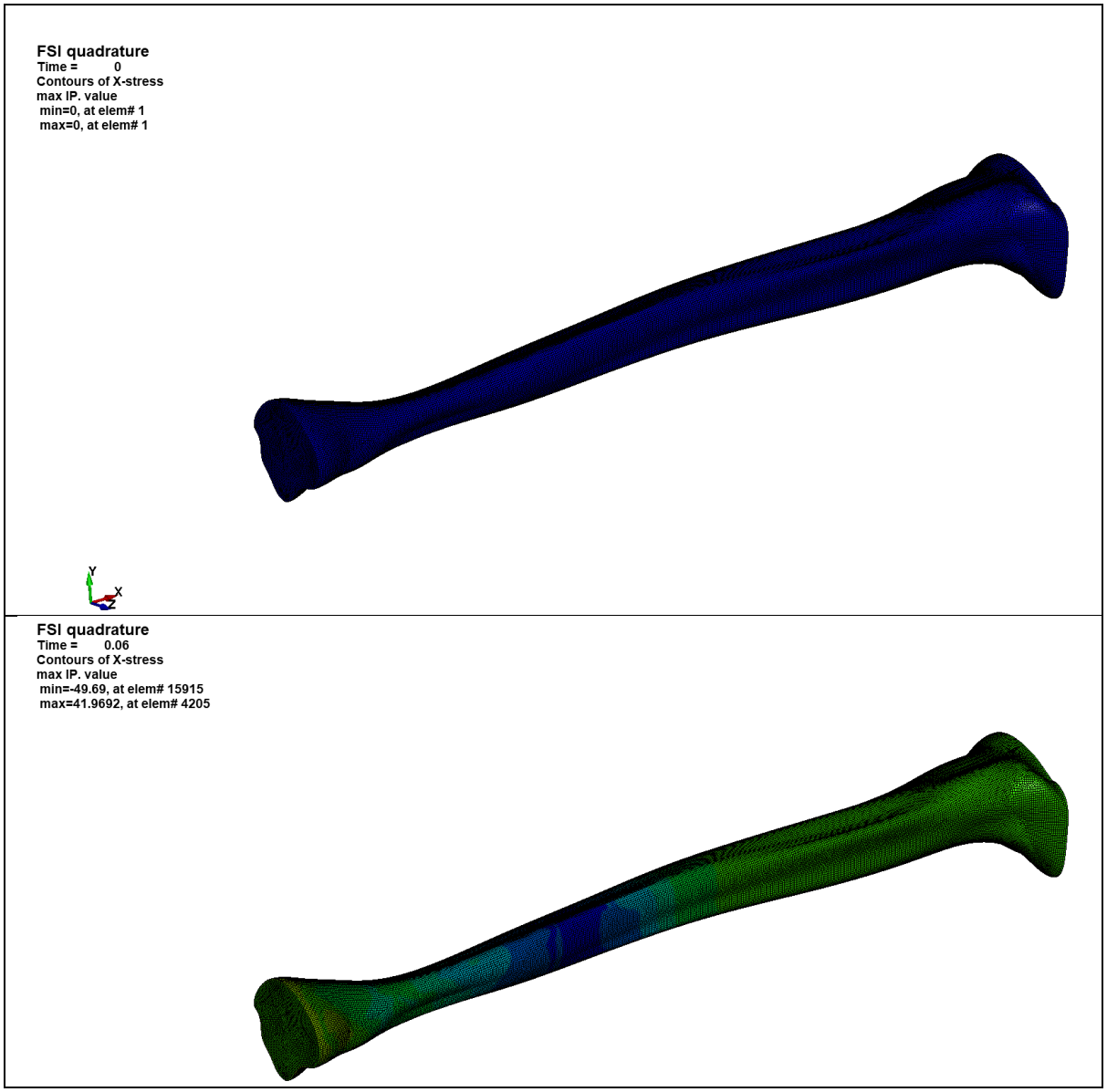

FSI quadrature
Time = 0.12
Contours of X-stress
max IP. value
min=-21.0445, at elem# 47460
max=84.0915, at elem# 29714

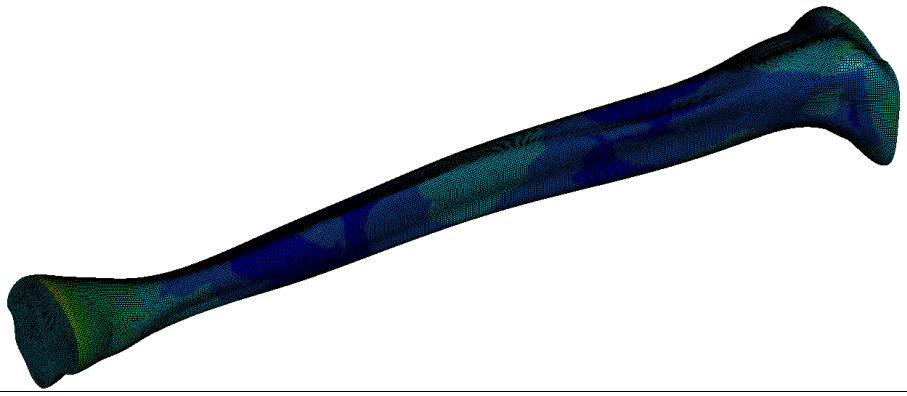

FSI quadrature
Time = 0.17999
Contours of X-stress
max IP. value
min=-20.6616, at elem# 11731
max=97.0835, at elem# 44698

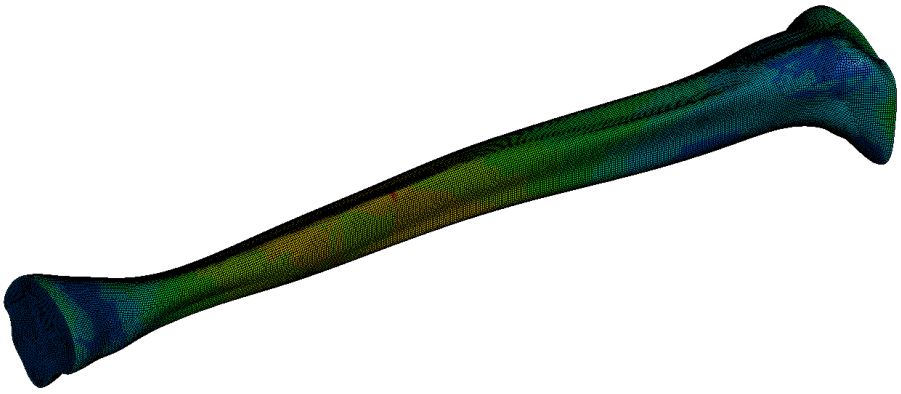

FSI quadrature
Time = 0.23999
Contours of X-stress
max IP. value
min=-25.2204, at elem# 12279
max=98.3132, at elem# 10702

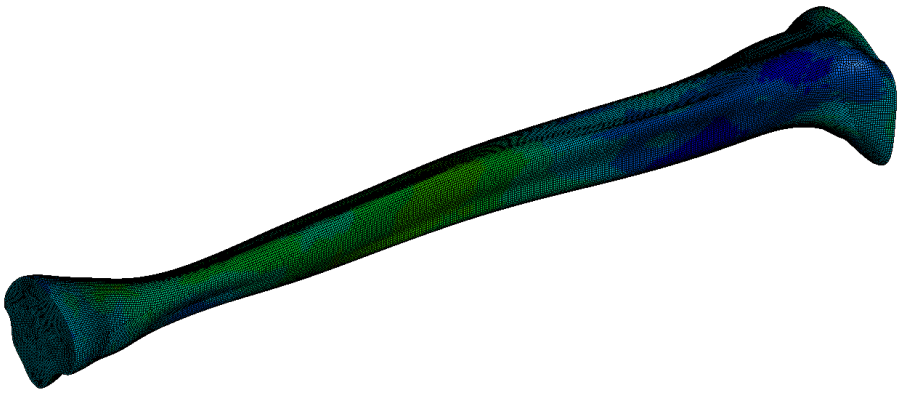

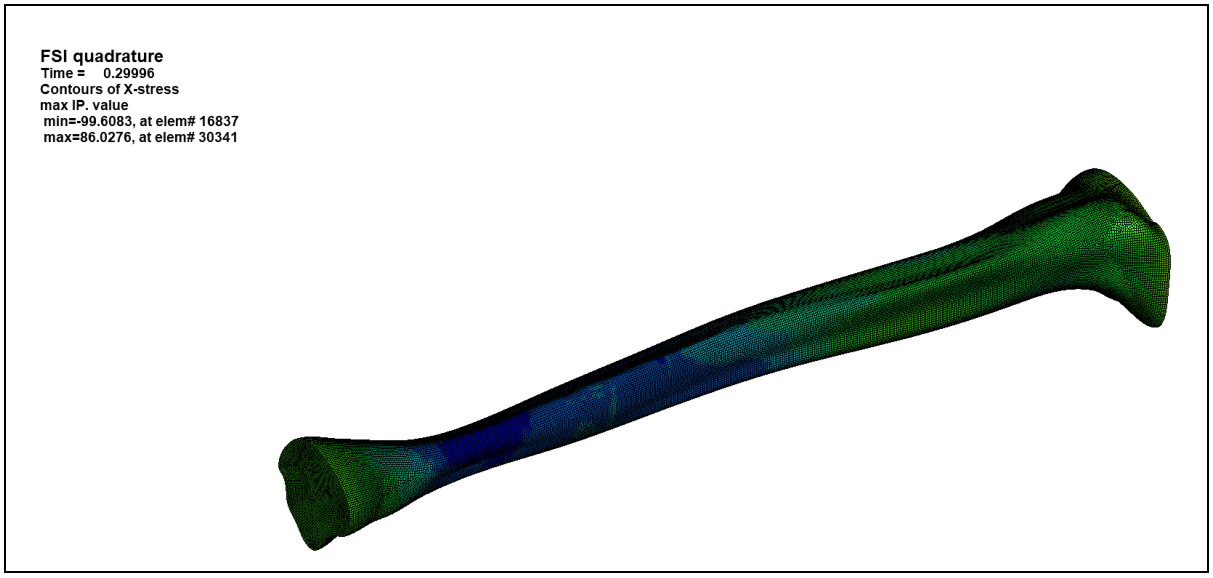
FSI quadrature
Time = 0.29996
Contours of X-stress
max IP. value
min=-99.6083, at elem# 16837
max=86.0276, at elem# 30341

Women Tibia

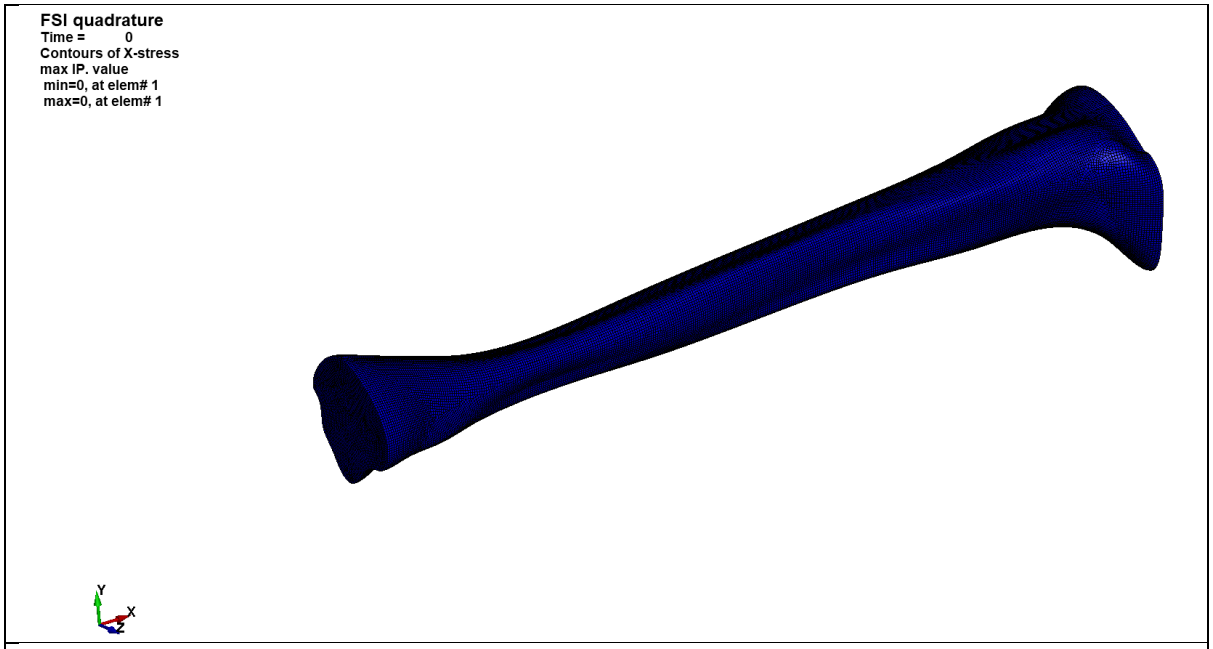
FSI quadrature
Time = 0
Contours of X-stress
max IP. value
min=0, at elem# 1
max=0, at elem# 1
Y
X
Z

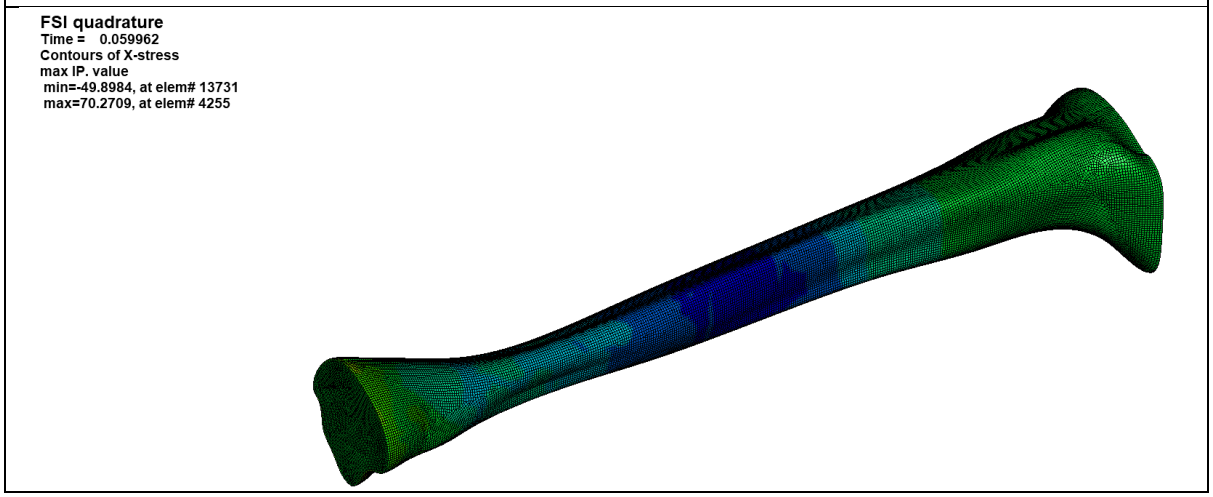
FSI quadrature
Time = 0.059962
Contours of X-stress
max IP. value
min=-49.8984, at elem# 13731
max=70.2709, at elem# 4255

FSI quadrature
Time = 0.11997
Contours of X-stress
max IP. value
min=-23.1163, at elem# 15341
max=88.4975, at elem# 24511

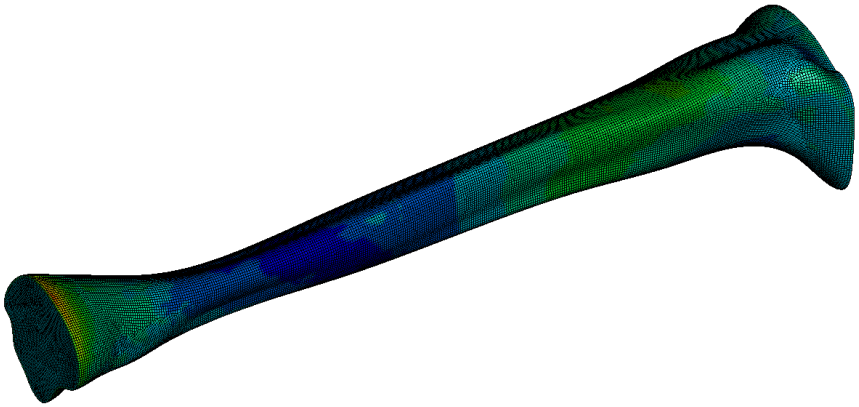

FSI quadrature
Time = 0.17998
Contours of X-stress
max IP. value
min=-3.8806, at elem# 12254
max=92.3893, at elem# 9169

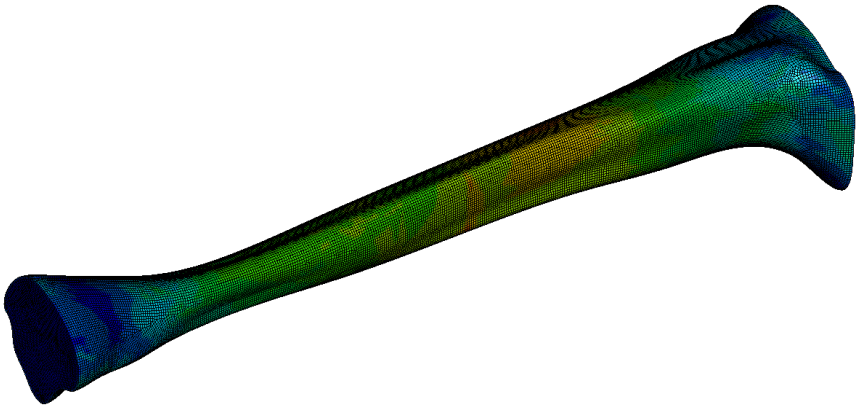

FSI quadrature
Time = 0.23999
Contours of X-stress
max IP. value
min=-64.4428, at elem# 14673
max=86.9783, at elem# 41078

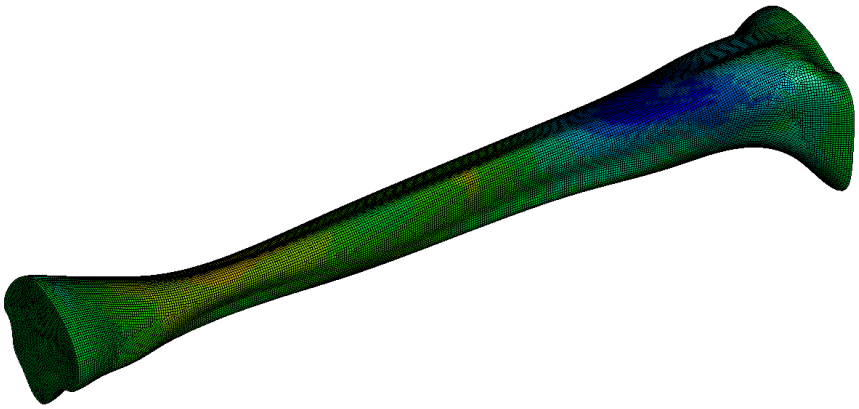

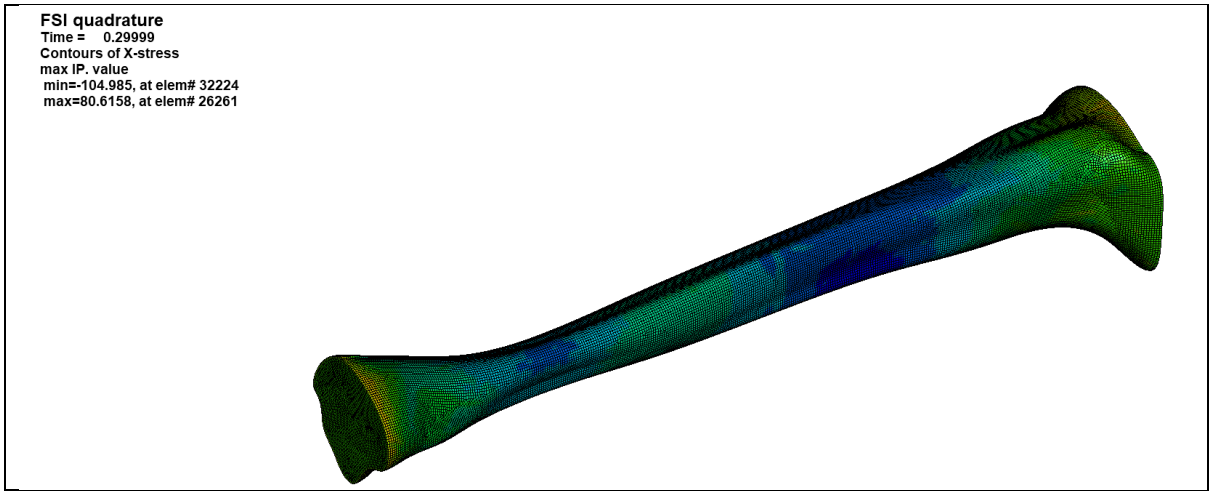

Deformable Plate Detonations

Men Tibia

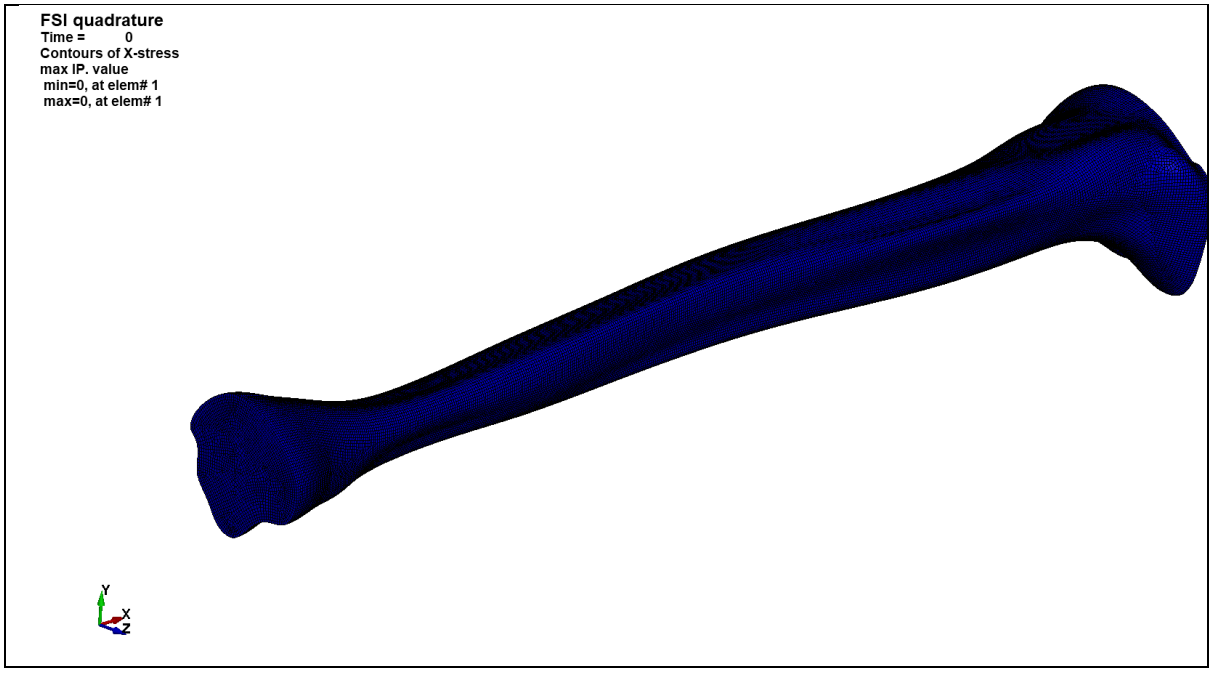

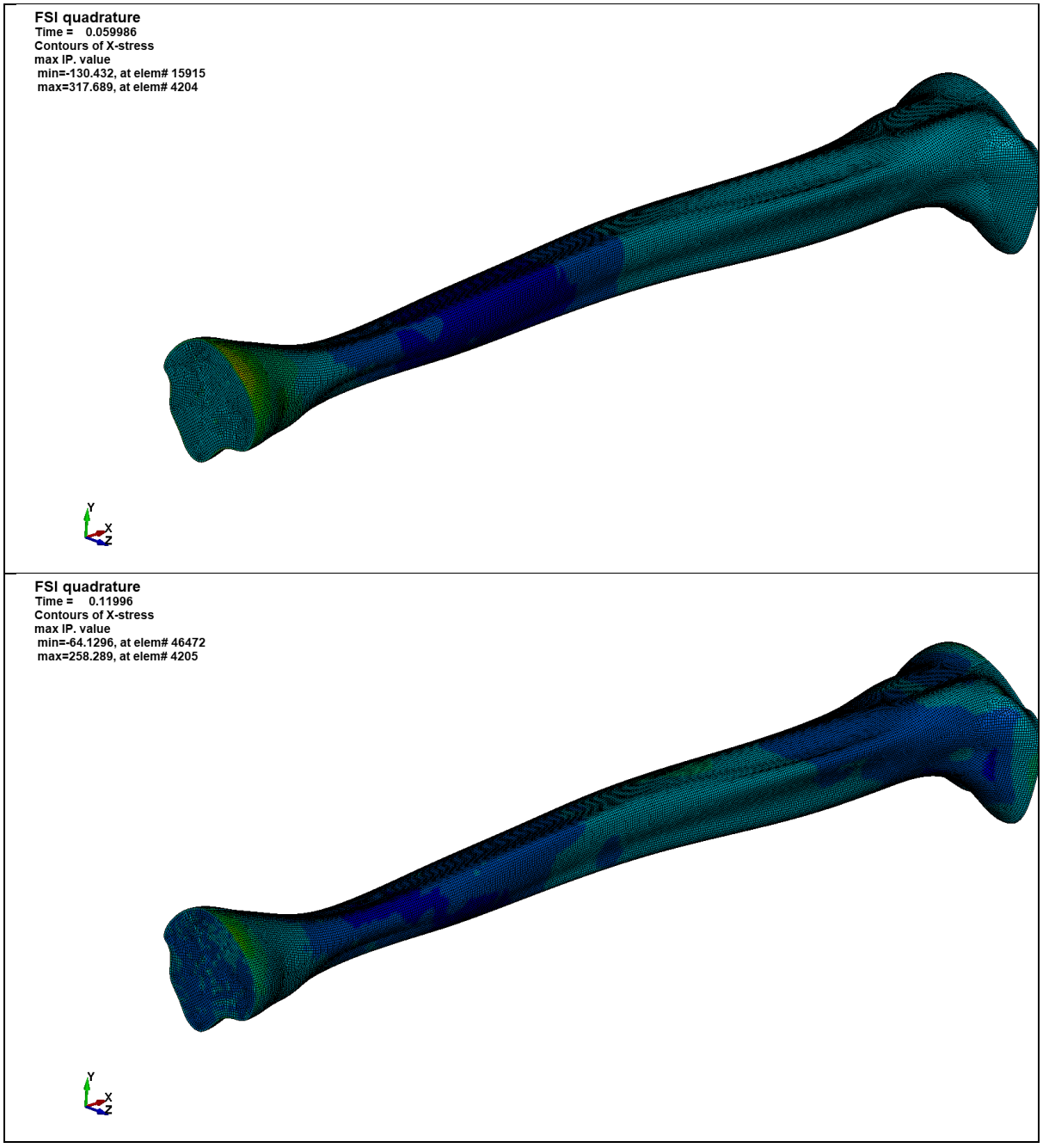
FSI quadrature
Time = 0.059986
Contours of X-stress
max IP. value
min=-130.432, at elem# 15915
max=317.689, at elem# 4204
Y
X
Z
FSI quadrature
Time = 0.11996
Contours of X-stress
max IP. value
min=-64.1296, at elem# 46472
max=258.289, at elem# 4205
Y
X
Z

FSI quadrature
Time = 0.17998
Contours of X-stress
max IP. value
min=-43.2959, at elem# 8089
max=225.861, at elem# 29712

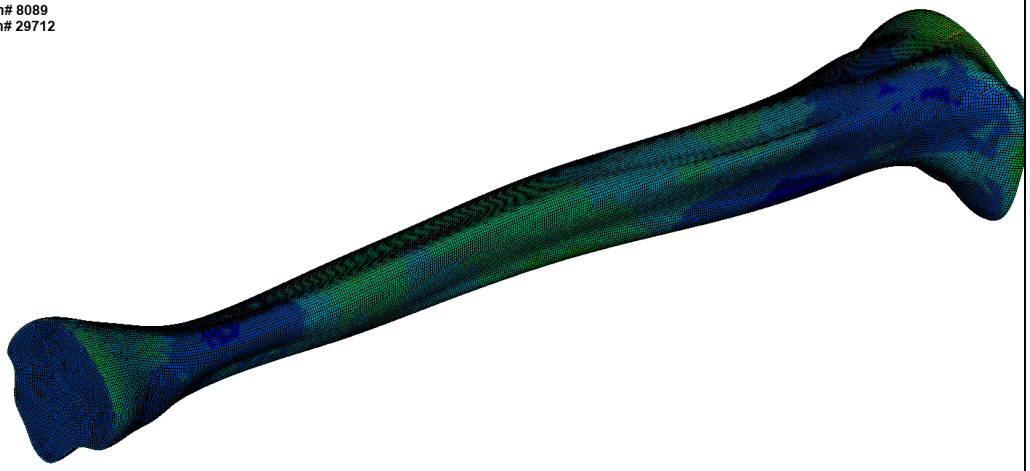

FSI quadrature
Time = 0.23995
Contours of X-stress
max IP. value
min=-75.395, at elem# 9430
max=144.697, at elem# 35986

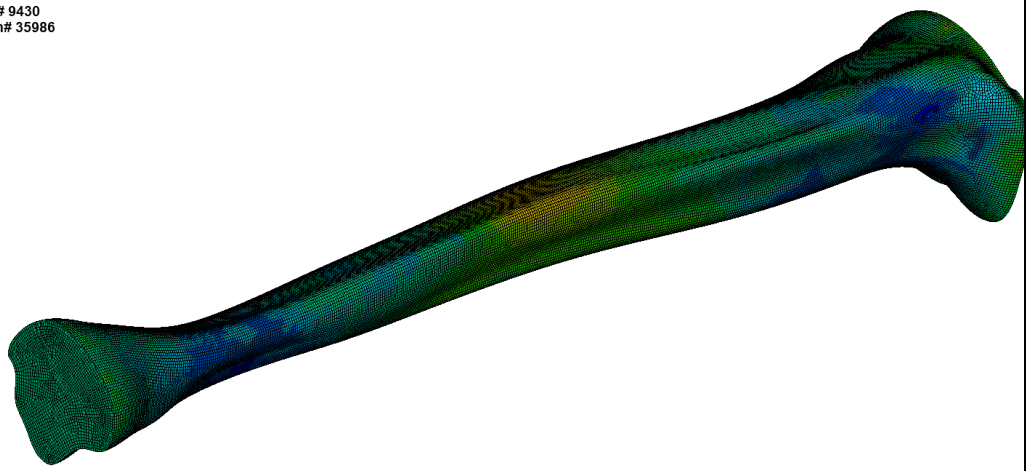

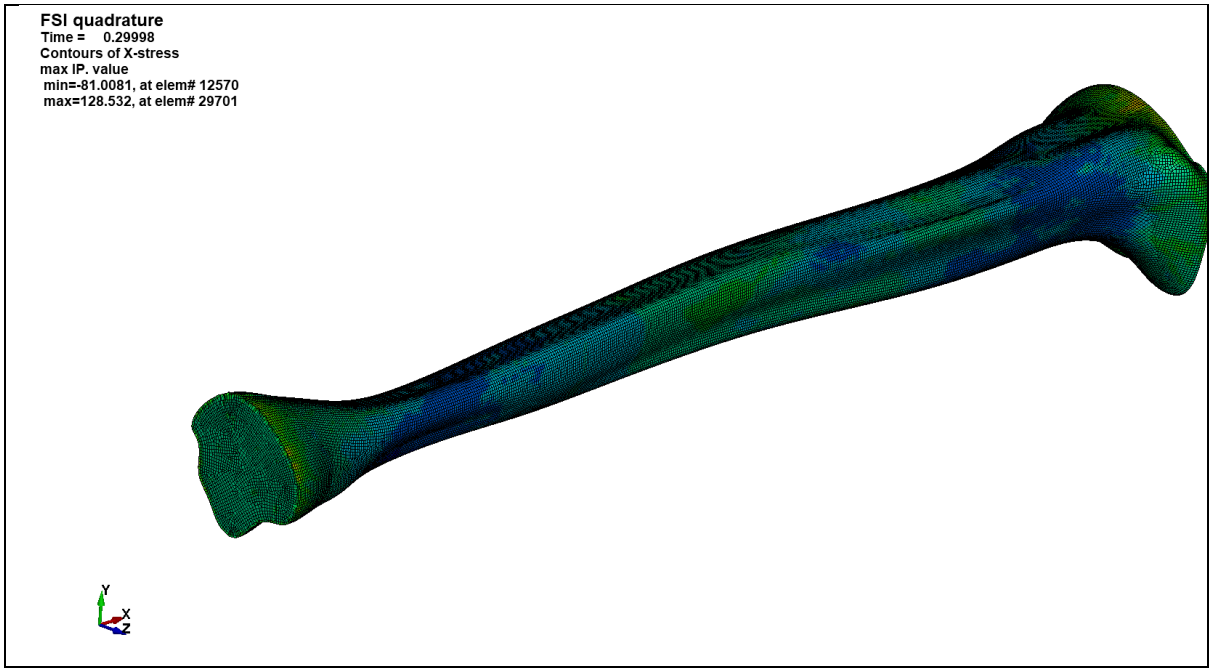
FSI quadrature
Time = 0.29998
Contours of X-stress
max IP. value
min=-81.0081, at elem# 12570
max=128.532, at elem# 29701
Y
X
Z

Women Tibia

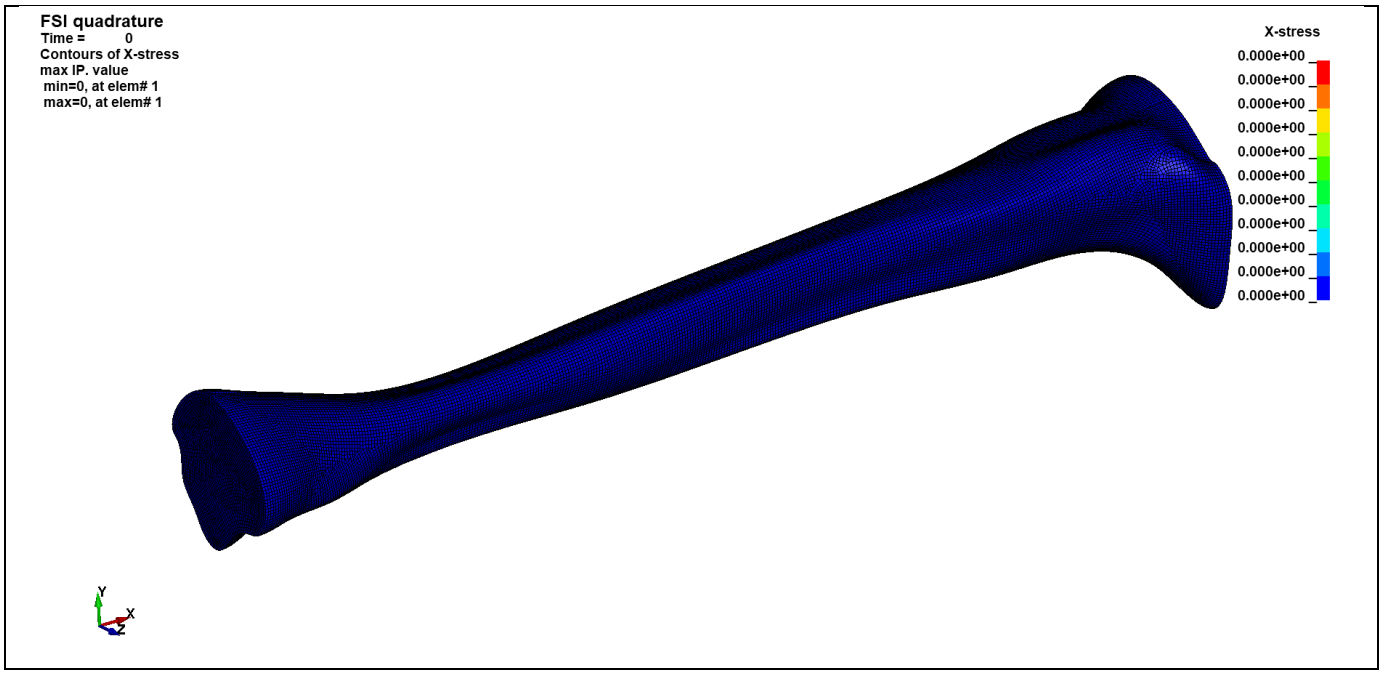
FSI quadrature
Time = 0
Contours of X-stress
max IP. value
min=0, at elem# 1
max=0, at elem# 1
X-stress
0.000e+00
0.000e+00
0.000e+00
0.000e+00
0.000e+00
0.000e+00
0.000e+00
0.000e+00
0.000e+00
0.000e+00
Y
X
Z

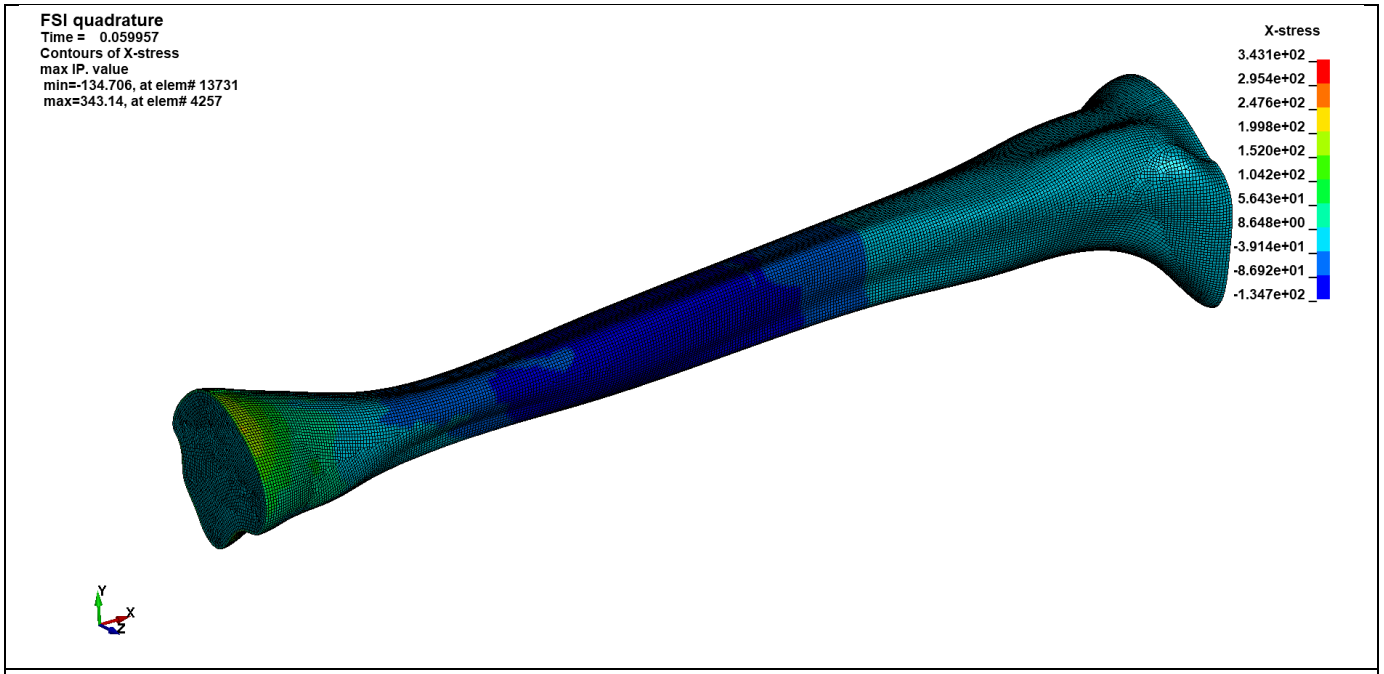
FSI quadrature
Time = 0.059957
Contours of X-stress
max IP. value
min=-134.706, at elem# 13731
max=343.14, at elem# 4257
X-stress
3.431e+02
2.954e+02
2.476e+02
1.998e+02
1.520e+02
1.042e+02
5.643e+01
8.648e+00
-3.914e+01
-8.692e+01
-1.347e+02
Y
X
Z

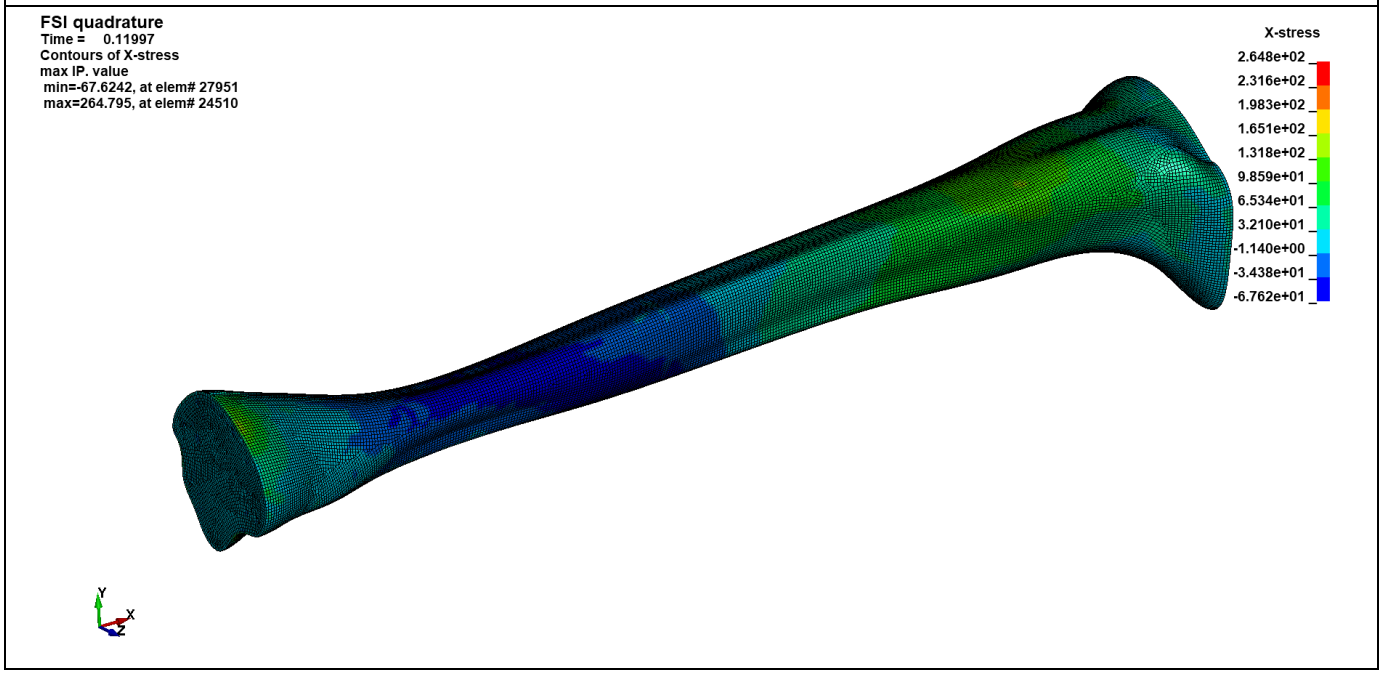
FSI quadrature
Time = 0.11997
Contours of X-stress
max IP. value
min=-67.6242, at elem# 27951
max=264.795, at elem# 24510
X-stress
2.648e+02
2.316e+02
1.983e+02
1.651e+02
1.318e+02
9.859e+01
6.534e+01
3.210e+01
-1.140e+00
-3.438e+01
-6.762e+01
Y
X
Z

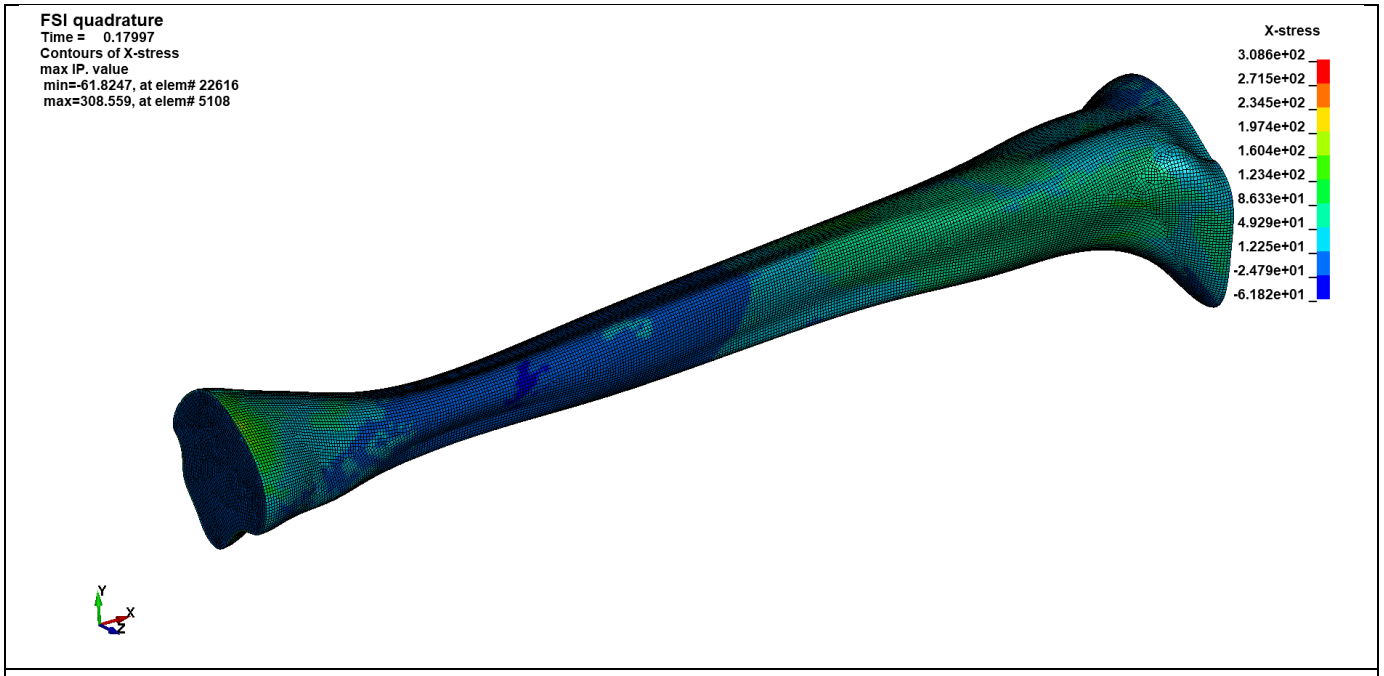
FSI quadrature
Time = 0.17997
Contours of X-stress
max IP. value
min=-61.8247, at elem# 22616
max=308.559, at elem# 5108
X-stress
3.086e+02
2.715e+02
2.345e+02
1.974e+02
1.604e+02
1.234e+02
8.633e+01
4.929e+01
1.225e+01
-2.479e+01
-6.182e+01
Y
X
Z

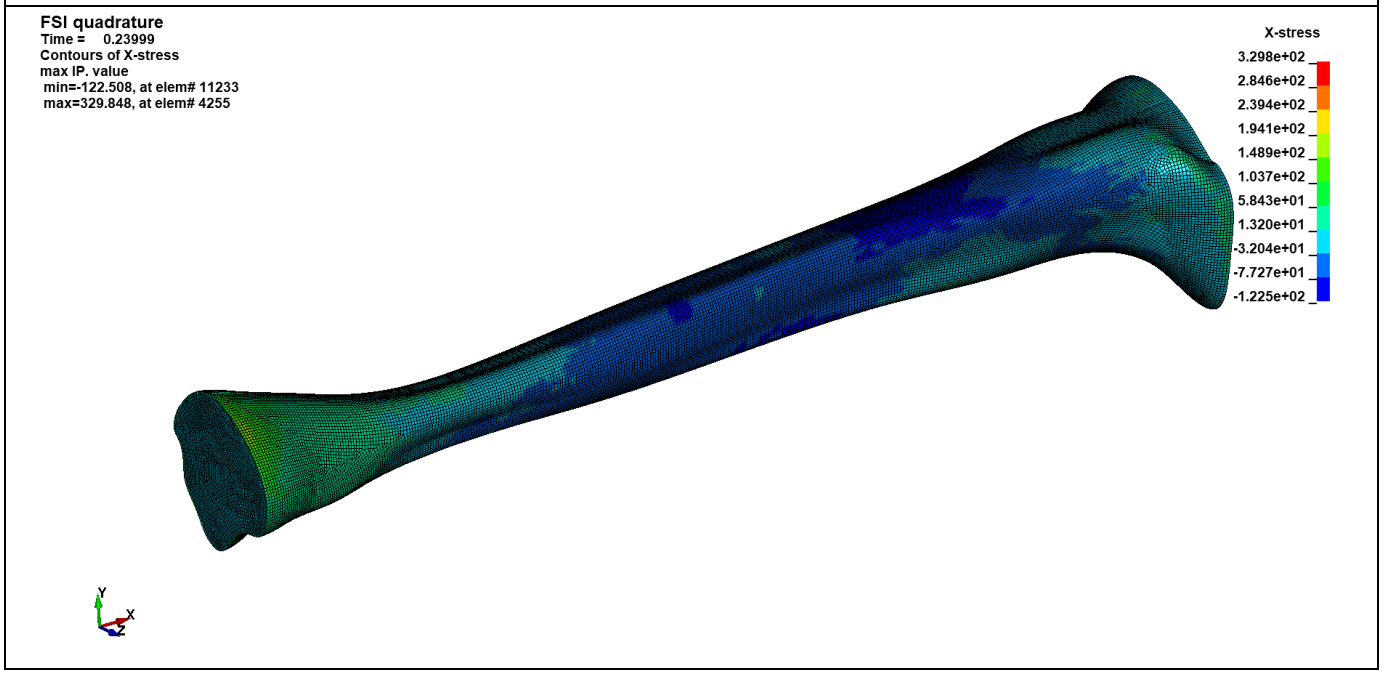
FSI quadrature
Time = 0.23999
Contours of X-stress
max IP. value
min=-122.508, at elem# 11233
max=329.848, at elem# 4255
X-stress
3.298e+02
2.846e+02
2.394e+02
1.941e+02
1.489e+02
1.037e+02
5.843e+01
1.320e+01
-3.204e+01
-7.727e+01
-1.225e+02
Y
X
Z

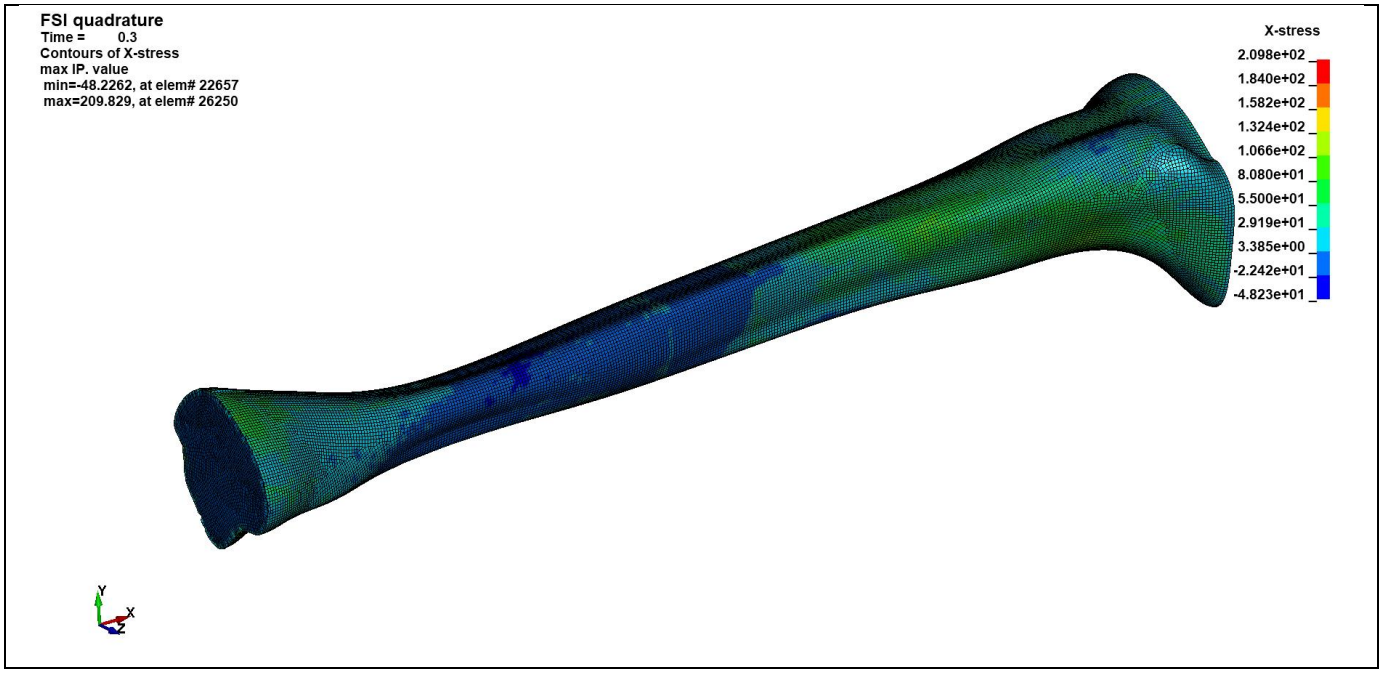
FSI quadrature
Time = 0.3
Contours of X-stress
max IP. value
min=-48.2262, at elem# 22657
max=209.829, at elem# 26250
X-stress
2.098e+02
1.840e+02
1.582e+02
1.324e+02
1.066e+02
8.080e+01
5.500e+01
2.919e+01
3.385e+00
-2.242e+01
-4.823e+01
Y
X
Z